IN-34
203618
p. 131

NASA Contractor Report 191573

Shock Tunnel Studies of Scramjet Phenomena

Supplement 8

R. J. Stalker, P. Hollis, G. A. Allen, G. T. Roberts,
S. Tuttle, R. J. Bakos, R. G. Morgan, M. V. Pulsonetti,
C. Brescianini, D. R. Buttsworth, K. Skinner, L. Porter,
D. Mee, J. Simmons, G. Kelly, N. Ward, and A. Neely

University of Queensland
St. Lucia, Queensland
Australia

Grant NAGW-674
December 1993

(NASA-CR-191573) SHOCK TUNNEL STUDIES OF SCRAMJET PHENOMENA, SUPPLEMENT 8 (Queensland Univ.) 131 p

N94-23532

Unclas

G3/34 0203618

National Aeronautics and
Space Administration

Langley Research Center
Hampton, Virginia 23681-0001

SHOCK TUNNEL STUDIES OF SCRAMJET PHENOMENA 1992
NASA GRANT NAGW 674 - SUPPLEMENT 8

Following the format of previous reports, this consists of a series of reports on specific projects, with a brief general introduction commenting on each report. The project reports follow the introduction in the order of the headings in the introduction.

The projects are considered under the headings "Program A", corresponding to work funded jointly by NAGW 674 and Australian sources, and "Program B", funded from Australian sources alone.

PROGRAM A

(i) Expansion Tube Studies

(a) Flow near the Diaphragm of an Expansion Tube

(R.J. Stalker, P. Hollis, G.A. Allen)

This started out to be a numerical study of expansion tube operation, with the aim of determining the minimum length of driver required. It soon became clear that the delay occasioned in opening the secondary diaphragm was a very important factor, and that this could not be estimated accurately, because of the flow through the opening diaphragm. Therefore this became the main objective of this project.

The conclusion reached by the study was that the flow was extremely difficult to model accurately, consisting of a mixed steady and unsteady expansion. It suggests that new emphasis be given to techniques for pre-opening the diaphragm.

(b) Influence of Secondary Diaphragm on Flow Quality in Expansion Tubes

(G.T. Roberts)

An experimental study of the effect of diaphragm mass on the flow. It showed that increasing diaphragm thickness may be expected to cause pitot pressure disturbances at the test section to occur earlier, as well as causing larger upstream static pressure disturbances. A somewhat surprising result was that allowing pre-deformation of the diaphragm has a beneficial effect on both the downstream pitot pressure and the upstream static pressure.

(c) Mass Loss of Test Gas in the Boundary Layer of an Expansion Tube

(R.J. Stalker)

What has been described as the "fountain effect" in expansion tubes is analysed here. This effect involves removal of gas from the test region by the boundary layer, thereby inducing an extra mass flow in the downstream direction to compensate for the mass loss. It is found that the effect is not likely to be important for practical flow conditions.

Thrust Balance Development
(Sean Tuttle)

This year was spent in perfecting the "twisted sting" configuration for removing the transverse bending modes and allowing thrust to be measured. A nozzle has been constructed, and subjected to satisfactory bench testing.

(iii) **Comparative Studies in T4 and Hypulse**

Effects of Oxygen Dissociation on Hypervelocity Combustion Experiments
(R.J. Bakos, R.G. Morgan & J. Tamagno)

A comparative experimental study involving combustion in T4 and in Hypulse was continued. An identical combustor model was tested in both facilities and, by appropriately choosing test conditions, it could be arranged that measured combustor duct pressures were sensitive to dissociation enhanced heat release alone. The difference between the two facilities was small, but this was due to the relatively high combustor inlet temperature used. Lower inlet temperatures are expected to yield a greater difference.

Axisymmetric Scramjet Thrust Production
(R.J. Bakos and R.G. Morgan)

An axisymmetric scramjet combustor and nozzle were tested in T4. It was found that the measured thrust agreed with computations.

PROGRAM B

Scaling and Ignition Effects in Scramjets
(M.V. Pulsonetti)

This is a more considered report on experiments which were conducted in 1991 on combustion in a large duct (48 mm x 100 mm x 1300 mm). Results were in qualitative agreement with theory, although at low pressure ignition delays were an order of magnitude less than predicted.

Hypersonic Ignition in a Scramjet
(A. Paull)

Combustion of Hydrogen and of Ethane in a 27 mm x 54 mm x 800 mm duct were compared. Ethane yielded the same pressure rise as Hydrogen at high stagnation enthalpies ($\geq$ 12 Mj kg^{-1}), but fell below it at low stagnation enthalpies ($\approx$ 9 Mj kg^{-1}). Ethane may suffer more from mixing limitations than Hydrogen.

Modelling of a Scramjet Flow using various Turbulence Models
(C. Brescianini and R. G. Morgan)

Testing of three turbulence models, of increasing degree of sophistication, by predicting the flow in a scramjet combustor. None of the models predicted the experimental results accurately over the entire length of the combustion duct.

Shock Interactions with Hypersonic Mixing Layers - Steady Flow Analysis and Experiments
(D.R. Buttsworth and R.G. Morgan)

A study of the interaction of a shock wave with the variable Mach number flow field produced by a mixing layer.

A Time-of-flight Mass Spectrometer for High Speed Flows
(K. Skinner and R.J. Stalker)

Results with a time-of-flight mass spectrometer are presented. The example studied is the detection of driver gas in a shock tunnel, and the development of driver gas concentration. However, the method can be applied to measurement of species concentration during the test flow period.

Measuring the effect on Drag produced by Nose Bluntness on a Cone in Hypervelocity Flow
(L. Porter, D. Mee and J. Simmons)

This reports work on the extension of the stress wave balance to measure the effect of nose blunting on the drag of a slender cone.

A Study of Reynold's Analogy in Hypersonic Boundary Layer using a new Skin Friction Gauge
(G. Kelly, A. Paull and J. Simmons)

A comparison between skin friction and heat transfer measurements on a flat plate, using the skin friction gauge which has been reported previously.

Energy Redistribution of Non Equilibrium Hypervelocity Flow in a Scramjet Duct
(N. Ward and R.J. Stalker)

Flow visualisation of nitrogen flow in a two dimensional intake and comparison with calculations.

Flow Measurements and Calibration of a Superorbital Expansion Tube
(A. Neely and R.G. Morgan)

This is a pilot study of an expansion tube in a configuration aimed at producing flow speeds in excess of 10 $km.s^{-1}$. Though the response of pressure transducers limits the value of the diagnostics used, it appears that a usable test flow has been produced at speeds of 13 $km.s^{-1}$.

FLOW NEAR THE DIAPHRAGM OF AN EXPANSION TUBE

(1 R.J. Stalker, P. Hollis and G.A. Allen)

1. Introduction

In the classical analysis of expansion tube flow, it is assumed that the secondary diaphragm is instantaneously removed from the flow upon arrival of the primary shock, and the supersonic flow behind that shock is subjected to a simple wave unsteady expansion which produces the test flow.

It is known that the finite mass of the secondary diaphragm must cause the flow to be different to this, and a more sophisticated model treats the diaphragm as a piston, which is set in motion by the arrival of the primary shock. Since the diaphragm is initially stationary, the shock reflects as from a rigid wall and propagates upstream. Then, as the diaphragm accelerates, expansion waves are generated which also propagate upstream. These continually overtake the shock wave and weaken it until, after a sufficiently long time, the reflected shock wave disappears. If the time to reach this state is sufficiently short with respect to the overall operating time of the expansion tube, then the flow in the tube approaches that produced by the classical model, with the differences that there is a delay occasioned by the need to accelerate the diaphragm, that the test gas close to the diaphragm suffers an increase in entropy due to the reflected shock, and that this gas may also suffer a change in composition due to the same cause. The importance of these effects depends on how much of the test gas is affected, and this can be minimised by minimising the mass of the diaphragm.

The purpose of the present investigation is to make a preliminary exploration of the consequence of bringing the model a step closer to physical reality. When the diaphragm is impacted by the primary shock, it not only moves but also ruptures, so that during the process of acceleration, it is also opening. This may take the form of the "petalling" of the diaphragm, or the gradual separation of the pieces of shattered diaphragm. Either way the diaphragm allows flow through itself - it becomes a "leaky" diaphragm, and it is this situation that we analyse.

2. Hueristic Analysis

It is convenient to begin by considering the motion of a free diaphragm (or a piston) accelerating into a vacuum under the action of a pressure p. The diaphragm moves in a tube of constant area, which is infinitely long in both directions. Therefore, as shown in Fig. 1., there is an unsteady expansion of gas upstream of the diaphragm from the undisturbed pressure and speed of sound p_r and u_r. This is a good approximation to the situation which prevails for a time after shock reflection if the diaphragm is not leaky.

---

1 Stalker, R.J. "An approximate theory of gun tunnel behaviour". Journ. Fl. Mech., Vol. 22, pp 657-670, 1965.

PRECEDING PAGE BLANK NOT FILMED

4 PAGE INTENTIONALLY BLANK

Thus the pressure at the diaphragm is given by the unsteady simple wave relation

$$P/P_R = \left(1 - \frac{\gamma - 1}{2} \frac{u}{a_R}\right)^{2\gamma / (\gamma - 1)}$$

where u is the velocity of the diaphragm, and γ the ratio of specific heats. The equation of motion for the diaphragm may therefore be written as

$$\alpha \frac{du}{dt} = \rho_R \left(1 - \frac{\gamma - 1}{2} \frac{u}{a_R}\right)^{2\gamma / (\gamma - 1)} ,$$

and this can be solved (eg. ref. 1) to yield the co-ordinates of the diaphragm trajectory as

$$x = \frac{2}{\gamma + 1} \frac{\alpha a_R^2}{P_R} \left[1 - \left(1 - \frac{\gamma + 1}{2} \frac{u}{a_R} \right) \left(1 - \frac{\gamma - 1}{2} \frac{u}{a_R} \right)^{-(\gamma + 1) / (\gamma - 1)} \right] \quad (1)$$

$$t = \frac{2}{\gamma + 1} \frac{\alpha a_R}{P_R} \left[\left(J - \frac{\gamma - 1}{2} \frac{u}{a_R} \right)^{-(\gamma + 1) / (\gamma - 1)} - 1 \right] \quad (2)$$

To yield a gain in stagnation enthalpy across an unsteady expansion it is necessary to use quite high values of u/a_R. Thus with $u/a_R = 2.0$ and $\gamma = 1.4$ there is only a 16% gain in stagnation enthalpy - for a gain by a factor of two, $u/a_R = 3$. Since the gain in stagnation enthalpy is the prime reason for choosing the expansion tube mode of operation, it seems reasonable to assume that $u/a_R = 3$ or greater. With a diaphragm of mylar 25 μ thick (0.001"), $\alpha = 6.0 \times 10^{-2}$ kg.m^{-2}, and with $a_R = 2000$ ms^{-1} and $P_R = 10$ MPa, equations (1) and (2) indicate that $u/a_R = 3$ at distance $x = 12.4$ m from the initial position of the diaphragm, at time $t = 2.4 \times 10^{-3}$ sec.

We now consider the flow through the diaphragm if it is leaky. In the early stages of the diaphragm motion, $u/a_R \leq 1$, so that the pressure and speed of sound, upstream of the diaphragm may be taken as the undisturbed values P_R and a_R. The "leakiness" of the diaphragm is represented as a single orifice in the diaphragm, of area b(t) A, where A is the area of the tube, and b(t) is a factor which generally varies with time, but for the present purpose is assumed to be constant. The flow at the orifice will be sonic and, with $\gamma = 1.4$, the mass flow rate through the diaphragm will be

$$\dot{m} = 0.578\ \rho_R\ a_R\ b(t)\ A, \qquad (3)$$

where ρ_R is the density in the undisturbed region.

The mass of gas in the test region of the expansion tube is $\rho_t AL$, where L is the length of the slug of gas constituting the test region, and ρ_t is the density in the test region, given by

$$\rho_t / \rho_R = \left(1 - \frac{\gamma - 1}{2}\ \frac{\mu}{a_R}\right)^{2/(\gamma - 1)},$$

and the time for this mass to pass through the diaphragm is

$$\Delta\tau = 1.73 \left(1 - \frac{\gamma - 1}{2}\ \frac{u}{a_R}\right)^{2/(\gamma - 1)}\ \ell/a_R\ b(t)$$

If ℓ = 2 m, a_R = 2000 ms^{-1}, u/a_R= 3, and we take the diaphragm as 10% open (i.e. b(t) = 0.1) then $\Delta t = 177 \times 10^{-6}$ sec.

These examples are fairly typical, involving values of diaphragm thickness, test slug length and other parameters which may be used in practice. They suggest that the behaviour of the diaphragm as it accelerates and ruptures may have an important influence on the state of the test gas. The turbulence induced by the fragments of diaphragm may affect the quality of flow produced as the test gas passes through the diaphragm, although the high quality of heat transfer records obtained in expansion tubes suggest that this is probably not the case.

The fact that an amount of gas sufficient to constitute the test flow passes through the diaphragm in a time which is an order of magnitude shorter than that required for the diaphragm (or fragments thereof) to reach the test velocity suggests that it may be necessary to think in terms of a different model for producing the test flow. Instead of being processed by an unsteady expansion, the test gas may first pass through a quasi-steady expansion before it is accelerated to the test velocity by the action of the gas which follows it. This could change the chemical state of the test gas, though it should be remembered that the quasi-steady expansion takes place from a stagnation enthalpy which is less than that of the test flow, and this will tend to reduce the effect of the history of the test flow on its chemical state.

3. Numerical Modelling

To explore this effect in somewhat more detail, a numerical model has been constructed.

Due to the nature of the physical processes involved in the bursting of the diaphragm and the subsequent complex flow pattern, simple models of the bursting process have been developed which will provide some estimate of the flow during this process.

The model for the bursting of the diaphragm itself is just to allow the area of the diaphragm to reduce from fully covering the tube to some minimum area in an exponential fashion. The mass of the diaphragm remains constant and it is assumed that the diaphragm remains in one plane throughout the process, i.e. the diaphragm fragments all travel at the same velocity. The time for the burst process to occur and also the reduction in area that occurred due to the diaphragm burst could be specified.

To calculate the velocity and acceleration of the diaphragm, the pressure on either side of the diaphragm must be found. This was found by an iterative procedure. The average velocity of the gas on the upstream and downstream sides of the diaphragm were calculated by assuming that sonic flow occurred through the open area of the diaphragm and the remainder of the flow (over the diaphragm itself) moved with the velocity of the diaphragm. These two velocities were then averaged taking into account the appropriate areas. From this average velocity, the average pressure on either side of the diaphragm could be calculated using simple wave relations and then the velocity of the diaphragm could again be estimated.

The flow upstream of the diaphragm was calculated using the wave model developed and solved by G. Allen. Bursting of the diaphragm was included in the model by forcing the velocity of the gas at the diaphragm to be the average velocity calculated by the above procedure.

Two simple models were developed to examine the location of the interface between the intermediate and acceleration section fluids. Both assumed that the mass flow passing through the diaphragm in any given timestep is known because sonic velocity is assumed to exist at the diaphragm. The models then considered two extreme situations, thus:-

1. Model 1

By assuming an isentropic expansion back to the original area of the tube, the density of the expanded mass can be found hence the length which this fluid parcel will take up can be calculated. These lengths were summed sequentially and an estimate of the location of the fluid interface can be found. No correction was made for variation of the length of each mass parcel as it progressed away from the diaphragm, i.e. each mass parcel is assumed to have constant volume.

2. Model 2

The isentropic expansion was continued until the density of the gas was equal to the density of the test flow. Then, knowing the mass which had passed through the diaphragm, the volume and therefore the length of the tube which was taken up by this mass could be calculated.

Test Conditions

Test conditions were chosen to match a well documented experimental case with Helium as the driver and test gases (NASA Tech. Paper 1317 "Experimental Perfect - Gas Study of Expansion-Tube Flow Characteristics". J.L. Shinn & C.G. Miller III)

	Sonic velocity (m/s)	Pressure (Pa)	Gamma
Driver	1068.87	33×10^6	1.6667
Intermediate	1019.3	690	1.6667
Acceleration	1019.3	16	1.6667

Primary diaphragm location: 2.44 metres
Seconday diaphragm location: 9.93 metres
Test section location: 24 metres
Pipe radius: 0.0762 metres
Secondary diaphragm thickness: 38×10^{-6} metres (Mylar diaphragm)
Secondary diaphragm density: 8.52×10^{-3} kg/m^3

PROGRAM OUTPUT

The main outputs of the program are:

(a) The path of the shockwave reflected from the secondary diaphragm
(b) The path of the secondary diaphragm
(c) The path of the interface between the intermediate and acceleration section fluids, for models 1 and 2.
(d) The mach line generated from the intersection between the shockwave transmitted from the primary diaphragm and the reflected shockwave from the secondary diaphragm.

The simulation has been run for burst times of 0.15 ms with area reductions of 10, 25, 50 and 75%. One further simulation was performed for a burst time of 0.30 ms and 25% area reduction for comparison. The results of these simulations are shown in the figures. The final figure is a simulation of the diaphragm acting as a frictionless piston, i.e. it does not burst but is allowed to move.

Figure Notation
Burst times

Since the area reduction is exponential, the burst time used in the calculations is the time for the area to reach 90% of its maximum reduction.

Area ratio

The area reduction figure quoted in the attached figures is the amount by which the area of the diaphragm has been reduced by the bursting process, $(A_{initial}-A_{final})/A_{initial}$. Thus, a 75% reduction indicates that the final diaphragm area is 25% of the initial area.

4. Results

The outstanding feature of the results is the wide disparity between the position of the acceleration gas - test gas interface as predicted by Model 1 and Model 2. Both models are apparently unrealistic. Model 1 because it does not allow for what is clearly a massive expansion to the test conditions, and Model 2 because it does not allow for large amounts of gas which have passed through the diaphragm but are not expanded to the test conditions. (This is witnessed by the velocity of the interface predicted by this model, which is far in excess of any reasonable value). It follows that the unsteady expansion after the diaphragm, which has been neglected in both models, is of prime importance.

The motion of the diaphragm tends to slow down as the opening increases. This motion depends on the velocity of the gas at the opening, and is calculated by assuming a simple wave compression from the undisturbed state in the acceleration tube on the downstream side of the diaphragm. It will therefore be unaffected by the choice between Model 1 and Model 2.

The overall picture which the results present are of a mixed steady and unsteady expansion of the test gas, with the accelerating remains of the diaphragm located somewhere in the unsteady expansion. It is difficult to analyse such a flow, and a new analysis would be required for each diaphragm thickness and each set of test conditions. To avoid the uncertainties associated with this, it may be better to think of means of removing the diaphragm before the shock wave arrives.

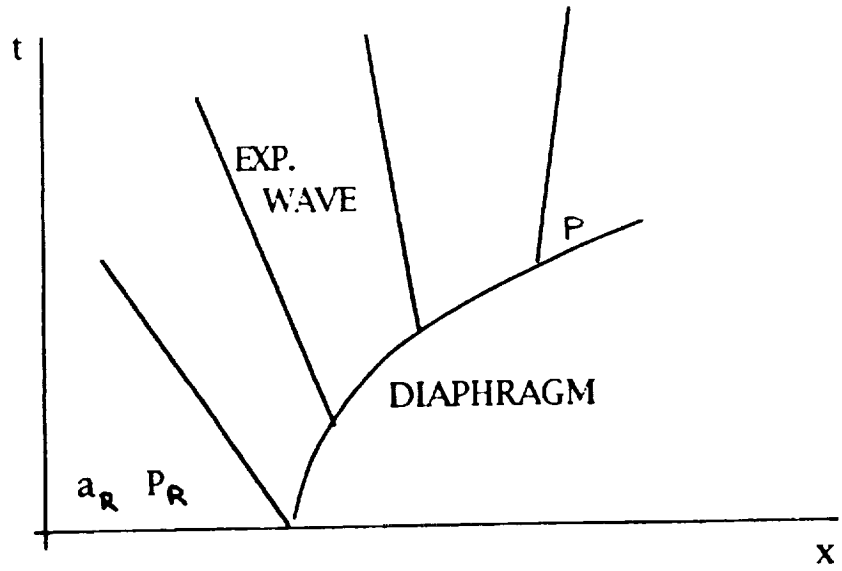

Wave Diagram for Diaphram Acceleration

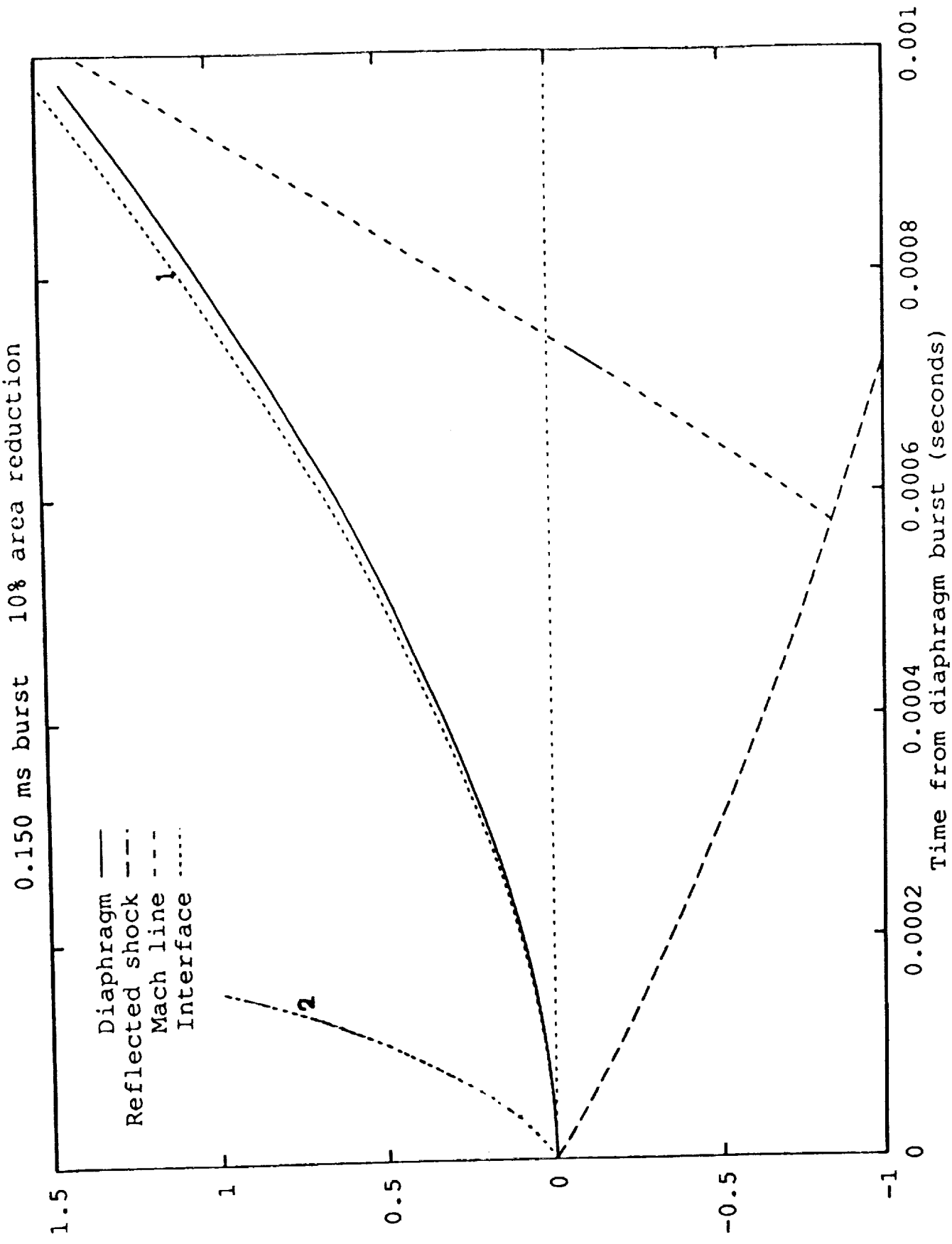
Distance from diaphragm burst (metres)
0.150 ms burst 10% area reduction
Diaphragm
Reflected shock
Mach line
Interface
1
2
1.5
1
0.5
0
-0.5
-1
0
0.0002
0.0004
0.0006
0.0008
0.001
Time from diaphragm burst (seconds)

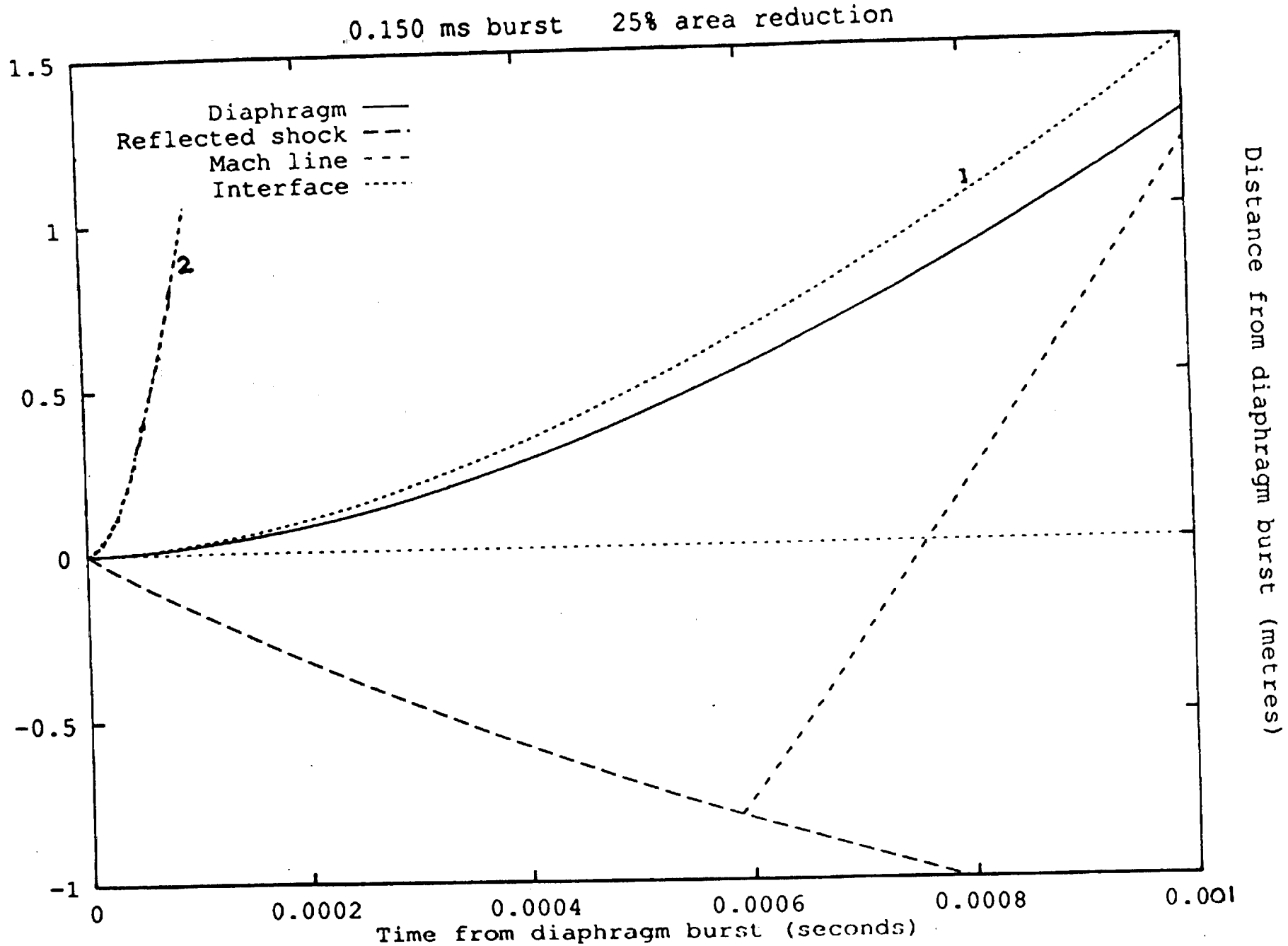
0.150 ms burst 25% area reduction
Diaphragm
Reflected shock
Mach line
Interface
1
2
1.5
1
0.5
0
-0.5
-1
0
0.0002
0.0004
0.0006
0.0008
0.001
Time from diaphragm burst (seconds)
Distance from diaphragm burst (metres)

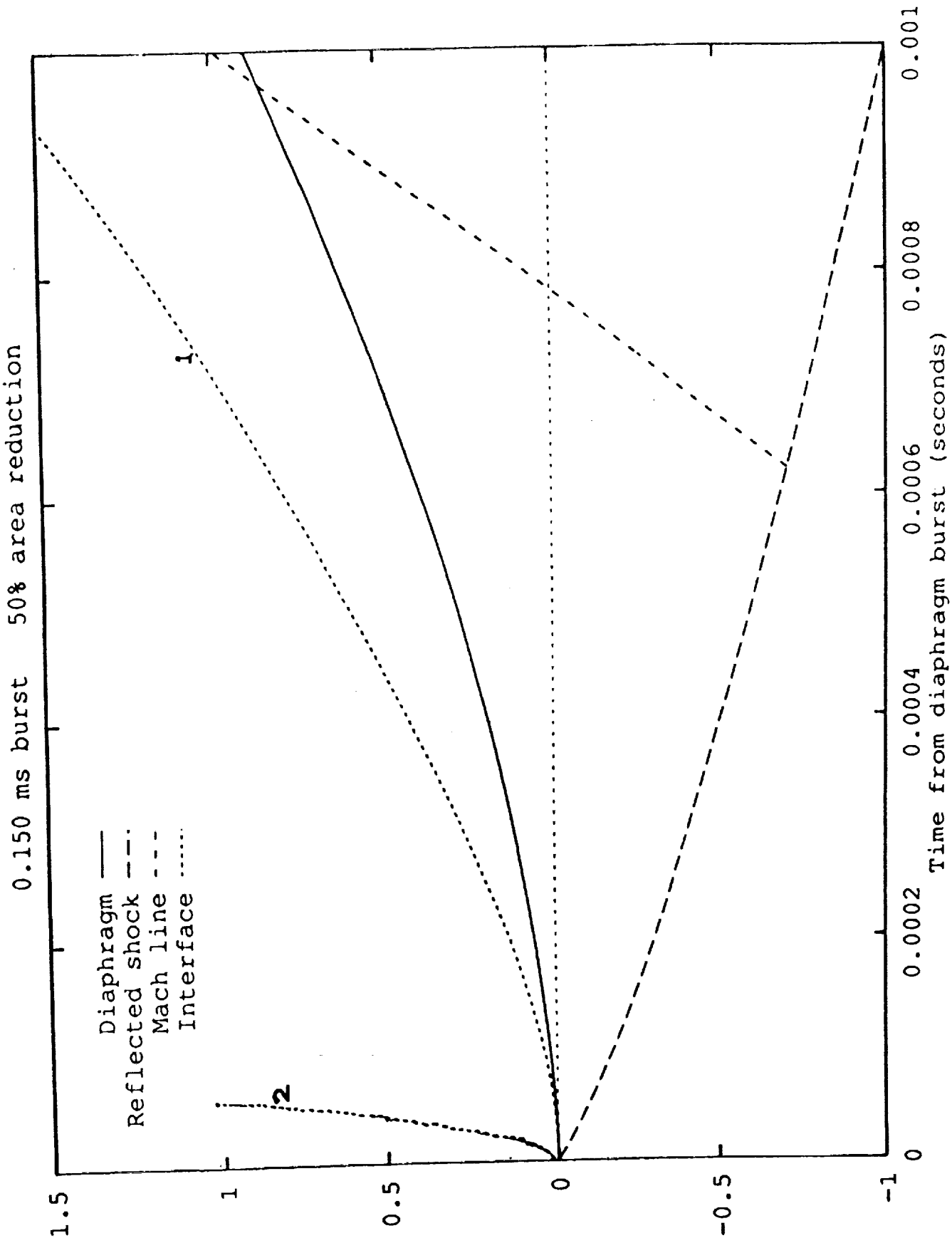
Distance from diaphragm burst (metres)
0.150 ms burst 50% area reduction
Time from diaphragm burst (seconds)
Diaphragm
Reflected shock
Mach line
Interface
1
2
1.5
1
0.5
0
-0.5
-1
0
0.0002
0.0004
0.0006
0.0008
0.001

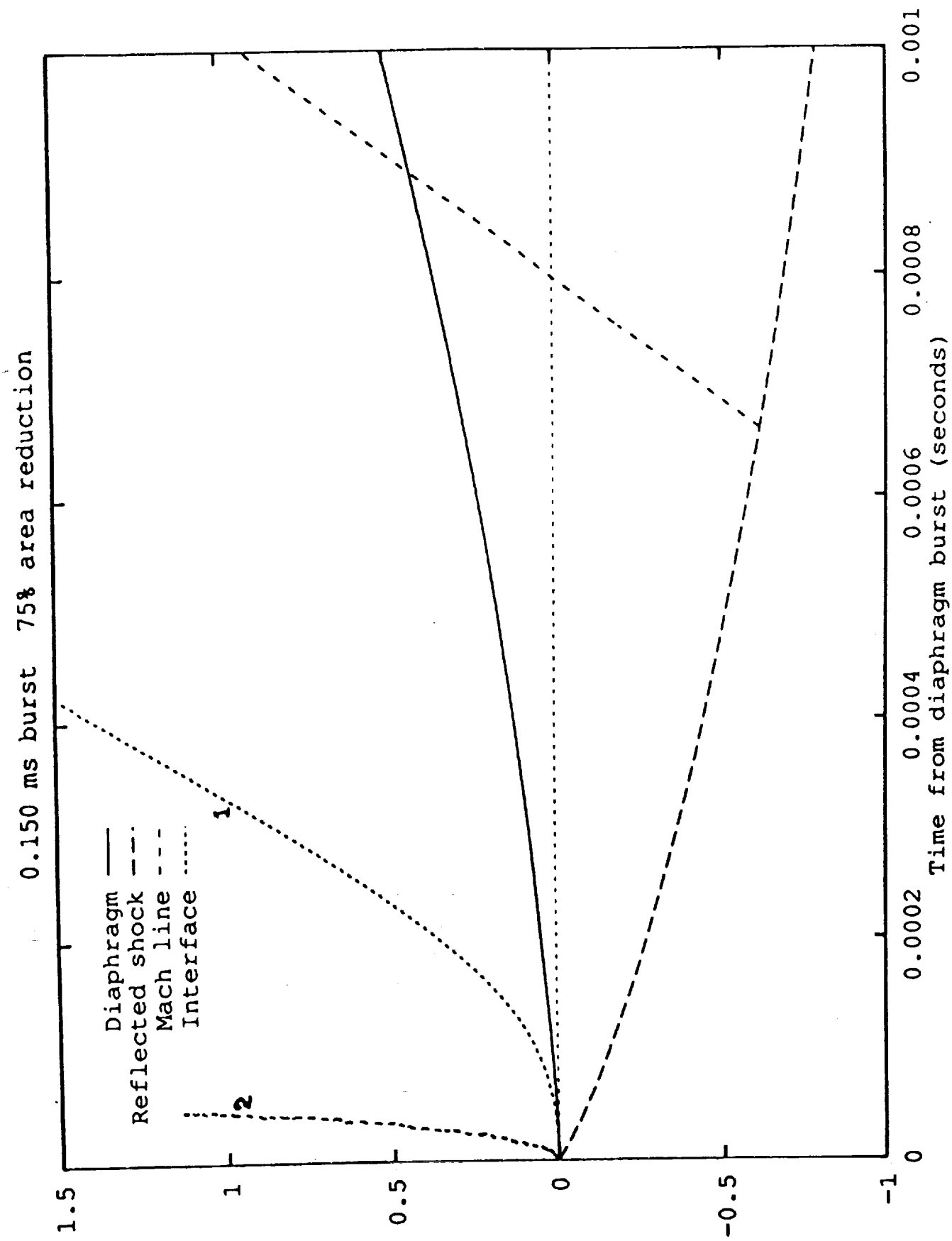
Distance from diaphragm burst (metres)
0.150 ms burst 75% area reduction
Diaphragm
Reflected shock
Mach line
Interface
1
2
1.5
1
0.5
0
-0.5
-1
0
0.0002
0.0004
0.0006
0.0008
0.001
Time from diaphragm burst (seconds)

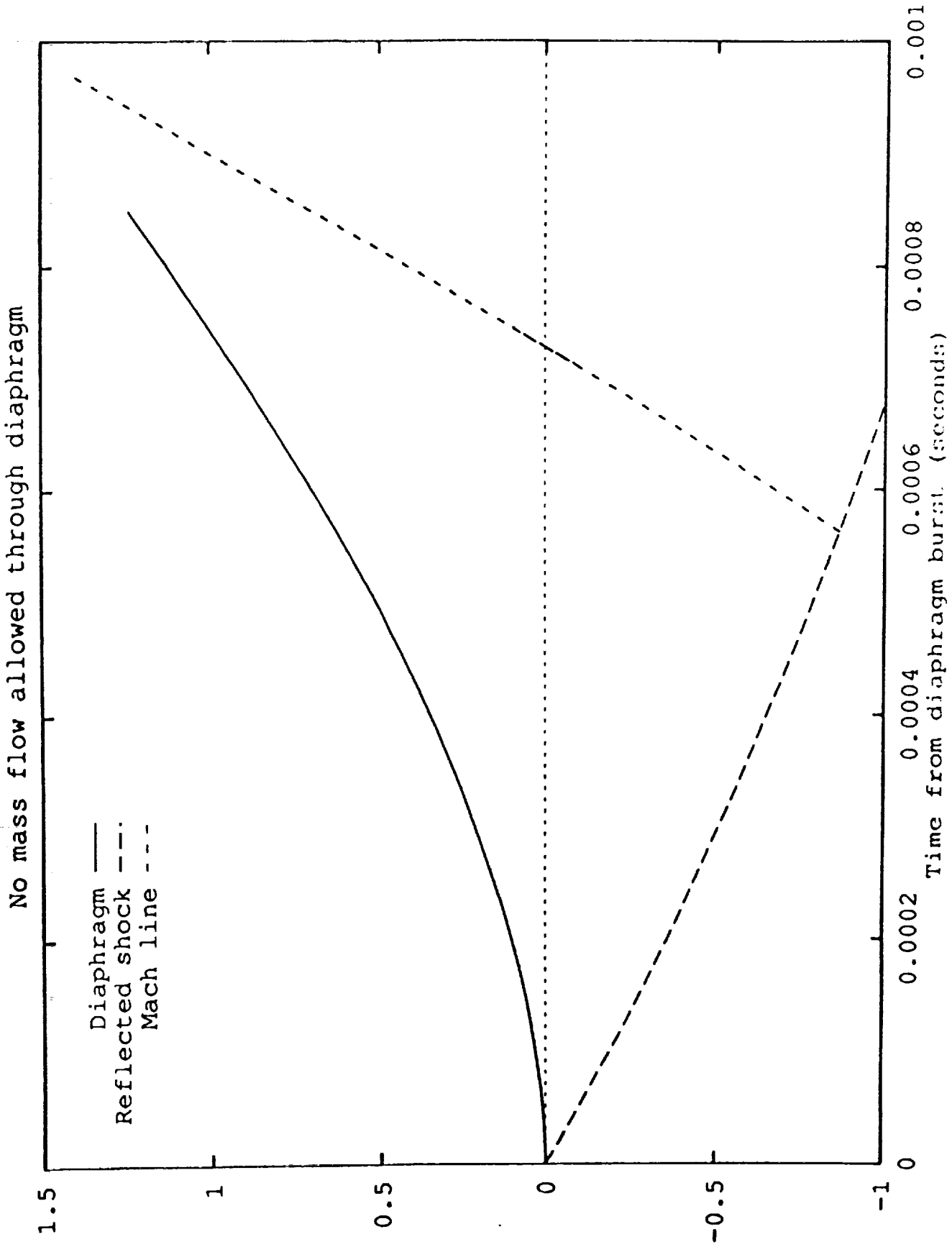
Distance from diaphragm burst (metres)
No mass flow allowed through diaphragm
Diaphragm
Reflected shock
Mach line
1.5
1
0.5
0
-0.5
-1
0
0.0002
0.0004
0.0006
0.0008
0.001
Time from diaphragm burst (seconds)

INFLUENCE OF SECONDARY DIAPHRAGM ON FLOW QUALITY IN EXPANSION TUBES

G.T.ROBERTS

Lecturer, Department of Aeronautics and Astronautics

University of Southampton, U.K.

SEPTEMBER 1992

ABSTRACT

Experiments were performed in the Department of Mechanical Engineering, University of Queensland free-piston driven expansion tube facility TQ in which the influence on flow quality of secondary diaphragm mass, location and pre-deformation was investigated. In these experiments, the facility was operated in shock tube mode (i.e. equal pressures either side of the secondary diaphragm) with argon as both the driver and test gases.

The results obtained indicate that the secondary diaphragm exerts a considerable influence not only on the test gas flow conditions but also on its duration. In general, the greater the inertia of the diaphragm (compared with the momentum of the test gas), the greater is the reflected shock strength and the shorter is the flow duration before the arrival of disturbances attributed to wave interactions with the driver-test gas interface. Pre-deforming the diaphragm was shown to have a beneficial effect by reducing the reflected shock overpressure and delaying the arrival of the interface disturbances.

CONTENTS PAGE

Title	1
Abstract	2
Contents	3
Nomenclature	4
1. INTRODUCTION	5
2. THE EXPANSION TUBE - PRINCIPLES OF OPERATION	5
3. TEST FLOW QUALITY IN EXPANSION TUBES - TYPICAL RESULTS	7
4. EXPERIMENTAL DETAILS	9
4.1 TQ expansion tube facility	9
4.2 Operating conditions	9
4.3 Secondary diaphragm variables	10
5. RESULTS	11
5.1 Without secondary diaphragm	11
5.2 Effect of diaphragm thickness	13
5.3 Effect of diaphragm pre-deformation	15
5.4 Effect of diaphragm location	16
6. CONCLUSIONS	16
ACKNOWLEDGEMENTS	17
REFERENCES	18
FIGURES 1 - 14	20 - 42

NOMENCLATURE

a - sound speed, ms^{-1}

f - frequency, Hz

M - Mach number

p - pressure, kPa

U_s - incident shock speed, ms^{-1}

x - distance from primary diaphragm, m

γ - ratio of specific heats (1.67 for argon)

σ - period between shock and test gas arrival (expansion tube only)

τ - steady run period, μs

Subcripts:

t - total (Pitot)

Shock tube region nomenclature:

1 - initial test gas

2 - post incident shock

3 - post primary unsteady expansion

4 - initial driver gas

5 - post reflected shock (reflected shock tunnel only)

- post secondary unsteady expansion (expansion tube only)

6 - post steady expansion (reflected shock tunnel only)

10 - initial acceleration gas (expansion tube only)

20 - post incident shock in acc^n tube (expansion tube only)

1. INTRODUCTION

This report describes work undertaken during the period July-September 1992 whilst the author was visiting the Department of Mechanical Engineering, University of Queensland (UNIQ) on sabbatical leave from the Department of Aeronautics and Astronautics, University of Southampton, U.K. The work involved performing a number of experiments in the UNIQ free-piston driven expansion tube facility (TQ) in order to investigate the influence of the secondary diaphragm on the quality of test gas flow. The topic was suggested by the head of the Shock Tunnel group at UNIQ, Prof.R.J.Stalker.

2. THE EXPANSION TUBE: PRINCIPLES OF OPERATION.

An expansion tube is an impulse-type wind tunnel facility that is capable of producing high enthalpy test gas flows suitable for aerothermodynamic testing of models of reentry vehicles or spaceplanes and also for performing supersonic combustion studies under reasonably well simulated operating conditions. Like the shock tunnel, it is basically a modified shock tube, in which a shock wave is propogated into a quiescent test gas after the rupture of a (thick) primary diaphragm separating the initially high pressure driver gas and the relatively low pressure test gas.

As described by Stalker et al [1], the essential difference between a reflected shock tunnel and an expansion tube is that, in the former, the shock heated test gas is further processed by a reflected shock, followed by steady expansion through a contoured nozzle from essentially stagnant reservoir conditions, to attain hypervelocity conditions in the test section, whereas in the expansion tube the shock-heated gas undergoes an unsteady expansion centred at the location of a (thin) secondary diaphragm which initially separates the test gas from a lower pressure acceleration gas.

Figure 1 shows typical wave diagrams for both types of facility. Note that, in the reflected shock tunnel, region 5 is the stagnant region behind the reflected shock whereas, in the expansion tube, region 5 is itself the high velocity test gas region. In both, the primary shock Mach number (and hence flow enthalpy) in the shock tube is maximised by employing a high driver-test gas pressure and sound speed ratio. The latter normally dictates the use of a light test gas (hydrogen or helium) although increasingly common is the use of a free-piston driver [2] to raise transiently both the pressure and sound speed of the driver gas above levels that could normally be obtained or tolerated under steady conditions.

In the expansion tube, the test flow velocity is also dependent on the pressure ratio across the secondary diaphragm, it being usual to employ the same test and acceleration gases. Subject to restrictions due to poor flow quality (described later) it is best if this pressure ratio is also large.

The expansion tube concept was first proposed by Trimpi [3], who showed that the unsteady expansion is theoretically superior to a steady expansion for producing high enthalpy flows. However, the primary advantage over the reflected shock tunnel is that the flow is never stagnated so that the levels of dissociation in (say) air flows, which are caused by the high temperatures in the stagnant reservoir, are not experienced in the expansion tube flow, which thus provides a better simulation of the flight conditions of a typical reentry vehicle or the conditions inside the combustor of a supersonic combustion ramjet (scramjet) engine (e.g. see Figure 2).

Their main disadvantage is that the run duration of such facilities is exceedingly small, typically being of $O(10^{-4})$s, which is about an order of magnitude less than that offered by most reflected shock tunnel facilities. The reason for this can easily be observed by reference to the wave diagrams illustrated in Figure 1. In the reflected shock tunnel the period of steady flow is limited by the disturbance (shock or expansion) reflected from the driver-test gas interface or, if (as is often the case) the tunnel is operated in tailored-interface mode where the interface is transparent to the reflected shock, by drainage of the stagnant reservoir gas through the nozzle. In the expansion tube, however, the run duration is limited by the arrival at the test section of either the tail of the unsteady expansion or the head of the expansion reflected off the driver-test gas interface. Paull and Stalker [4] have shown that the run duration is optimised when both of these events occur simultaneously.

Unfortunately, even the short run times predicted theoretically often considerably overestimate the actual run times observed in tests in expansion tubes. One reason for this is the attenuation of the incident shocks due to viscous effects: as noted by Mirels [5], the boundary layer growing from the foot of the shock wave not only attenuates the shock speed but also causes the test gas (and the interface between it and the driver gas) to accelerate. In a shock tube of sufficient length the shock and test gas speeds would eventually equalize and the period of uniform test gas flow behind the incident shock would then remain constant with further increase in length. The acceleration of the driver-test gas interface causes the reflection of the unsteady expansion to occur much earlier than would have been the case in inviscid flow and therefore causes the run duration to be truncated early.

Nevertheless it is possible to make use of the short test times offered and currently facilities are being developed and tested at a number of establishments [e.g. 6,7] in the hope of realising their theoretical advantages over the reflected shock tunnel. What has tended to inhibit the wide acceptance of expansion tubes within the aerodynamic community is the rather narrow range of operating conditions for which steady test conditions have been observed even during the short run durations predicted taking viscous effects into account.

Early tests conducted with expansion tubes concluded there was either no steady test period at all [e.g. 8,9] or, at best, there was only a single operating condition during which the flow unsteadiness was acceptably low [10]. However, more recent tests [4,11] have indicated that, for any given facility, there ought to be a number of acceptable operating conditions, depending on the driver and test gases employed. In addition, recent studies have also indicated that the disturbances observed (particularly in pitot pressure) during the run are related to the transmission of transverse acoustic waves [12,13].

3. TEST FLOW QUALITY IN EXPANSION TUBES: TYPICAL RESULTS

In work performed to date, including that reported here, pitot pressure measurements have provided the main diagnostic method for determining flow quality during the expansion tube run period. Figure 3 shows an ideal pitot pressure signal for an expansion tube. The initial rise is due to the arrival of the low density acceleration gas; this is soon followed by a further increase as the test gas arrives. As described above, the run is terminated either by the arrival of the tail of the unsteady expansion or the reflection of the head of the expansion from the driver-test gas interface. In either case the run termination is indicated by a further rise in pitot pressure.

Figure 4 (taken from [13]) indicates the signals obtained in practice for various operating conditions. In each case, the small increase in pitot pressure corresponding to the acceleration gas arrival is smeared out by the larger increase due to the test gas arrival (this is probably caused by the finite response rate of the pitot pressure probe). In figures 4a and 4b there are periods of steady flow (of approximately 75 and 40 μs, respectively) before the arrival of the terminating disturbance. However, in 4c there is no steady period indicated; instead, the pitot signal has a periodic fluctuation of sufficiently large magnitude to render the operating condition unusable.

Paull and Stalker [12,13] have shown that these fluctuations are due to transverse acoustic waves, probably originating from the primary diaphragm rupture process. They argue that these disturbances are always present in the driver gas, but whether (or not) they are propogated into the test gas (prior to secondary diaphragm rupture) depends on the ratio of the sound speeds across the driver-test gas interface: whenever the test gas sound speed is greater than that in the driver gas, the interface acts as a low frequency filter with a tendency to attenuate the disturbances, whereas in the converse situation the disturbances are transmitted through the interface unattenuated. The cut-off frequency for the filtering effect is shown to be Mach number, as well as sound speed ratio, dependent.

Inspection of the flow properties for the runs illustrated in Figure 4 support this hypothesis. Furthermore, Paull and Stalker show that, if the test gas is subsequently processed (by, for example, an unsteady expansion, as in the expansion tube) the residual noise present will be focussed to a particular frequency by a Doppler shift effect. The appearance of disturbances of regular frequency in expansion tube flows has been observed in many experiments in different facilities and has caused the major limitation on the range of satifactory conditions under which the facilities can be operated.

Another feature which has been a cause for concern in expansion tube developments has been the influence of the secondary diaphragm (and its rupturing process) on the test gas quality [14]. In the ideal case, the diaphragm should behave as though it were massless and should rupture immediately after impact of the incident shock wave or else the test gas will be processed by an unwanted reflected shock, leading to increased levels of dissociation and stagnation pressure loss. Clearly, the ideal behaviour of the diaphragm will not occur in practice, but commonly a diaphragm that is as thin as possible (but capable of supporting the necessary pressure difference across it initially) is used to minimise any reflected disturbance. Alternatively, a mechanical fast-acting valve arrangement may be employed instead of a diaphragm.

Additionally, with the evidence that many of the disturbances causing early truncation of the run period are caused by transverse acoustic waves, it is reasonable to question the role of the secondary diaphragm in their production. Despite the possible importance of the secondary diaphragm on flow quality in expansion tube flows, a systematic experimental investigation of this had not been carried out prior to the work described here.

4. EXPERIMENTAL DETAILS

4.1 TQ expansion tube facilty.

Figure 5 is a schematic of the TQ expansion tube facility used in this study. It comprises a free-piston driver section, in which the driver gas is compressed by a heavy (approx. 3 kg) piston, itself accelerated by high pressure air behind it, a shock tube section in which the test gas initially resides at pressures of order 1-10 kPa and a section containing the acceleration gas (usually, but not necessarily, the same as the test gas) at pressures of order 1-100 Pa. Downstream of the acceleration section is the test section/dump tank with a rotary and diffusion pump attached. A full description of the facility appears elsewhere (e.g.[6]).

The usual arrangement is to use helium or argon as the driver gas and air as the test/acceleration gases. The bursting pressure of the aluminium or steel primary diaphragms normaly employed is in the range 19.5 to 34.5 MPa. The secondary diaphragms are usually either 13 μm polyethylene or 25 μm cellophane; prior to this study both were thought to offer a reasonable approximation to the ideal massless condition. Shown in Figure 5 is the forward location of the secondary diaphragm (at x = 2.111 m downstream of the primary diaphragm); in this study most of the experiments were conducted with the secondary diaphragm in its aft location (x = 3.736 m).

The measurements taken were of pitot pressure ($p_{2,t}$) and the sidewall pressure (p_2) at various locations along the shock and acceleration tubes; the latter were also used to determine the variation in shock speed (U_s). All pressures were measured using PCB piezo-electric transducers, which were pre-calibrated. The data were recorded on a Physical Data Inc. multichannel transient recorder operating on some channels at sample rates of 2MHz, whilst on others at 40 kHz.

4.2 Operating conditions.

As the primary aim of these experiments was to explore the influence of the secondary diapragm on the flow quality and, in particular, to determine whether pre-deforming the diaphragm has any adverse influence, it was decided to operate the facility in shock (rather than expansion) tube mode in order to simplify the flow and its analysis. Also, since the thin diaphragms required a finite pressure difference (< 1 kPa) across them to maintain their deformed state, it was necessary to operate at reasonably high shock tube

filling pressures (p_1) in order to ensure that any unsteady expansion that results is weak.

Finally, according to the analysis of Paull and Stalker [13], it was necessary to operate at conditions where the test gas sound speed was greater than the driver gas sound speed (i.e. $a_2 > a_3$) if the driver-test gas interface was to act as an effective filter to disturbances originating in the driver gas due to primary diaphragm rupture.

These criteria led to the choice of argon driving argon as the test gas (the latter was preferred to air to avoid causing vibration and dissociation real gas effects). A summary of the run conditions employed is given in Table 1.

Table 1: Typical Run Conditions

P_1 (kPa)	$U_{s_{-1}}$ (kms^{-1})	a_2/a_3
20	1.65	2.0
4	2.25	3.7
1	2.75	7.3

Air reservoir pressure: 1.85 MPa

Primary diaphragm: 0.6 mm. mild steel, burst pressure p_4 = 19.5 MPa

Driver reservoir pressure: 75 KPa (argon)

4.3 Secondary diaphragm variables

Besides the shock tube operating conditions, the main variables in the experiments concerned the secondary diaphragm. Parameters that were varied included:

- thickness (or mass)
- deformation (prior to the run)
- location within the shock tube

The diaphragms tested were 13 μm thick polyethylene, 25 μm and 50 μm thick cellophane, 102 μm and 191 μm thick mylar. When tested in their undeformed state, care was taken to ensure that the pressures either side of the diaphragms were equalised during the pump-down process.

5. RESULTS

5.1 Without secondary diaphragm.

Figure 6 shows typical pitot signals obtained at the three nominal operating conditions listed in Table 1 without any secondary diaphragm. The signals are similar to those obtained in expansion tube mode, except that one would not, of course, expect to see any initial rise due to the arrival of acceleration gas and the run is terminated by the arrival of the driver-test gas interface, which manifests itself as an abrupt rise in pitot pressure. It can be seen that this rise in pressure becomes comparatively larger at higher shock speeds as both the gas velocity and the density ratio across the interface increases.

As expected, the run period (τ) decreases with increasing shock speed; also shown in Figure 6 is the predicted time of arrival of the interface according to the theory of Mirels [5], assuming turbulent boundary layer growth behind the incident shock. It can be seen that the theoretical run time is slightly less than that observed experimentally, the discrepancy becoming greater at the higher shock speeds. This is attributed to the unrealistically high post-shock temperatures (> 7000 K) predicted by ideal gas shock wave theory, which will cause the viscous effects to be overestimated.

After the arrival of the interface, the pitot signals exhibit large scale periodic fluctuations (of approximate frequency $25 < f < 45$ kHz) which were also observed by Paull and Stalker [13] and were attributed by them to disturbances arising from the non-ideal primary diaphragm rupture process. The periodicity of the disturbances is due to frequency focusing caused by the steady expansion undergone by the driver gas during the area ratio change at the diaphragm location. One might expect the focus frequency to change with different driver gas expansion ratios, but this does not seem to be occuring in a systematic manner: the disturbance frequency illustrated in Figure 6(b) (p_1 = 4 kPa) is greater than that for either of the runs illustrated in 6(a) or 6(c) (p_1 = 20, 1 kPa, respectively, the driver pressure being nominally constant throughout all of these tests).

The pitot pressure during the run period remains fairly steady, although the signal illustrated in Figure 6(a) exhibits some (small) fluctuations occuring at a slightly higher frequency than those observed after the driver test-gas interface has arrived (34 kHz vs. 28 kHz, respectively). This may be a manifestation of the weaker filtering effect occurring at this run

condition, where the sound speed ratio across the interface is comparitively low, since these fluctuations are not evident on the signals obtained from runs at higher shock speeds where the sound speed ratio is greater.

At the lower test gas pressures, in particular, the pitot pressure tends to increase slightly with time, a phenomenon normally attributed to viscous effects which cause the gas arriving towards the end of the run to have been processed by a stronger shock than that at the beginning. However, the measurements of the shock speed profile along the shock tube (Figure 7) indicate that, contrary to expectations, the shock actually tends to accelerate along the length of the tube as the test gas pressure is lowered, which should cause the pitot pressure to fall with time. [n.b. In Figure 7 the shock speeds have been normalised with respect to that measured furthest upstream (x ~ 2.0 m)]. Despite the uncertainty in the shock speed measurements (due to the 2.5 μs data sampling interval) being rather large, there appears to be no obvious explanation for the observed acceleration of the shock.

Table 2 compares the measured pitot and static pressures with those predicted by 1-D, ideal inviscid gas theory, taking into account the non-ideal driver gas behaviour for this piston-driven facility [6]. It is clear that, at high p_1 (or low U_s), the theoretical pitot pressure is very similar to that measured whilst the static pressure is slightly greater. However, at low p_1 (high U_s) the theoretical pitot pressure is much less than that measured whilst the static pressure is in good agreement with measurements.

Table 2: Post shock conditions

RUN NO.	p_1 (kPa)	U_s (kms^{-1})	THEORY			EXPERIMENT		
			$p_{2,t}$ (kPa)	p_2 (kPa)	M_2	$p_{2,t}$ (kPa)	p_2 (kPa)	M_2
279	20	1660	1788	665	1.22	1783	583	1.32
280	4	2200	678	234	1.27	843	243	1.44
289	1	2570	234	79	1.28	387	81	1.64

The post shock Mach numbers were calculated using the Rayleigh pitot formula:

$$\frac{P_{2,t}}{P_2} = M^2 \left[\frac{\gamma+1}{2}\right]^{\frac{\gamma+1}{\gamma-1}} \left[\gamma - \frac{\gamma-1}{2} M^{-2}\right]^{\frac{1}{1-\gamma}}$$

The values obtained are, however, somewhat greater than predicted, with the discrepancy becoming progressively worse at higher shock speeds. Again, this is attributed to the unrealistically high temperatures predicted by ideal gas theory, which would cause the predicted test gas density (and hence pitot pressure) to be lower than the experimental values.

5.2 Effect of diaphragm thickness.

Figure 8 shows the effect on pitot pressure of varying the diaphragm thickness for the operating conditions in Table 1. For each condition it appears that fluctuations on the pitot signal occur before the theoretical time of arrival of the driver-test gas interface (except when there is no secondary diaphragm) and arrive earlier the thicker the diaphragm. The effect becomes more pronounced at the lower pressures (or higher shock speeds) where a rise in pitot pressure is also observed ahead of the theoretically predicted time of arrival of the interface; the rise becomes steeper the thicker the diaphragm. Thus it is clear that the prescence of the diaphragm is having a marked influence on the available test time.

Figure 9 shows the effect of the diaphragm thickness on the sidewall pressure measured 15 mm upstream of the diaphragm (i.e. at x = 3.721 m). The pressure level is observed to increase markedly with increasing thickness at all operating conditions. Also shown on the figures are the theoretically predicted incident and reflected shock pressures: it is clear that, for the thickest diaphragms (particularly at low pressure) the pressures recorded are considerably in excess of the reflected shock pressure and it has been shown [15] that, when the diaphragm inertia is large, the test gas is processed by multiple shocks reflecting between the diaphragm and contact surface, the run conditions being overtailored.

Clearly these reflections are detrimental to the flow quality, since they would lead to increased levels of dissociation in a diatomic test gas. Of those tested, only the 13 μm polyethylene diaphragm had apparently negligible effect on sidewall pressure under all conditions tested.

Figure 10 shows the effect of diaphragm thickness on the measured shock speed (normalised with respect to the value obtained nearest the primary diaphragm, x = 2.0 m) along the length of the shock tube for p_1 = 1 kPa. The data obtained suggest that the shock speed decreases in the vicinity of the secondary diaphragm and then rapidly overshoots before decaying towards the no-diaphragm value near the end of the shock tube. Both the decrease and the susbsequent overshoot in shock speed become more pronounced the thicker the diaphragm. Figure 11 shows the effect of shock tube fill pressure on the shock speed profile for a fixed diaphragm thickness (191 μm mylar): it is clear that the decrease in shock speed and the overshoot are greater at lower pressures.

The apparent decrease in shock speed is probably an artifice caused by the finite rupture time of the diaphragms, which can be estimated by extrapolating the shock speed profiles either side of the diaphragm and calculating the delay between them. The results are shown in Table 3.

As may be expected, the rupture time increases as both the diaphragm thickness (or mass) increases and test gas density (or momentum) decreases. However, it is clear that the rupture times obtained for the 13 μm polyethylene diaphragm are unrealistic and illustrate the approximate nature of the estimation.

Table 3: Estimation of diaphragm rupture time.

Diaphragm material	Burst time (μs)		
	p_1 = 20 kPa	p_1 = 4 kPa	p_1 = 1 kPa
191 μm mylar	61	112	207
102 μm mylar	50	53	120
50 μm cellophane	15	23	44
25 μm cellophane	13	16	37
13 μm polyethylene	6	5	- 4

The overshoot in shock speed illustrated in Figure 10 is, however, believed to be genuine and probably arises as a result of the increased pressure and temperature of the test gas behind the reflected shock driving a stronger shock into the acceleration section of the tube. The reflected shock is weakened (eventually to a Mach wave) by the unsteady expansion that occurs after diaphragm rupture [6]; as this will occur more rapidly the thinner the diaphragm, the overshoot in shock speed will be greater for the thicker diaphragms, as observed.

5.3 Effect of diaphragm pre-deformation.

Experiments were performed with the 25 μm cellophane diaphragm material deliberately deformed prior to initiation of the shock tube run. The deformation was caused by maintaining a pressure differential of about 80% of the burst pressure (i.e. about 80 kPa in this case) for approximately 20 mins prior to pump-down of both sections of the shock tube. Inspection of diaphragms subjected to this loading indicated that they had deformed to about 25% of the shock tube diameter (i.e. approx. 10 mm) at the centre after this period of time and maintained their shape even after the pressure differential had been removed. Tests were conducted at p_1 = 1, 4 kPa only.

Figure 12a shows the effect of the deformation on the sidewall pressure measured 15 mm upstream of the diaphragm. Apparently the deformation reduces the pressure after shock reflection considerably. Indeed, the results at p_1 = 4 kPa (Figure 12b) show no increase in pressure above that behind the incident shock. However, it was not certain whether the deformation had actually influenced the shock reflection process significantly, or had merely shifted the effective position of the diaphragm far enough downstream to prevent the reflected shock from returning upstream over the transducer before being attenuated to a Mach wave.

In order to test this, the diaphragm location was moved downstream by 4.5 mm (this being the estimated effective centre of reflection for the deformed diaphragm) and tests repeated with both planar and deformed diaphragms. The results are shown in Figure 12c for p_1 = 1 kPa and indicate a similar level of reduction in sidewall pressure in the deformed case as was obtained with the diaphragm located further forward.

It is thus concluded that deformation of the secondary diaphragm weakens the reflected shock. This could be brought about by a reduction in the diaphragm burst time, allowing the unsteady expansion wave resulting from the diaphragm rupture to reach the reflected shock sooner. The diaphragm burst time (estimated in the manner described in 5.2) is approximately 29 μs for p_1 = 1 kPa and 12 μs for p_1 = 4 kPa; both are slightly less than the corresponding values for the planar diaphragm (37 μs and 16 μs, respectively), although the degree of uncertainty in this estimation is probably greater than the differences calculated. It is not yet clear whether such reductions in burst time (if they are real) are sufficient to cause the observed reduction in reflected shock pressure, or whether the shock reflection process is itself modified due to the curvature of the diaphragm.

In either case, however, pre-deforming the diaphragms does appear to have a beneficial effect on flow quality, since weakening the reflected shock should reduce both the level of molecular dissociation and stagnation pressure loss. Figure 13 shows the pitot pressure signals obtained and indicates that deformation also has a beneficial influence on the steady run period (compared with the planar diaphragm); again this is probably a consequence of the weakened reflected shock. The curvature of the diaphragm does not seem to enhance the production or transmission of lateral acoustic wave disturbances, as was originally thought possible.

5.4 Effect of diaphragm location.

Figure 14 shows the effect of moving the diaphragm location on the recorded pitot signals; the diaphragm material used in these experiments was 102 μm mylar and tests were conducted at p_1 = 1, 4 and 20 kPa.

Moving the location of the diaphragm upstream from x = 3.736 m to x = 2.111 m delays the arrival of disturbances associated with the driver gas; the effect becomes more pronounced at the lower pressures, where the driver-test gas interface arrival is indicated by a sharp rise in pitot pressure (as in experiments under the same conditions with no diaphragm present). Thus it would appear that these disturbances are affected by the interaction of the incident shock with the secondary diaphragm and the resulting reflected waves.

6. CONCLUSIONS

From the results described above it is clear that the influence of the secondary diaphragm on the flow quality in shock tubes (and therefore, by inference, also in expansion tubes) is considerable. The thickness (or mass) of the diaphragm material affects its rupture time which, in turn, affects the magnitude of the reflected shock pressure, particularly if the time to rupture is sufficiently long for multiple shock reflections to occur between the diaphragm and the driver-test gas interface.

The shock reflection process has shown to be weakened by pre-deforming the diaphragms so that they are non-planar. It has also been shown that the duration of steady flow with acceptable levels of fluctuation in pitot pressure is increased as the diaphragm thickness is reduced and as the diaphragm is located further from the tube exit. The latter is probably only true, however, provided the test gas core length has already approached its

asymptotic value due to viscous effects (as in the experiments here), otherwise the time between the passage of the incident shock wave and the driver-test gas interface will not be maximised.

All of these observations are consistent with the view that the interaction of the shock reflected from the diaphragm with the driver-test gas interface is causing disturbances to be propogated forwards into the test gas at a velocity greater than that of the interface. However, the details of the interaction require further theoretical investigation (possibly by computational methods).

Although the conditions tested (especially those with very thick diaphragms) are unrepresentative of those which would be commonly employed in expansion tube experiments, it is nevertheless hoped that the results obtained will provide a useful experimental database to aid the development of theoretical models attempting to describe the influence of the secondary diaphragm on flow quality in expansion tube flows. These, in turn, should lead to reliable design and operation criteria for such facilities.

ACKNOWLEDGEMENTS

The author wishes to acknowledge the help of following:

Prof.R.J.Stalker for suggesting the project and for arranging the details of the visit,

Dr.R.G.Morgan for his enthusiastic help and advice throughout,

Dr.A.Paull for his advice and help in times of need,

the postgraduate and staff members of the Department of Mechanical Engimeering, University of Queensland, for making the visit so enjoyable,

The University of Southampton, for making the visit possible.

The financial assistance of the Royal Society of Great Britain (under the Anglo-Australian Exchange Scheme), The UK Defence Research Agency (who financed the international air fares under the (unrelated) Research Agreement number 2040/475/RAE with the University of Southampton) and The Department of Mechanical Engineering, University of Queensland is also gratefully acknowledged.

REFERENCES

[1] Stalker, R.J., Paull, A and Neely, A.J. "Comparitive features of free piston shock tunnel and expansion tube facilities", 10th National Aero-Space Plane Technology Symposium, April 1991. Paper no. 241.

[2] Stalker, R.J. "The free piston shock tunnel" Aeronautical Quarterly, vol.17, 1966, pp.351-370.

[3] Trimpi, R.L. "A preliminary theoretical study of the expansion tube, a new device for producing high-enthalpy short-duration hypersonic gas flows" NASA TR R-133, 1962.

[4] Paull, A and Stalker, R.J. "Experiments on an expansion tube with a free piston driver - Phase 2" Dept. of Mech. Eng., University of Queensland, report, March 1989.

[5] Mirels, H. "Shock tube test time limitation due to turbulent boundary layer" AIAA J., vol.2, 1964, pp.84-93.

[6] Morgan, R.G. and Stalker, R.J. "Double diaphragm driven free piston expansion tube" 18th Int. Symp. on Shock Waves, Sendai, 1991.

[7] Tamagno, J., Bakos, R., Pulsonetti, M. and Erdos, J. "Hypervelocity real gas capabilities of GASL's expansion tube (HYPULSE) facility" AIAA paper no. 90-1390, presented at 16th Aerodynamic Ground Testing Conference, Seattle, June 1990.

[8] Spurk, J.H. "Design, operation and preliminary results of the BRL expansion tube" 4th Hypervelocity Tech. Symp., A.E.D.C. Tullahoma, Tenn., 1965, pp.111-144.

[9] Norfleet, G.D., Lacey, J.J. and Whitfield, J.D. "Results of an experimental investigation of an expansion tube" 4th Hypervelocity Tech. Symp., A.E.D.C. Tullahoma, Tenn., 1965, pp.49-110.

[10] Miller, C.G. "Shock shapes on blunt bodies in hypersonic-hypervelocity helium, air and CO_2 flows, and calibartion results in Langley 6-inch expansion tube" NASA TN D-7800, Feb. 1975.

[11] Stalker, R.J., Paull, A and Stringer, I. "Experiments on an expansion tube with a free piston driver - Phase 1" Dept. of Mech. Eng., University of Queensland, report Sept. 1987.

[12] Paull, A and Stalker, R.J. "The effect of an acoustic wave as it traverses an unsteady expansion" Phys. Fluids A, Vol.3, 1991, pp. 717-719.

[13] Paull, A. and Stalker, R.J. "Test flow disturbances in an expansion tube" J. Fluid Mech., to be published.

[14] Weilmuenster, K.J. "A self opening diaphragm for expansion tubes and expansion tunnels" AIAA J., vol.8, no.3, March 1970.

[15] Morgan, R.G. (private communication), 1992.

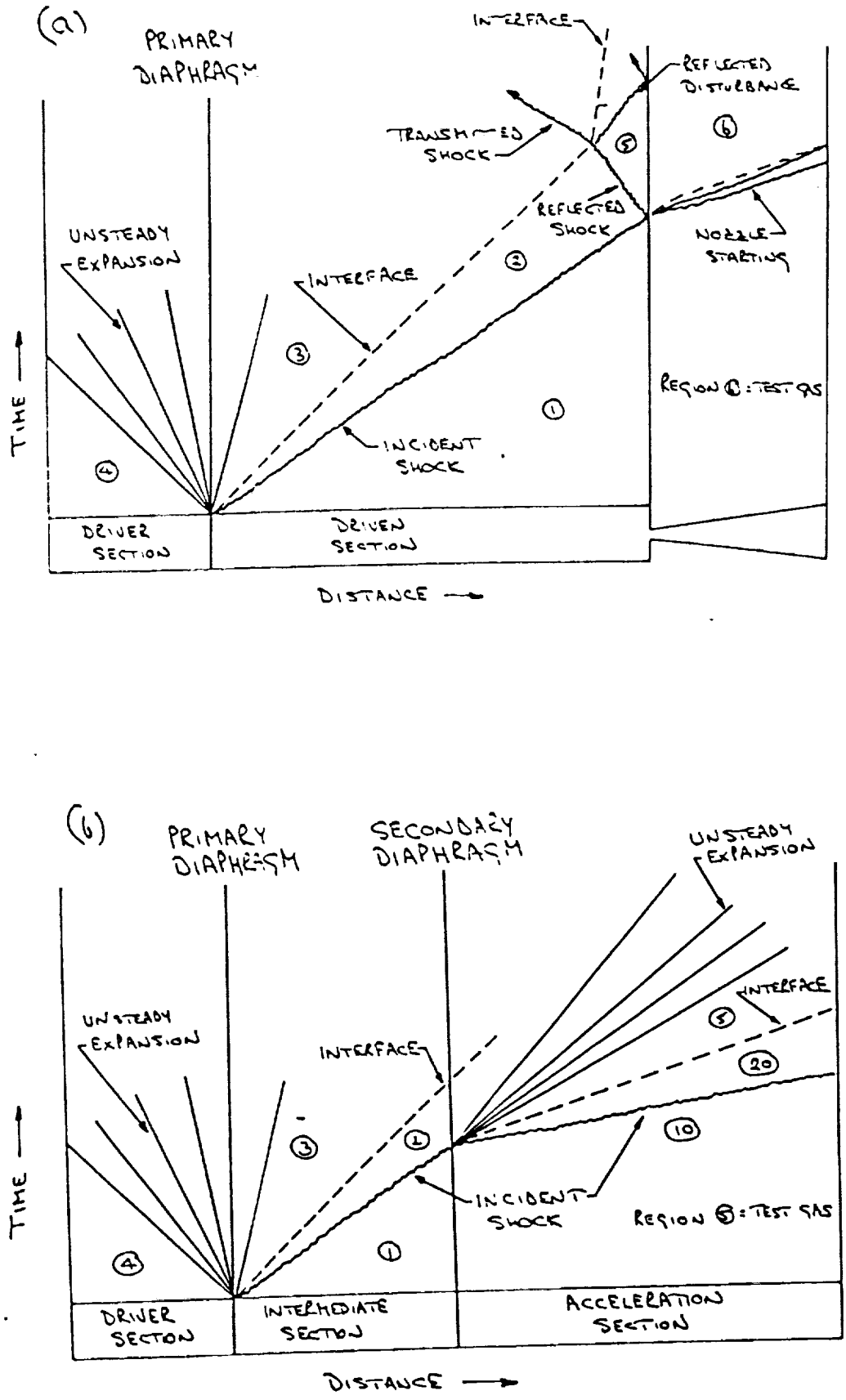

Figure 1: Wave Diagrams for

(a) Reflected Shock Tunnel
(b) Expansion Tube

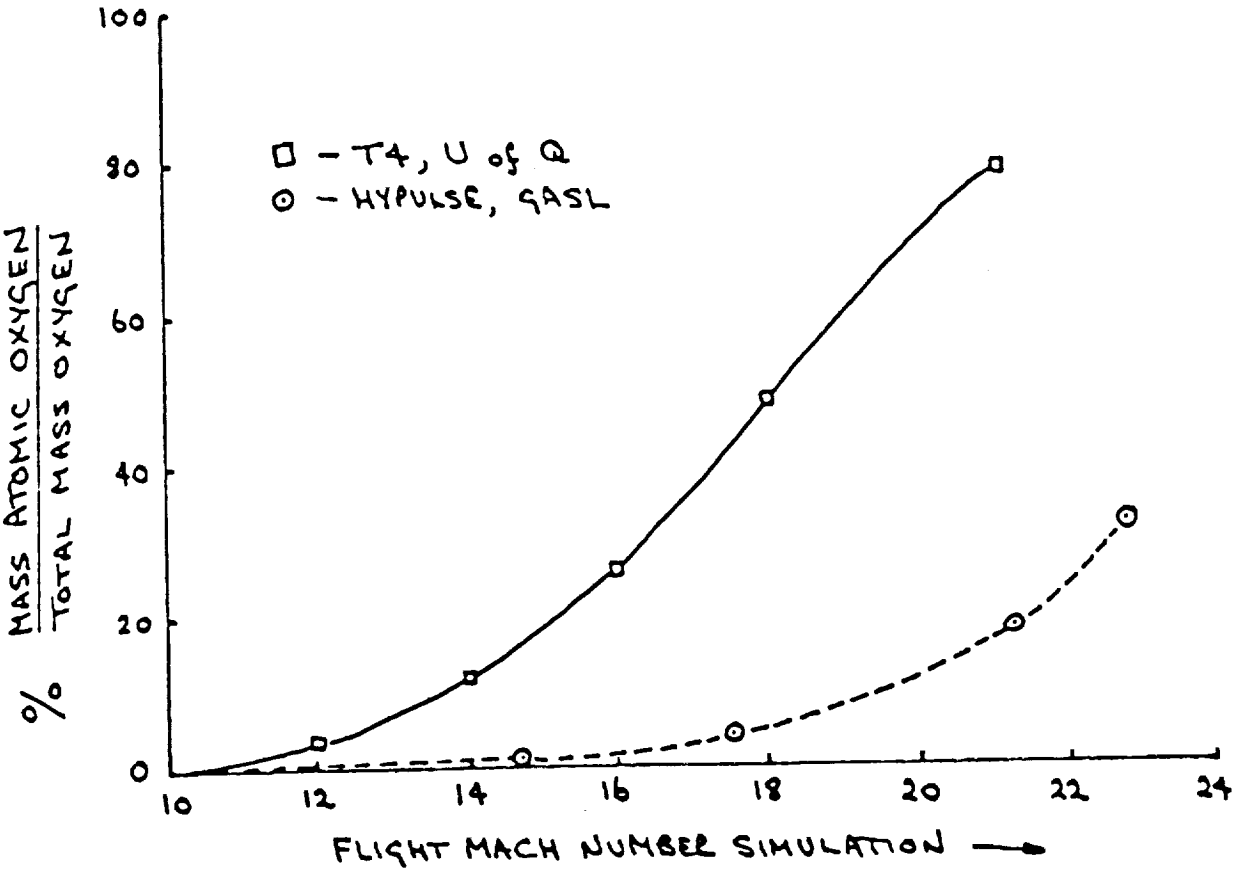

Figure 2: Comparison of Oxygen Dissociation Levels In T4 Reflected Shock Tunnel and GASL Hypulse Expansion Tube. [7].

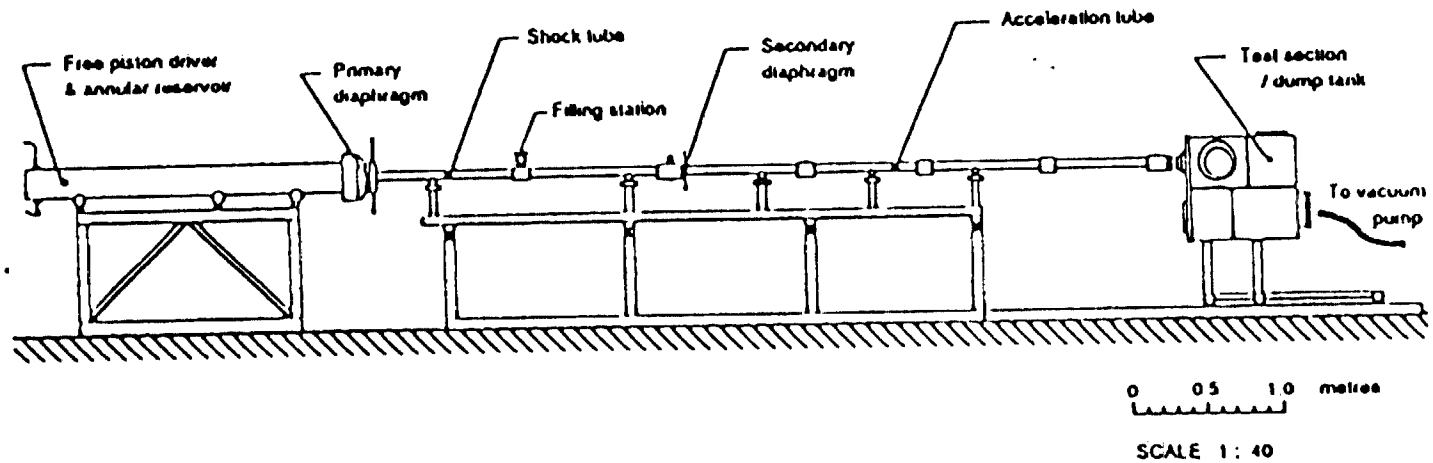

Figure 5: Schematic of TQ Expansion Tube Facility

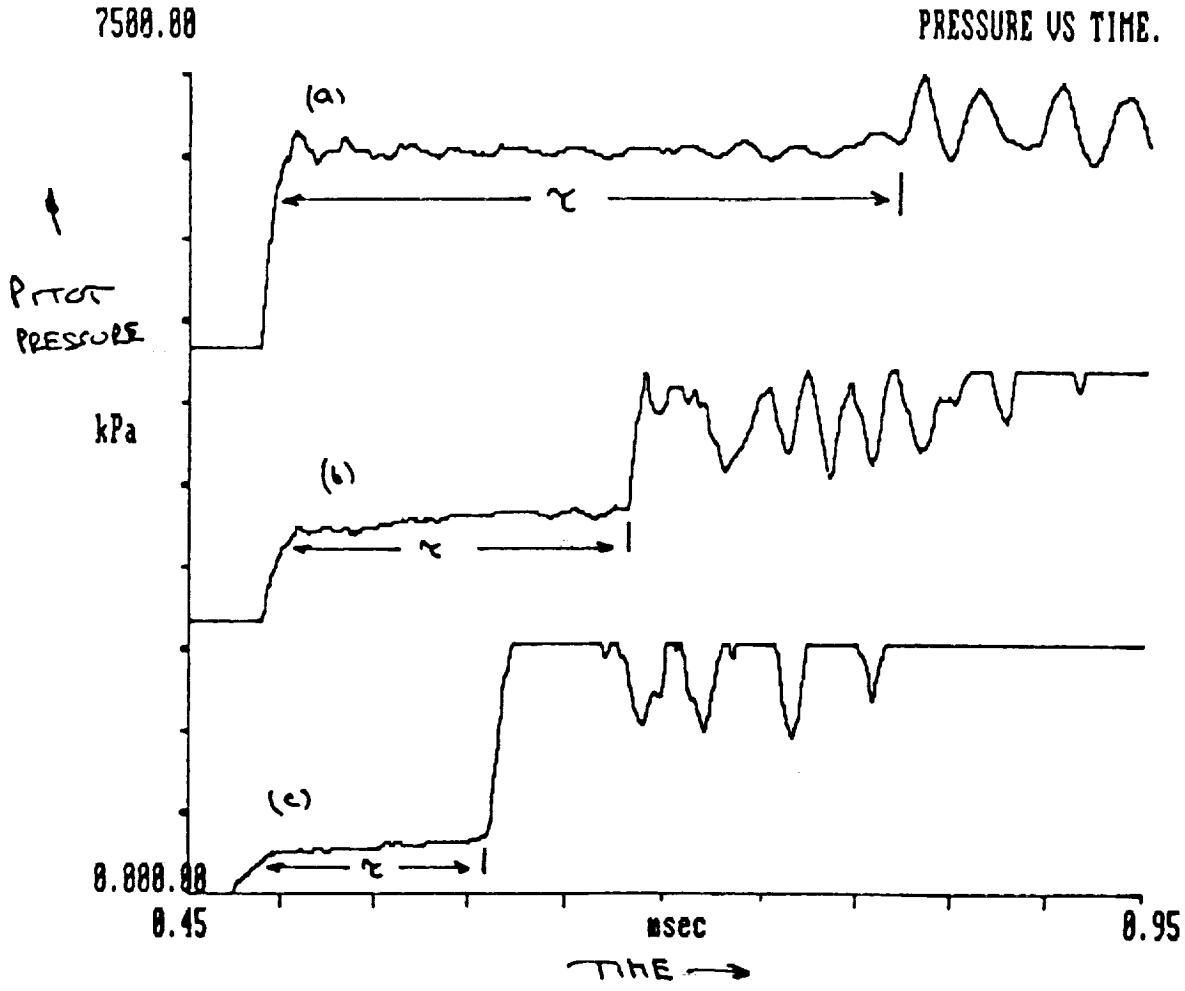

Figure 6: Plot of Pitot Pressure Vs Time

(a) p_1 = 20kPa
(b) p_1 = 4 kPa
(c) p_1 = 1 kPa

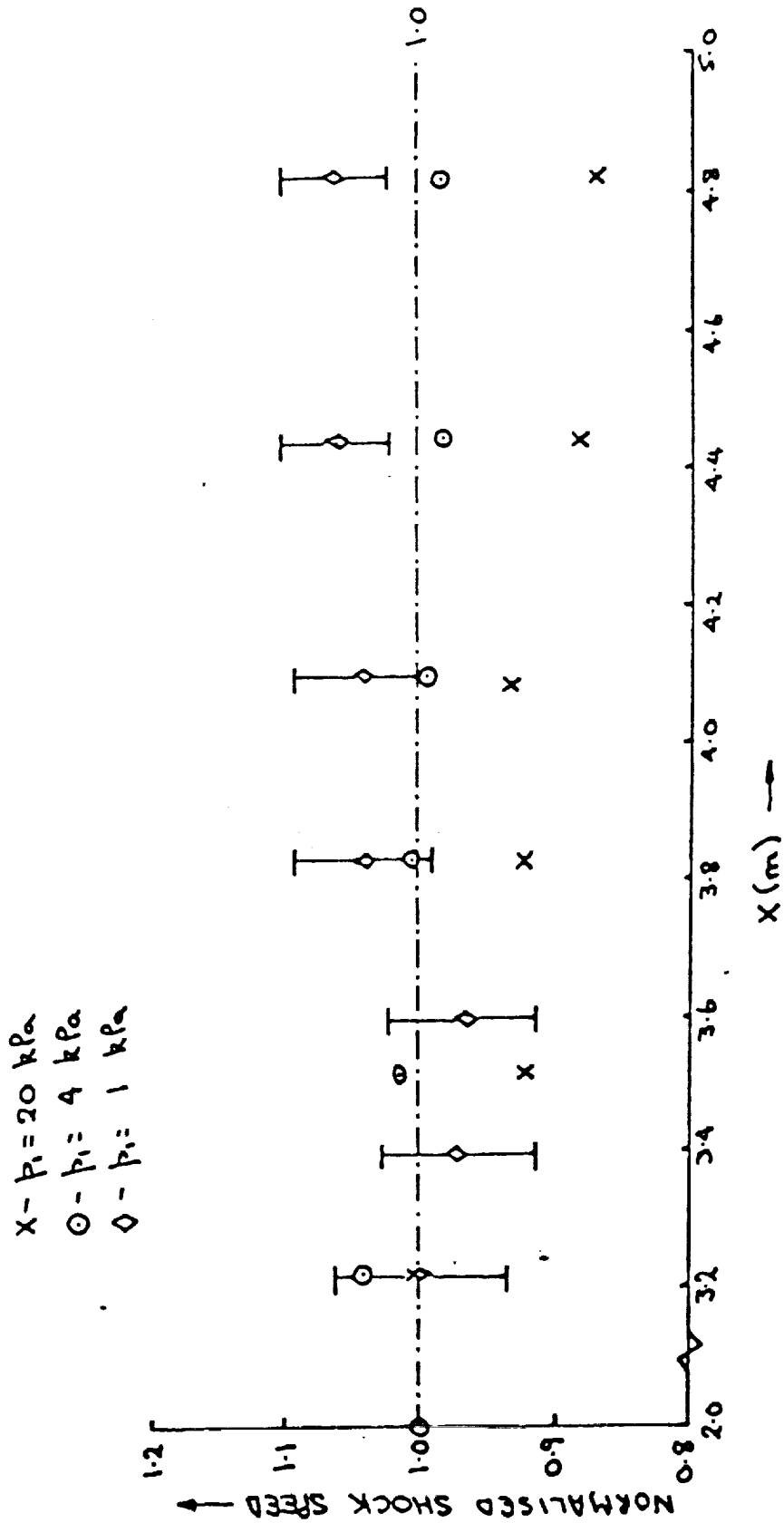

Figure 7: Shock Speed Variation Along Tube

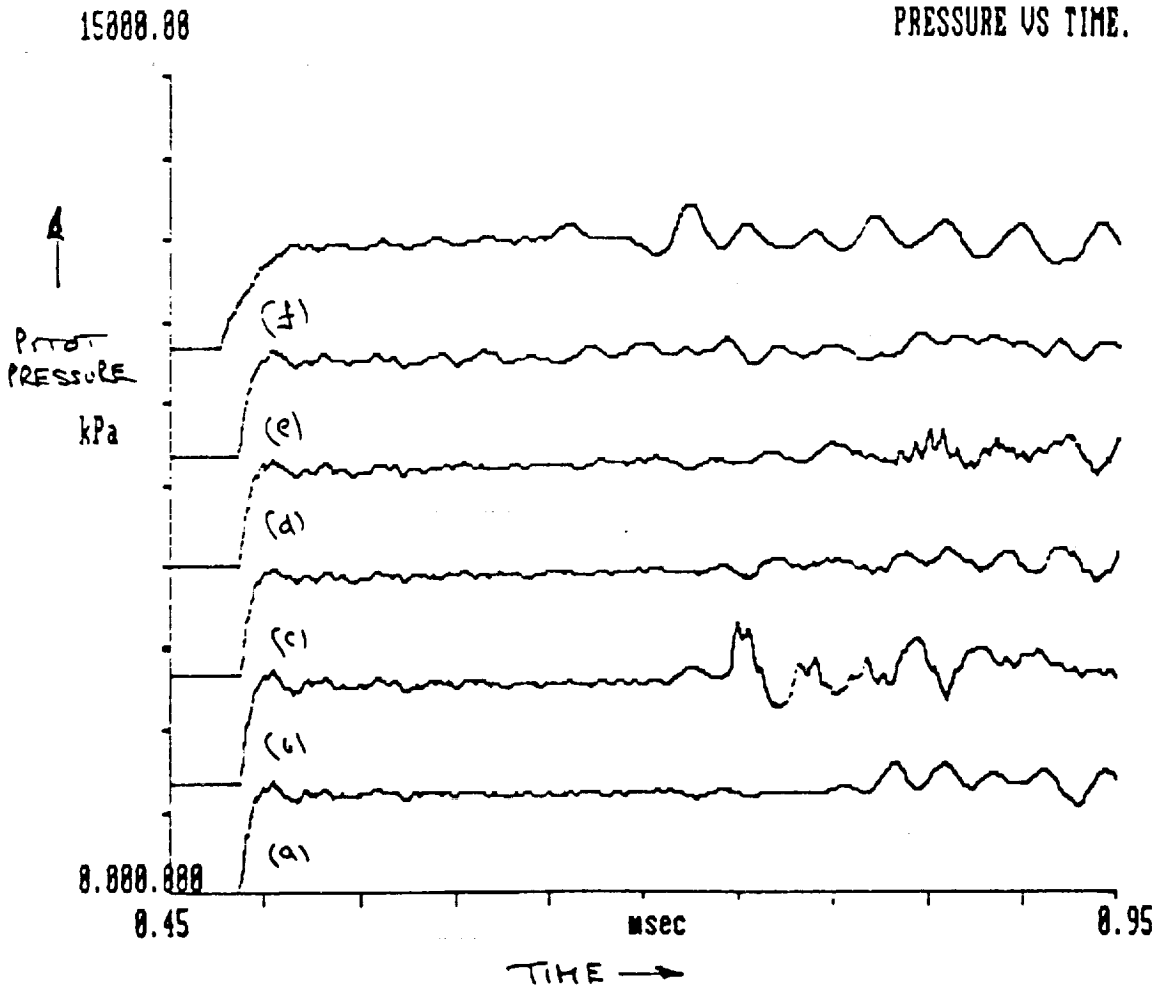

Figure 8(a): Effect of Diaphragm Thickness on Pitot Pressure
p_1 = 20 kPa

(a) - no diaphragm
(b) - 13 μm polyethylene
(c) - 25 μm cellophane
(d) - 50 μm cellophane
(e) - 102 μm mylar
(f) - 191 μm mylar

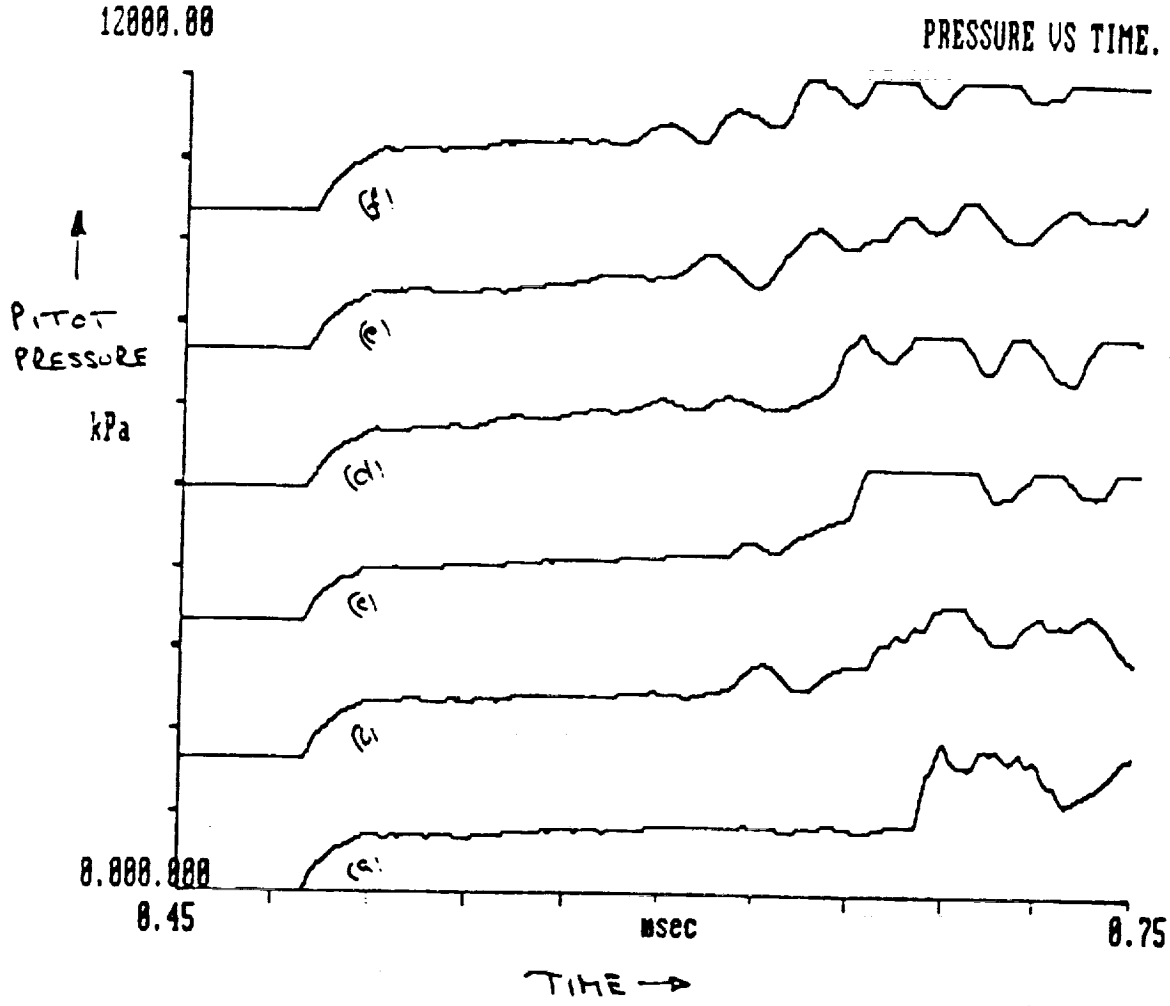

Figure 8(b): Effect of Diaphragm Thickness on Pitot Pressure
p_1 = 4 kPa

(a) - no diaphragm
(b) - 13 μm polyethylene
(c) - 25 μm cellophane
(d) - 50 μm cellophane
(e) - 102 μm mylar
(f) - 191 μm mylar

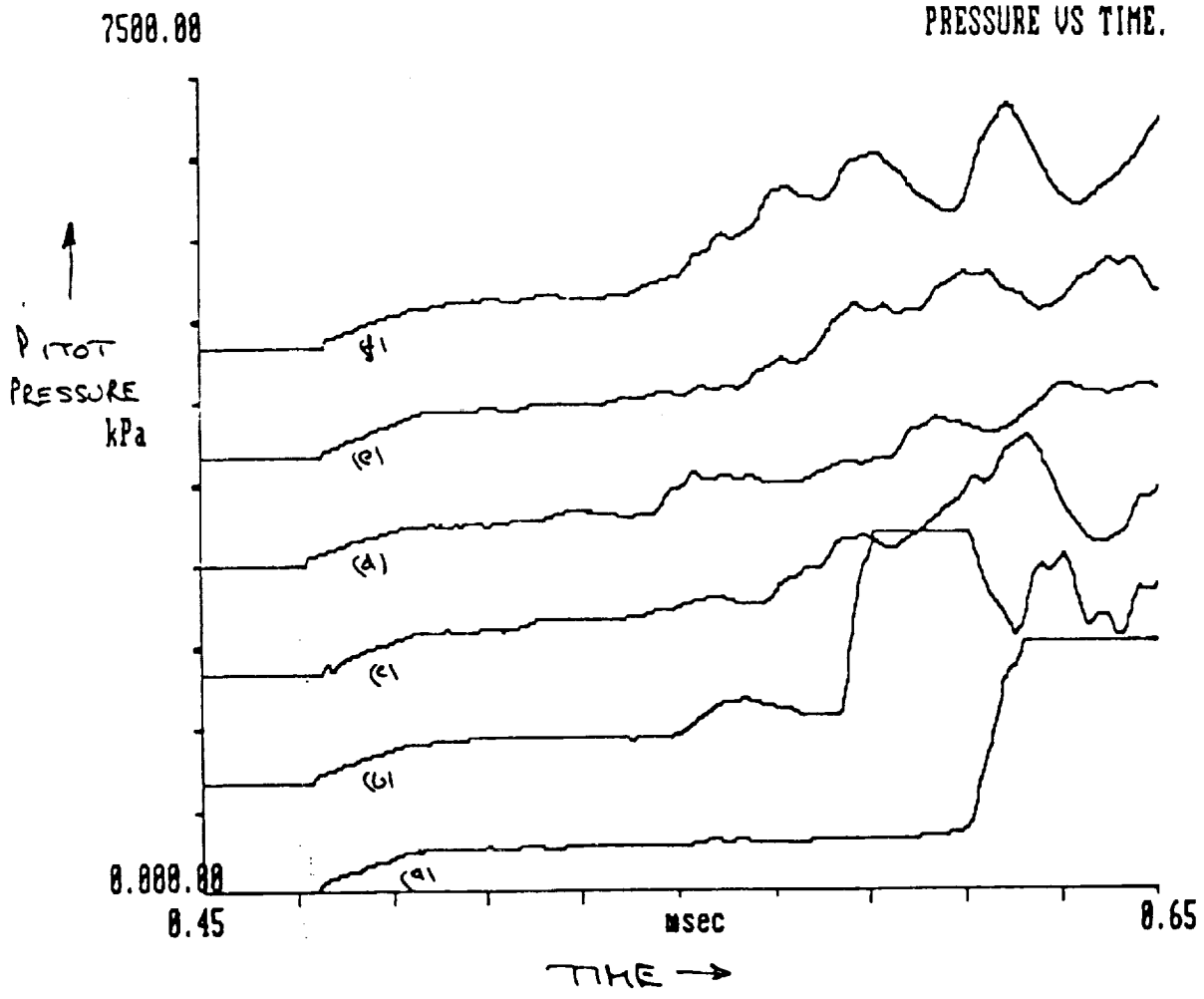

Figure 8(c): Effect of Diaphragm Thickness on Pitot Pressure
p_1 = 1 kPa

(a) - no diaphragm
(b) - 13 μm polyethylene
(c) - 25 μm cellophane
(d) - 50 μm cellophane
(e) - 102 μm mylar
(f) - 191 μm mylar

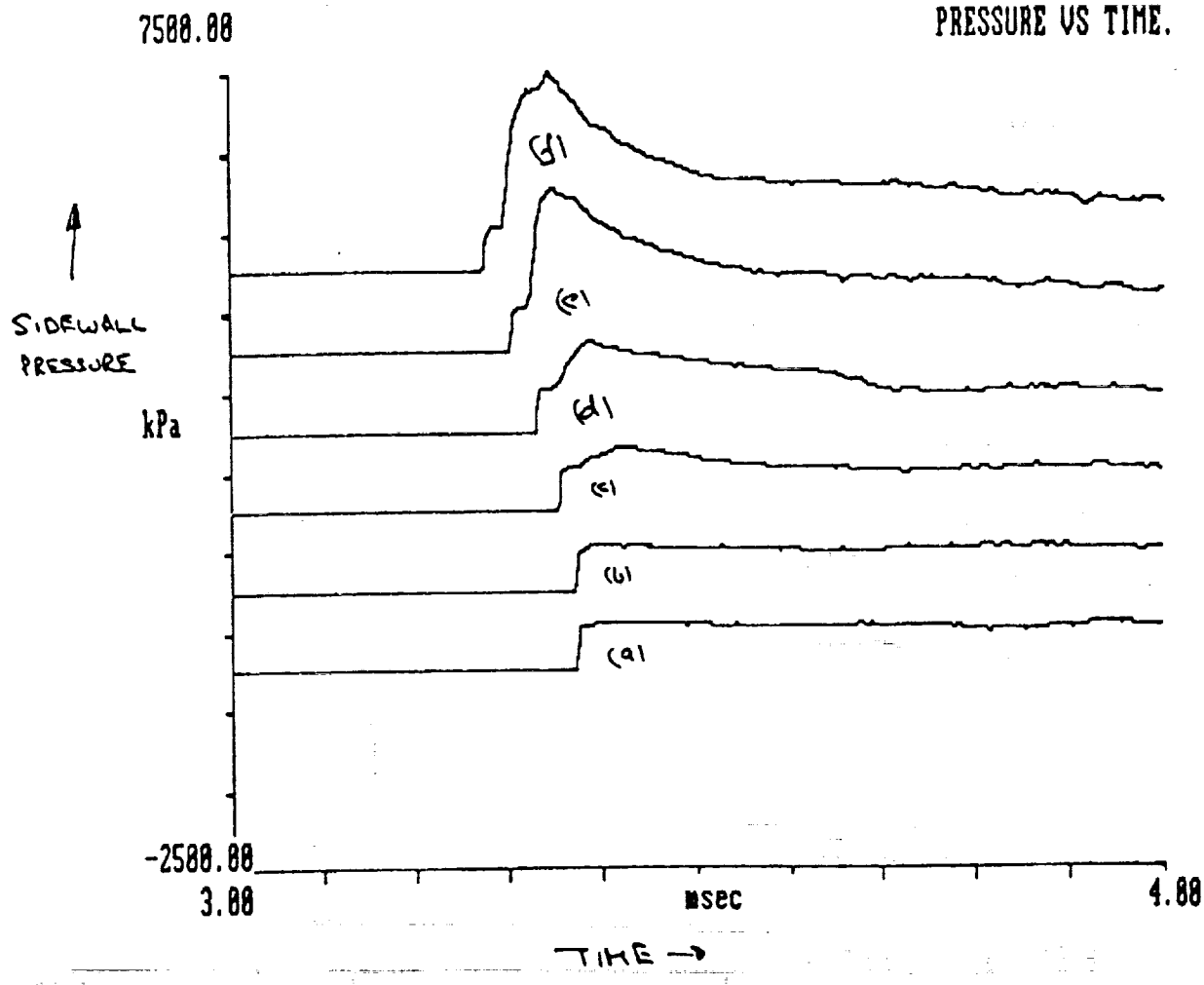

Figure 9(a): Effect of Diaphragm Thickness on Sidewall Pressure (Measured 15 mm Upstream of Diaphragm)
p_1 = 20 kPa

(a) - no diaphragm
(b) - 13 μm polyethylene
(c) - 25 μm cellophane
(d) - 50 μm cellophane
(e) - 102 μm mylar
(f) - 191 μm mylar

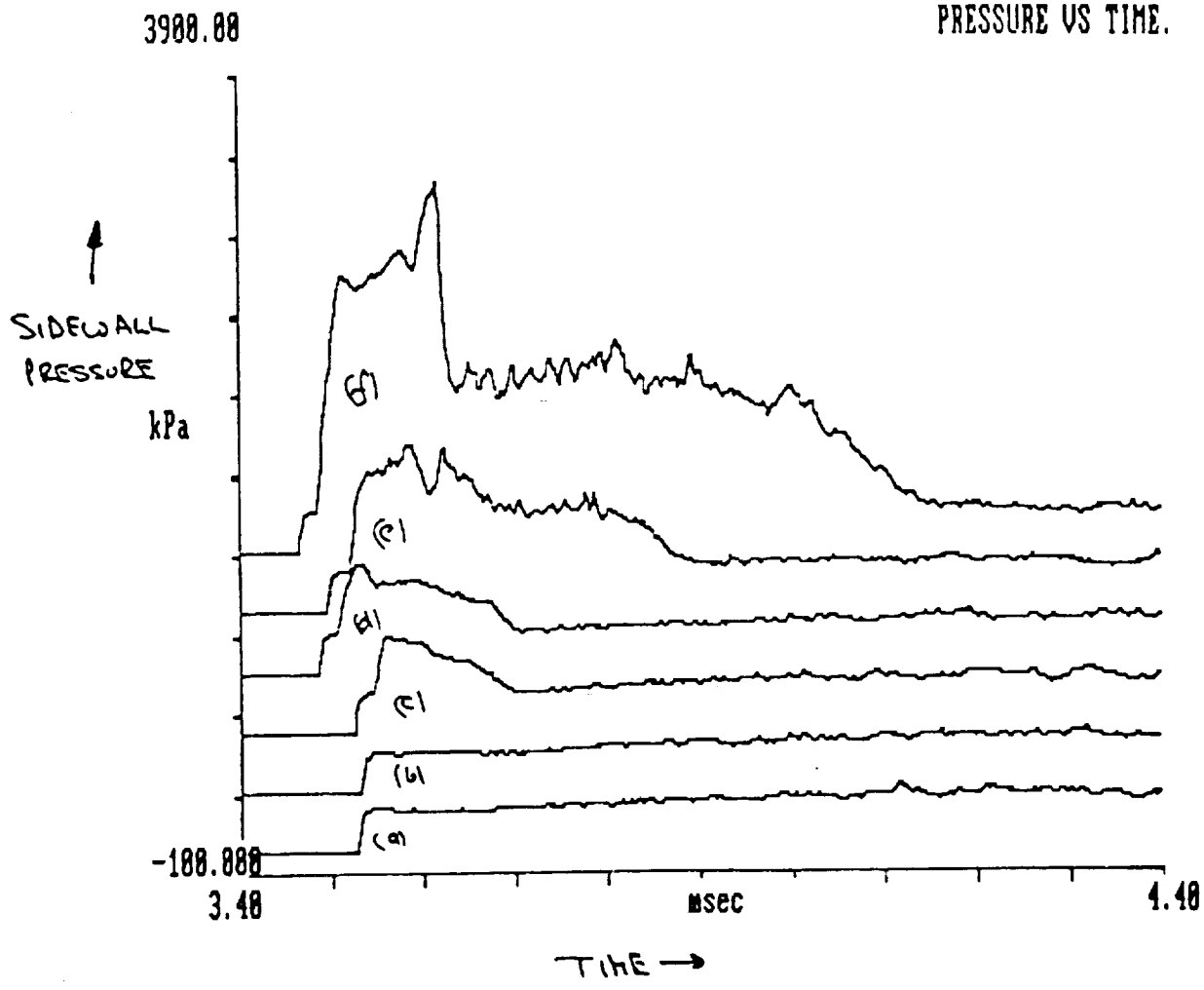

Figure 9(b): Effect of Diaphragm Thickness on Sidewall Pressure (Measured 15 mm Upstream of Diaphragm)
p_1 = 4 kPa

(a) - no diaphragm
(b) - 13 μm polyethylene
(c) - 25 μm cellophane
(d) - 50 μm cellophane
(e) - 102 μm mylar
(f) - 191 μm mylar

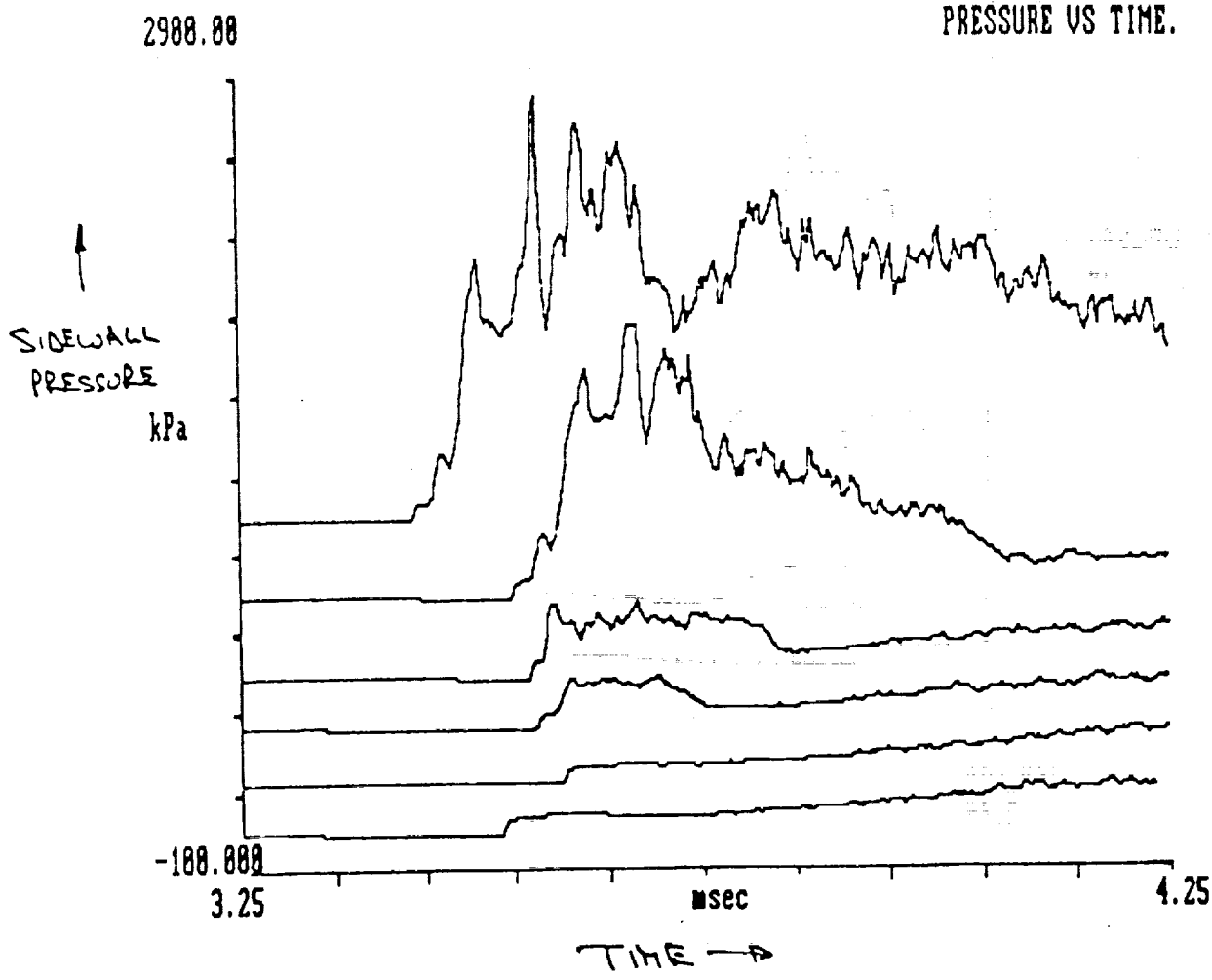

Figure 9(c): Effect of Diaphragm Thickness on Sidewall Pressure (Measured 15 mm Upstream of Diaphragm)
p_1 = 1 kPa

(a) - no diaphragm
(b) - 13 μm polyethylene
(c) - 25 μm cellophane
(d) - 50 μm cellophane
(e) - 102 μm mylar
(f) - 191 μm mylar

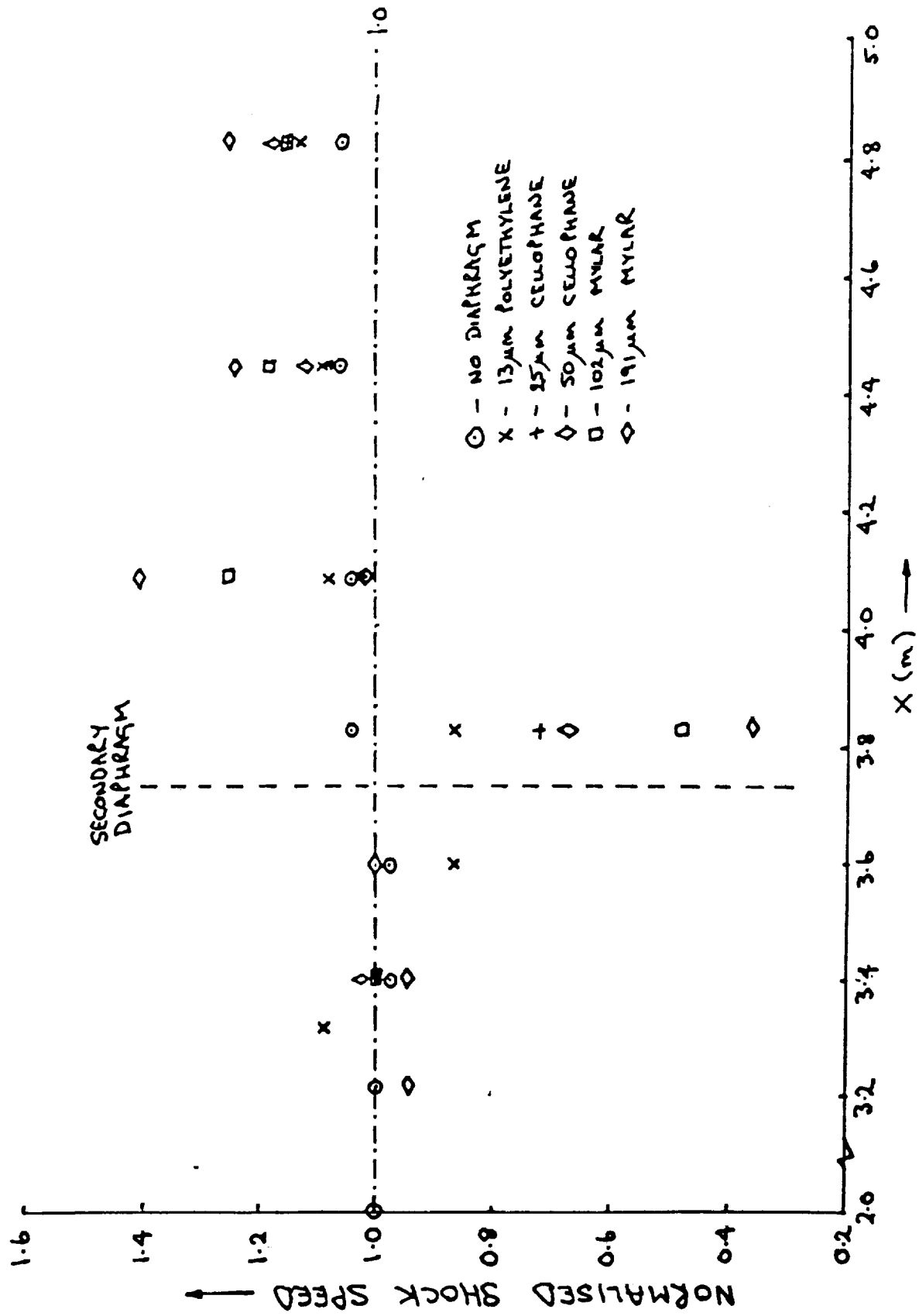

Figure 10: Effect of Diaphragm Thickness on Shock Speed (p_1 = 1 kPa)

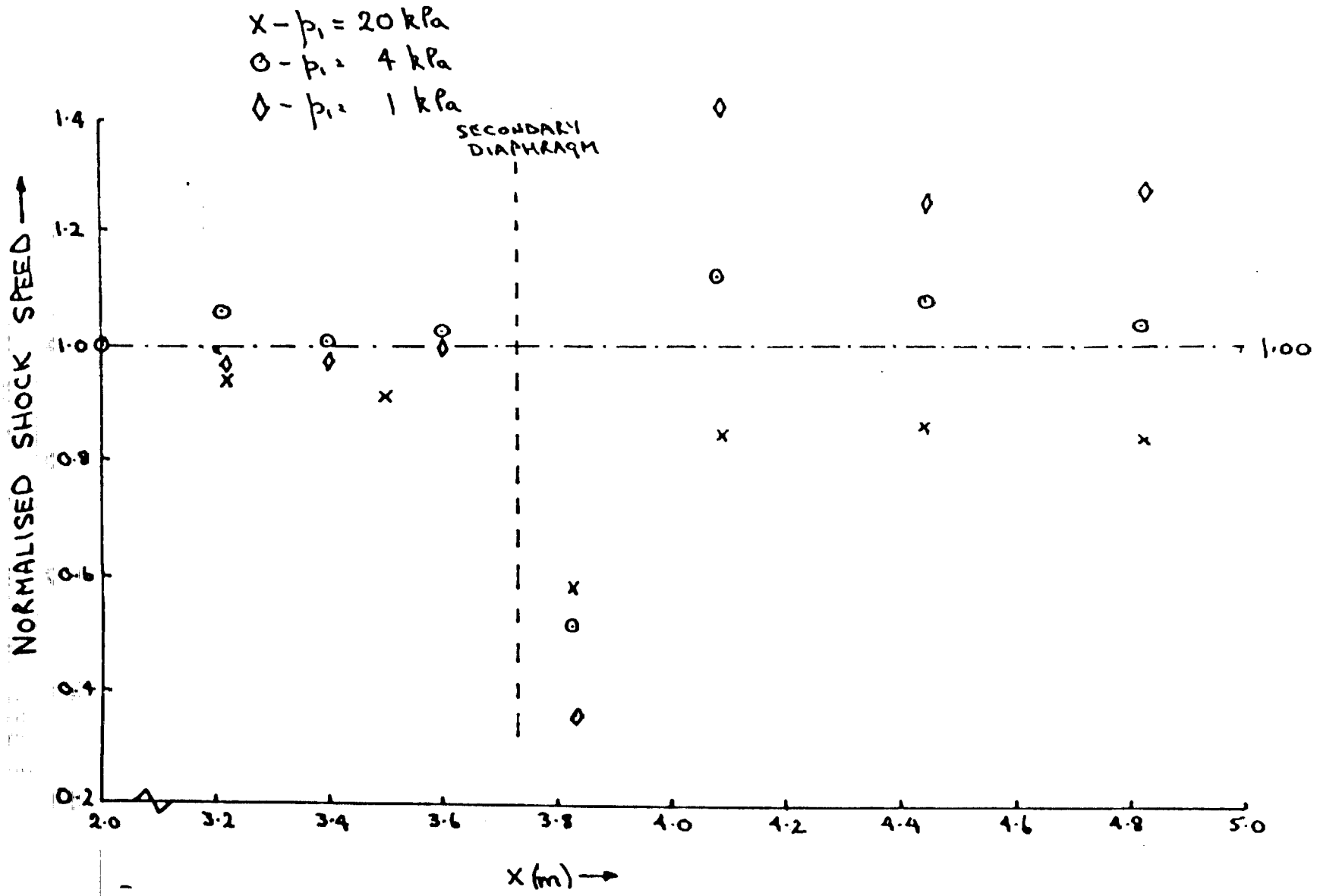

Figure 11: Effect of Initial Pressure on Shock Speed
Diaphragm Thickness = 191 μm (MYLAR)

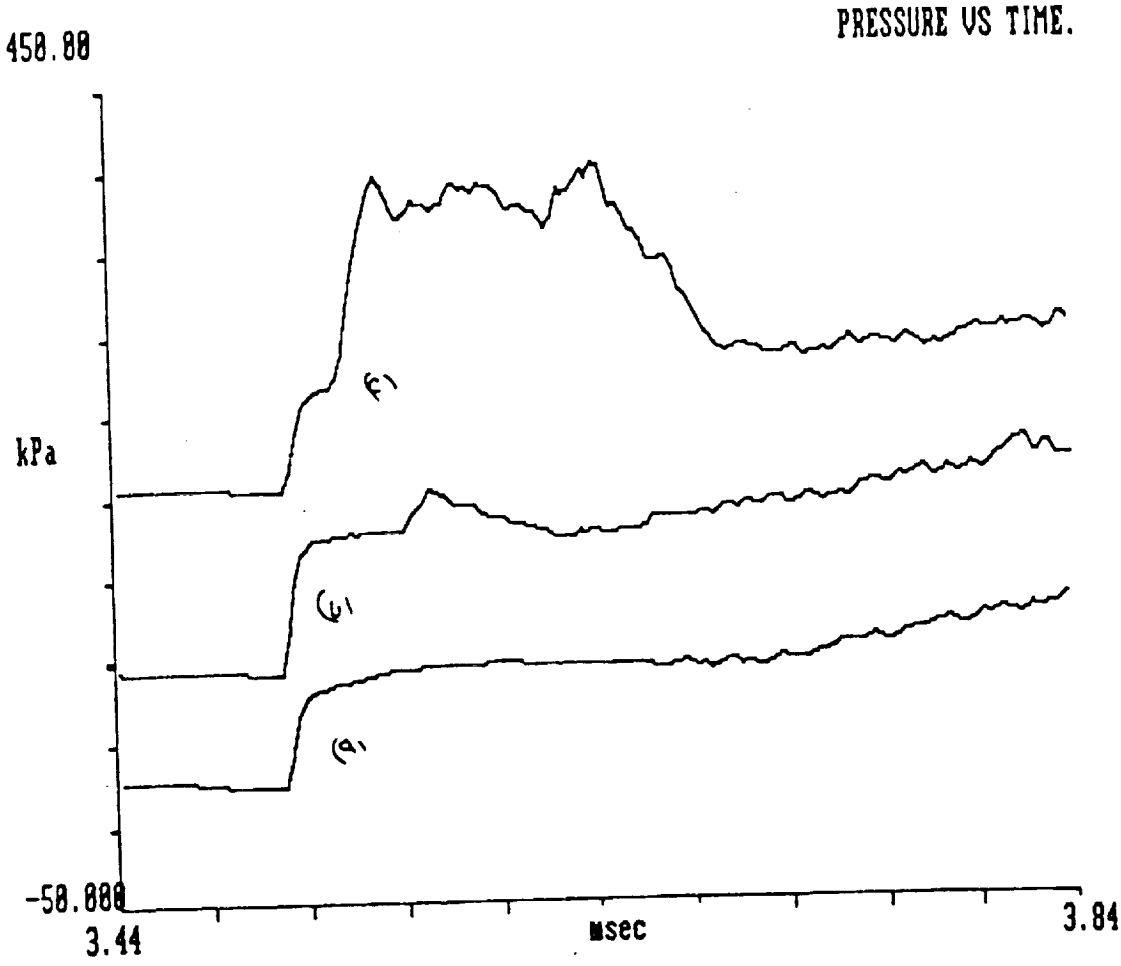

Figure 12(a): Effect of Diaphragm Deformation on Sidewall Pressure
(Measured 15 mm Upstream of Diaphragm)
p_1 = 1 kPa

(a) - no diaphragm
(b) - 25 μm cellophane diaphragm, pre-deformed
(c) - 25 μm cellophane, planar

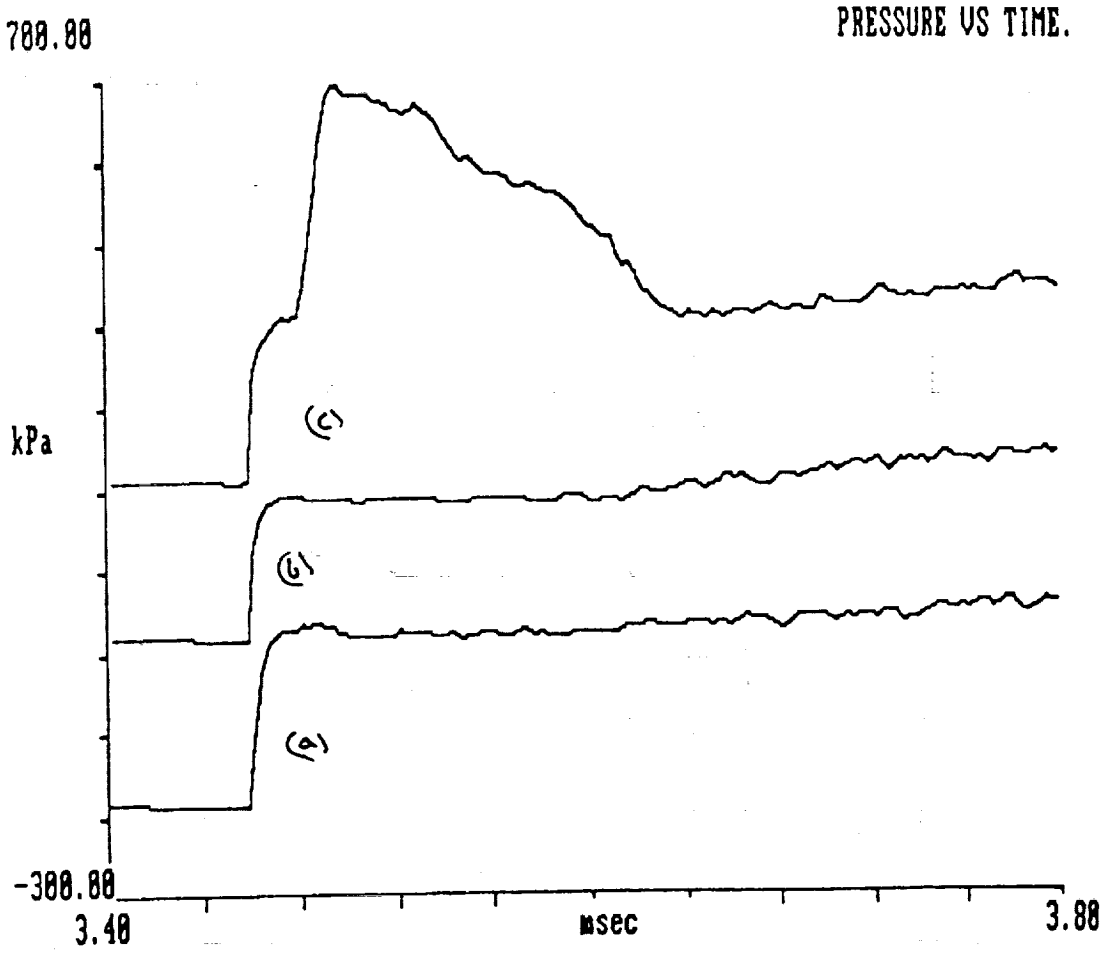

Figure 12(b): Effect of Diaphragm Pre-Deformation on Sidewall Pressure
(Measured 15 mm Upstream of Diaphragm)
p_1 = 4 kPa

(a) - no diaphragm
(b) - 25 μm cellophane diaphragm, pre-deformed
(c) - 25 μm cellophane, planar

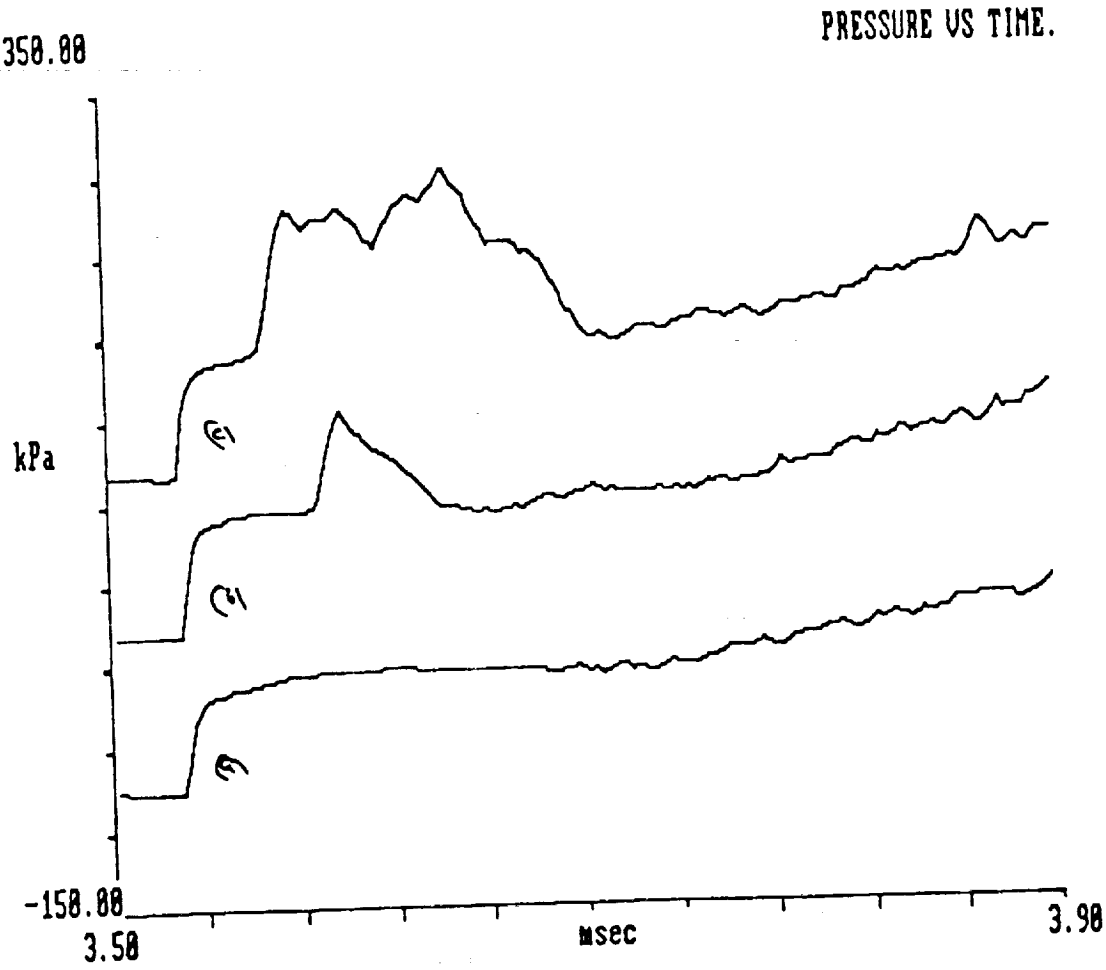

Figure 12(c): Effect of Diaphragm Pre-Deformation on Sidewall Pressure (Measured 19.5 mm Upstream of Diaphragm)
p_1 = 1 kPa

(a) - no diaphragm
(b) - 25 μm cellophane diaphragm, pre-deformed
(c) - 25 μm cellophane, planar

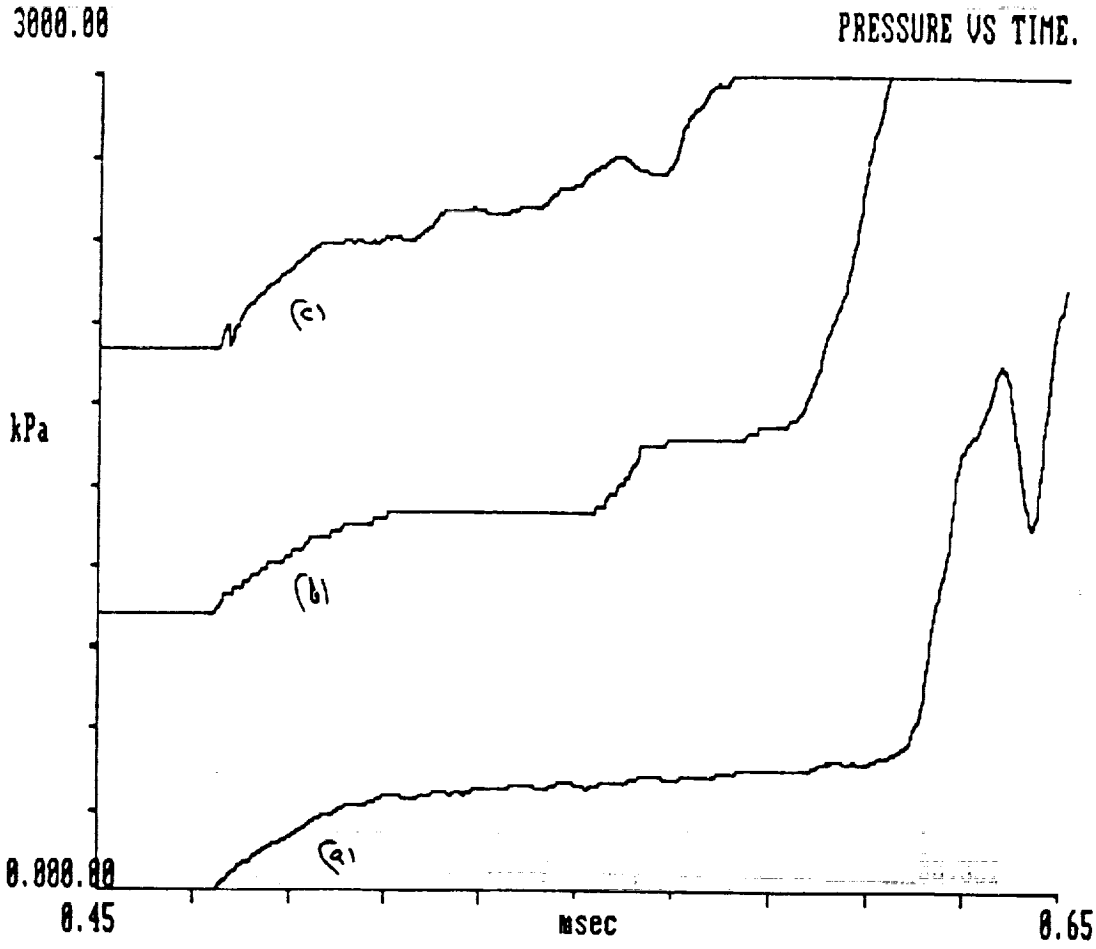

Figure 13(a): Effect of Diaphragm Pre-Deformation on Pitot Pressure
p_1 = 1 kPa

(a) - no diaphragm
(b) - 25 μm cellophane diaphragm, pre-deformed
(c) - 25 μm cellophane, planar

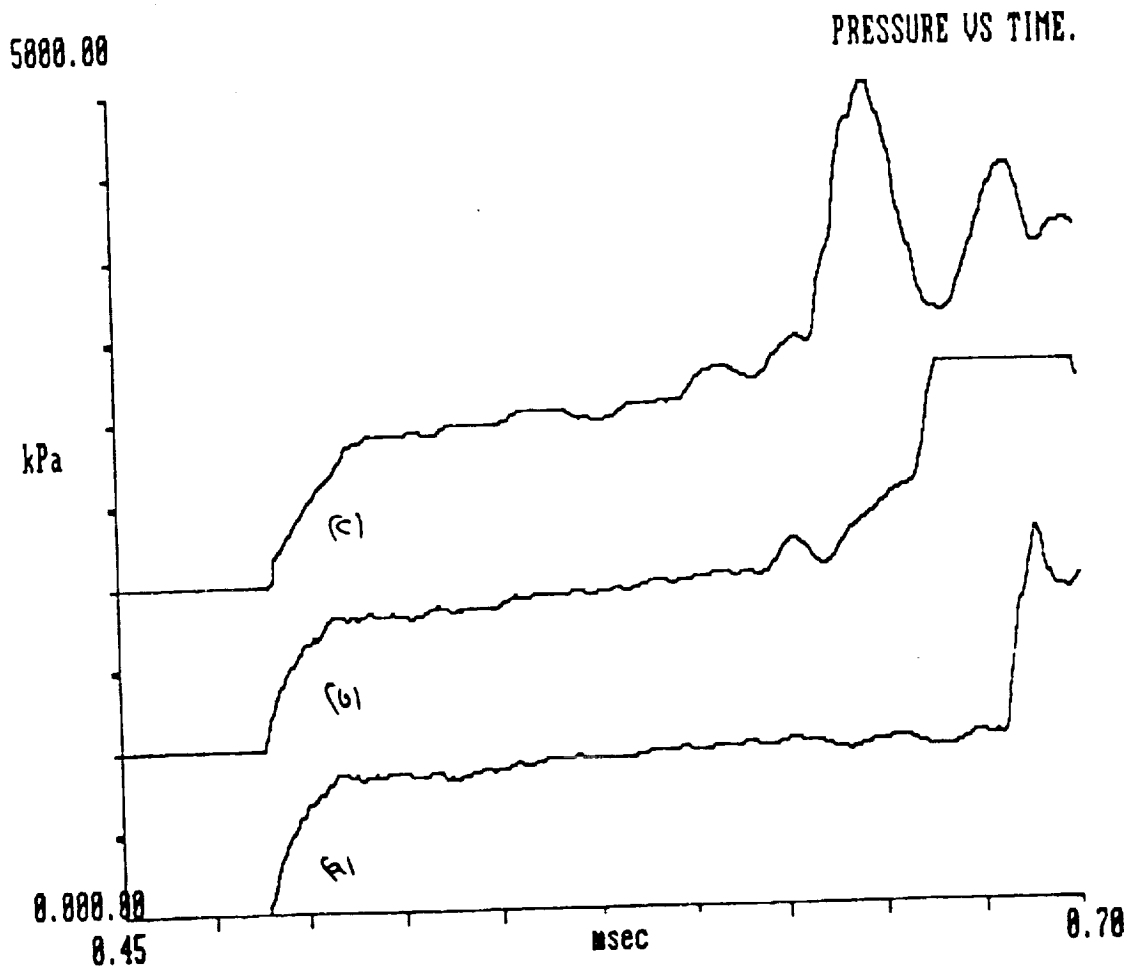

Figure 13(b): Effect of Diaphragm Pre-Deformation on Pitot Pressure
p_1 = 4 kPa

(a) - no diaphragm
(b) - 25 μm cellophane diaphragm, pre-deformed
(c) - 25 μm cellophane, planar

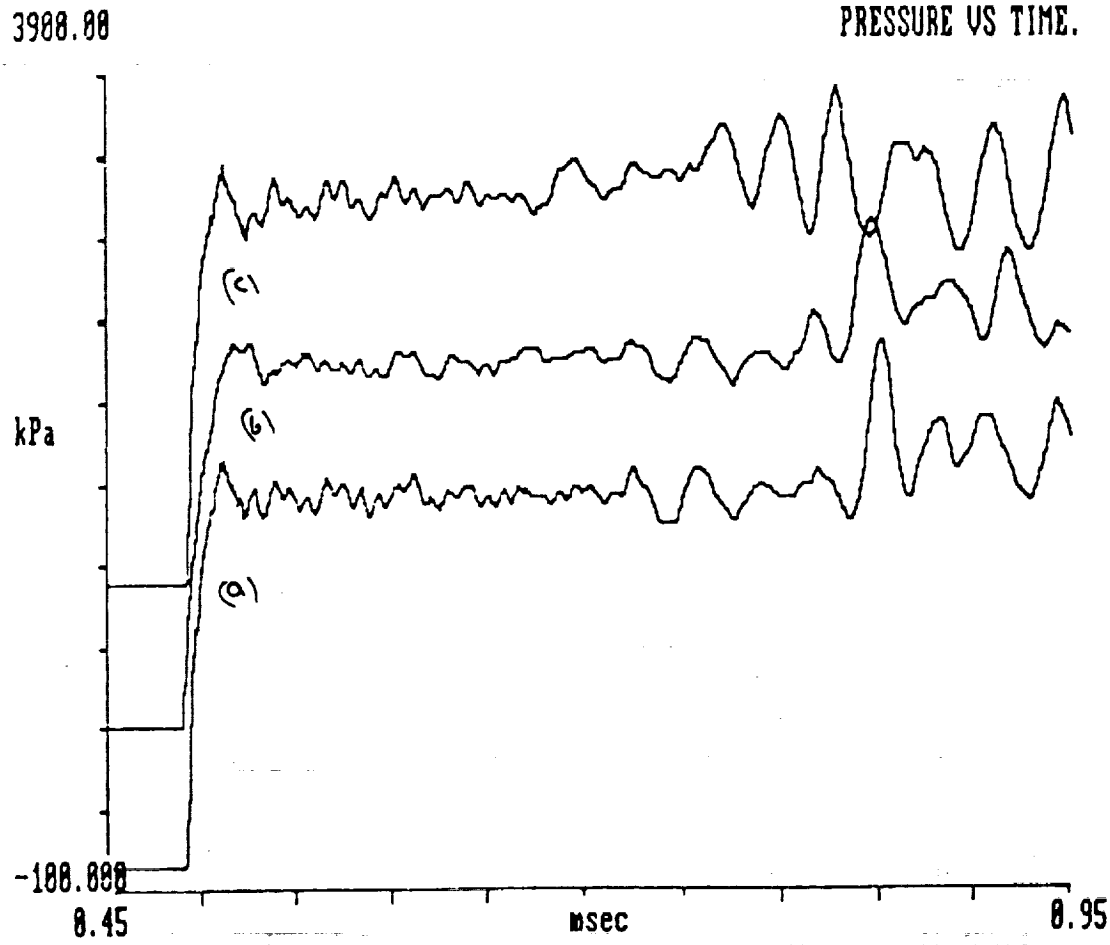

Figure 14(a): Effect of Diaphragm Location on Pitot Pressure
p_1 = 20 kPa

(a) - no diaphragm
(b) - 102 μm mylar diaphragm, x = 3.736 m
(c) - 102 μm mylar diaphragm, x = 2.111 m

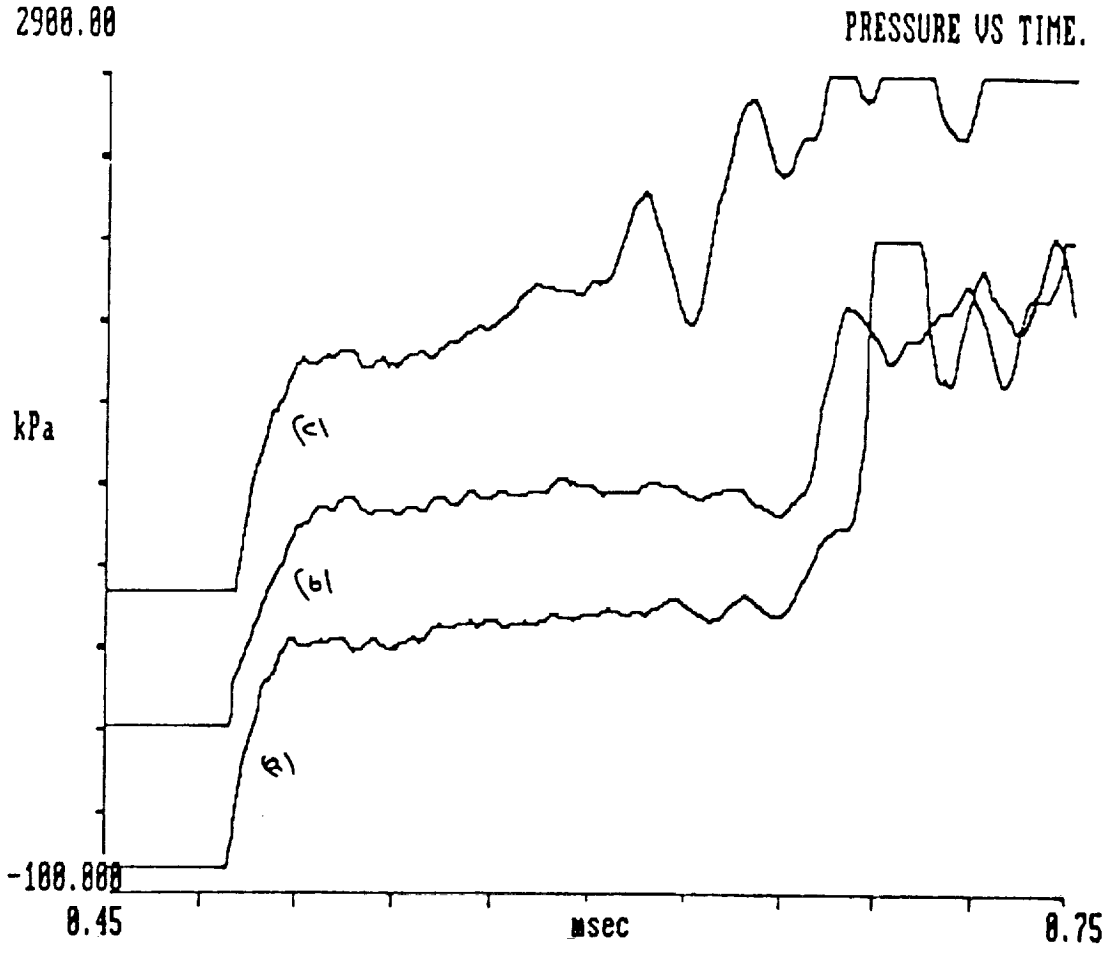

Figure 14(b): Effect of Diaphragm Location on Pitot Pressure
p_1 = 4 kPa

(a) - no diaphragm
(b) - 102 μm mylar diaphragm, x = 3.736 m
(c) - 102 μm mylar diaphragm, x = 2.111 m

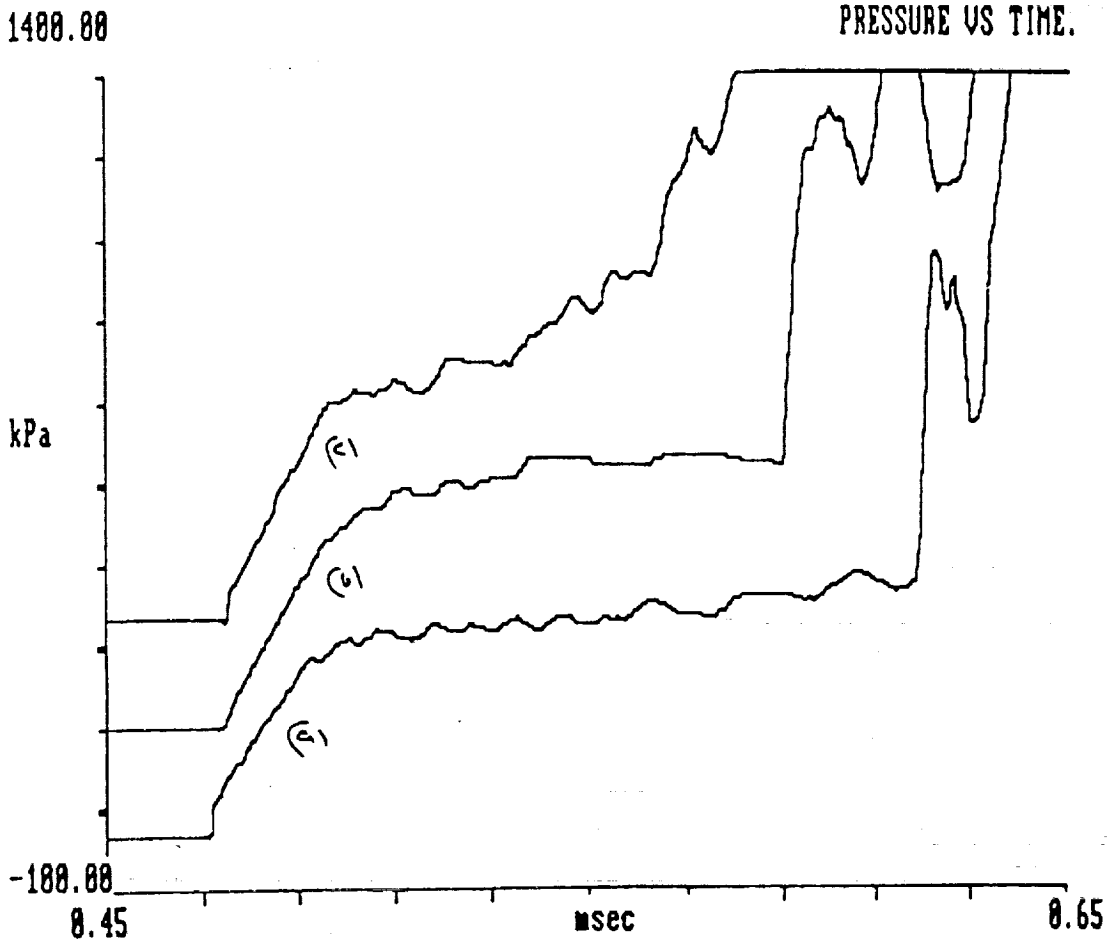

Figure 14(c): Effect of Diaphragm Location on Pitot Pressure
p_1 = 1 kPa

(a) - no diaphragm
(b) - 102 μm mylar diaphragm, x = 3.736 m
(c) - 102 μm mylar diaphragm, x = 2.111 m

MASS LOSS OF TEST GAS IN THE BOUNDARY LAYER OF AN EXPANSION TUBE

(R.J. Stalker)

1. Introduction

It is well known that the boundary layer in a shock tube causes loss of gas from the test region between the shock wave and the interface, and limits the size of the test region that can be produced. In a similar manner, the continued growth of the boundary layer after the contact surface can cause loss of gas from that region, and if this is the test region of an expansion tube, it may cause a significant flow of gas through that region. Whereas simple expansion tube theory would demand that the test gas is stationary with respect to the interface, this boundary layer effect would cause test gas to flow towards the interface in the inviscid part of the flow, and away from the interface in the boundary layer. This may lead to an axial velocity gradient in the test flow, and give rise to uncertainty concerning the history of the test gas. There is therefore a need for a preliminary analysis to determine the magnitude of this effect.

Mirels[1] presented an analysis of the shock tube boundary layer effect. He used the Howarth transformation, and the assumption that the product of viscosity and density was constant across the boundary layer at a value determined by a reference enthalpy, to determine the mass flow in the boundary layer. These same approximations have been used to good effect in conventional high speed boundary layer analyses, and they were found to yield reasonable agreement with experiment for the shock tube boundary layer case also. Therefore these approximations will be used here as the basis of an analysis to determine the effect of the boundary layer in expansion tube flow.

2. Analysis

The flow situation envisaged is showing in Fig. 1. The frame of reference is fixed in the interface between the shocked acceleration gas, 20, and the expansion tube test flow, 5. It is assumed that boundary layer effects in the region 20 are sufficiently developed to ensure that the mass of gas flowing in from the region 10 is balanced by the mass which leaves 20 by boundary flow at the interface, so that the distance from the interface to the shock wave, X_s, is constant in time. The boundary layer consists only of acceleration gas upstream of the interface, but downstream of the interface it involves a mixture of acceleration gas and test gas. It will be assumed, however, that acceleration and test gases are the same. In the test region, in general the boundary layer will grow at a different rate to that in the post-shock region, and it will appear to originate at a distance X_e upstream of the interface.

The momentum in the boundary layer at any station may be written as (for a thin boundary layer)

---

[1] Mirels. H. "Shock tube test time limitation due to turbulent-wall boundary layer". AIAA Journal, V2, pp 84-93, 1964.

$$q = \Pi D \int_w^{\delta} \rho\, u^2\, dy \qquad (1)$$

where u and ρ are the boundary layer velocity and density, y is the distance normal to the surface, D is the tube diameter, w signifies conditions at the surface, and δ is the thickness of the boundary layer. Using the Howarth transformation, put

$$\rho\, dy = \rho^*\, dy_i \qquad (2)$$

where y_i is the co-ordinate of y in an incompressible flow of density ρ^*. This is the density determined at the pressure prevailing in the flow, and a temperature determined at the same pressure and a reference enthalpy given by

$$h^* = 0.5\,(h_\delta + h_w) + 0.22\,(h_r - h_\delta)$$

where h_w and h_δ are the enthalpy at the surface and at the edge of the boundary layer, and $h_r = h_\delta + 0.5\, u_w^2$ is the recovery enthalpy with Prandtl number unity while u_w is the velocity at the surface.

It can be shown that, using the Howarth transformation, a laminar compressible boundary layer is transformed into an incompressible form, and it is assumed that the same applies to a turbulent boundary layer. Equation 1 therefore can be written

$$q = \rho^*\, u_w^2 \int_w^{\delta_i} \left(\frac{u}{u_w}\right)^2 dy_i = \rho^*\, u_w^2\, \delta_i \int_0^1 \left(\frac{u}{u_w}\right)^2 d(y_i/\delta_i) \qquad (3)$$

where u is the velocity in the boundary layer. The profiles of velocity obey similarity in both laminar and turbulent incompressible boundary layers, wherefore

$$\int_0^1 \left(\frac{u}{u_w}\right)^2 d(y_i/\delta_i) = k_\ell \text{ or } k_t \qquad (4)$$

where k_ℓ and k_t are constants depending only on the ratio of surface to mainstream velocity (essentially the same on either side of the interface). For a laminar layer.

$$\delta_i = k_1 \left(\frac{\mu^*}{\rho^* u_w}\right)^{1/2} x^{1/2} \qquad (5)$$

and for the turbulent case

$$\delta_i = k_2 \left(\frac{\mu^*}{\rho^* u_w} \right)^{1/5} x^{4/5} \qquad (6)$$

where k_1 and k_2 are constants, x is the distance from the origin of the boundary layer, and μ^* is the viscosity at the reference enthalpy temperature.

The effective origin of the test region boundary layer (i.e. the value of X_e) can be obtained by assuming that adjustment from the acceleration region to the test region in the boundary layer takes place in a few boundary layer thicknesses. The impulse of the skin friction at the surface is then negligible compared with the momentum in the boundary layer, implying that this remains constant as the boundary layer passes the interface (there are no pressure gradient forces). Thus, putting $q_5 = q_{20}$ at the interface equations (3), (4) and (5) yield

$$\rho_{20}^* \; u_w^2 \; k_1 \left(\frac{\mu_{20}^*}{\rho_{20}^* \; u_w} \right)^{1/2} (x_s)^{1/2} \; k_\ell = \rho_5^* \; u_w^2 \; k_1 \left(\frac{\mu_5^*}{\rho_5^* \; u_w} \right)^{1/2} (x_e)^{1/2} \; k_\ell$$

which becomes

$$x_e / x_s = \mu_{20}^* \; \rho_{20}^* / \mu_5^* \; \rho_5^* \qquad (7)$$

for a laminar boundary layer, and equations (3), (4) and (6) yield

$$\rho_{20}^* \; u_w^2 \; k_2 \left(\frac{\mu_{20}^*}{\rho_{20}^* \; u_w} \right)^{1/5} (x_s)^{4/5} \; k_1 = \rho_5^* \; u_w^2 \; k_2 \left(\frac{\mu_5^*}{\rho_5^* \; u_w} \right)^{1/5} (x_e)^{4/5} \; k_1$$

which becomes

$$x_e / x_s = (\rho_{20}^* / \rho_5^*) (\mu_{20}^* / \mu_5^*)^{1/4} \qquad (8)$$

for a turbulent boundary layer. Here the subscript 20 indicates the region in the acceleration gas between the shock wave and the interface, and the subscript 5 indicates the test region. These equations determine x_e if x_s is known, and therefore allow the boundary layer in the test region to be defined.

The mass flow within the boundary layer at any station can be written as

$$m_{bl} = \Pi D \int_w^{\delta} \rho y \, dy$$

and, using the Howarth transformation again, this becomes

$$m_{bl} = \Pi D \rho^* u_w \delta_t \int_0^1 \frac{u}{u_w} d(y_i / \delta_t) = \Pi D \rho^* u_w \delta_t k^1$$

where k^1 is a constant k_ℓ^1 for laminar layers and k_t^1 for turbulent layers. Considering the laminar case first, the mass flow in the boundary layer in the test region may be written. by equation 5. as

$$(m_{b\ell})_5 = \pi D \rho_5^* u_w k_1 \left(\frac{\mu_5^*}{\rho_5^* u_w} \right)^{1/2} (z + X_e)^{1/2} k_\ell^1$$

where z is the distance from the interface, and using equation 7, this becomes

$$(m_{b\ell})_5 = \pi D \rho_{20}^* u_w k_1 \left(\frac{\mu_{20}^*}{\rho_{20}^* u_w} \right)^{1/2} X_s^{1/2} k_\ell^1 \left(\frac{z + X_e}{X_e} \right)^{1/2}$$

and, since the mass flow in the boundary layer at the interface is equal to the mass flow through the shock wave,

$$(m_{b\ell})_5 = A \rho_{10} u_{10} \left\{ \frac{z}{X_e} + 1 \right\}^{1/2}$$

where A is the area of the tube cross-section, and ρ_{10} and u_{10} are the density and velocity in the acceleration gas passing into the shock. The mass of test gas which has been swept into the boundary layer is equal to the boundary layer mass flow less the boundary layer mass flow at the interface, i.e. $(m_{b\ell})_5 - (m_{b\ell})_0$, and this may be written as

$$(m_{b\ell})_5 - (m_{b\ell})_0 = A\rho_{10}\, u_{10} \left\{ \left(\frac{z}{X_e} + 1 \right)^{1/2} - 1 \right\} \tag{9}$$

for a laminar boundary layer. For a turbulent boundary layer, a similar analysis yields

$$(m_{b\ell})_5 - (m_{b\ell})_0 = A\rho_{10}\, u_{10} \left\{ \left(\frac{z}{X_e} + 1 \right)^{4/5} - 1 \right\} \tag{10}$$

The axial velocity perturbation, Δu_5, induced by this boundary layer flow returning upstream may now be obtained. At any station, the mass flow of test gas in the inviscid region towards the interface must match the mass flow of boundary layer fluid away from the interface. That is, assuming that the boundary layer is thin,

$$\rho_5\, A\, \Delta u_5 = (m_{b\ell})_5 - (m_{b\ell})_0 , \tag{11}$$

and, remembering that $\rho_{10} = \epsilon\rho_{20}$, where ϵ is the inverse shock density ratio, and putting $\rho_{20} = \rho_5\, a_5^2 / a_{20}^2 = \rho_5\, M_{20}^2 / M_5^2$, equations 9 and 11 yield, for a laminar boundary layer

$$\Delta u_5 = \epsilon\, u_{10}\, (M_{20} / M_5)^2 \left\{ \left(\frac{z}{X_e} + 1 \right)^{1/2} - 1 \right\} , \tag{12}$$

and for a turbulent boundary layer

$$\Delta u_5 = \epsilon u_{10}\, (M_{20} / M_5)^2 \left\{ \left(\frac{z}{X_e} + 1 \right)^{4/5} - 1 \right\} . \tag{13}$$

The significance of equations 12 and 13 can be seen by reference to the wave diagram of Figure 2. The velocity Δu_5 is constant along lines parallel to the interface, with Δu_5 increasing with distance from the interface, implying that the greater

the distance from the interface, the more test gas needs to be brought forward in a given time interval to replace that which is removed by the boundary layer. To estimate the amount of test gas brought forward for stations which are close to the interface, the time interval can be taken as t, the time since the secondary diaphragm was ruptured, and the expansion tube flow was initiated. Therefore the amount of test gas brought forward, expressed as the length of test region that this gas would occupy, can be written as $\Delta Z = \Delta u_5 \, t$ and since Z, the length of the test region is given by $Z = u_{10} t / M_5$, it follows that the proportion of the test region gas which is lost to the boundary layer at station z is given by

$$\frac{\Delta Z}{Z} = \frac{\Delta u_5}{u_{10}} M_5 \qquad (14)$$

For stations which are not close to the interface this expression will be in error, since the boundary layer no longer develops in a constant pressure region for most of the time 5. However, it can then be used to provide a useful estimate of the order of magnitude of the effect.

It is worth noting that factors which may be expected to influence a boundary layer analysis, such as the Reynold's number and the tube diameter, do not appear explicitly in equations 12 and 13. In fact, these effects are incorporated through X_e, which by equation 7 is directly related to X_s, where the effects are clearly evident.

3. CALCULATIONS

To demonstrate the magnitude of the boundary layer effect, calculations are carried out for a laminar and for a turbulent boundary layer.

(a) Laminar boundary layer

$u_5 = u_{10} = 6$ km.s^{-1}, $P_{10} = 50$ Pa (0.0005 atm), D = 150 mm, $M_5 = 7.0$

By eqn (7), $X_e = (\mu^*_{20} \rho^*_{20} / \mu^*_5 \rho^*_5) X_s = (\mu^*_{20} T^*_5 / \mu^*_5 T^*_{20}) X_s$

$T^*_5 = 2{,}700$ k, $T^*_{20} = 6{,}000$ k

$\therefore X_e = 0.68 X_s$

From Mirels [1], $X_s = 0.64$ m , $\therefore X_e = 0.44$ m.

From real gas calculations, $\epsilon = 14^{-1}$, $M_{20} = 3.4$

$$\therefore \Delta u_5 / u_{10} = \frac{1}{14} \left(\frac{3.4}{7.0} \right)^2 \left\{ \left(\frac{z}{0.44} + 1 \right)^{1/2} - 1 \right\}, \text{ by eqn (12)}$$

and $\Delta Z = 7.0 \, \Delta u_5 / u_{10}$, by eqn (14)

These two results are plotted in Fig. 3.

(b) Turbulent boundary layer

u_s = 6 km.s^{-1}, P_{10} = 500 Pa (0.005 atm), D = 150 mm, M_s = 7.0

As above, from eqn (8), $X_e = 0.50\ X_s$ m.

From Mirels [1], X_s = 0.443 m, $\therefore$ X_e = 0.222 m.

From real gas calculations, $\epsilon = 13^{-1}$, M_{20} = 3.0

$$\therefore \Delta u_5 / u_{10} = \frac{1}{13}\left(\frac{3.0}{7.0}\right)^2 \left\{\left(\frac{z}{0.222} + 1\right)^{4/5} - 1\right\}, \text{ by eqn (13)}$$

and $\Delta Z_z = 7.0\ \Delta u_5 / u_{10}$ as before

These two results are also plotted in Fig. 3.

The results show that, as would be expected, the turbulent boundary layer has a much larger effect than the laminar one, yielding a perturbation velocity and movement of test gas towards the interface which is about four times the laminar case. The magnitude of the movement of test gas towards the interface, when the boundary layer is turbulent and the distance from the interface is two metres for example, is approximately one metre during the time that the expansion tube flow takes place. At the expanded Mach number of 7, this implies that this test gas, instead of originating approximately 7 cm. from the secondary diaphragm immediately before it bursts (assuming no shock reflection at the diaphragm), in fact originates 10.5 cm from the diaphragm. This does not appear to be a very significant effect.

As mentioned previously, this assumes that the boundary layer two metres from the interface develops under the conditions of the expanded test flow. In fact, during most of the time that the expansion tube is operating, the fluid which is to constitute this part of the flow is at a higher density than the test region, and the boundary flows into an adverse pressure gradient due to its flow in the upstream direction in the presence of the unsteady expansion. Both these effects may be expected to reduce the mass flow in the boundary layer when it is enveloped by the test region. This suggests that the present analysis may somewhat overestimate the boundary layer effect.

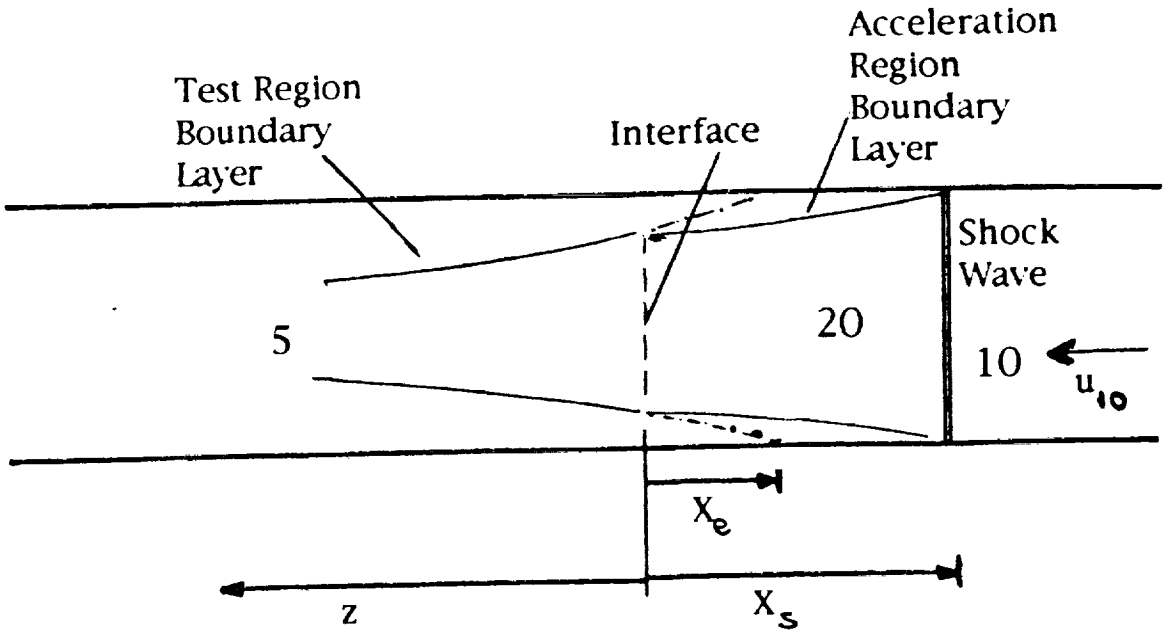

Fig.1. FLOW CONFIGURATION

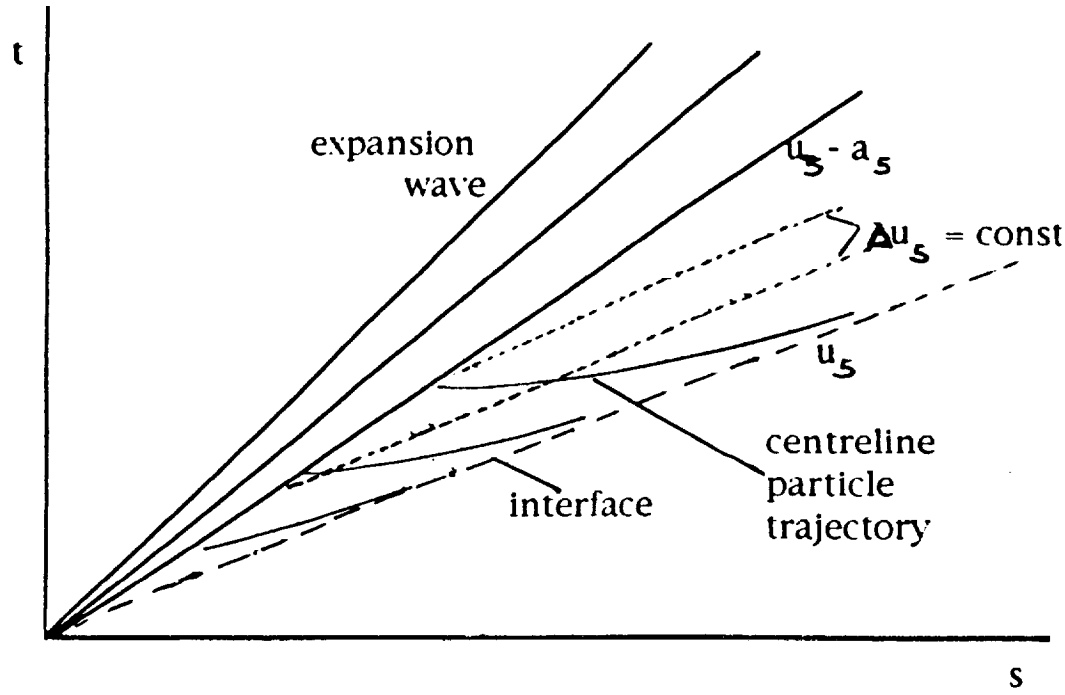

Fig. 2. WAVE DIAGRAM SHOWING BOUNDARY LAYER INDUCED VELOCITY PERTURBATIONS

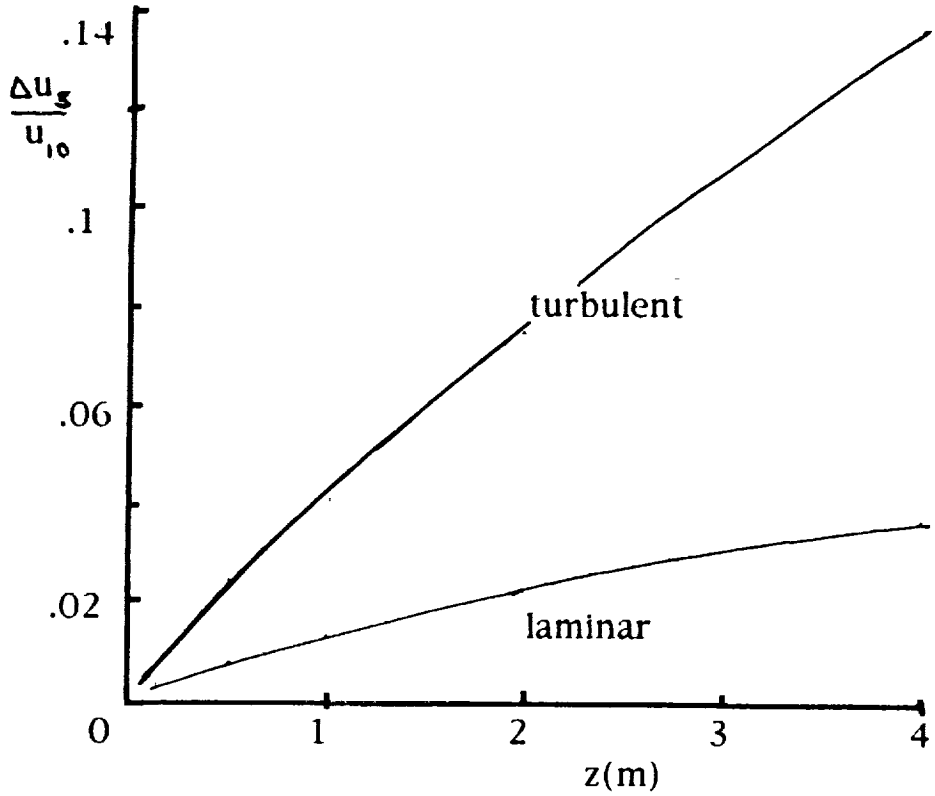

(a) VELOCITY PERTURBATIONS

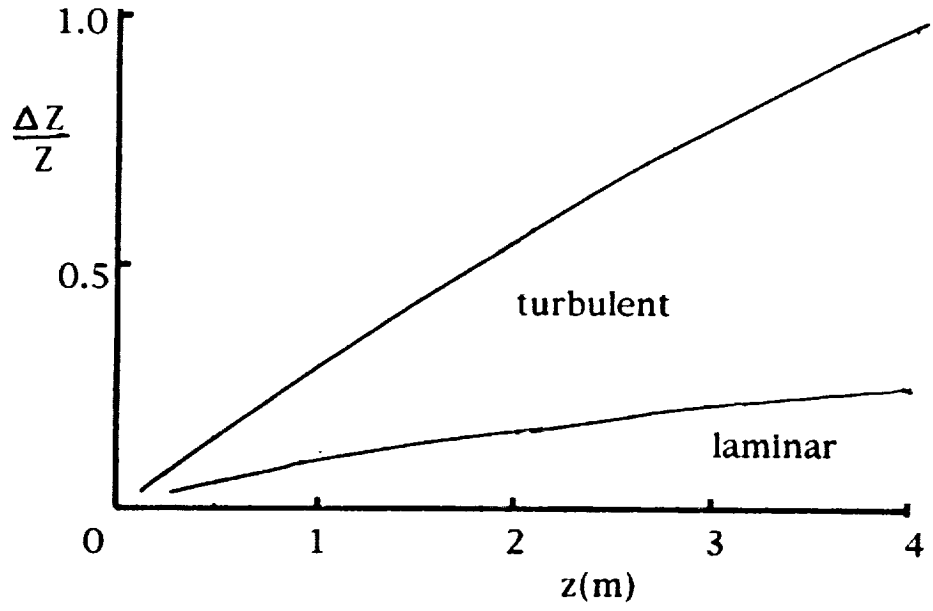

(b) MOVEMENT OF TEST GAS DUE TO VELOCITY PERTURBATIONS

Fig. 3. MOTION OF TEST GAS DUE TO BOUNDARY LAYER EFFECT

THRUST BALANCE DEVELOPMENT

by Sean Tuttle

Extensive finite element modelling of the proposed thrust balance with the two twisted stings (Fig. 1) using NASTRAN has shown that the axial stress wave will propagate down the stings without distortion (the axial strain in the sting is proportional to the net axial thrust). The nozzle to be used is a symmetrically diverging nozzle with 11^{o} ramp walls. The area ratio is approximately 5.5. Its length is 300 mm - this is to ensure sufficient thrust is produced and that the pressure hump predicted by Allen (1991) is not spilt.

The scramjet to be used is 600 mm long with a 54x27 mm rectangular cross-section. Central injection will be used. The nozzle-sting system will be free to move i.e. it is not attached to the combustor section. The joint between the combustor and the nozzle is such that there is no flow spillage and no transmission of combustor wall stresses to the nozzle.

The stings are twisted through 90^{o} just aft of the nozzle to provide rigidity and bending stiffness. The finite element modelling has shown this to be acceptable. There are strain gauge bridges before and after the twist on each sting. The static pressure along the ramp walls will be measured. The pitot pressure across the nozzle exit plane will also be measured. The difference between the thrust measured by the pressure transducers and that measured by the strain gauges is the skin friction.

A simulated tunnel loading has been successfully deconvovled using an impulse response based on the finite element model of the system (Fig. 2). The results from initial bench tests performed on the nozzle show encouraging agreement with the finite element predictions (Fig. 3). The difference between the two signals after the arrival of the reflection is due to the different end conditions of the stings in the finite element model and the laboratory test. Therefore, it is felt that it will be possible to measure the thrust produced by this nozzle during the tests in T4 in August-September 1993.

References:

Allen, G.A., Parametric Study on Thrust Production in the Two Dimensional Scramjet, AIAA, 1991

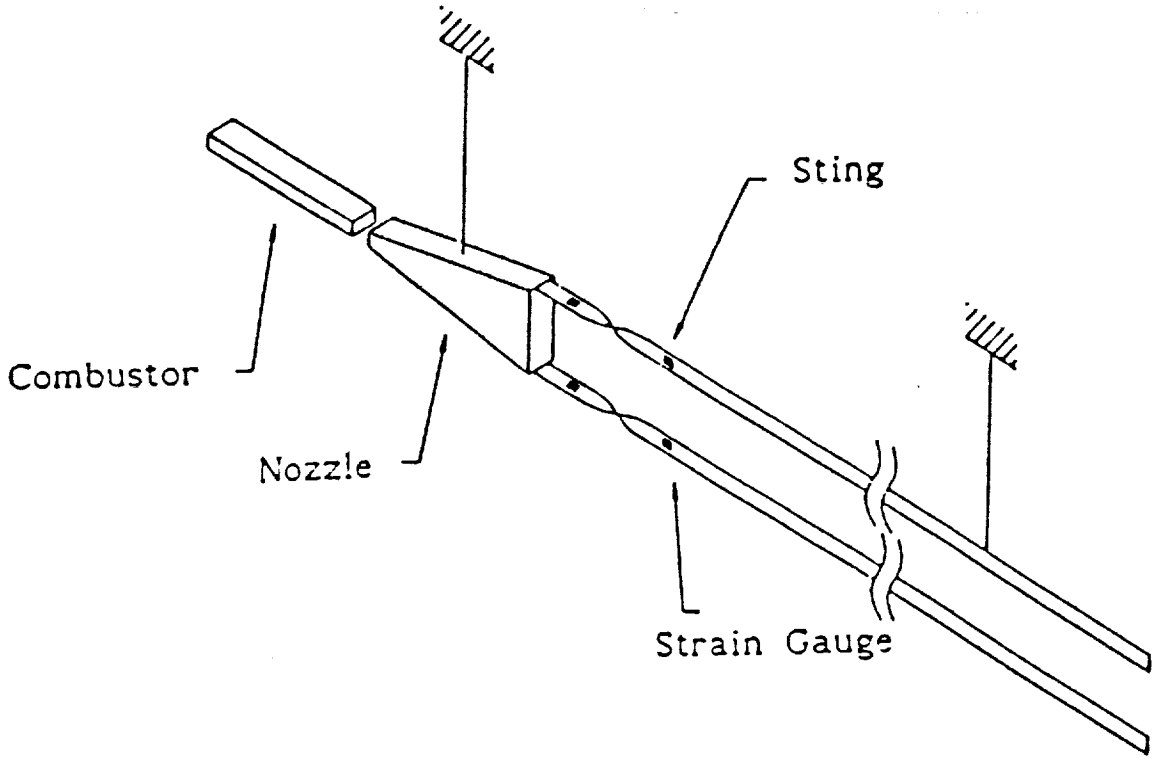

Figure 1. Thrust Balance Configuration

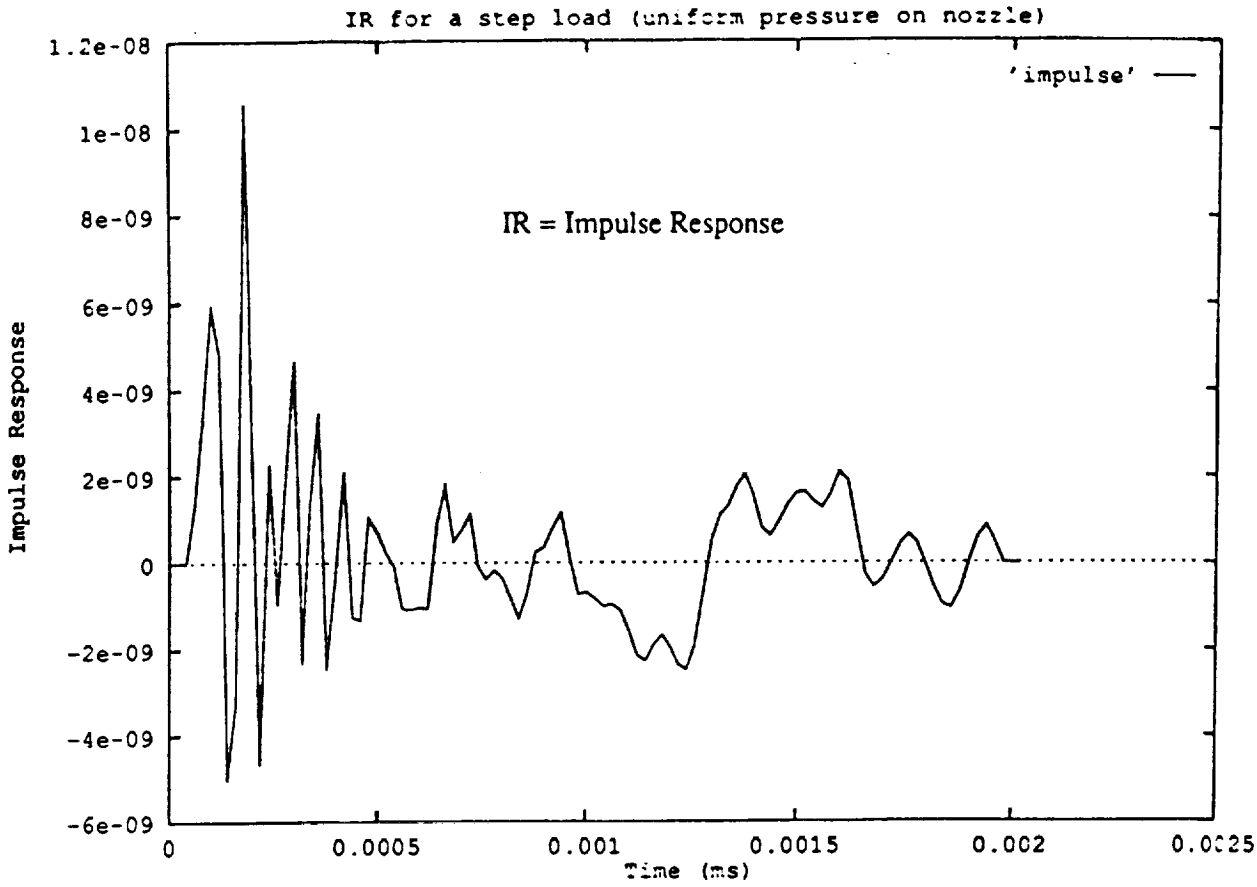

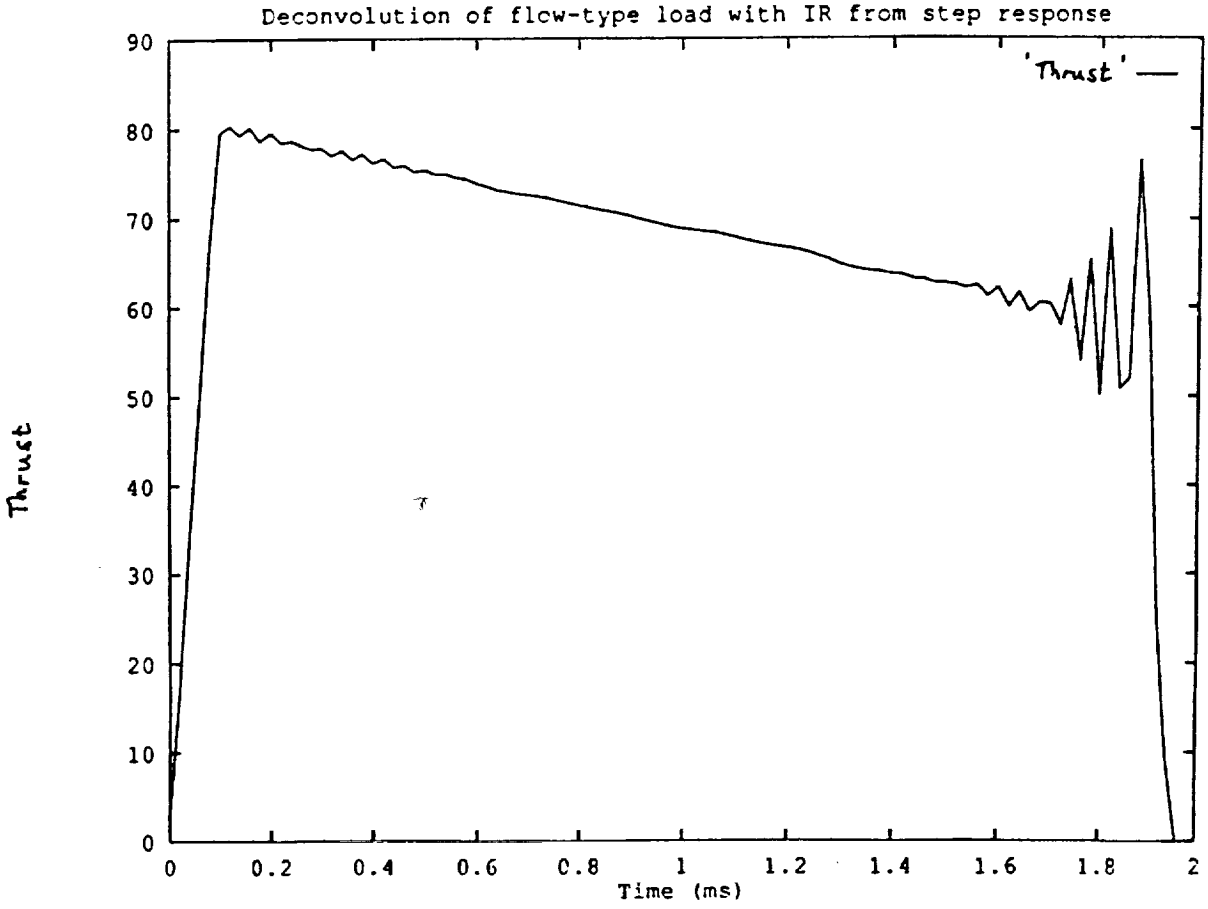

Figure 2. Impulse Response & Deconvolved Tunnel Loading

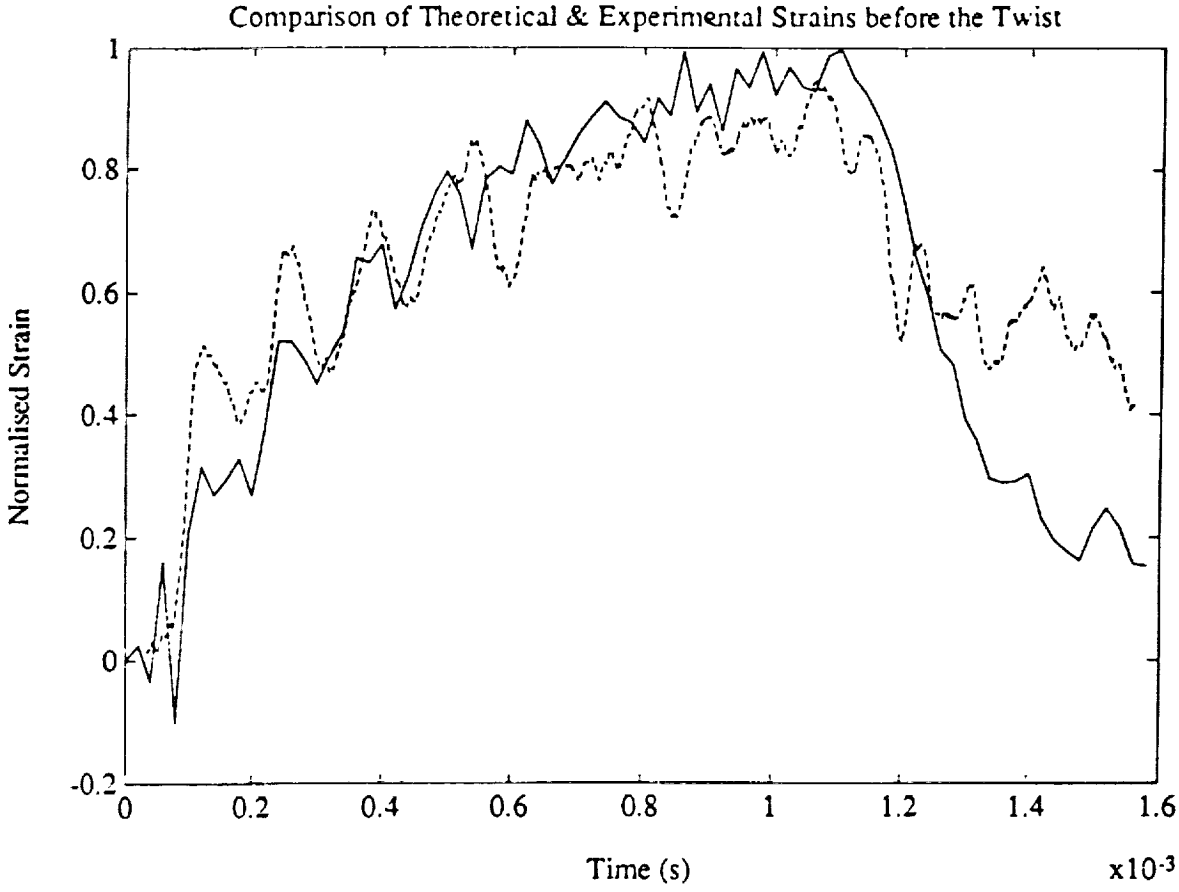

Figure 3. Comparison of Theoretical & Experimental Strains Before the Twist

Effects of Oxygen Dissociation on Hypervelocity Combustion Experiments

R.J. Bakos and R.G. Morgan
The University of Queensland, Brisbane,
Australia

J. Tamagno
General Applied Science Laboratories,
Ronkonkoma, New York

ABSTRACT

Results of a comparative experimental study are reported which was conducted to measure the effects of the test gas oxygen dissociation produced in reflected shock tunnels on hypervelocity combustion data. An identical combustor model was tested in a reflected shock tunnel with test gas containing approximately 50% by mass of oxygen in dissociated form, as either atomic oxygen or nitric oxide, and in an expansion tube having test gas containing negligible dissociated oxygen. Comparisons were made at two test conditions which were energy equivalent to flight conditions at Mach 13.5 and Mach 17. Because combustion induced pressure rise in supersonic ducted flow has a complex dependence on many flow parameters, it is important to carefully define the test conditions for the two facilities. A method was developed and applied for selection of comparison test conditions in the shock tunnel such that differences in measured combustor duct pressures should be sensitive to dissociation enhanced heat release alone. Comparison of measured combustor pressure distributions shows a very similar wave structure is produced with a small but measurable increase in pressure rise due to dissociation occurring in the shock tunnel. The maximum absolute combustion pressure difference detected over a range of hydrogen-air equivalence ratios was 11%. This range of difference is also predicted by equilibrium combustion simulations and its small magnitude is a result of the relatively high combustor inlet temperatures (>2000 K°) at which the tests were run.

NOMENCLATURE

a	mass fraction of total oxygen if the form of O atoms
a_n	mass fraction of total oxygen in the form of NO radicals
ϕ	hydrogen -air equivalence ratio
C_p, C_v	Specific heats at constant pressure and volume
γ	isentropic exponent, = C_p/C_v for an ideal gas
d	Combustor diameter
D_1	First Damkohler number, = the ratio of residence time in the combustor to chemical reaction time
D_2	Second Damkohler number, = $\Delta h_{C,NET}/h_0$ the ratio of energy released by combustion to the sum of thermal and kinetic energy
h_s	sensible enthalpy
h_c	chemical enthalpy
h_0	total sensible enthalpy, = $h_s + u^2/2$
H_{ST}	Stagnation enthalpy
$\Delta h_{C,NET}$	Net amount of heat release from combustion
M	Mach Number
P	Pressure
U	Velocity
T	Temperature
x	Axial distance form injection
Y_i	Mass fraction of specie i

Subscripts

C	hydrogen-air combustion test
M	hydrogen-nitrogen mixing test
FO	Fuel-off test
i	Specie i
r	Reactants
p	Products
A	Non-dissociated test gas
B	Dissociated test gas

INTRODUCTION

Ground testing of air breathing propulsion systems for hypervelocity operation requires the use of pulse facilities. Two types of pulse facilities, the reflected shock tunnel [1] and the expansion tube [3], have proved effective for producing subscale scramjet combustor data in the hypervelocity regime, above 3 km/s. These devices each produce a short duration of steady test

environment which is energy and nearly Reynolds number equivalent to flight conditions. However, differences in their operating cycles renders each with potential advantages and disadvantages for credibly simulating flight conditions over an entire air-breathing-to-orbit trajectory. Presently, comparative experiments are reported which aim to explore these differences by testing identical hydrogen fueled combustors in each facility.

Of concern for high stagnation enthalpy simulations in reflected shock tunnels is the chemical state of the test gas as it enters the combustor. At high enthalpy levels significant dissociated species are formed in the nozzle reservoir which do not completely recombine in the subsequent expansion, producing a test flow with a different composition and energy distribution than would exist in flight.

The operation of an expansion tube is such that it avoids this difficulty by adding stagnation enthalpy and pressure through acceleration in an unsteady expansion process. Because the high enthalpy flow is never stagnated, it is not subjected to the static enthalpies necessary for significant dissociation. The trade-off for this advantage is that the unsteady wave process restricts the test time available as compared to the reflected shock tunnel for test conditions below 6 km/s. This then limits the length scale of models which can be tested.

For an air test medium in a shock tunnel upwards of 50% of the oxygen content may leave the nozzle in dissociated species; as atomic oxygen and nitric oxide. In a preliminary study of dissociation effects on combustion by Morgan [2], it was proposed that there are three probable mechanisms by which the presence of dissociated oxygen may enhance the combustion process in a scramjet. Primary among these is additional heat release from combustion. In combustion with atomic oxygen, the atomic oxygen heat of formation adds directly to the potential heat release. For complete oxidation of hydrogen to form water, this increases the heat released from 120 MJ/kg to 215 MJ/kg of hydrogen burned. In an actual combustion situation the difference in net heat released will be less as some of the additional chemical energy remains tied up in dissociated products of combustion.

Second, because formation of oxygen radicals is a necessary step in the combustion of hydrogen, pre-dissociated oxygen may exhibit shorter ignition delay times and a faster overall reaction rate. In a finite rate chemistry study [4], it was shown that more rapid chemical energy yield occurs in the presence of oxygen atoms primarily due to an increased rate of the reaction

$$O + H_2 \rightarrow H + OH,$$

producing additional free radicals and increasing the overall reaction rate.

Finally, it is not clear to what extent oxygen atoms will have a direct effect on the mixing of fuel and oxidizer. Assuming similar macroscopic mixing layer development, the presence of dissociated oxygen will alter the flow Reynolds number and Schmidt number affecting mixing on the molecular level, although evidence [5] suggests that the dependence on these parameters is weak over the range of variation expected.

It is the objective of these tests to detect dissociated oxygen enhanced heat release by testing identical combustor geometries at comparable test conditions in each facility. The most reliable means for detecting heat release in pulse facility combustion experiments is through static pressure measurements in ducted flow. To this end a preliminary study was carried out by the authors and reported in [6]. There, in a similar test program to the current one, it was found that the static pressure rise upon combustion was significantly greater in the presence of dissociated oxygen. Although a considerable difference in fuel-off combustor pressure, as measured in the two facilities, left the results open for further interpretation.

For this investigation test condition duplication is of primary concern. Noting that the differences in test gas composition and energy distribution alter the flow variables so that combustion similitude parameters including Mach number, Reynolds number, and the Damkohler numbers cannot be matched simultaneously, it is necessary to choose which test parameters must be conserved in the comparison experiments. This is done so that differences in measured combustor pressure can be directly attributed to dissociated oxygen changing the net heat released and not to other coincidental fluid dynamic effects caused by test condition mismatch.

This paper presents test methodology and data which address the influence of test gas composition on combustion heat release as tested in two pulse facilities. The operating principles of each facility are explained and an analysis of the sensitivity of combustor pressure ratio to test conditions is described. Using these criteria, comparison test conditions were developed in a reflected shock tunnel to be compared with existing expansion tube data which were obtained at conditions energy equivalent to Mach 13.5 and 17 flight. Test data are presented along with results from a simulation assuming equilibrium combustion which indicates the validity of the data as well as its sensitivity to minor mismatches in meeting the comparison criteria.

TEST FACILITIES

The operating principles of the two facilities used in these experiments are given below. The T4-Reflected Shock Tunnel is located at the University of Queensland in Australia and the HYPULSE-Expansion Tube is located at the General Applied Science Laboratories in Ronkonkoma, New York, USA.

T4-Reflected Shock Tunnel

The arrangement and operation of the T4-Reflected Shock Tunnel is shown schematically in Figure 1a. The

test gas is held in the shock tube which is separated from the compression tube containing the initially low pressure driver gas (a mixture of argon in helium) by a steel diaphragm. The downstream end of the shock tube is fitted with a nozzle having a throat area of approximately one-nineth the shock tube area and is sealed from the evacuated test section by a thin Mylar secondary diaphragm.

The driver gas is pressurized by means of a single stroke free-piston which is launched from the breech end of the compression tube and, propelled by high pressure air from the reservoir, accelerates down the compression tube compressing the driver gas until the rupture pressure of the steel diaphragm is reached.

Upon diaphragm rupture, the driver gas expands into the shock tube initiating a strong shock wave in the test gas. The shock wave reflects from the downstream end of the shock tube creating a stagnant reservoir of test gas at high temperature (6000-9000 K) and pressure (10-50 MPa). For these tests the driver gas molecular weight is chosen for operation in "tailored" mode resulting in a steady reservoir pressure for approximately 1.0 ms duration. At shock reflection the secondary diaphragm bursts and the test gas expands through the facility nozzle. A time history of static pressure as measured on a flat plate at the exit of a Mach 5 contoured nozzle is as shown in Figure 2a.

For combustion studies in a reflected shock tunnel, the useful test period is limited by driver gas contamination [7]. The interaction of the reflected shock with the tube wall boundary layer in the driver gas results in a jetting of driver gas ahead of the test gas contact surface and into the nozzle throat. Using the prediction method from [7], at a test condition having flight Mach 17 flow energy, driver gas contamination is calculated to occur at approximately 0.7 ms after shock reflection, although no evidence of contamination is evident in the current experiments until after 1.2 ms. This is consistent with mass spectrometer measurements reported in [7] which showed the analysis to be conservative.

For hypervelocity air test flows the enthalpy in the nozzle reservoir is sufficient to significantly dissociate the oxygen present. The rapid expansion from reservoir conditions to the test condition results in the dissociation level freezing at a value above equilibrium for the test condition. Freezing is a consequence of the density and temperature in the nozzle falling sufficiently to cause the recombination rate to become negligible relative to the rate at which fluid moves through the nozzle. The remainder of the expansion then proceeds with little chemical composition change.

HYPULSE - Expansion Tube

A schematic representation of an expansion tube is shown in Figure 1b. The test gas is initially located in the shock tube section at sub-atmospheric pressure and separated from the driver by the main diaphragm assembly and downstream from the acceleration tube by a light Mylar secondary diaphragm. The HYPULSE facility uses a cold helium driver gas which is initially contained in the driver at 38-51MPa. The acceleration tube is a constant area tube of approximately twice the shock tube length and is evacuated to a low but precise vacuum level which is important for proper operation. The test section is located at the downstream end of the acceleration tube.

Initiation of a test begins by rupturing the main diaphragm. The helium expands into the shock tube sending a shock wave through the test gas. On reaching the end of the shock tube the secondary diaphragm ruptures and the shock continues into the lower pressure acceleration gas at greater speed. To balance velocity and pressure between the acceleration and test gases, a centered unsteady expansion wave is formed which expands the test gas to the desired test condition.

The steady flow begins with the arrival of the expanded test gas and is terminated approximately 0.4 ms later by the arrival of the centered expansion wave, or by its reflection off the driver gas interface. Driver gas contamination is not an issue in an expansion tube because the expansion wave must precede it out of the facility. A static pressure time history measured at the facility exit is shown in Figure 2b for comparison with the reflected shock tunnel trace, Figure 2a. It is seen that although a somewhat shorter steady flow period is achieved, no time is used for nozzle starting.

The key feature of the expansion tube operation is that the centered expansion wave imparts the bulk of the energy to the test gas. Thus, only a modest primary shock strength is required to achieve a desired energy level and therefore a greater performance potential for a given driver pressure and sound speed is achieved. In addition, the high energy test gas is delivered without first being contained in a stagnant nozzle reservoir permitting greater stagnation pressures to be achieved and greatly reducing the dissociation level of the test gas.

COMPARISON TEST METHODOLOGY

For an exact simulation of atmospheric flight conditions in a propulsion test facility it is necessary to match identically the primitive variables of pressure, temperature, velocity, and specie composition entering the combustor. However, as conveniently set out in [8], there exist simulation parameters or non-dimensional combinations of the primitive variables which when duplicated have the same effect, although it is not generally possible to achieve complete similarity for a dissociated test gas. For comparison of data between the two facilities the same general criteria apply.

For simulating chemically reacting flows behind strong shock waves, hypersonic Mach number independence has lead to adopting stagnation enthalpy as the primary simulation parameter to be matched when relating reflected shock tunnel data to ideal air. It is instructive to first examine the implications of matching stagnation

enthalpy before developing a preferred choice of similitudes for the present case of a flow where no strong shock waves occur.

There are three components of the stagnation enthalpy in a dissociated test gas,

$$H_{ST} = h_c + h_s + \frac{u^2}{2}$$

which are defined as follows,

$$h_c = \sum_i Y_i h^\circ_{f,i} \qquad \text{Chemical contribution}$$

$$h_s = \sum_i Y_i \int_0^T C_{p,i}\, dT \qquad \text{Sensible contribution}$$

$$\frac{u^2}{2} \qquad \text{Kinetic contribution}$$

For a test gas composed of only elemental species, the chemical enthalpy is zero.

Consider two air flows, A and B, at equal stagnation enthalpy, static temperature, and static pressure. Flow A is in equilibrium at this condition which is such that no dissociation occurs. Flow B is far from equilibrium and contains significant fractions of atomic oxygen and nitric oxide and therefore its chemical enthalpy is non-zero and may be of the order of the sensible enthalpy. This enthalpy partitioning is shown schematically in Figures 3a and b. Because B has positive chemical enthalpy, the sum of its sensible and kinetic contributions will be less than for A. However, because the dissociated gas will have lower molecular weight, there will also be more moles of B in a given mass and thus at the same temperature it will have greater sensible enthalpy per unit mass. This leaves B necessarily having a lower mass motion kinetic energy and thus a lower velocity than A. Thus, at matched stagnation enthalpy the dissociated gas will have lower velocity and higher sensible enthalpy and hence a significantly lower Mach number than the non-dissociated gas.

Beyond these fundamental limitations for test condition duplication, there are practical bounds to the degree of accuracy with which test conditions can be contrived in each facility so that they are matched. It is therefore of interest to know the sensitivities of measured quantities to variations in test conditions. It is assumed fuel conditions including injector geometry, pressure, and mass flow can be duplicated.

To identif which parameters must be matched it is useful to examine a simplified model of a scramjet combustor. The combustion process in a constant area scramjet is approximated by a pre-mixed one-dimensional flow with heat addition and composition change. A perfect gas is assumed and no change in the isentropic exponent with reaction, although a change in specific heats is permitted between end states. Viscous effects are neglected. These approximations are necessary to achieve analytical closure and thus determine sensitivities to the choice of simulation parameters. A more complete numerical model of combustion is described subsequently.

From the conservation equations and the equation of state the duct pressure, enthalpy, and total enthalpy ratio are functions of the reactant Mach number, M_r, and product Mach number, M_p, alone as given by the following:

$$\frac{p_p}{p_r} = \frac{(1+\gamma M_r^2)}{(1+\gamma M_p^2)} \qquad (1)$$

$$\frac{h_{s,p}}{h_{s,r}} = \left(\frac{1+\gamma M_r^2}{1+\gamma M_p^2}\right)^2 \left(\frac{M_p^2}{M_r^2}\right) \qquad (2)$$

$$\frac{h_{0,p}}{h_{0,r}} = \left(\frac{1+\gamma M_r^2}{1+\gamma M_p^2}\right)^2 \left(\frac{M_p^2}{M_r^2}\right) \left(\frac{1+\frac{\gamma-1}{2}M_p^2}{1+\frac{\gamma-1}{2}M_r^2}\right) \qquad (3)$$

where,

$$h_0 = h_s\left(1+\frac{\gamma-1}{2}M^2\right)$$

has been used as is appropriate for a calorically perfect gas. These equations are a somewhat generalized form of the Rayleigh flow equations given in [9]. The product Mach number is determined from (3) after evaluating the total sensible enthalpy ratio from the energy conservation equation,

$$\frac{h_{0,p}}{h_{0,r}} = \frac{\Delta h_{C,NET}}{h_{0,r}} + 1 \qquad (4)$$

where $\Delta h_{C,NET}$ is the net heat release from combustion and equals the difference in standard heats of formation between products and reactants. Denoting D_2 as the ratio of net heat release to total sensible enthalpy of the reactants (Damkohler's second number), equation (4) is rewritten as,

$$D_2 = \frac{h_{0,p}}{h_{0,r}} - 1 \qquad (4a)$$

From this equation and (3) it is seen that for given values of D_2 and M_r, the product Mach number and duct pressure and static enthalpy ratios are uniquely determined.

In the context of the comparison experiments, the additional chemical energy available in the reflected shock tunnel oxidizer will alter D_2 and thus the measured pressure rise. This change will only be purely a result of modified heat release if the M_r and h_0 are matched between experiments.

Because h_0 depends on the velocity and hence M_r, D_2 is not independent of Mach number. Another way of writing (4a) that will more clearly show the sensitivity of pressure ratio to Mach number is to move all of the Mach number contributions to the right-hand side giving an alternate non-dimensional heat release parameter,

$$\frac{\Delta h_{C,NET}}{h_{s_2}} = (1 + \frac{\gamma - 1}{2} M_r^2)(\frac{h_{0_2}}{h_{0_1}} - 1) \qquad (4b)$$

Figure 4 shows duct pressure ratio plotted against reactant Mach number for constant values of D_2 and $\Delta h_{C,NET}/h_s$. Practically, for a given heat release, lines of constant D_2 may be achieved by adjusting the test flow Mach number while maintaining flow energy, for instance by diffusing the combustor inlet flow. Constant $\Delta h_{C,NET}/h_s$ lines require adjustment of Mach number while keeping the temperature constant. For the latter it is seen that at Mach numbers near three an increase in sensitivity of pressure ratio to Mach number occurs. Because M_r is the mass averaged Mach number of the oxidizer and fuel, even for hypersonic test conditions, it will be in this range. Therefore it is important that the reactant Mach numbers be nearly matched between experiments so that differences in combustor pressure ratio may be unambiguously interpreted. If a mismatch in Mach number is unavoidable, its significance can be minimized by duplicating the sensible enthalpy by itself rather than the total sensible enthalpy.

The foregoing analysis identifies M_r and either h_0 or h_s as the two prime parameters which when matched will make the pressure ratio sensitive only to the effects of atomic oxygen. However, the extent of heat release also depends on the pressure and temperature of the reactants in that they influence both reaction rates (first Damkohler number, D_1) and equilibrium conditions. Reactant pressure is therefore chosen as the third flow parameter and h_s as the preferred flow energy parameter. For the conditions of interest, differences in C_p due to composition will be small, on the order of 5%, and therefore matching of h_s is nearly synonymous with matching temperature.

Referring to Figure 5c it is seen that the stagnation enthalpy for the reflected shock tunnel, test gas B, needs modification so that the criteria for matching ideal air conditions are met. At equal values of h_s and Mach number, the stagnation enthalpy of B is greater both because of its chemical contribution and the additional velocity necessary to match the Mach numbers. For a perfect gas the velocity required is as shown in the figure.

TEST CONDITIONS

Results of the expansion tube combustion experiments tests have been reported in [10] and [11] at conditions simulating flight Mach 13.5 and Mach 17 flow energies. Test conditions were established in the reflected shock tunnel which targeted these test conditions subject to the matching criteria discussed above. Due to practical experimental limitations, precise tuning of test conditions in the reflected shock tunnel cannot be done, and further, uncertainties exist as to the exact value of some flow parameters.

Expansion Tube

Details of the expansion tube test flow calibration method are given in [12]. Reported facility exit conditions are given for the two test conditions in Tables 1 and 2a. The table entries are derived from a combination of instream pitot and static pressure, wall pressure, and facility shock speeds approaching the test section assuming chemical equilibrium of the test flow. To raise the test gas pressure at the Mach 17 condition to a level capable of supporting hydrogen/air combustion it was necessary to diffuse the acceleration tube exit flow. For this purpose an axisymmetric diffuser was designed and calibrated as described in [9]. Pitot surveys of the diffuser exit identified an uncancelled wave system leaving the diffuser, however, comparison to a numerical solution suggested that the wave system was quite weak.

Repeatability of the expansion tube test conditions has been found to be quite good. Secondary shock speeds repeat with a standard deviation of 0.7% and tube exit static pressures with a deviation of 4.6%. No significant difference is found in operating conditions between air and nitrogen test gases.

Reflected Shock Tunnel

Two nozzles have been used for these experiments having nominal exit Mach numbers of 4 (for flight Mach 13.5 tests) and 5 (for flight Mach 17 tests) as required to match the expansion tube conditions. Previously, full pitot pressure calibrations have been done for each of these nozzles (reported in [1] and [13] respectively) over a range of reservoir enthalpies and pressures. At conditions near the present ones flow uniformity was found to be adequate.

Conditions were chosen for Mach 13.5 tests to approximately match Mach number, sensible enthalpy, and pressure of the expansion tube condition. Table 1 summarizes the shock tunnel reservoir and calculated nozzle exit conditions for both air and nitrogen test gases. Time of flight shock speed measurements and nozzle reservoir pressure measurements are used to determine the nozzle supply conditions. The non-equilibrium nozzle flow is calculated with the quasi-one-dimensional NENZF program [14]. The reaction set for air includes 11 reactions for the species N_2, N, O_2, O, NO, NO^+, and e^-.

A significant portion of the oxygen is dissociated at this condition which is primarily a consequence of the relatively low operating pressure. (At higher operating pressures obtainable in T4 less of the oxygen dissociates in the reservoir and recombination is more complete in the nozzle). In comparing to the expansion tube conditions note that the Mach number, sensible, and total sensible enthalpies are quite close as required. Better matching of static pressure between facilities was not possible due to practical considerations. For nitrogen test gas the nozzle exit pressure is calculated to be lower than air because of a lack of chemical recombination effects.

Nozzle exit conditions established to match the expansion tube Mach 17 test condition are shown in Table 2a. The calculation procedure is identical to that for the Mach 13.5 condition.

Preliminary facility comparison experiments at this condition, [5], showed that although the shock tunnel nozzle exit pressure nearly matched the expansion tube diffuser exit pressure, a mismatch in scramjet duct pressures without fuel injection persisted. Measured duct pressures in the expansion tube tests were 50% greater. An attempt to remedy the deficiency was made by raising the shock tunnel operating pressures, however, a 25% error remained. In addition the Mach number, at 5.17, is below the required value of 5.75.

To remedy the pressure mismatch for the current experiments the Mach 5 nozzle flow was recompressed through a 0.852 area ratio conical inlet attached to the model front. The geometrical area change was completed in 2.67 model diameters with a surface inclination half-angle of 0.9°. For analysis purposes the entropy change through the very weak shock wave formed (normal Mach number of 1.05 for Mach 5.17 nozzle exit flow) is ignored and the change in test conditions are calculated from the area ratio giving approximately the 25% pressure increase desired. These conditions are summarized in Table 2b for both air and nitrogen.

Clearly this could make the Mach number mismatch worse. But it is postulated, based on the pressure mismatch found, that the expansion tube diffuser is actually compressing the flow beyond the pressure quoted in Table 2a and hence the Mach number is below 5.75. An estimate of the diffuser exit conditions based on a further (isentropic) compression to the same pressure as calculated for the recompressed reflected shock tube flow is also given in Table 2b. The temperatures are now nearly equal for the facilities, and although the total sensible enthalpies do not agree the sensible enthalpies do. In Figure 6 matching of h_s was shown to be the preferred matching criteria when a Mach number error exists.

Repeatability of the shock tunnel is similar to the expansion tube with shock speeds repeating with a standard deviation of 1.0% and stagnation pressures with a deviation of 3.5%.

COMBUSTOR MODEL AND INSTRUMENTATION

Two identical copies of the model shown in Figure 5 were used for the comparison experiments. The cylindrical combustor has a constant diameter with approximately five diameters from the leading edge of the inlet to the fuel injector and 19.3 diameters downstream of injection. For the reflected shock tunnel tests at Mach 17, the 1.5 diameter long straight inlet was replaced by the 0.852 area ratio inlet described previously.

Two different injection geometries were used. The first was a circumferential slot injector issuing at Mach 1.9 from the combustor wall at an angle of 15° measured from the model axis. The injector throat area to model cross-section area ratio is 0.0628. The second consisted of four discrete wall jets, positioned at 90° azimuth around the perimeter and issuing sonically inward at 30° measured from the model axis. Each injector had a throat to model cross section area ratio of 0.00694. In both facilities the model was positioned in a free jet configuration, capturing the core of the facility exit flows.

Fuel flow was supplied to the injector plenum by a Ludweig tube system opened by a fast acting valve in both facilities. Fuel plenum pressure was monitored upstream of the injector throat at an area ratio greater than four. Fuel to oxidizer equivalence ratio was controlled by adjusting the fuel injector plenum pressure through the Ludweig tube fill pressure.

Model instrumentation included high frequency, high sensitivity pressure transducers. Twelve were located at 1.33 diameter intervals downstream of the injector in the expansion tube tests. In the reflected shock tunnel, 23 were used at 0.67 diameter intervals.

COMPARISON TEST RESULTS AND DISCUSSION

In this section the results of the comparison tests at two flight conditions are presented. At the Mach 17 condition data for both injector configurations, the 15° slot and the 4 by 30° discrete orifices, is compared. At the Mach 13.5 only data for the discrete orifice injection is available for comparison.

Mach 17 Condition - Slot Injection

Results for the slot injector at Mach 17 enthalpy as tested in the expansion tube have been reported previously [11]. Pressure and wall heat flux data were obtained at three hydrogen-air equivalence ratios and fuel-off conditions. Both air and nitrogen test gases were used. The effect of mass addition and mixing alone on the combustor pressure distribution were identified by injecting fuel into a nitrogen test gas. Comparing these data with results from fuel into air tests, at the same fuel flow rate, allowed detection of combustion heat release.

Tests were run in the shock tunnel for each of the three

equivalence ratios tested in the expansion tube. The fuel flow rate, as dictated by the fuel plenum pressure, was chosen to be matched in each case. Note that this choice does not exactly conserve equivalence ratio because of the different oxidizer mass flows entering the combustor in each facility. However, it does conserve fuel to oxidizer static pressure ratio at injection which for equal oxidizer Mach numbers dictates the duct wave pattern generated by oxidizer stream interaction with the fuel. The calculated equivalence ratios achieved for all test conditions in each facility, as calculated based on the test conditions in Tables 1 and 2b, are given in Table 3.

A comparison of the pressure distributions measured in both facilities for air test gas without fuel is shown in Figure 6a. Pressure is plotted as a function of distance from the injector station for each facility. In the shock tunnel the combustor was fitted with the 0.852 area ratio conical inlet. Very similar pressure development with distance and overall mean pressure level is seen indicating that the effect of the inlet is to approximately mimic the uncancelled waves leaving the expansion tube diffuser. The closer spacing of pressure transducers in the shock tunnel tests gives much better resolution of the distribution. Results for a nitrogen fuel-off test is shown in Figure 6b compared to the air result for the expansion tube. The lower pressure achieved for nitrogen is a result of real gas effects in the facility nozzle as mentioned previously.

Comparisons of fuel injection results are shown in Figure 6c and 6d for air and nitrogen test gases. Very good agreement is seen between the pressure distributions for air with both pressure level and wave structure appearing similar. For the nitrogen test gas the shock tunnel pressures are lower because of the lower inlet pressure. To extract a more instrumentation independent comparison, the point-by-point ratio of fuel-on to fuel-off pressures is shown in Figure 6e and 6f for the two test gases.

Although no clear evidence of dissociation enhanced release is apparent, a further manipulation of the data by forming the ratio of the data sets from Figures 6e and 6f shows that there is a subtle difference in pressure level. This was done for all three equivalence ratios tested and is shown in Figure 7. A straight line was fit to each data set to obtain a quantitative measure of the extent of pressure difference.

Although the differences are small, a trend toward greater heat release and a larger difference between facilities with increasing equivalence ratio is evident. There are two probable contributors to these trends. First, better mixing results from greater fuel penetration at the higher injection pressures, and second with more fuel present beyond stoichiometric, more heat release results as the additional fuel cools the products of combustion tending to increase formation of water. The shock tunnel results are more oscillatory which is probably a result of the combustor inlet Mach number mismatch between air and nitrogen test gases. Because wave angles are Mach number dependant, this provides an offset in the wave patterns produced in each gas. Naturally, some offset must exist if combustion occurs and this is evidenced in the expansion tube plots where the oscillations increase with equivalence ratio and thus heat release.

Mach 17 - Discrete Wall Jet Injection

Expansion tube results for the discrete injector are reported in [10]. Two equivalence ratios were tested at nominally two and three times stoichiometric. The anticipated advantage of this injector over the slot injector was to increase the rate of mixing.

For the expansion tube, the fuel-off data for air was found to differ slightly from the slot injector test data. Figure 8a compares fuel-off data from the shock tunnel with the expansion tube results and a less definite agreement is seen, although it is considered satisfactory.

Comparison of raw pressure distributions in Figure 8b at a nominal equivalence ratio of three shows fair agreement. When the ratio of fuel-on to fuel-off data is formed, Figure 8c, strong agreement of the wave patterns is apparent while the reflected shock tunnel appears to give higher pressure levels in the center and end of the duct.

Figure 9 summarizes the normalized ratio of combustion and mixing results formed in the same way as for the slot injector. In both cases a larger combustion pressure is seen for the shock tunnel. Also of note is that the shock tunnel pressures for combustion tests seem to rise immediately above the mixing tests, while in the expansion tunnel a slower separation is seen. Although not conclusive, this may be evidence of more rapid ignition in the presence of dissociated oxygen. As the flow proceeds down the duct the pressure distributions tend to converge.

Mach 13.5 - Discrete Wall Jet Injection

Figures 10a-c show facility comparisons of pressure distributions for fuel-off and fuel into air at 2.4 times stoichiometric. The pressures values are shown normalized by the theoretical facility exit pressure to remove the calculated pressure mismatch and reasonable agreement is seen. When the fuel-on data are normalized by fuel-off data the duct exit pressure levels are similar, however the strong wave pattern caused by injection and seen in the shock tunnel data is not found in the expansion tube results. Apparently the transducer spacing is not sufficient to capture the short wavelength oscillations which appear to be approximately equal one expansion tube transducer gap in length.

The ratios of normalized combustion to mixing pressure for equivalence ratios of 1.2 and 2.4 are presented in Figure 11. The straight lines fit to the data show nearly identical combustion induced pressure rise with distance. Again the shock tunnel ratio appears more oscillatory as a consequence of the nitrogen and air inlet Mach number mismatch.

EQUILIBRIUM COMBUSTION CALCULATIONS - DATA COMPARISON

A more realistic model of scramjet combustion has been developed to verify the above analytical results and to correlate experimental results. It is an extension of the entrainment model reported in [15], to include equilibrium chemistry, wall heat transfer, and skin friction. The fuel and oxidizer are modelled as quasi-one-dimensional stream tubes of arbitrary composition, with the oxidizer stream held frozen at the inlet composition. Startline conditions are calculated by pressure and direction matching the fuel and oxidizer streams with a specified total pressure loss for one stream, and the other stream then determined by conservation of streamwise momentum. At each stream wise step through the combustor an increment of oxidizer mass is entrained into the fuel stream (mixing stream) where it is mixed and reacted to equilibrium. The rate of entrainment is prescribed by a mixing schedule. Pressure is assumed to be laterally uniform and is chosen along with the area of the two streams such that the conservation equations are satisfied at each step. Wall boundary layer effects are computed from and act upon the mixing stream using specified skin friction and Stanton number coefficients. This assumes that only the mixing stream is in contact with the wall.

Simulations were run for the data available. To maintain an equal means for comparison of the different injector schemes, all simulations were run assuming a constant rate of mixing to a fully mixed condition at the duct exit. Boundary layer parameters of $C_f = 0.003$ and $St = 0.0015$ were used throughout. Subsequently the ratio of duct exit pressure for combustion to mixing runs was formed and it is compared to the measured data in Figure 12 for the three test series. Plotted data points are the combustor exit values of the straight lines fit to the ratio of combustion to mixing pressure data. Error bars of $\pm .06$ represent the ratio of the shot-to-shot repeatability, approximately 3% for both facilities.

For the slot injector in Figure 12a, the measured pressure rise is well below the equilibrium combustion predictions for both facilities, suggesting incomplete mixing and/or reaction. Note that the predicted differences between facilities is approximately consistent with the data. The test condition corrected data are simulations run for the shock tunnel test gas at conditions exactly matching the pressure, Mach number, sensible enthalpy and equivalence ratio of the expansion tube tests. The difference between these predictions and those for the actual conditions run in the shock tunnel are indicative of the errors in the comparison data due to test condition mismatch.

Similar results are plotted for the discrete orifice injector at both test conditions in Figures 12b and 12c. Test condition mismatch appears to have had a significant effect on the Mach 13.5 data in Figure 12c where the predicted equilibrium pressures for the shock tunnel are below the expansion tube. The simulation run for exact test condition duplication shows the expected difference.

Overall the relative difference both predicted and measured between facilities is surprisingly small. Representing the maximum departure measured, taken as the Mach 17 condition with the discrete orifice injector at equivalence ratio of 2, in terms of a ratio of absolute combustor exit pressures, only a 11% increase due to oxygen dissociation has been measured. Ratios of absolute combustor exit pressures for all tests are summarized in Table 3.

An possible explanation for this small difference comes from the high static enthalpies at which these tests were run. The high static temperature inhibits recombination of combustion products. The additional chemical enthalpy available from dissociated oxygen goes primarily toward further dissociating the combustion products and is not detectable as elevated flow temperature and pressure.

CONCLUSIONS

The results of the facility comparison tests have shown that very similar pressure data can be achieved in a reflected shock tunnel and an expansion tube. Wave structure was found to be quite similar once instrumentation dependant factors were normalized out. Macroscopic flow features were duplicated between facilities and a valid comparison was made indicating the effects of dissociated test gas on combustion.

Analysis was presented which identified the key test flow variables which need to be conserved in the comparison tests such that the pressure distributions are sensitive to differences in heat release alone.

Subject to these test criteria, overall pressure rise resulting from combustion was found to be only slightly greater in the reflected shock tunnel as predicted by equilibrium analysis. This difference, although small, can be confidently attributed to effects of pre-dissociated oxygen on combustion due to the careful choice of test conditions and subsequent data analysis.

The high static temperature level at which these comparison tests were run is offered as an explanation for this small difference. This rendered the combustor exit pressure less sensitive to the additional heat release arising from combustion with atomic oxygen. The excess heat does not appear as temperature and pressure but remains tied up in the chemical enthalpy of dissociated products of combustion.

The data similarity is in itself compelling because it serves as validation of the simulations run in each facility. The difference in operation of the facilities clearly requires a different flow establishment process. That these ultimate states tend to agree justifies their validity as steady state solutions.

In considering future lower temperature tests, where the effects of dissociation would appear more significantly, two options exist. The first is to lower the stagnation

enthalpy at which the tests are run although the dissociation in the shock tunnel then also decreases, defeating the purpose. A second alternative is to expand the test flow to higher Mach numbers at the same stagnation enthalpy level. In principle this is possible, but requires facility hardware which is not available at present.

ACKNOWLEDGMENTS

The portion of this work conducted at the University of Queensland was sponsored by the NASA Langley Research Center through grant NAGW674, contract monitor R.C. Rogers, and the work at GASL by the National AeroSpace Plane Joint Program Office, C.D. Snyder was the Task Manager. Mr. Bakos was also supported by a DEET scholarship.

REFERENCES

1. Stalker, R.J., Morgan,R.G., Paull,A., and Brescianni, C.P., "Scramjet Experiments in Free Piston Shock Tunnels," Paper No. 28, 8th National AeroSpace Plane Technology Symposium, March 26-30, 1990.

2. Morgan, R.G., "Dissociated Test Gas, Effects on Scramjet Combustors," Extract from NASA CR-1882096, October 1990.

3. Tamagno, J., Bakos, R.J., Pulsonetti, M.V., and Erdos, J.I., "Hypervelocity Real Gas Capabilities of GASL's Expansion Tube (HYPULSE) Facility," Paper 90-1390, AIAA 16th Aerodynamic Ground Testing Conference, Seattle, WA, June 1990.

4. Jachimowski, C.J., "Analytical Study of Combustion in Shock Expansion Tunnels and Reflected Shock Tunnels," (Future NASA TP), January 1992.

5. Dimotakis, P.E., "Turbulent Free Shear Layer Mixing and Combustion," Paper 89-7006, 9th ISABE, Athens Greece, September 1989.

6. Morgan, R.G., Stalker, R.J., Bakos, R.J., Tamagno, J., and Erdos, J.I., "Scramjet Testing - Ground Facility Comparisons," Paper 91-194(L), X-ISABE, Nottingham, UK, September 1991.

7. Stalker, R.J, and Crane, C.A., "Driver Gas Contamination in a High-Enthalpy Reflected Shock Tunnel," AIAA Journal, Vol. 16, March 1978.

8. Anderson, G., Kumar, A., and Erdos, J., "Progress in Hypersonic Combustion Technology with Computation and Experiment," Paper 90-5254, AIAA Second International AeroSpace Planes Conference, Orlando Fl., October 1990.

9. Anderson, J.D. Jr., "Modern Compressible Flow with Historical Perspective," McGraw-Hill, 1982.

10. Tamagno, J., et al, "Axisymmetric Scramjet Combustor Tests at Mach 13.5 and 17 Flight Conditions," GASL-TR-353, (In preparation).

11. Bakos, R.J., Tamagno, J., Rizkalla, O., Pulsonetti, M.V., Chinitz, W., and Erdos, J.I., "Hypersonic Mixing and Combustion Studies in the GASL HYPULSE Facility," AIAA Paper 90-2095, AIAA/SAE/ASME/ASEE 26th Joint Propulsion Conference, July 1990.

12. Calleja, J., Tamagno, J., and Erdos, J., "Calibration of the GASL 6-inch Expansion Tube (HYPULSE) for Air, Helium, and CO_2 Test Gases," GASL-TR-325, September 1990.

13. Jacobs, P.A., "A Mach 4 Nozzle for Hypervelocity Flow," University of Queensland, Department of Mechanical Engineering Report 9/89.

14. Lordi, J.A., Mates, R.E., and Moselle, J.R., "Computer Program for the Numerical Solution of Non-Equilibrium Expansions of Reacting Gas Mixtures," NASA CR-472, 1966.

15. Morgan, R.G., Bakos, R.J., and Tamagno, J., "Bulk Parameter Analysis of Hypersonic Combustion Experiments," GASL-TR-321, August 1990.

Table 1. Test conditions at Mach 13.5 in expansion tube and shock tunnel.

Parameter	Expansion Tube (Air & N_2)	Shock Tunnel (Air)	Shock Tunnel (N_2)
P_∞ (MPa)	14.2	10.2	10.2
H_∞ (MJ/kg)	10.1	12.3	11.6
P (kPa)	23.5	28.0	24.1
T (K°)	2270	2360	2410
M	4.18	4.01	4.34
U (m/s)	3840	3960	4250
h_0	9.96	10.6	11.6
h_s	2.59	2.76	2.80
C_p/C_v	1.294	1.323	1.307
α	0.009	0.420	-
α_∞	0.036	0.118	-
R (J/kg/K)	287.6	312.4	304.4

Table 2a. Mach 17 expansion tube diffuser exit conditions and nozzle exit conditions for shock tunnel. Diffuser values assuming i entropic compression to area ratio.

Parameter	Expansion Tube Diffuser Exit - Ideal	Shock Tunnel Nozzle Exit
P_{t_2} (MPa)	141.	40.3
H_{t_2} (MJ/kg)	15.3	14.5
P (kPa)	16.4	16.6
T (K°)	2090	2010
M	5.75	5.17

Table 2b. Mach 17 conditions after 0.852 area ratio inlet for reflected shock tunnel. Expansion tube conditions modified by compression to shock tunnel static pressure.

Parameters	Expansion Tube - Modified (Air & N_2)	Shock Tunnel after Inlet (Air)	Shock Tunnel after Inlet (N_2)
P_{t_2} (MPa)	136.	40.3	40.3
H_{t_2} (MJ/kg)	15.3	14.5	13.6
P (kPa)	20.9	20.9	17.9
T (K°)	2200	2120	2010
M	5.56	5.00	5.38
U (m/s)	5030	4630	4740
h_0	15.2	13.2	13.6
h_s	2.51	2.45	2.33
C_p/C_v	1.294	1.326	1.309
α	0.006	0.332	-
α_e	0.031	0.125	-
R (J/kg/K)	287.5	307.3	301.7

Table 3. Nominal and actual equivalence ratios. Predicted and measured combustor exit pressure increase due to combustion.

Test Condition - Model Config.	Equivalence Ratio - ϕ			Combustor exit pressure increase due to dissociation (%)	
	Nominal	Exp. Tube	Shock Tunnel	Equil. Comb. Calc.	Measured
Mach 17 Slot Injector	1	0.88	0.98	6.7	0
	2	1.75	1.96	6.0	7.1
	3	2.71	3.03	7.0	6.6
Mach 17 Discrete Injector	2	1.66	1.93	5.2	11.1
	3	2.42	2.72	5.5	8.9
Mach 13.5 Discrete Injector	1.2	1.21	1.15	-1.5	3.5
	2.4	2.32	2.42	-2.0	3.1

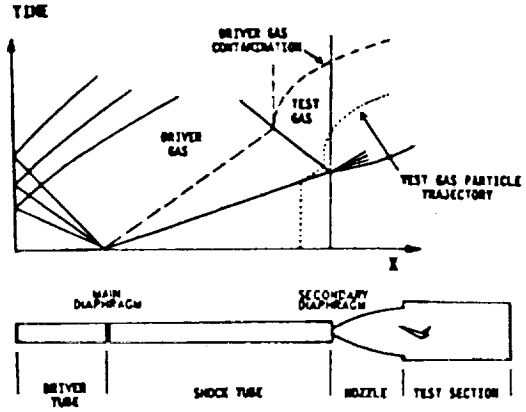

(a) T4-Free Piston Driven Retlected Shock Tunnel.

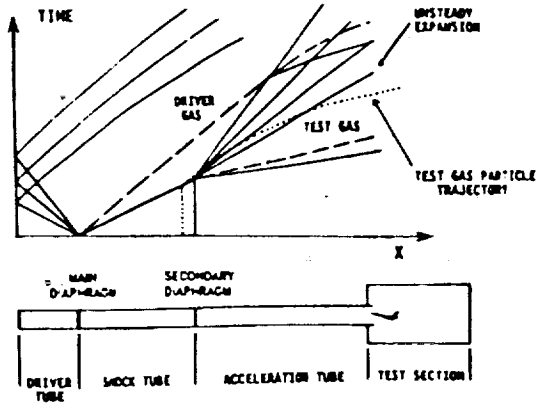

(b) HYPULSE Expansion Tube.

Figure 1. Facility schematic and distance time wave diagrams.

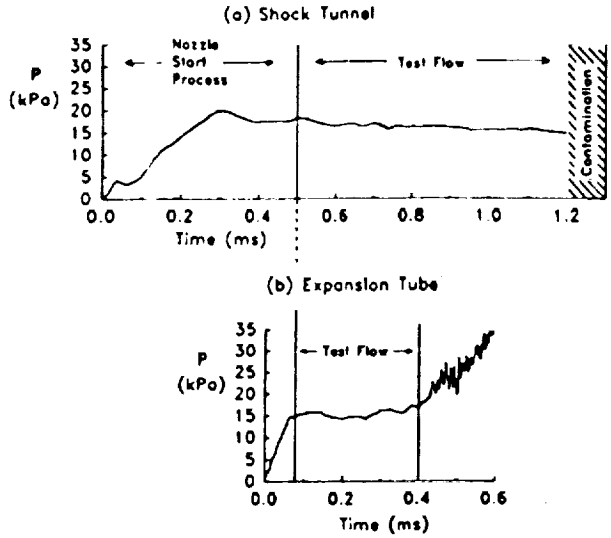

Figure 2. Facility exit static pressure time histories
(a) Measured on a flat plate in the reflected shock tunnel.
(b) Measured on the wall at the exit of the expansion tube diffuser.

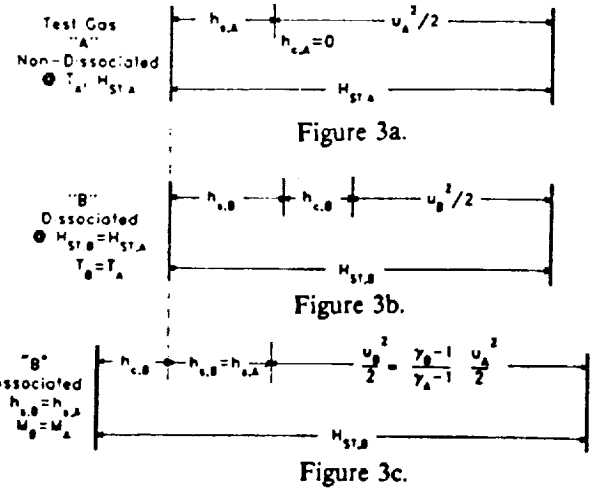

Figure 3. Schematic representation of stagnation enthalpy partitioning in dissociated and non dissociated test gas.

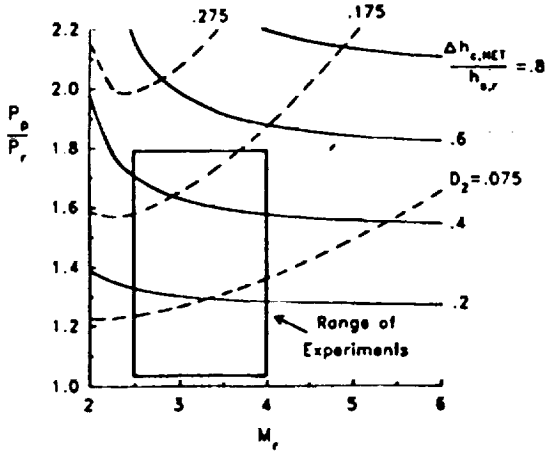

Figure 4. Constant area duct static pressure ratio from equations 1-4 for varying non-dimensional heat release.

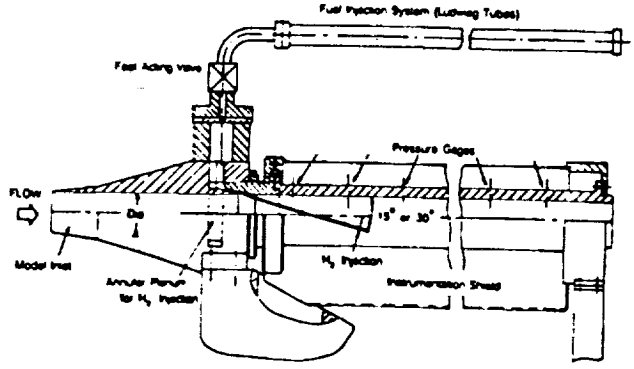

Figure 5. Cylindrical combustor duct schematic.

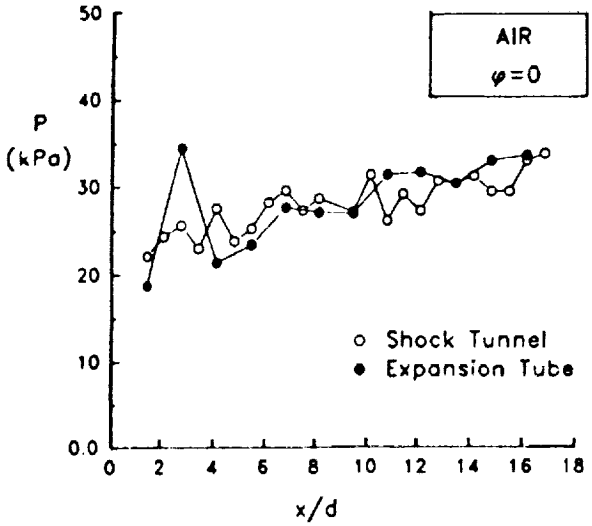

Figure 6a.

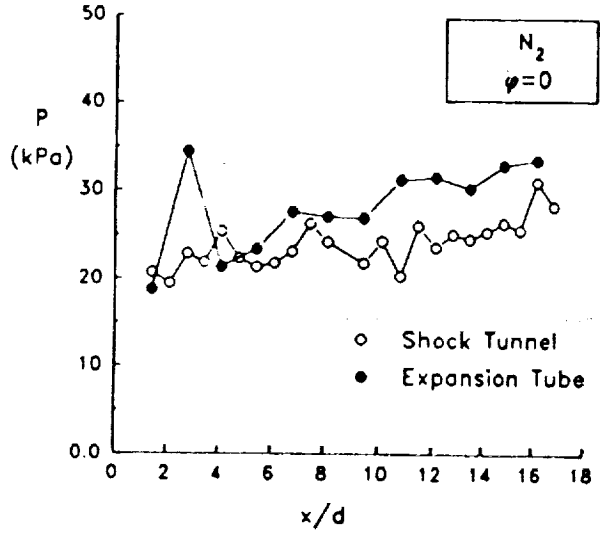

Figure 6b.

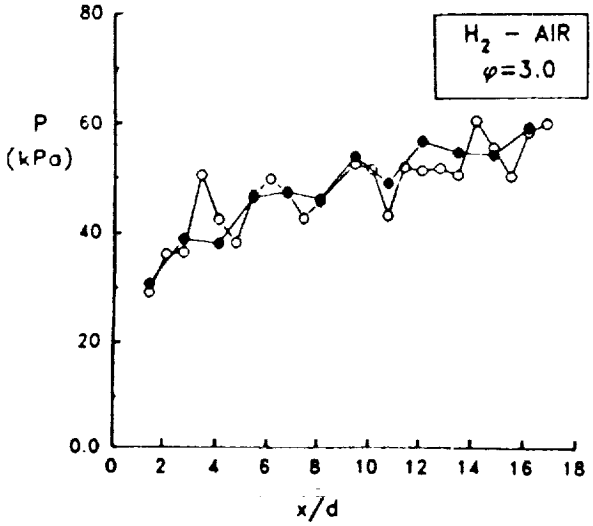

Figure 6c.

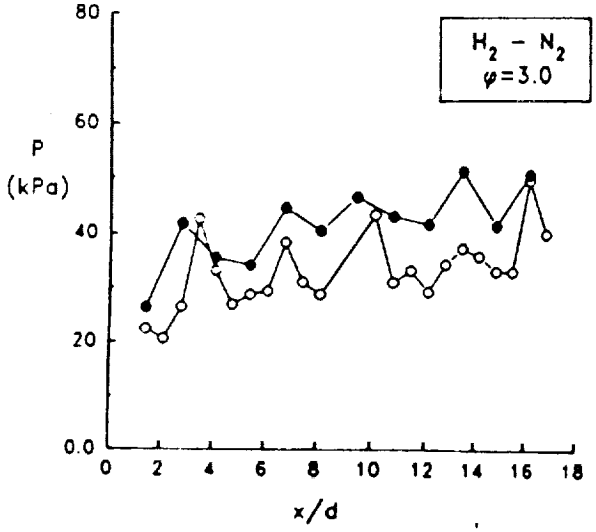

Figure 6d.

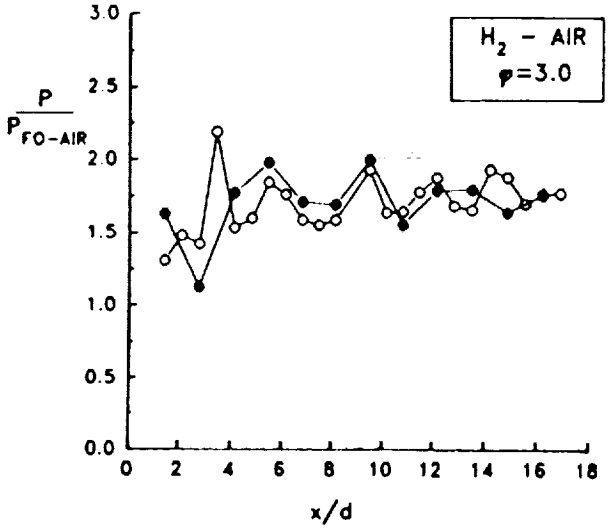

Figure 6e.

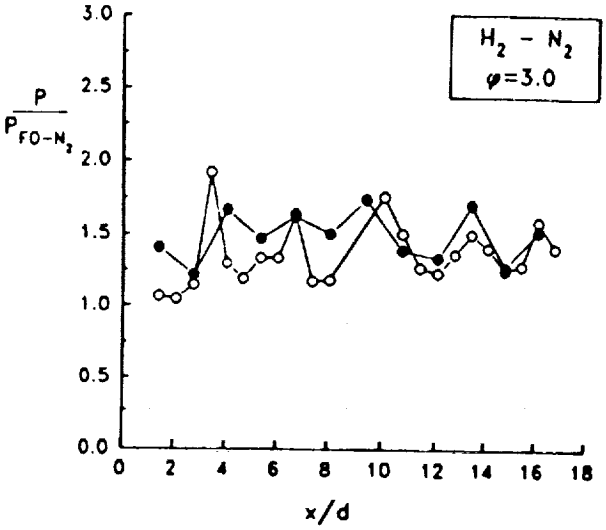

Figure 6f.

Figure 6. Comparative static pressure distributions for slot injection at the Mach 17 test condition.

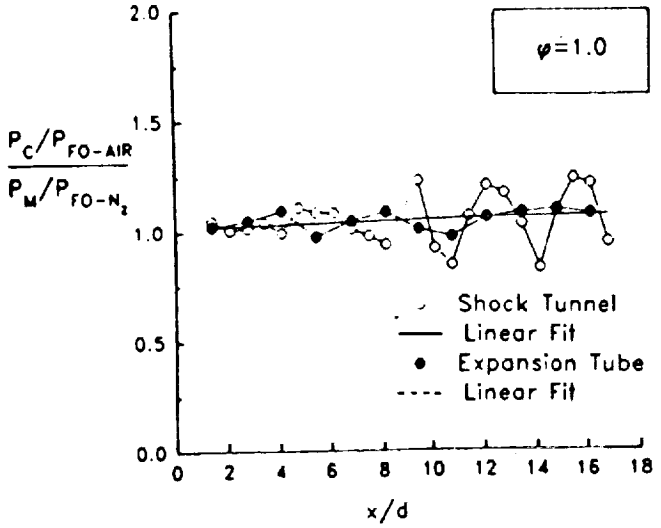

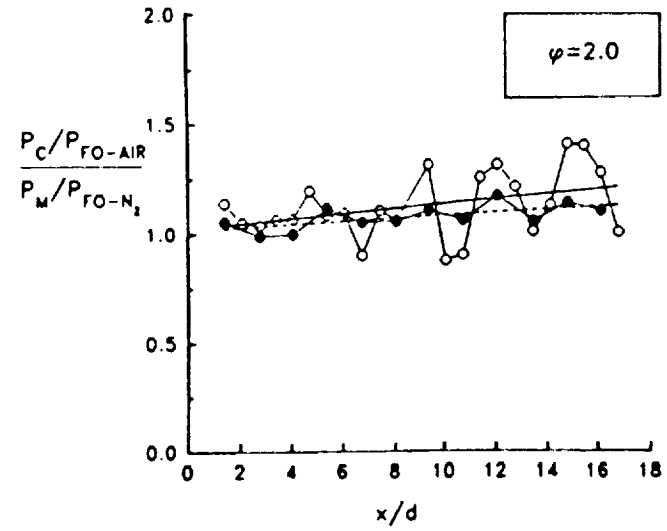

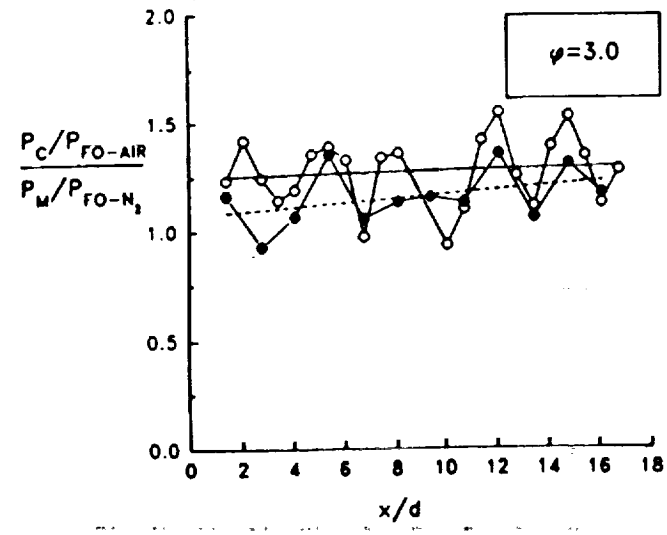

Figure 7. Combustion induced pressure rise comparisons. Slot injection at three equivalence ratios for the Mach 17 test condition.

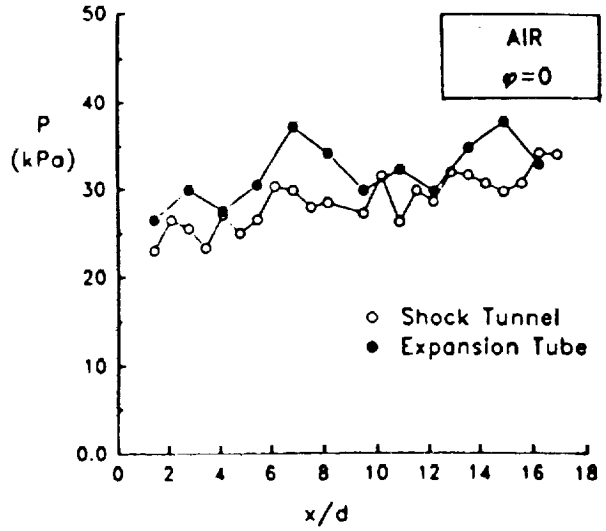

Figure 8a.

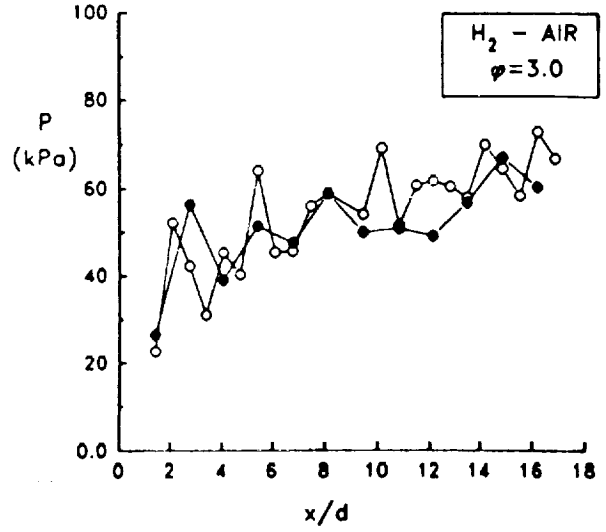

Figure 8b.

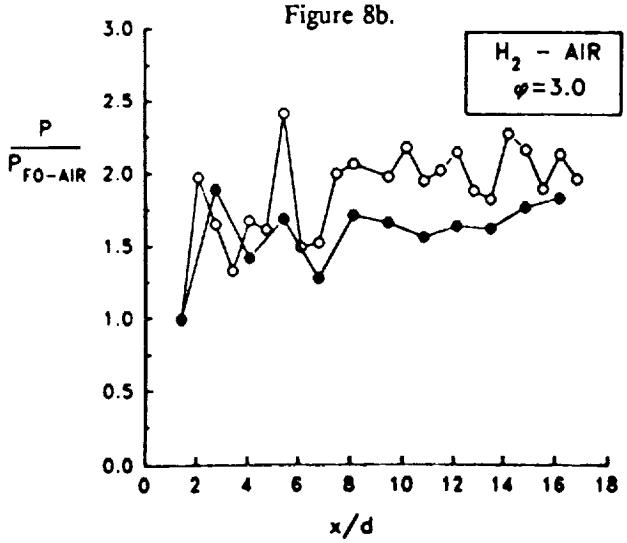

Figure 8c.

Figure 8. Comparative static pressure distributions for discrete wall jet injection at the Mach 17 condition.

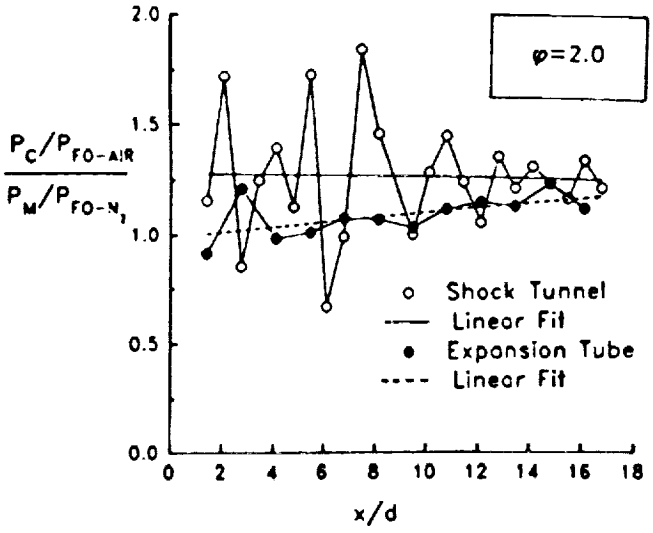

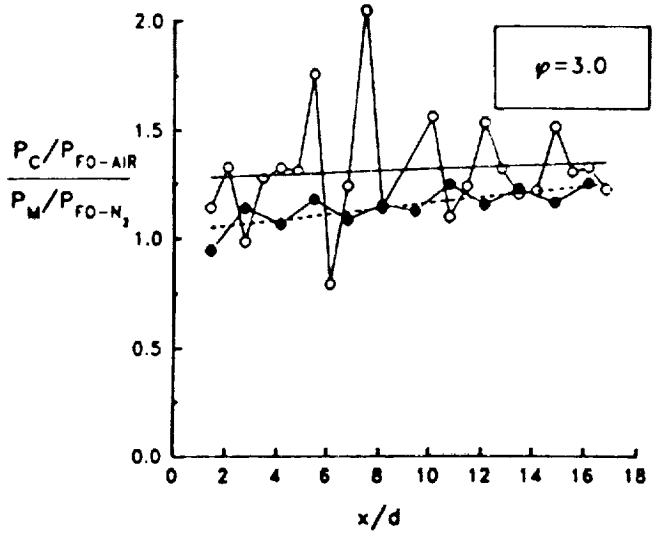

Figure 9. Combustion induced pressure rise comparisons. Discrete wall jet injection at two equivalence ratios for the Mach 17 condition.

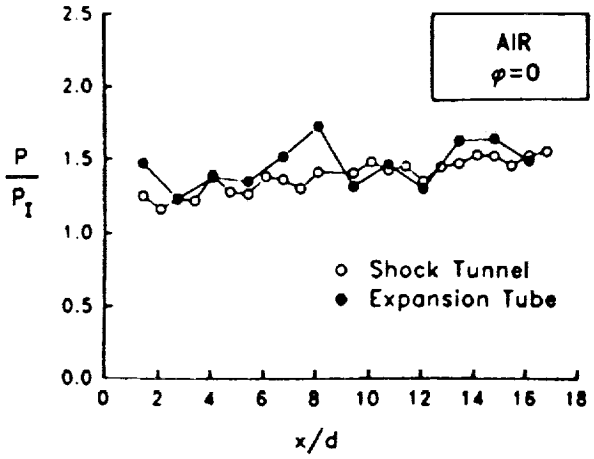

Figure 10a.

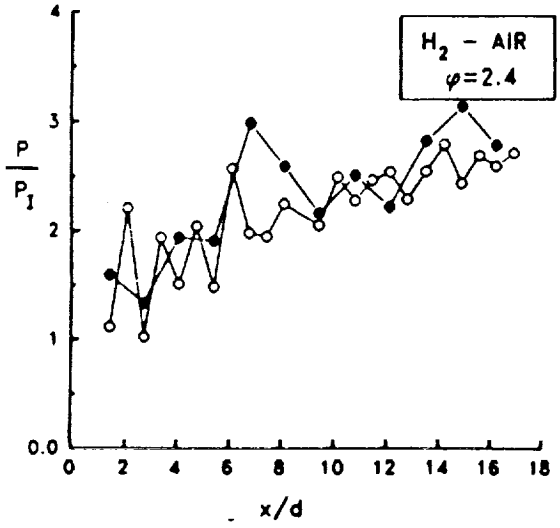

Figure 10b.

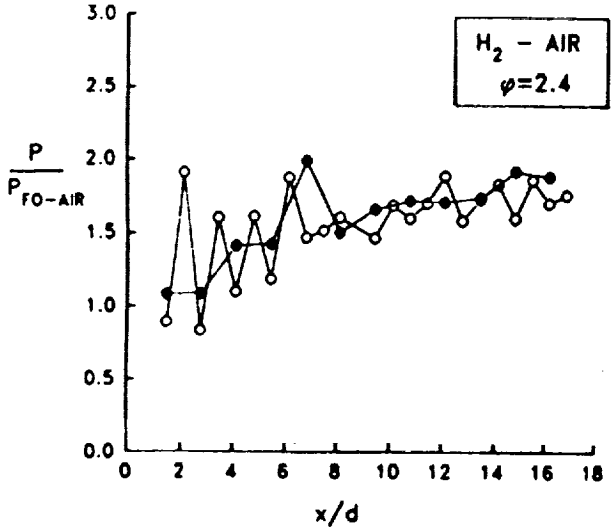

Figure 10c.

Figure 10. Comparative static pressure distributions for discrete wall injection at the Mach 13.5 condition.

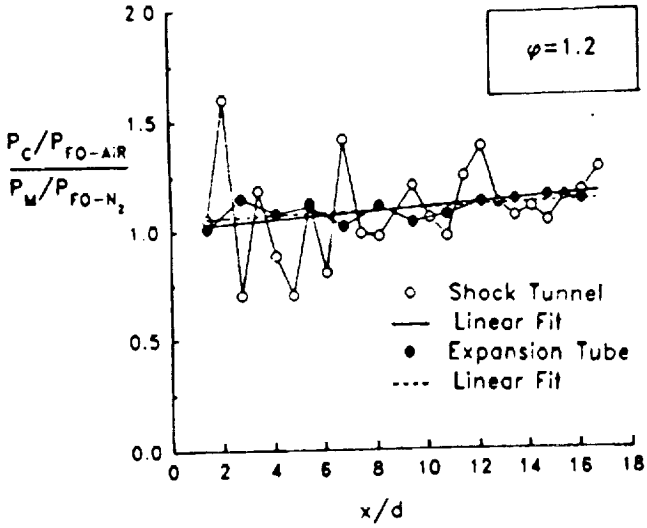

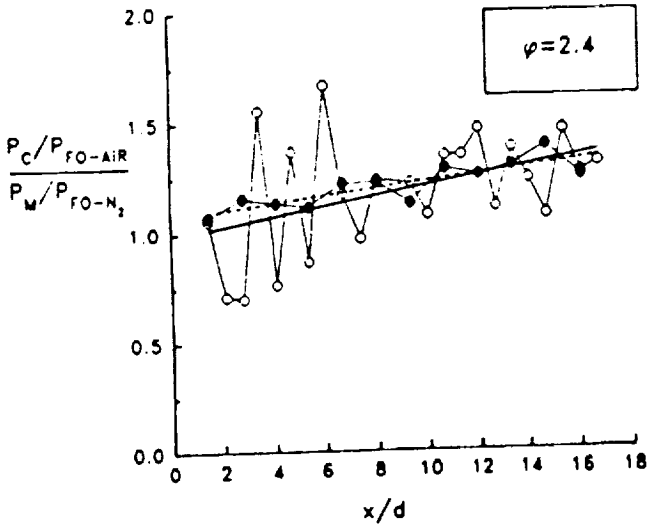

Figure 11. Combustion induced pressure rise comparisons. Discrete wall jet injection at two equivalence ratios for the Mach 13.5 condition.

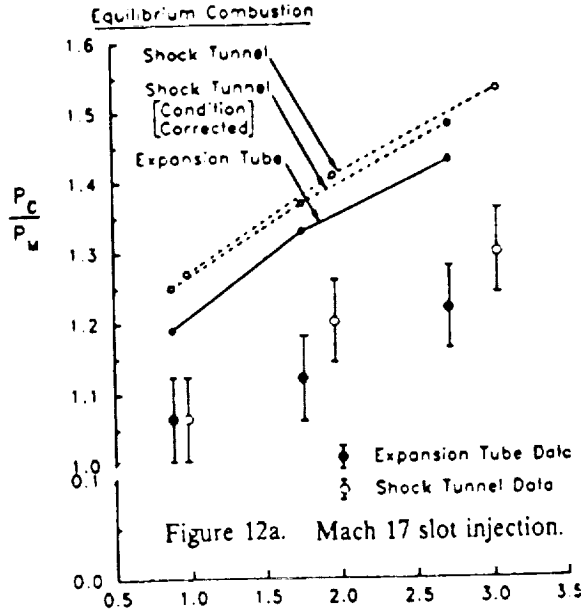

Figure 12a. Mach 17 slot injection.

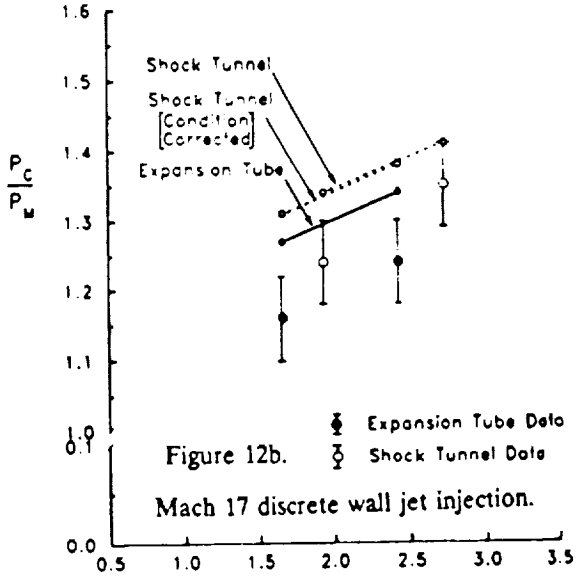

Figure 12b. Mach 17 discrete wall jet injection.

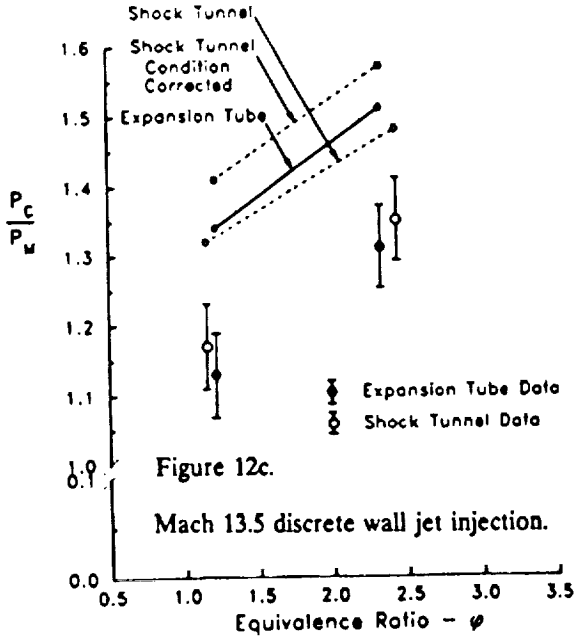

Figure 12c. Mach 13.5 discrete wall jet injection.

Figure 12. Combustor exit value of combustor induced pressure rise as measured and predicted assuming complete mixing and combustion

AXISYMMETRIC SCRAMJET THRUST PRODUCTION

R.J. Bakos and R.G. Morgan

11th Australasian Fluid Mechanics Conference
December 14-18, 1992
Hobart, TN Australia

ABSTRACT

Experimental and computational results for thrust production in an axisymmetric scramjet with wall fuel injection are reported. Test conditions were established in a reflected shock tunnel which were energy equivalent to flight at Mach 17. Thrust was determined by integrating static pressure measurements along a conical nozzle. Computational modelling of the flowfield was done with a Parabolic-Navier-Stokes code and good agreement was found between measured and predicted combustor pressure distributions. The level of agreement between the nozzle gross thrust coefficients is also good. Measured nozzle thrust is found to increase with increasing fuel equivalence ratio and is primarily a result of the combustion induced pressure rise. The effect of two-dimensional wave processes in the nozzle are also examined.

INTRODUCTION

A primary objective of hypervelocity scramjet tests is to evaluate the thrust producing potential of a combustor configuration. For a given nozzle area ratio, a one-dimensional analysis ignoring finite rate chemistry in the nozzle shows the thrust force produced depends on the nozzle entrance Mach number and pressure alone. In a two- or three-dimensional expansion geometry, non-uniformity of the Mach number and pressure at the combustor exit plane and in the nozzle may modify the thrust achieved.

The degree of modification and whether the Mach number profile augments or reduces the thrust relative to a uniform profile depends on the transverse location and sign of the Mach number gradient, and the shape and length of the thrust nozzle (Stalker 1989). In a two-dimensional scramjet, operating at hypervelocity, a partially mixed and reacted fuel jet will form a low Mach number region in the combustor exit plane. The sign of the Mach number gradient created by the jet depends on whether the fuel is injected along the wall, or is centred in the duct, separated from the wall by unmixed air. The latter case has been studied by Stalker and Morgan (1984) for a plane two-dimensional scramjet. It was found that the interaction of the centred expansion which originates at the nozzle expansion corner, with the lower Mach number fuel jet, produces compression waves and a thrust increment on the nozzle surface relative to a fuel-off situation.

To achieve the nozzle geometric area ratio necessary for sufficient thrust production in a working scramjet, a three-dimensional expansion geometry is required. Presently, a wall-injected axisymmetric scramjet and conical nozzle is studied. This geometry achieves a larger geometric area ratio than a plane geometry of the same expansion angle and therefore includes in a readily analysable flowfield some of the advantage of a three-dimensional expansion.

Experiments with an axisymmetric scramjet with a conical thrust nozzle are described and measured pressures are compared to a computational solution. The nozzle thrust produced is calculated and the influence of fuel equivalence ratio on nozzle performance is evaluated by examining the nozzle thrust coefficient.

EXPERIMENTAL CONDITIONS AND APPARATUS

The tests were performed in a reflected shock tunnel with a contoured nozzle producing uniform air flow at Mach 5.3, pressure of 16.0 kPa, and temperature of 2000 K. The pressure level at the exit of the facility nozzle was confirmed by flat plate static pressure measurements. The Mach number and temperature values were determined from a finite rate chemistry calculation of the nozzle flow (Lordi et al. 1966) terminating when the static pressure achieved the measured value. The test gas was calculated to be out of equilibrium having 33% and 12.5% by mass of its oxygen in atomic oxygen and nitric oxide forms respectively.

The axisymmetric combustor and nozzle configuration are shown in Figure 1. Hydrogen fuel was injected at Mach 1.9 from an annular wall jet at an angle of 15° from the combustor wall. Fuel conditions were varied by adjusting the injector plenum pressure to achieve equivalence ratios of 0.93, 1.91, and 3.05. A thrust nozzle is formed by a conical expansion of 10° half angle. It begins from a sharp corner and terminates at an exit geometric area ratio of 9.17. Upstream of injection a short 0.851 area ratio conical inlet captured the facility flow producing a 25% increase in static pressure. This inlet was necessary to fine tune the test condition to achieve desired combustor inlet conditions. Combustor and thrust nozzle instrumentation included wall static pressure transducers at 25 mm intervals in the combustor and nozzle.

COMPUTATIONAL MODELLING

Simulations of the complete scramjet and nozzle flows were done using the SHARC computer code developed by Brescianini (1992a). SHARC is a two-dimensional, steady, parabolic Navier-Stokes solver using the finite volume method of method of Patankar and Spalding (1970) with the pressure field calculated by the SIMPLE algorithm, (Elghobashi and Spalding, 1977).

PRECEDING PAGE BLANK NOT FILMED

PAGE 56 INTENTIONALLY BLANK

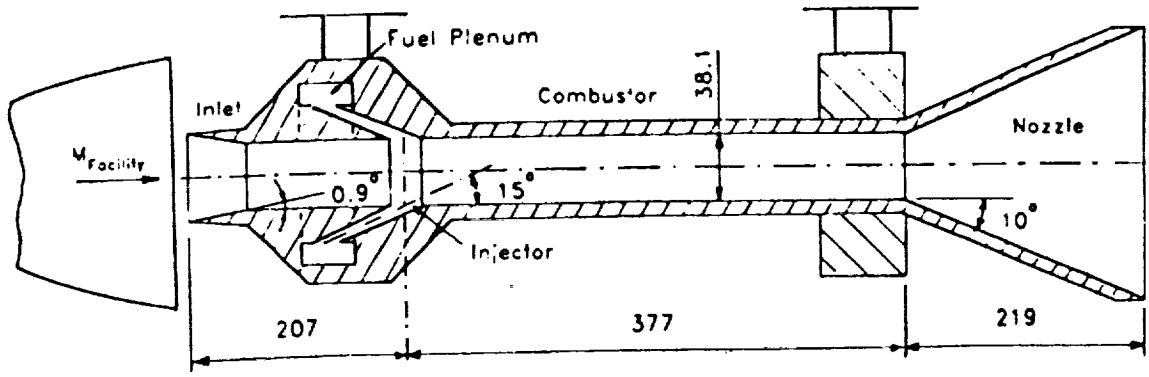

Figure 1. Configuration of axisymmetric scramjet and conical thrust nozzle (dimensions in mm).

Turbulence was modelled using a compressibility corrected k-ε1 turbulence model described in Brescianini (1992b). It was implemented in the manner described in that reference. For hydrogen-air reaction chemistry the 8-reaction mechanism as given by Evans and Schexnayder (1980) was chosen to allow rapid turn around of computer solutions. A spot check comparing to a more complete 25 reaction set from the same reference showed negligible difference in predicted scramjet pressure distribution.

The portion of the model from the inlet leading edge to the injection station was modelled using the facility exit conditions quoted above as initial conditions. The computational grid was slightly compressed toward the wall and 80 grid points were used over the duct radius. For fuel-on simulations the calculation was restarted at the injector station using a modified grid which included the inclined fuel jet. Again an 80 point grid was used, slightly compressed toward the outer wall. The air initial conditions were calculated to give the same boundary layer thickness on the injector wall as the inlet solution without retaining the details of the weak wave system formed in the inlet.

MEASURED AND COMPUTED PRESSURES

Measured and SHARC predicted distributions of wall surface pressure are shown in Figure 2a. Scatter bars represent the spread of data points over several (up to seven) tests and are seen to be typically within +/- 10% of the mean. No normalisation of the data was done to remove the scatter associated with repeatability of facility pressures, which accounts for approximately +/- 5% of the scatter. Where no bars are shown insufficient data points (less than three) were available to evaluate data scatter.

For the fuel-off case, the mean pressure level is well predicted while the measured wave pattern created by the inlet appears to damp more quickly than is predicted. The thrust surface pressure is of the correct magnitude although the shape of the distribution is not picked up by the calculation.

For the fuel-on case, a large amplitude standing wave pattern has been created by the slightly transverse fuel injector which is underexpanded by approximately a factor of three at the injector lip. Agreement in the combustor is excellent with the wave pattern and combustion and mixing induced pressure rise well predicted. The calculated injection shock persists into the thrust nozzle as seen by the bump in the computed solution there, while no clearly defined perturbation appears in the data at this location.

Measured and computed pressures for the other equivalence ratios tested are shown in subsequent Figures 2b and 2c. The injection induced shock system and the mixing/combustion pressure rise decrease in intensity for the lower equivalence ratios and the computed location of shock reflection in the nozzle moves downstream. The level of agreement between the computation and the data in the combustor is again seen to be good.

MEASURED AND PREDICTED NOZZLE PERFORMANCE

The nozzle thrust, F_T, is obtained from the measured nozzle surface pressure distribution and geometry by numerical integration using Simpson's rule. The accuracy of this integrated value is limited by the number of points in the pressure distribution and the degree of data scatter noted previously. However, the relative smoothness of the nozzle pressure distributions should make the numerical integration procedure reliable. Therefore, it is expected that the thrust values are of accuracy comparable to the combustor data, +/- 10%. For comparison, values of F_T were calculated from the SHARC nozzle pressure distributions. These are summarised for the three fuel equivalence ratios and the fuel-off run, along with the measured values, in Table 1. The values computed agree with the data to well within the data reliability limit of 10%.

Table 1. Nozzle thrust as measured and predicted by SHARC

Equiv. Ratio	Measured Thrust F_T(N)	SHARC Thrust F_T(N)
0	51.7	48.0
0.93	67.3	66.5
1.91	80.3	77.0
3.05	89.0	89.0

Both measurements and predictions show increasing thrust is produced by the nozzle with increasing equivalence ratio. This increase reflects changes in both the mean pressure at the combustor exit, which alters the

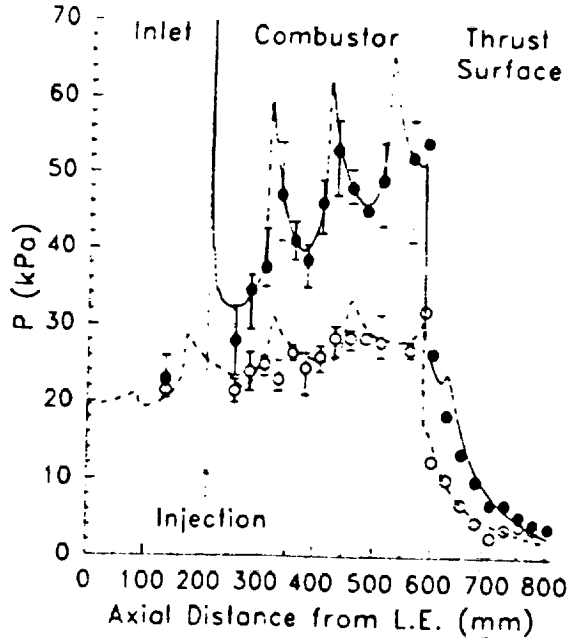

Figure 2a. Comparison of measured and SHARC predicted duct wall pressures for fuel-off (o - - -) and equivalence ratio of 3.05 (● ——) tests.

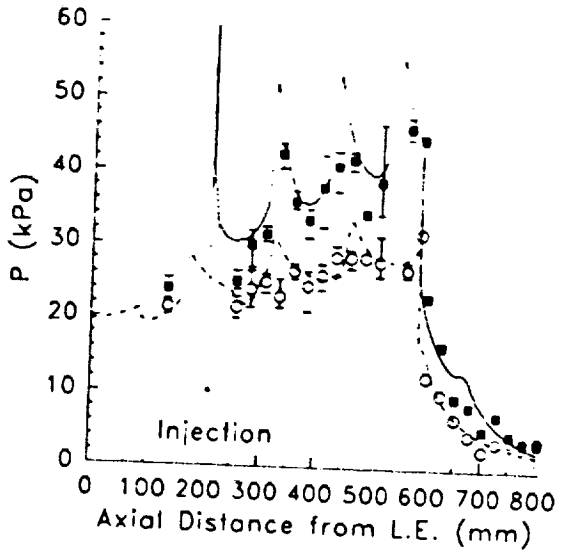

Figure 2b. Comparison for fuel-off and equivalence ratio of 1.91 (■ ——) tests.

pressure level in the nozzle, and changes to the Mach number distribution at the combustor exit, which results in a modification of the wave pattern in the nozzle. The relative importance of the wave pattern changes alone can be examined by forming a thrust coefficient, C_F, defined as the nozzle thrust normalised by the combustor exit area and mean pressure. A mean exit pressure was determined for each equivalence ratio by area averaging the SHARC calculated pressure distribution. Considering the good agreement found between the SHARC solution and the combustor pressure data, this mean pressure was used to form both the measured and SHARC C_F values.

Thrust coefficients (Table 2.) from both the measurements and the SHARC solutions show only slight variation (up to 6%) with fuel equivalence ratio, while the thrust itself varies considerably. Thus, the major factor influencing the thrust as the equivalence ratio changes is the mean static pressure at the combustor exit, while alteration of the Mach number distribution and subsequent nozzle wave pattern changes do not strongly influence the thrust produced. This strong pressure, weak wave pattern dependence is consistent with the fuel being well mixed across the duct, resulting in a relatively uniform Mach number distribution which only weakly interacts with wave propagation.

Although only a slight dependence of thrust on wave pattern changes due to fuel addition has been demonstrated for this flow, it is of interest to determine how close the conical nozzle is to an optimum thrust contour for the given area ratio and combustor exit conditions. An optimum contour acts to cancel all waves intersecting its surface, producing a uniform pressure exit plane.

To see this, SHARC was run for the four fuel conditions with a uniform lateral pressure condition imposed in the combustor and nozzle. The nozzle thrust found is thus nearly equivalent to a perfect, wave cancelling expansion in a contoured nozzle of the same

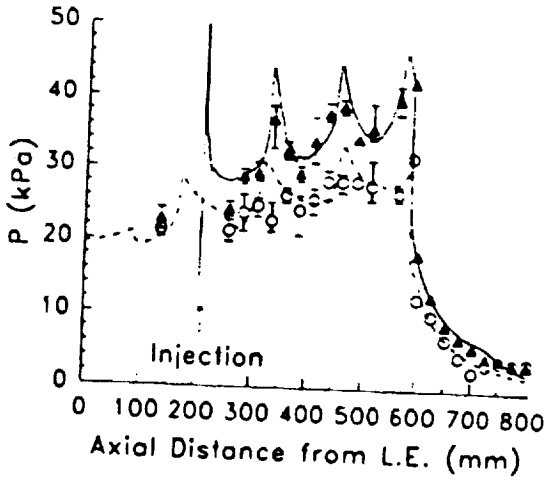

Figure 2c. Comparison for fuel-off and equivalence ratio of 0.93 (▲ ——) tests.

Table 2. Thrust coefficients determined from measured nozzle pressure and predicted by SHARC for conical and contoured nozzles.

Equiv. Ratio	Measured C_F Conical	SHARC C_F Conical	SHARC C_F Contoured
0	1.49	1.39	1.55
0.93	1.47	1.46	1.55
1.91	1.50	1.43	1.50
3.05	1.41	1.41	1.47

geometric area ratio. (Slight differences arise in the combustor exit conditions from the absence of waves in the combustor, however, combustor exit stream thrust is found to agree to within 1% of the full wave capturing solution). The "contoured" thrust coefficients calculated are given in Table 2. It is seen that the conical nozzle performance, as simulated by SHARC, approaches the ideal contour for the highest equivalence ratio, and is within 89% of the optimum for the worst, fuel-off case. Therefore, it is expected that the thrust measured in the conical nozzle is within approximately 10% of the thrust that would have been achieved had a perfectly contoured nozzle been tested.

CONCLUSIONS

Surface pressure distributions have been measured and thrust values calculated for a scramjet with a conical expansion nozzle when tested in a shock tunnel at conditions equivalent to flight Mach 17. Flowfield simulations with a parabolic Navier-Stokes code were found to predict the combustor pressure distribution and the thrust produced by the nozzle to within the data scatter of +/-10%. The details of the pressure distribution in the nozzle, including the location of injection generated wave reflections, is not well predicted, however, considering the agreement in integrated thrust, this discrepancy appears less important.

The nozzle thrust coefficient was examined to determine the effect of fuel addition on the combustor exit plane Mach number distribution and on the wave pattern formed in the nozzle. The addition of fuel was found to alter the thrust coefficient by a maximum of 6% for both the measured and predicted nozzle flows. However, changes in absolute thrust were much greater indicating that combustion induced pressure rise was the major contributor to thrust.

An ideal wave cancelling prediction of nozzle performance for the calculated nozzle exit Mach number distribution was found to give up to 11% greater thrust coefficient than the conical nozzle geometry which was tested. It is expected therefore that the measured thrust values are also approximately 90% of the maximum achievable for the nozzle geometric area ratio.

REFERENCES

STALKER, R J (1989) Thermodynamics and Wave Processes in High Mach Number Propulsive Ducts. AIAA 89-0261, Presented at the 27th Aerospace Sciences Meeting, Reno Nevada.

STALKER, R J and MORGAN, R G (1984) Supersonic Hydrogen Combustion with a Short Thrust Nozzle. Combustion and Flame, 55, 55-70.

LORDI, J A, MATES, R E and MOSELLE, J R (1966) Computer Program for the Numerical Solution of Nonequilibrium Expansions of Reacting Gas Mixtures. NASA Contractor Report 472.

BRESCIANINI, C P (1992a) An Investigation of the Wall-Injected Scramjet. PhD Thesis (submitted), The University of Queensland, Brisbane, Australia.

PATANKAR, S V and SPALDING, D B (1970) Heat and Mass Transfer in Boundary Layers. Second ed, International Textbook Company Ltd, London.

ELGHOBASHI, S and SPALDING, D B (1977) Equilibrium Chemical Reaction of Supersonic Hydrogen-Air Jets (The ALMA Computer Program). NASA Contractor Report 2725.

BRESCIANINI, C P (1992b) An Investigation of a Wall-Injected Scramjet Using a Shock Tunnel. AIAA 92-3965, Presented at the 17th AeroSpace Ground Testing Conference, Nashville TN.

EVANS, J S and SCHEXNAYDER, C J (1980) Influence of Chemical Kinetics and Unmixedness on Burning in Supersonic Hydrogen Flames. AIAA Journal, 18, 188-193.

11th Australasian Fluid Mechanics Conference
University of Tasmania, Hobart, Australia
14-18 December 1992

SCALING AND IGNITION EFFECTS IN SCRAMJETS

Maria V. PULSONETTI

Mechanical Engineering Department
University of Queensland
QLD 4072, AUSTRALIA

ABSTRACT

Some effects that could influence pressure scaling in a scramjet are presented, namely viscous effects, ignition time, and complete reaction time. Results are presented from the first scramjet model which is the largest to be tested in the study. For stagnation pressures from 13 to 40 MPa and stagnation enthalpys from 5.4 to 10.7 MJ/kg ignition was achieved in all combustion runs. As theoretically expected, ignition time decreased with increasing stagnation enthalpy and stagnation pressure. In addition, the ratio of the pressure at the exit of the scramjet to that at the beginning was found to decrease with increasing stagnation enthalpy.

NOTATION

C	species concentration
k_f	forward specific reaction rate constant
l	length
l_{ig}	ignition length
M	Mach number
P	pressure
R	specific gas constant
R_e	Reynolds number
T	temperature
t	time
U	velocity
x	axial distance
ϕ	equivalence ratio
γ	ratio of specific heats
μ	absolute viscosity
ρ	density
τ_{ig}	ignition time

INTRODUCTION

There is at present no facility capable of testing a full size scramjet engine over the full operating range. Scaling laws are therefore needed to relate the data obtained by testing scaled down models to a full size scramjet engine. Ramjet engine data scales with a pressure-length scaling factor, meaning that keeping all other properties (Mach number, velocity, species concentrations, etc.) the same the data would scale the same for twice the pressure and half the length. This may be associated with viscous effects. In a scramjet engine, however, there are a number of factors that can potentially affect the scaling, the most important of which are the viscous effects, the ignition time, the complete reaction time, the mixing process, and the effect of temperature and pressure on equilibrium heat release. With these effects acting simultaneously it will be difficult to determine which effect is dominating the scaling factor. An experiment has therefore been set up to determine how scramjet engines scale with pressure while keeping all other flow properties constant. The experiments cover a range of length scales with similar geometries, maintaining the pressure length product constant. Ignition delay, reynolds number effects and possibly mixing are expected to scale directly with this parameter. Therefore the experiment should give an indication if other effects which do not scale this way have a significant influence on the static pressure which is fundamental for evaluating the performance of a scramjet.

THEORY

Viscous effects scale with Reynolds number. With Mach number, velocity, entropy, and species concentrations held constant, viscous effects will scale by the pressure-length factor.

$$R_e = \frac{\rho U x}{\mu} \tag{1}$$

$$R_e = (\mathrm{Pl})\, T^{-1.2}\, M \sqrt{\frac{\gamma}{R}}\, \frac{T_o^{0.7}}{\mu_o} \tag{2}$$

The ignition reaction is a two body reaction. Thus it may be shown that the fractional change in concentration of one of the reactants is directly proportional to the concentration of the other. One may then integrate to find that the relative reaction rate is proportional to the concentration of one of the reactants and thus the pressure. Hence ignition length will scale by the factor pressure-length.

$$A + B \xrightarrow{k_f} C + D \tag{3}$$

$$\frac{dC_A}{C_A} = -\, k_f C_B\, dt \tag{4}$$

$$\tau_{ig} \propto \frac{1}{C_B} \tag{5}$$

$$\tau_{ig} \propto \frac{1}{P} \tag{6}$$

ORIGINAL PAGE IS
OF POOR QUALITY

The final combustion reaction which produces H_2O is a three-body reaction. In an analogous analysis to the two-body ignition reaction it may be shown that the relative reaction rate will be proportional to the concentration squared and thus to pressure squared. Thus the reaction length will scale by the factor pressure squared-length.

$$A + B + C \overset{k_f}{\rightleftharpoons} D + E \tag{7}$$

$$\frac{dC_A}{C_A} = - k_f C_B C_C dt \tag{8}$$

$$\tau_{ig} \propto \frac{1}{C_B C_C} \tag{9}$$

$$\tau_{ig} \propto \frac{1}{p^2} \tag{10}$$

EXPERIMENTS

Mixing and combustion experiments have been performed in the University of Queensland's reflected shock tunnel (T4) using a 1.32 metre long scramjet model. This model is the largest of the scramjets to be tested in this study. The model was two-dimensional with a duct height of 48 mm and a width of 100 mm. It was instrumented with thirty PCB pressure transducers to read static pressure and twelve thin film heat flux gauges manufactured at the University. The flow was processed by a contoured mach 8 nozzle, a set of opposing 15 degree wedges and an internal expansion inside the duct. This was done in order to match all the flow conditions (mach number, temperature, density, species concentrations) except pressure which were expected when testing the smallest scramjet using a mach 4.5 contoured nozzle.

Seven test conditions were chosen in order to show the effect of stagnation pressure and stagnation enthalpy on pressure scaling. Figure 1 shows the variation of stagnation pressure and stagnation enthalpy for the seven test conditions used. Holding the stagnation pressure essentially constant, stagnation enthalpy was varied from 5.7 to 10.7 MJ/kg causing variations in static temperature and velocity in the model from 1100 to 2100 K and 2.9 to 3.9 km/s, respectively. Also, while holding stagnation enthalpy constant, stagnation pressure was varied from 13 to 38 MPa causing variations in static pressure in the model from 6.6 to 17 KPa. Table 1 shows the flow properties at the point of fuel injection for the seven test conditions.

DISCUSSION

In all cases ignition was achieved. Figure 2 shows pressure distributions for a combustion, mixing, and tare run at condition 1. (A tare run is a run in which air is the test gas and no fuel is injected through the central injector. A mixing run is when gaseous hydrogen is injected into Nitrogen and a combustion run is when gaseous hydrogen is injected into air.) The pressure rise in a tare run is due to viscous effects at the walls. By comparing the pressure distributions between a tare and a mixing run one can see the extent of the pressure rise due to mixing. The difference in pressure levels between the combustion and mixing runs, therefore, can be attributed to combustion alone. From figure 2 it is quite easy to see that combustion has occurred.

The ignition point, as well, can quite easily be determined from figure 2 as the point where the pressure level of the combustion run rises suddenly above that of the mixing run. Using the duct velocity for each run, ignition times can be determined. Figure 3 shows the variation of ignition times with stagnation enthalpy. Note how the ignition time decreases with increasing stagnation enthalpy. This trend agrees with the theoretical relation for ignition time by Pergament (1963) which follows.

$$\tau_{ig} = \frac{l_{ig}}{U} = \frac{8 \times 10^{-9} e^{(9600/T)}}{p} \tag{11}$$

This global model for ignition was developed on the basis of an eight-reaction, six species chemistry system. The pressure and temperature in the relation correspond to the local static pressure and temperature at the point of ignition. Hence the temperature used in the relation is the mixture temperature at the ignition location. Huber et al. (1979) found that for cold Hydrogen injected into a scramjet, self ignition would most likely originate in a mixing layer where the equivalence ratio (ϕ) was 0.2. From an energy balance between the fuel and air, neglecting heat transfer and dissipation effects, the mixture temperature can be determined by the following.

$$T_{mix} = T_{air} - \frac{0.327\phi}{1 + 0.327\phi}(T_{air} - T_{fuel}) \tag{12}$$

The values predicted using the theoretical ignition relation, however, do not match the experimental results very well. Table 2 shows the difference between the experimental values of ignition time obtained in the large model and the theoretical relation. For conditions 2, 3 and 4 the theoretical relation under predicts the ignition time. This could be due to the fact that the theoretical analysis did not take mixing into account in determining the time to achieve five percent of the complete reaction temperature rise (ignition time). The lowest enthalpy condition (condition 1), however, had a lower experimental ignition time than the theoretical value. The theoretical relation has a strong non-linear variation with temperature at lower temperatures due to the required activation energy which must be overcome to start the chain reaction. The experimental results, however, do not show this strong non-linearity at the low temperatures. This could be because the flow may have some free radicals or chain carriers such as atomic oxygen in it due to the fact that the flow was stagnated at the end of the shock tube and then chemically frozen through the nozzle.

Figure 4 shows the variation of ignition time with stagnation pressure. The predicted trend of decreasing ignition time with increasing stagnation pressure is observed for all four conditions. Table 3 shows the difference between the experimental values of ignition time obtained in the large model and the theoretical relation. The theoretical values over predicted the ignition time in all four cases. This again can be due to the fact that my flow did not exhibit a strong non-linearity of ignition at low temperatures. The most surprising result was the fact that ignition was achieved for condition 5 and 6 where it was thought that for such low pressures ignition should take four and six model lengths, respectively, to ignite.

The ratio of the final pressure at the exit of the duct to the initial pressure in the duct before injection is shown as a function of stagnation enthalpy in figure 5. From this figure one can see that the pressure rise due to combustion decreased with increasing stagnation enthalpy. This is a

result expected from theory since at the higher temperatures the dissociation process will work against the final combustion reaction.

CONCLUSIONS

Ignition was achieved for stagnation enthalpys from 5.4 to 10.7 MJ/kg and stagnation pressure from 13 to 40 MPa. Trends of decreasing ignition time with increasing stagnation enthalpy and increasing stagnation pressure were observed. These trends match theoretical trends, however, the ignition time predicted by theory was less than the experimental ignition time for stagnation enthalpys greater than 7.6 MJ/kg. This was most probably due to the fact that the theoretical model did not take mixing times into account. For enthalpys less than 5.9 MJ/kg the experimental ignition times under predicted the theoretical values which may be due to the presence of chain carriers in the flow wavier the need for activation energy to initiate the reaction.The ratios of final to initial pressures in the duct were found to decrease with increasing stagnation enthalpy as was expected from theory due to the higher levels of dissociation at the higher enthalpys.

Further work includes the design and testing of the smallest scramjet in this study. This scramjet will be one fifth the size of the large scramjet with a 2 mm central injector. Experiments are scheduled for early 1993.

ACKNOWLEDGEMENTS

The author wishes to thank Dr. Richard Morgan for his invaluable input, Professor Ray Stalker for his expert supervision, and the University of Queensland and NASA (grant #NGW674) for their financial assistance.

REFERENCES

HUBER, P W, SCHEXNAYDER, C J, McCLINTON, C R (1979) Criteria for self-ignition of supersonic Hydrogen-air mixtures. NASA-TP-1457

PERGAMENT, H (1963) A theoretical analysis of non-equilibrium Hydrogen-air reactions in flow systems. [Preprint] 63113, American Inst. of Aeronaut & Astronaut.

Table 1 : Test Conditions in Large Scramjet

	cond. 1	cond. 2	cond. 3	cond. 4	cond. 5	cond. 6	cond. 7
M_{air}	4.42	4.36	4.38	4.26	4.38	4.47	4.45
P_{Tair} (MPa)	38	40	34	36	13	19	32
H_{Tair} (MJ/kg)	5.7	7.6	8.5	10.7	5.5	5.4	5.9
P_{air} (kPa)	17	19	14	21	6.6	7.8	13
T_{air} (K)	1100	1500	1600	2100	1100	1000	1100
U_{air} (km/s)	2.9	3.4	3.5	3.9	2.9	2.8	3.0
ϕ	1.23	1.36	1.26	1.32	1.23	1.53	1.29

M_{fuel}=3.41

T_{Tfuel}=296 K

Table 2. Experimentally and Theoretically Obtained Ignition Time for Various Stagnation Enthalpys

Condition	H_{stag} (MJ/kg)	τ_{ig} (μs) (experiment)	τ_{ig} (μs) (theory)
1	5.7	183	487
2	7.6	171	36
3	8.5	129	29
4	10.7	25	5

Table 3. Experimentally and Theoretically Obtained Ignition Times for Various Stagnation Pressures

Condition	P_{stag} (MPa)	τ_{ig} (μs) (experiment)	τ_{ig} (μs) (theory)
5	13	243	1780
6	19	231	2500
7	32	219	493
1	38	183	487

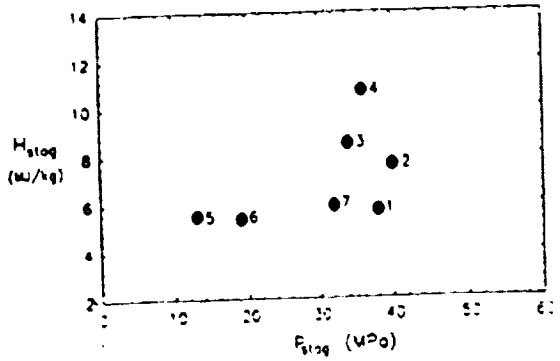

Figure 1 Variation of stagnation enthalpy and stagnation pressure for the seven test conditions in the large scramjet

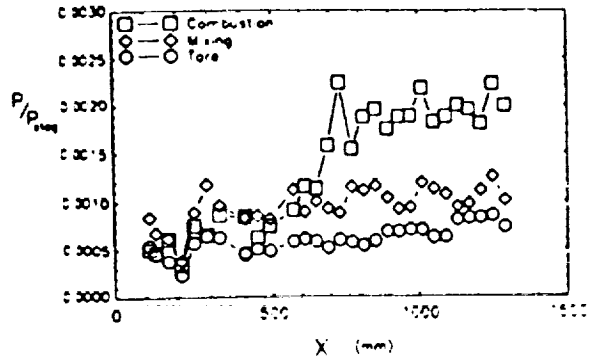

Figure 2 Pressure Distributions for a Combustion, Mixing, and Tare Run at Condition 1

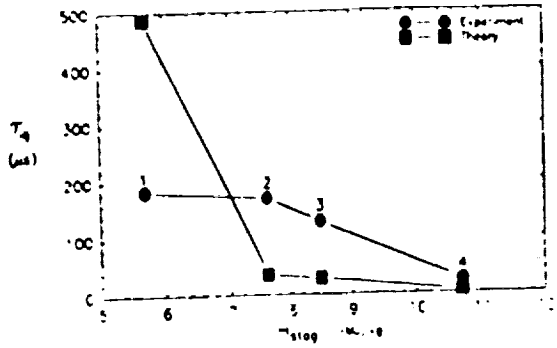

Figure 3 Variation of Ignition Time with Stagnation Enthalpy

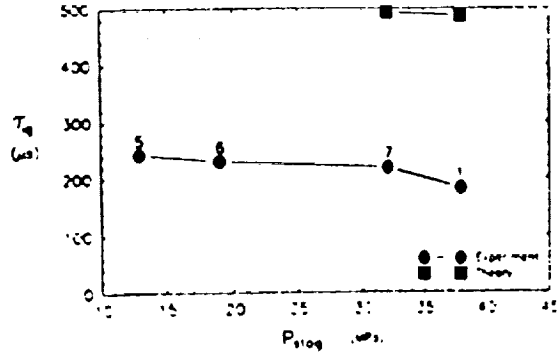

Figure 4 Variation of Ignition Time with Stagnation Pressure

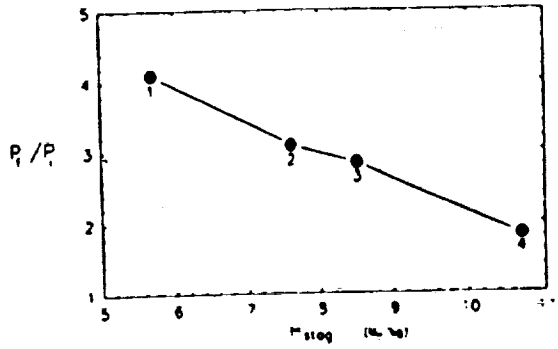

Figure 5 Ratio of Final to Initial Pressure in the Duct as a Function of Stagnation Enthalpy

11th Australasian Fluid Mechanics Conference
University of Tasmania, Hobart, Australia
14-18 December 1992

HYPERSONIC IGNITION IN A SCRAMJET

A. PAULL

Department of Mechanical Engineering
University of Queensland
QLD 4072, AUSTRALIA

ORIGINAL PAGE IS
OF POOR QUALITY

1. Introduction

Scramjets have been proposed as the main propulsion system for hypersonic reusable aircraft such as the National Aerospace Plane (NASP), Hermes and S enger. A significant amount of the research into scramjet propulsion systems has been done in Australia using the hypersonic shock tunnels T3 and T4. Unfortunately, the application of this research to an Australian funded project of the size of the above mentioned aircraft is not likely to be realized. However, a scramjet has also been proposed as the propulsion system for a disposable launcher which deploys small payloads into low earth orbit. Such a project could be funded in Australia and furthermore, is a means for Australia to enter the space industry based on technology which is to be used for future launch vehicles. It is such a project that this research into scramjets is directed towards.

2. Experimental Aims

The experiments reported here were undertaken to determine to what extent both hydrogen and ethane would burn at hypersonic conditions. They were required to determine the extent of mixing and at what distance downstream of the injector was combustion complete. It is important to determine this length as too short a combustion chamber will result in inefficient burning, whereas too long a combustion chamber could produce sufficient drag to offset the thrust production.

Results are presented for hypersonic burning of hydrogen and ethane in a rectangular duct. Wall pressures were measured downstream of the injector. From these measurements it is shown that, in contrast to general belief, mixing of hydrogen fuel with air occurs quit rapidly. Furthermore, significant combustion does occur at hypersonic conditions.

Hydrogen was used as a fuel because of its good heat release and therefore good performance in thrust production. The disadvantage with hydrogen is that it is a very bulky fuel. Ethane on the other hand is relatively compact and was believed to have a similar chemistry to that of hydrogen when burnt in air and is thus an attractive fuel.

3. Experimental Apparatus

The experiments reported here were done in the free piston driven hypersonic reflected shock tunnel T4 (Stalker (1966)), figure 1. Typically, the order of the test time in this facility is 1 ms. Data was recorded from each transducer every 2 s.

The scramjet model used in these combustion experiments is shown in figure 2. It a constant area duct into which fuel is injected centrally. The duct is 27 mm high and 54 mm wide and 800mm long. The injector which extends the full width of the duct is 5mm thick. The splitter plate, or upstream edge of the injector, is 76 mm wide and extends 74 mm upstream of the scramjet intake. The splitter plate has been designed so that all shocks and expansions created by the leading edge of the splitter plate are spilled outside the intake to the scramjet.

4. Experimental Results

Two different experiments will be presented. In the first set of experiments the effect on the pressure distribution downstream of the injector produced by injecting different amounts of hydrogen is displayed. In the second set of experiments a comparison between the combustion of hydrogen and ethane is made.

4.1. Equivalence ratio study

In these experiments the measure of the amount of fuel injected into the freestream is made in terms of the equivalence ratio (ϕ). A fuel rich mixture has an equivalence ratio greater than one, whereas a fuel lean mixture's equivalence ratio is less than one. The equivalence ratio for hydrogen fuel is equal to 8 times the fuel mass flux through the injector divided by the mass flux of oxygen through the intake.

The mass flow of oxygen into the intake is determined numerically from conditions upstream of the shock tube nozzle using the code NENZF (Lordi et.al (1966)). This program is a one-dimensional nonequilibrum real gas calculations which determines the physical and chemical properties of the test gas at the exit of the nozzle. Input to the calculations are the nozzle contour and the stagnation temperature and pressure.

The stagnation pressure is measured and the stagnation temperature is determined numerically from another real gas calculation performed by the program ESTC (McIntosh (1968)). The inputs for this calculation are the shock tube shock speed and the shock tube filling pressure, both of which are measured.

Fuel was injected at equivalence ratios of 0, 1.1, 1.8 and 4.3. The pressure measurements taken downstream of the injector are displayed in figures 3, 4 and 5. Also displayed in these figures are the effects of injecting similar mass fluxes of fuel into a nitrogen test gas.

ORIGINAL PAGE IS
OF POOR QUALITY

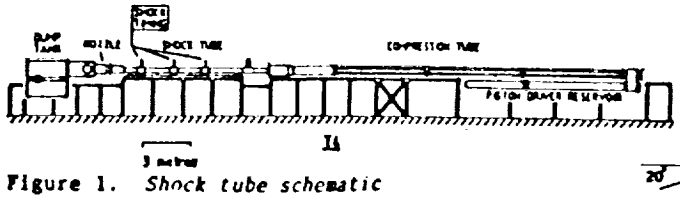

Figure 1. *Shock tube schematic*

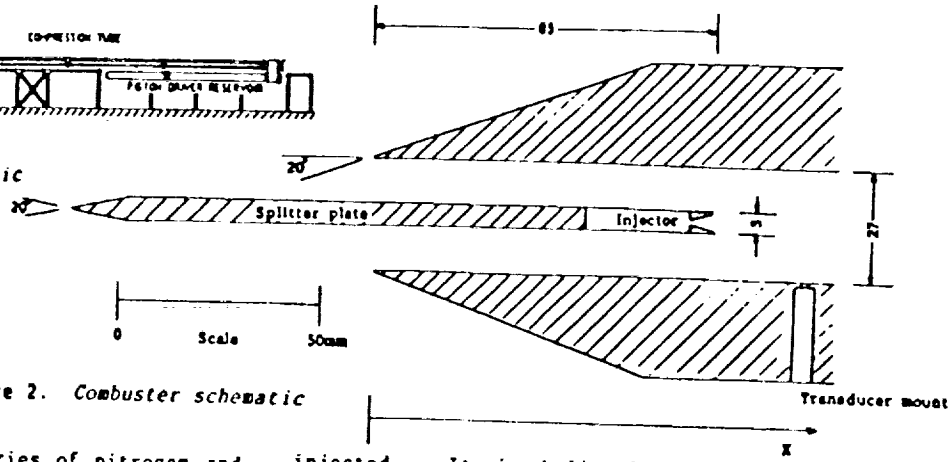

Figure 2. *Combuster schematic*

Due to the different chemistries of nitrogen and air the nitrogen test gas properties at the nozzle exit differ to that of the air's for the same stagnation pressure. The times at which the pressure profiles displayed in figures 3, 4, and 5 have been taken, were chosen so that the static pressure of the nitrogen test gas at the nozzle exit matched that of the air. This can be done as the shock tunnel was run in an under taylored mode and therefore the static pressure was falling with time. Hence, a time could be chosen for which the static pressure was at the required level. The properties of the test gases for each figure are given in table 1.

It can be seen that the pressure rise due to the injection of fuel into air is always greater than that when injected into nitrogen which in turn is greater than that when no fuel is injected. The greater pressure rise produced when fuel is injected into air than that when fuel is injected into nitrogen suggests that the fuel is burning.

Another phenomena which is apparent when the results of figures 3 and 5 are compared is that the pressure rise associated with the injection of fuel at =4.2 is significantly larger than that for =1.1. It might be concluded that the injection of more fuel somehow increases the mixing and thus leads to greater combustion and therefore an increase in pressure. However, it is not believed that extra combustion produces the greater pressure rise observed in figure 5.

4.1.1. Mixing analysis

To understand the mechanism which produces the increase in pressure at the higher equivalence ratios the injection of fuel into nitrogen should be considered. Here there is no combustion and yet there is still a significant increase in pressure at the higher equivalence ratio.

If the fuel did not mix with the air then there would be an obvious increase in pressure when more fuel is injected. To obtain an estimate of the pressure rise expected due to the injection of fuel it was assumed that the test gas and the fuel would expand isentropicly from their properties at the exit plane of the injector to one at which their static pressures were matched. If this is done then the final static pressures for =1.1 and 4.3 are 17.4 and 19.6 kPa, respectively. If fuel were not injected the static pressure would be 16.4 kPa.

There is an added complication in the interpretation of these results. The above pressure rises are superimposed on a pressure rise which occurs in the duct even when fuel is not injected. It is believed that this rise is produced by boundary layer growth. If the test gas was assumed to be isentropicly compressed from 16.4 kPa to the measured value of 24.3 kPa at the end of the duct then this would correspond to a boundary layer thickness of approximately 2.5 mm at the end of the duct. This is not unreasonable when boundary layer theory is considered.

If this boundary layer growth is assumed to remain the same even when the fuel is injected and if it is assumed that the fuel and air do not mix but are compressed by the effect of the boundary layer then it can be shown that the static pressures would rise from 17.4 and 19.6 kPa to 25.9 and 29.0 kPa, respectively for =1.1 and 4.2. However, as can be seen from figures 3 and 5, this still does not fully explain the increase in pressures which are observed, especially at the higher equivalence ratio.

To include the effects of mixing Morgan et.al.(1990) has assumed that
(a) the fuel and the test gas mix after their static pressures have been matched and
(b) the momentum loss observed in the fuel off results is also lost from the mixed gases.
If these assumptions are made then by enforcing the conservation of mass, momentum and energy it can be shown that the final pressures for a fully mixed nitrogen test gas with the hydrogen fuel would expected to be 27.1 and 35.3 kPa for =1.1 and 4.23, respectively. It can be seen from figures 3 and 5 that these pressures correspond reasonable well with those measured at the end of the duct. It is concluded that mixing is complete at the latest by the end of the duct.

4.1.2. Combustion analysis

An estimate of the pressure rise due to the effects of combustion are now obtained in the same way that Morgan et.al.(1990) has proposed. When the fuel mixes with air and combustion occurs there is energy released and new products are formed. The effects of combustion are then included by assuming that
(a) the energy released for complete consumption of the available oxygen is added to the energy equation,
(b) the change in specific heat and gas constant due to the combustion products are accounted for in the final mixture, and
(c) the momentum loss due to the boundary layer growth determined from the fuel off results is the same when combustion occurs.

Although this technique would appear to be a gross simplification of the combustion process, it is a

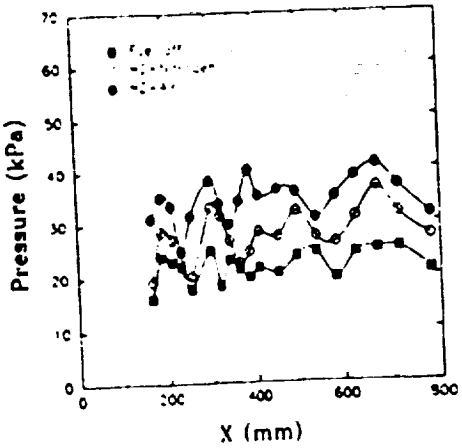

Figure 3. *Pressure vs Distance from intake leading edge* :=1.1

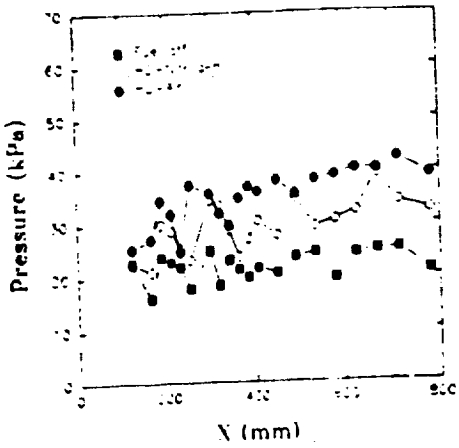

Figure 4. *Pressure vs Distance from intake leading edge* :=1.8

first order approximation to combustion and gives insight into the main mechanisms involved in combustion. If the limitations of this approximations are understood, this type of approximation can be valuable in the understanding of such complex phenomena.

Using the above assumptions it can be shown that the pressures at the exit of the duct could be expected to be 43 kPa and 57 kPa for :=1.1 and 4.2, respectively. From these estimates the experimental results indicate that all oxygen is consumed at both equivalence ratios.

It is concluded that the higher pressures observed at higher equivalence ratios results from more unburnt fuel mixing with the combustion products rather than more complete combustion.

4.1.3. Combustion length

Figure 6 displays the difference between hydrogen injected into air and hydrogen injected into nitrogen at :=1.1, 1.8 and 4.2. These pressure differences have be averaged over spatially adjacent pressure differences to display the trend in pressure differences rather than the actual pressure differences. The actual differences in general undergo large variations between adjacent spatial points. This results from the different intake Mach numbers of the air and nitrogen test

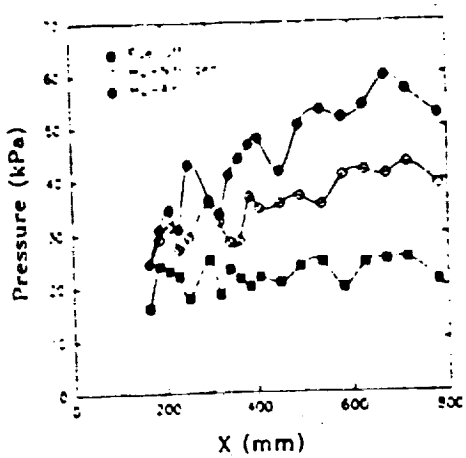

Figure 5. *Pressure vs Distance from intake leading edge* :=4.2

gases producing different Mach wave angles. Thus, the expansion and compressions which are travelling down the duct will be observed at different lateral locations. Spatial averaging over the adjacent points removes this separation. Two observations can be made from figures 6
(a) The pressure rise increases as the equivalence ratio increases and
(b) a significant jump in the pressure can be observed at the wall at x=350 mm downstream of the injector at the higher equivalence ratio.

The first observation was discussed above and results from mixing. The second observation

suggests that either there is a significant increase in mixing at this point or combustion occurs rapidly at this point.

From figure 6 it is seen that for :=1.1 and 1.8 the pressure difference at 200mm is essentially the same as that at the end of the duct. This would indicate that combustion was complete at 200mm (i.e. 115 mm downstream of injection). This does not contradict the induction lengths predicted by Nettleton (1992) which indicate that a stoichometric mixture of hydrogen and air has an induction length of approximately 50mm for the intake conditions of these experiments.

If it is assumed that combustion also takes place at the same rate for :=4.2 as :=1.1 and :=1.8 (as is indicated in figure 6 for x<300) then the large jump in pressure observed at the higher equivalence ratio at x=350 is probable caused by significant mixing at this point. It can be seen from figure 5 that at this point there is a shock and expansion system which is propagating through the mixture at this point. It is possible that this system enhances mixing and is thus possibly a useful mechanism.

4.2. Ethane-Hydrogen comparison

The combustion of ethane was compared with that of hydrogen at the stagnation enthalpies of 8.6 and 11.6 MJ/kg. Table 1 lists the flow parameters.

It can be seen that at the higher stagnation enthalpy the pressure rise produced by ethane and hydrogen were almost indistinguishable. Whereas, at the lower enthalpy the net increase in pressure produced by the ethane was approximately half that produced by the hydrogen. If the duct were longer it is not clear whether or not this would have been the case. Ethane may be mixing limited.

ORIGINAL PAGE IS
OF POOR QUALITY

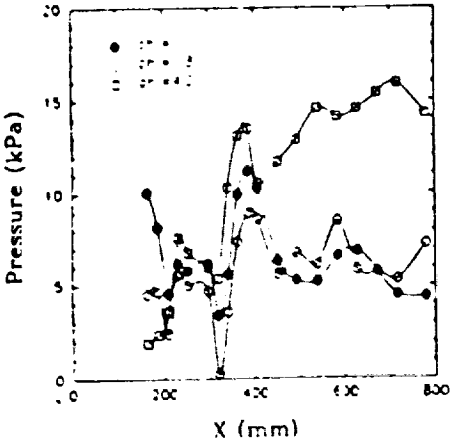

Figure 6. *Pressure difference between fuel into air and into nitrogen vs Distance from the intake leading edge for different equivalent ratios.*

Not-with-standing the pressure rise associated with ethane, even at the higher enthalpies, would indicated that ethane is not as an efficient fuel as hydrogen if efficiency is based on specific impulse. This follows because for the same equivalence ratio the mass of ethane is 15/7 times that of hydrogen. Hence, to produce the same thrust per unit mass of fuel the pressure rise produced by the ethane would have to be 15/7 times that produced by hydrogen.

However, it should be understood that efficiency based upon specific impulse is not necessarily applicable when comparing different fuels for flight vehicles. This is because more dense fuels require smaller fuel tanks and therefore less drag will be produced by the vehicle which runs on higher density fuels. Hence, dense fuels with smaller specific impulses than less dense fuels may in fact be more efficient overall.

Conclusions

At the enthalpy of 15 MJ/kg hydrogen can be made to burn effectively. The burning process does appear to be limited by mixing, but the experimental results indicate that it is not a server limitation. In practical terms these mixing limitations would not pose a problem to the design of a workable engine.

The induction process for the combustion of hydrogen predicted by Nettleton (1992) would appear to be consistent, at least to an order of magnitude, to that measured.

Ethane fuel produces pressure rise which is at most equal to that produced by hydrogen. Hence, if efficiency is based upon specific impulse it is expected that ethane would not be as an efficient fuel as hydrogen.

Acknowledgements

This work was done under grants supplied by The Australian Research Council and NASA.

Bibliography

Lordi, J.A., Mates, R.E. and Moselle, J.R. 1966 Comp. prog. for numerical soln. of nonequilibrum expansion of reacting gas mixtures. NASA CR-472

McIntosh, M.K. 1968 Computer. program for the numerical calculation of frozen and equilibrium conditions in shock tunnels. Dept. of Phys. ANU

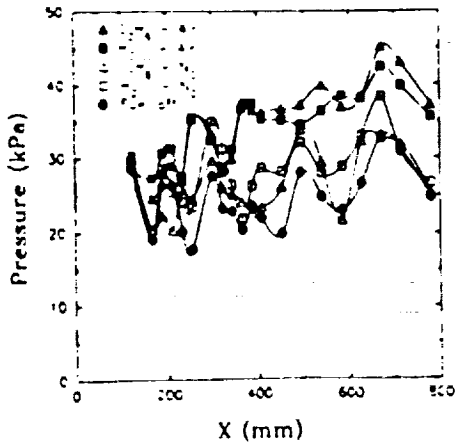

Figure 7. *Pressure vs Distance for hydrogen and ethane fuels. Stag. enthalpy nominally 12MJ/kg*

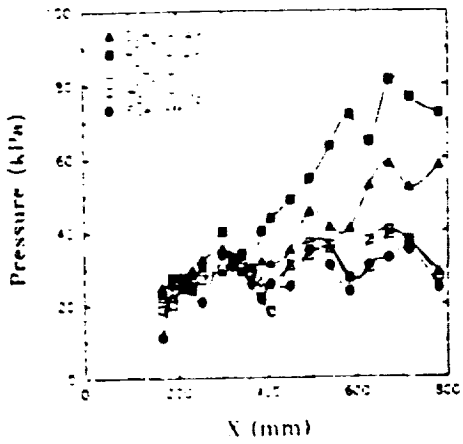

Figure 8. *Pressure vs Distance for hydrogen and ethane fuels. Stag. enthalpy nominally 9MJ/kg*

Morgan R.G. Bakos, R.J. and Tamagno, J. 1990 Bulk parameter analysis of hypersonic combustion experiments CASL TR321

Nettleton M. 1992 On the existance of real standing detonations in scramjet ducts AFMC 1992

Stalker, R.J. 1966 The free piston shock tunnel. Aeronaut. Q. V17 pp351-370.

Fig.	gas	Enth. MJ/kg	Press. kPa	Vel. m/s	Den. kg/m	M	:	Fuel
3	Air	14.7	20.3	4608	.032	5.1	1.1	H2
3	N2	15.5	20.7	4926	.032	5.4	1.2	H2
3,4,5	Air	14.9	20.3	4627	.032	5.1	0.0	
4	Air	15.0	19.0	4648	.030	5.1	1.8	H2
4	N2	15.6	19.0	4929	.029	5.4	1.7	H2
5	Air	14.7	20.3	4634	.032	5.1	4.2	H2
5	N2	15.4	20.5	4914	.032	5.4	4.4	H2
7	Air	11.7	18.3	4186	.032	5.2	1.6	H2,C2H6
7	Air	11.7	18.3	4186	.032	5.2	0.0	
7	N2	12.6	18.3	4556	.036	5.6	1.8	H2,C2H6
8	Air	8.64	18.9	3718	.054	5.5	1.9	H2,C2H6
8	Air	8.64	18.9	3718	.054	5.5	0.0	
8	N2	9.13	19.1	3952	.055	5.8	1.7	H2,C2H6

Table 1. *Test conditions.*

C-2

ORIGINAL PAGE IS
OF POOR QUALITY

11th Australasian Fluid Mechanics Conference
University of Tasmania, Hobart, Australia
14-18 December 1992

MODELLING OF A SCRAMJET FLOW USING VARIOUS TURBULENCE MODELS

Craig BRESCIANINI and Richard MORGAN

Mechanical Engineering Department
University of Queensland, QLD 4072
AUSTRALIA

ORIGINAL PAGE IS
OF POOR QUALITY

ABSTRACT

Three turbulence models of varying sophistication are compared in a high-Mach-number reacting flow field which is typical of many shock-tunnel scramjet experiments. The simulations confirm that there are some significant differences in the predictions obtained with the different models. A comparison with experimental data shows that none of the models give completely satisfactory results over the entire length of the scramjet engine, however, all models indicate that the fuel/air mixing rate is insufficient to achieve complete mixing within the given engine length.

NOTATION

$C_{\varepsilon 1}, C_{\varepsilon 2}, C_\mu$	constant coefficients in turbulence models
H_j	injector step height
k	kinetic energy of turbulence
ℓ_m	mixing length
ℓ_ε	dissipation length scale
p	pressure
p_i	inlet pressure
St	Stanton number based on inlet conditions
u	axial velocity
v	transverse velocity
x	axial distance measured from injector
y	transverse distance
y_G	characteristic width
ε	rate of turbulence dissipation
η_{mix}	*mixing efficiency*
η_{RR}	*reaction-rate efficiency*
λ	constant in mixing-length model
μ_t	turbulent viscosity
ρ	density
σ	"Prandtl" number

INTRODUCTION

The sophisticated instruments required to measure detailed profiles, such as velocity, temperature, composition, etc., in hypervelocity, short-duration flows created by a shock-tunnel, are only in the development stage. As a consequence, heavy reliance must be placed upon current CFD (Computational Fluid Dynamics) to extract detailed information from a shock-tunnel scramjet experiment. However, a large amount of uncertainty is attached to present-day CFD, particularly if the flows being modelled are turbulent, since the turbulence and combustion models used are unlikely to have been validated in hypervelocity flows.

Turbulence models are usually developed from reference to simple, incompressible, low-speed flows. However, it is well known that these models can give poor predictions if they are extended to flows which contain (a) compressibility effects, (b) pressure gradients, (c) wall-damping effects, and (d) combustion. A scramjet, unfortunately, can suffer from all of these complications simultaneously. Several methods have been suggested in the literature for improving these models in "complex" flows, eg. by incorporating algebraic Reynolds stresses and also by incorporating multiple-time-scale effects. However, the complexity of the turbulence models increase substantially with these modifications, and it is not clear whether these modifications will have a substantial effect on the predictions in a scramjet flow, or even if the effects will be beneficial. In this current study, a series of numerical scramjet experiments were performed using different turbulence models to see how the predictions were affected by the different turbulence models. The test conditions chosen for the study correspond to a particular flow condition produced by the T4 shock tunnel at the University of Queensland, and hence, some experimental data was also available for comparison.

TURBULENCE MODELS

Three turbulence models were chosen for the present study. The first was Prandtl's (1925) *Mixing Length Hypothesis* (MLH). The model assumes that the turbulent viscosity may be evaluated from the formula

$$\mu_t = \rho \ell_m^2 \left|\frac{\partial u}{\partial y}\right| \qquad (1)$$

where the mixing length, ℓ_m, is determined from the relation

$$\ell_m = \lambda y_G \qquad (2)$$

where λ is a constant, and y_G is a characteristic width in the flow. For the current study, the flow field was divided into several regions with different characteristic widths. The method used to determine the characteristic widths was that suggested by Spalding (1977). A value of $\lambda = 0.118$ was chosen for the present scramjet computations. This value is slightly higher that the value of 0.09 suggested by Spalding, however, it is slightly lower that the value of 0.125 used by

Launder et al. (1973). A value of 0.118 was found to give satisfactory predictions for the spreading rates of single-stream, incompressible, free shear layers.

The second model chosen was the well-known k-ε model (see eg. Launder and Spalding, 1974). The *high-Reynolds-number* version of the model evaluates the turbulent viscosity from the formula

$$\mu_t = C_\mu \rho \frac{k^2}{\varepsilon} \qquad (3)$$

where the values of k and ε are determined from solving the following transport equations

$$\rho u \frac{\partial k}{\partial x} + \rho v \frac{\partial k}{\partial y} = \frac{\partial}{\partial y}\left[\frac{\mu}{\sigma_k}\frac{\partial k}{\partial y}\right] + \mu_t\left[\frac{\partial u}{\partial y}\right]^2 - \rho\varepsilon \qquad (4)$$

and

$$\rho u \frac{\partial \varepsilon}{\partial x} + \rho v \frac{\partial \varepsilon}{\partial y} = \frac{\partial}{\partial y}\left[\frac{\mu}{\sigma_\varepsilon}\frac{\partial \varepsilon}{\partial y}\right] + C_{\varepsilon 1}\left[\frac{\varepsilon}{k}\right]\mu_t\left[\frac{\partial u}{\partial y}\right]^2 - C_{\varepsilon 2}\left[\frac{\varepsilon}{k}\right]\rho\varepsilon \qquad (5)$$

The k-ε model is generally applicable in a larger range of flows than the simpler MLH model. The "standard" model constants recommended by Launder and Spalding (1974) where used during the computations.

For simple, parabolic flows, both the MLH and k-ε models are usually reliable (although the MLH model usually requires an adjustment of λ from one flow geometry to another). However, it is well documented that the predictions from these models can break down under certain "complex flow" conditions. One of the shortcomings of the k-ε model is that it does not allow for the transport effects on the Reynolds stresses (eg. $\overline{uv}$). Rodi (1976) proposed an extension to the k-ε model to help introduce these transport effects. The extension proposed by Rodi effectively converts the k-ε model into an *Algebraic-Reynolds-Stress* (ARS) model. Experiments have also indicated that the Reynolds stresses $\overline{uv}$ and $\overline{v^2}$ may be decreased in the proximity of walls, and that this can decrease the spreading rate of wall jets. Ljuboja and Rodi (1980) have proposed a similar ARS model which allows these wall-damping effects to be predicted.

Another significant advance in turbulence modelling has been the development of *Multiple-Time-Scale* (MTS) models (Hanjalić, Launder, and Schiestel, 1979). MTS models are similar to the k-ε model, except that they require the solutions of four transport equations, rather than the customary two associated with the standard k-ε model (i.e. Eqs. 4 and 5). The MTS model proposed by Hanjalić et al. also included a dissipation equation which was *sensitized to irrotational strains*. Such a modification is often beneficial in flows with adverse pressure gradients. Fabris, Harsha and Edelman (1981) have indicated that MTS models are probably the best available for scramjet-combustor calculations.

The third model tested (which will be referred to as the ARS-MTS model) was effectively a hybrid model which incorporated the ARS and MTS ideas together. Full details of this model, and the model constants used, are available in Brescianini (1992).

Because all three models were being used in highly-compressible flows, compressibility corrections were also applied to each model. For the MLH model, the compressibility correction suggested by Kim (1990) was adopted. For both the k-ε and ARS-MTS models the correction suggested by Brescianini (1991) was adopted. Predictions obtained with these "corrected" models have been found to agree well with compressible-free-shear-layer data taken in conventional wind tunnels, however, their performance in high-enthalpy flows remains relatively unexplored.

The fluxes of heat and shear-stress to the walls of the scramjet were evaluated using *wall functions*. The wall functions used were similar to those developed by Spalding (1977), except that they were extended to account for the compressible flow.

TEST CONDITIONS

The scramjet test condition used corresponded to an actual scramjet experiment performed in the T4 shock tunnel at the University of Queensland, and reported in Brescianini and Morgan (1992). In this earlier scramjet study, four numerical/experimental test cases were examined, with the numerical simulations being based on a k-ε model. Three of the test cases were found to give quite satisfactory agreement, however, a fourth condition (namely Run 697) was not predicted so well. As a result, it was decided to concentrate on Run 697 for this current study to see if the predictions were substantially altered or improved by using different turbulence models.

A schematic of the constant-area scramjet engine used to perform the experiment is shown in Fig. 1. The main-stream flow within the combustion chamber consisted of a Mach 3.6 air stream, with a static temperature of 1500 K, and static pressure of 40 kPa. Hydrogen fuel was injected from a step along the wall of the model with a stagnation pressure of 357 kPa, stagnation temperature of 300 K, and a fuel/air equivalence ratio of 1.5. The model was essentially two-dimensional, with a duct height of 25 mm and a fuel-injector step height of 5 mm. A lip of 2.25 mm was present on the wall injector. This lip could not be modelled with the Parabolic Navier-Stokes (PNS) code used in the current study, and as a result, the initial hydrogen fuel was assumed to expand to the full hydrogen step height. In view of the modeling assumptions required near the thick lip, the initial boundary layer on the injector was also ignored. The two-dimensional, supersonic-combustion program developed by Brescianini (1992) was used to compute the flow field, and the finite-rate hydrogen/air chemistry was modelled using the *basic hydrogen/air mechanism* and the *nitrogen-oxides supplement* recommended by Oldenborg et al. (1990). The effects of turbulence on the chemical reaction rates were not considered.

RESULTS

Figure 2 compares the numerically predicted pressure distributions along the wall of the model which contains the fuel injector. None of the models predict the experimentally noted wave structure correctly, however, a large part of this discrepancy may be due to the thick lip on the injector. Flow visualisation was not available during the experiments, and hence the true source of the waves within the scramjet was difficult to identify. The large wave structure present in the numerical results is due to the initial mismatch in the hydrogen/air static pressures ($p_{H2}/p_{AIR} = 0.2$) at the injector step.

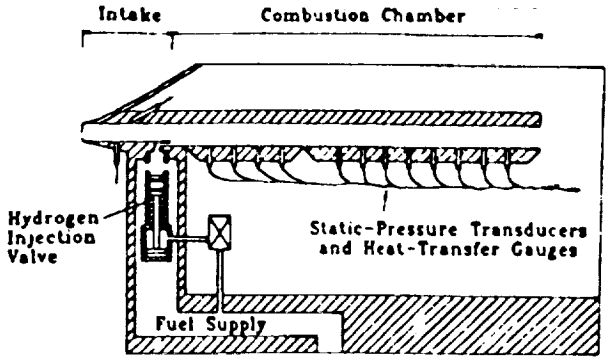

Fig. 1 Schematic of scramjet model.

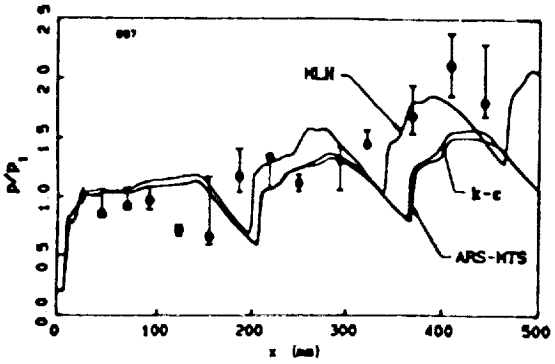

Fig. 2 Pressure variation along wall of scramjet.

The MLH model clearly predicts a significantly higher pressure rise than either the k-ε model or the ARS-MTS models. Between x = 200-300 mm, the MLH model over-predicts the experimental pressures, however, towards the rear of the duct the MLH predictions are in quite good agreement with the experiments.

The k-ε and ARS-MTS predictions are very similar. The pressure rises predicted in the centre of the duct are in good agreement with the experiments, however, towards the rear of the duct the predicted pressures fall short of the experimental pressures.

The Stanton-number predictions obtained with the three models are shown in Fig. 3. The MLH model clearly predicts the highest heat-transfer rate, with the heat-transfer rate near the injector being significantly larger than the experimental measurements. Around the x=200 mm position, however, the numerical and experimental heat-transfer rates are quite similar. In comparison, the k-ε model predicts the initial heat-transfer rate, and the film-cooling length, quite successfully, however, further downstream the heat-transfer rate is significantly under-predicted.

It should be noted that the predicted heat-transfer rate obtained with the k-ε model near the injector is quite sensitive to the initial turbulent length scale ($\ell_\varepsilon = C_\mu k^{3/2}/\varepsilon$). It is possible to improve the heat-transfer prediction at the x = 200 mm station by increasing the initial value of ℓ_ε, but only at the expense of the film-cooling-length prediction. The value of ℓ_ε/H_j which was adopted here (namely, 0.002), as well as the initial turbulence levels, were the same as those used in Brescianini and Morgan (1992). In a similar fashion, the film-cooling length predicted by the MLH model could be improved by decreasing λ, but only at the expense of the downstream heat-transfer and pressure predictions.

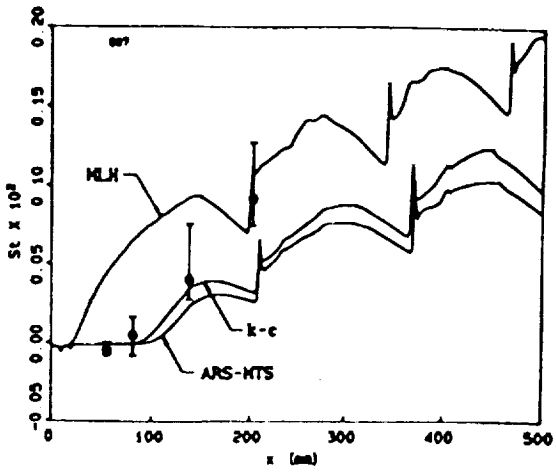

Fig. 3 Stanton-number variation along wall of scramjet.

For the ARS-MTS model, an initial length scale was chosen which was identical to the k-ε model. It can be seen that the Stanton number predictions obtained with the ARS-MTS and k-ε models are very similar, with the ARS-MTS predictions being only slightly lower.

Two of the major parameters of interest in the scramjet, namely the *mixing* and *reaction-rate efficiencies*, are shown in Fig. 4. (The mixing efficiency is defined here as the amount of reacted hydrogen if all mixed hydrogen reacted completely, divided by the same quantity if mixing had been complete. The reaction-rate efficiency is defined as the reacted hydrogen, divided by the amount of reacted hydrogen if the hydrogen which has mixed with oxygen reacted completely). It can be seen that the MLH model has predicted a significantly larger amount of mixing than either the k-ε model or the ARS-MTS models. However, what is also important is the fact that all three models predict the fuel/air mixing to be far from complete by the time the flow has reached the end of the duct. This is in general agreement with the results obtained by Brescianini and Morgan (1992). In comparison to the mixing efficiencies, the reaction-rate efficiencies shown in Fig. 4 are virtually identical for all the turbulence models. This shows that a change in the fuel/air mixing rate has not affected the overall reaction rate.

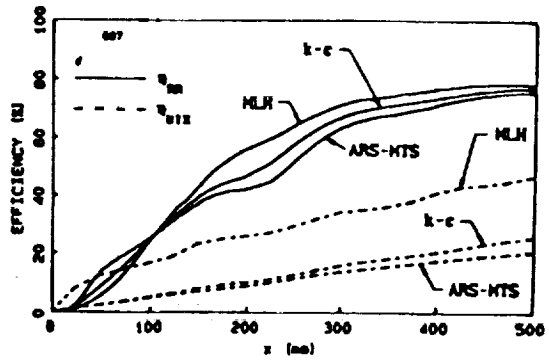

Fig. 4 Mixing and reaction-rate efficiencies along length of scramjet.

CONCLUDING REMARKS

Three turbulence models of varying sophistication were compared in a supersonic scramjet flow. A significant difference between the MLH model and the k-ε model was noted. The k-ε results and the ARS-MTS results also differed, but by a much smaller extent. The MLH model predicted the highest mixing rate, while the ARS-MTS model predicted the lowest. All models showed that the fuel/air mixing rate was insufficient to produce complete mixing within the given length of combustion chamber. None of the models appeared to predict the experimental results accurately over the entire length of model. The k-ε and ARS-MTS models appeared to give the best results near the injector, however, further downstream the MLH model appeared to perform better. The reasons why none of the models appears to be completely satisfactory over the entire model length is uncertain at this stage, although transition-to-turbulence effects, and also the injector's thick lip, are possible explanations.

ACKNOWLEDGEMENTS

The authors gratefully acknowledge the support given by the Australian Research Council and by the NASA Langley Research Center, Hypersonic Propulsion Branch, through NASA Grant NAGW-674.

REFERENCES

BRESCIANINI CP (1991) A modified k-ε model for compressible shear flows. Accepted for publication in the AIAA Journal.

BRESCIANINI CP (1992) An investigation of the wall-injected scramjet. Ph.D. Thesis. Dept. of Mechanical Eng., University of Queensland.

BRESCIANINI, CP and MORGAN, RG (1992) An investigation of a wall-injected scramjet using a shock-tunnel. AIAA 17th Aerospace Ground Testing Conference. Nashville, Tennessee. July 6-8. AIAA Paper 92-3965.

FABRIS, G, HARSHA, PT, and EDELMAN, RB (1981), Multiple-scale turbulence modeling of boundary layer flows for scramjet applications. NASA CR-3433.

HANJALIĆ K, LAUNDER BE, and SCHIESTEL R (1979), Multiple-time-scale concepts in turbulent transport modeling. Second Symposium on Turbulent Shear Flows. July 2-4, Imperial College, London.

KIM SC (1990) New mixing-length model for supersonic shear layers. AIAA Journal. 28, 1999-2000.

LAUNDER BE, MORSE A, SPALDING DB, and RODI W (1973) Predictions of free shear flow- A comparison of the performance of six turbulence models. Proc. of Free Shear Flows Conference. NASA SP-321.

LAUNDER BE, and SPALDING DB (1974) The numerical computation of turbulent flow. Computer Methods in Applied Mechanics and Engineering. 3, 269-289.

LJUBOJA M, and RODI W (1980) Calculation of turbulent wall jets with an algebraic Reynolds stress model. Journal of Fluids Engineering, 102, 350-356.

OLDENBORG R, CHINITZ W, FRIEDMAN M, JAFFE R, JACHIMOWSKI C, RABINOWITZ M, and SCHOTT G (1990) Hypersonic combustion kinetics. NASP TM-1107.

PRANDTL L (1925) Bericht über untersuchungen zur ausgebildete turbulenz. Z. Angew. Math., Bd. 5, Heft. 2, 136-139.

RODI W (1976) A new algebraic relation for calculating the Reynolds stresses. Zeitschrift Für Angewandte Mathematik und Mechanik, 56, 219-221.

SPALDING DB (1977) GENMIX- A Computer Program for Two-dimensional Parabolic Phenomena. Pergamon Press, Oxford.

11th Australasian Fluid Mechanics Conference
University of Tasmania, Hobart, Australia
14-18 December 1992

SHOCK INTERACTIONS WITH HYPERSONIC MIXING LAYERS - STEADY FLOW ANALYSIS AND EXPERIMENTS

D.R. BUTTSWORTH and R.G. MORGAN

Department of Mechanical Engineering
University of Queensland
QLD 4072, AUSTRALIA

ABSTRACT

Interest in scramjet powered flight has led to the study of shock induced mixing and combustion effects. To provide further understanding of phenomena associated with shock induced mixing and combustion, an experiment investigating the interaction of shock waves and a mixing region was undertaken. Hydrogen was injected parallel to a co-flowing stream of nitrogen, from the base of a central strut injector. Pitot pressure measurements were taken within the mixing region. After the pitot rake was removed, static pressure measurements were made downstream of the shock wave mixing layer interaction on the surface of 3 different shock inducing wedges. The flow was turned through angles of 5, 10, or 15 degrees with these wedges. Theoretical calculations of the static pressure were performed using a shock interaction model based on the time average flow properties, and the results from the pitot survey. Agreement between the theoretical model and experimental results was reasonable, but more data is required to fully validate the shock interaction model, and to demonstrate its usefulness in understanding the processes of shock induced mixing.

INTRODUCTION

If hypersonic flight using scramjet (supersonic combustion ramjet) propulsion is to be realized, the problem of significantly enhancing supersonic mixing and combustion must be solved. The scramjet is an airbreathing concept which requires the injection of fuel (usually hydrogen) into the high speed air stream entering the engine. The fuel is resident within the engine for only short periods of time and must mix and burn rapidly in order to produce the required thrust. Unfortunately, supersonic flow is not conducive to rapid mixing. It has been known for some time that mixing can be profoundly influenced by compressibility effects (Papamoschou and Roshko, 1988). Therefore, methods to enhance the mixing rates in supersonic flows are currently being sought.

The impingement of shock waves on mixing regions has received some attention as a candidate method for improving the mixing in supersonic streams. Varying degrees of shock induced mixing augmentation have been observed in recent supersonic mixing layer experiments (e.g., Hyde et al., 1990, Sullins et al., 1991, and Roy, 1991). Based on a survey of previous literature, Kumar et al. (1989) state that through the interaction of turbulence and shock waves, the turbulence and mixing may be amplified by a factor of 2 to 5. Numerical studies of their own (presented in the same paper) suggest that an oscillating shock wave may also provide efficient mixing enhancement. However, fluctuations in either the pre-shock flow or the shock itself are not essential for mixing augmentation. Jacobs (1992) experimentally demonstrated the mixing enhancement resulting from shock wave impingement on a cylindrical gas region of lower density. Additionally, it is well known that vorticity is generally discontinuous across a shock wave in steady compressible flow (e.g., Hayes, 1957).

It is evident therefore that the passage of a shock wave may influence mixing through modifications to both the fluctuating and steady flow properties. Fluctuations associated with the interaction process have been dealt with previously (e.g. Kumar et al., 1989), however, there is a paucity of research treating the interaction process on a time average level. Therefore, the true influence of the fluctuating flow properties cannot be fully assessed. In the current study, theoretical modelling of the interaction process is achieved using a simple steady flow shock interaction analysis. It is felt that a steady flow analysis of a shock mixing region interaction provides a useful benchmark for assessing the influence of unsteady turbulence effects, and gives good physical insight into the shock propagation process. Experimental investigations of shock wave interactions with mixing regions were performed using a central strut injection model, in conjunction with a shock tunnel facility.

INTERACTION MODEL

The current interaction model is based on steady flow properties ahead of the shock wave. No interaction between fluctuating quantities and the shock is treated with this approach. A stable oblique shock wave generated by a straight wedge, which does not decelerate the flow to subsonic velocities, is assumed. Since mixing typically occurs slowly under supersonic conditions, a non-uniform distribution of properties is likely within a supersonic mixing layer. The mixing region ahead of the shock wave is treated as unidirectional with a uniform pressure, and is modelled using the distribution of the steady Mach number alone. A constant value for the ratio of specific heats is also assumed to exist across the mixing region. Modelling of the shock wave is achieved using the Rankine-Hugoniot relations (Liepmann and Roshko, 1957).

Consider the situation depicted in Fig. 1a. By employing the conditions of matched pressure and flow direction on either side of the dividing streamline, it is possible to derive an expression describing the propagation of the shock wave in the variable Mach number region. This expression takes the form,

$$\frac{\partial\theta}{\partial M_1} = f_1(M_1, \theta) \qquad (1)$$

The function $f_1(M_1, \theta)$ is analytic, but quite complicated and will not be further detailed in the current paper. The Mach number distribution ahead of the shock is the initial factor causing the shock wave to change direction. However, further shock curvature may arise due to the nonuniform pressure field behind the shock resulting in isentropic waves impinging on the shock wave from behind, Fig. 1b. In this case, the equation which describes the effect on the shock wave shape takes the form,

$$\frac{\partial\theta}{\partial\alpha} = f_2(M_1, \theta) \qquad (2)$$

Again, the function of M_1 and θ is analytic, but will not be further defined in the current paper. If the distribution of Mach number and the strength of the waves impinging on the shock from behind are known, the shock wave shape through the mixing region may be calculated. The change in shock direction will then be given by

$$d\theta = f_1(M_1, \theta)\, dM_1 + f_2(M_1, \theta)\, d\alpha \qquad (3)$$

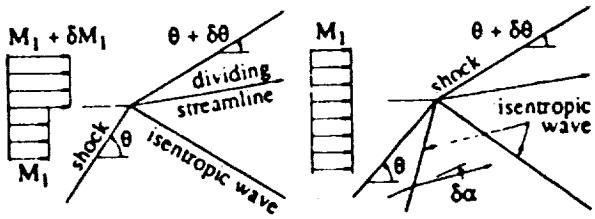

a) Primary shock curvature. b) Secondary curvature effects.

Fig. 1 Shock wave interaction model.

A method of characteristics solution was used to implement Eqn (3). Calculations begin with the solution of the Rankine-Hugoniot shock relations at the leading edge of the shock-inducing wedge. The Mach number distribution, the wedge angle, and the ratio of specific heats are the only parameters necessary for solution of this problem. Steps of equal size are taken across the Mach number distribution, and Eqn (3) is employed at each calculation point on the shock wave to find the new shock angle.

EXPERIMENT

Facility

An experiment investigating reflected waves generated by the oblique shock as it passes through the mixing region (with the general arrangement given in Fig. 2) was performed in the T4 free piston shock tunnel facility at the University of Queensland (Stalker and Morgan, 1988). A contoured nozzle, nominally designated "Mach 5," was used to accelerate the stagnated test gas to the required flow conditions. For the present experiments, the tunnel was operated using an argon driver at a volumetric compression ratio of 60 with a 2 mm mild steel primary diaphragm. The shock tube was filled with nitrogen to 100 kPa. An example of the stagnation pressure signals recorded at this condition is presented in Fig. 3. A relatively low enthalpy condition was chosen for the present study (Table I), so that the velocity of the shock tunnel and the injected streams would be approximately equal. It was thought that matched velocities would simplify description of the mixing region, and that the shock interaction process for such a region would be amenable to solution via the steady flow interaction model. At this condition, a conservative estimate (Gourlay, 1992) based on the analysis of Stalker and Crane (1978) suggests that 3 ms of test time should be available prior to driver gas contamination.

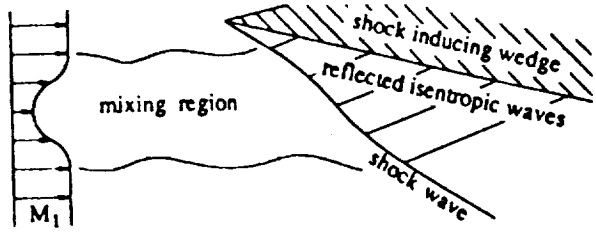

Fig. 2 Schematic of experimental arrangement.

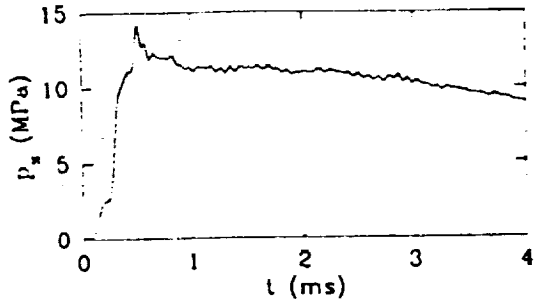

Fig. 3 Example of shock tube stagnation pressure.

An estimation of the flow conditions generated by the tunnel was achieved through a two stage calculation process. From the shock tube filling conditions, the measured shock speed and stagnation pressure, the conditions at the end of the shock tube (the nozzle supply conditions) were calculated with a equilibrium shock tube calculation, ESTC (McIntosh, 1968). These conditions were then used in a nonequilibrium nozzle flow calculation, NENZF (Lordi et al, 1966). The nozzle flow expansion calculation was continued until the measured pitot pressure was reached.

Table I Initial primary and secondary stream conditions.

Parameter	Primary Stream (nitrogen)	Secondary Stream (hydrogen)
H_o (MJ/kg)	3.05	4.24
M	6.42	2.68
p (kPa)	3.18	5.13
u (km/s)	2.33	2.24
T (K)	317	121
ρ (kg/m^3)	0.0338	0.0102

Model and Instrumentation

A rectangular duct, 164 mm high and 80 mm wide (Fig. 4) was located at the nozzle exit plane. Hydrogen was injected through a contoured nozzle (Fig. 5) from the base of a central strut which had a thickness of 5.38 mm. The hydrogen was supplied to the injector by a Ludwieg tube and fast acting valve combination (Morgan and Stalker, 1983). An asymmetric design for the leading edge of the strut injector was chosen to facilitate spillage of the shock away from the primary shock inducing wedge. Using gas dynamic relations, the pressure mismatch caused by the asymmetry of the strut was estimated to be less than 0.1 %. The contoured

nozzle was designed using a method of characteristics. During the experiments, attempts were made to match the static pressure of the injected flow with that of the shock tunnel flow. To this end, a pitot rake was set up at the exit of the injector nozzle, and the Ludwieg tube was fired at a number of different filling pressures without running the shock tunnel. Using the area ratio of the nozzle, and the average pitot pressure over the nozzle distance surveyed, Fig. 6, a condition was chosen which approximately matched the calculated static pressure supplied by the shock tunnel. However, on re-examination of the results, it was found that the injection condition was probably under-expanded (see Table I).

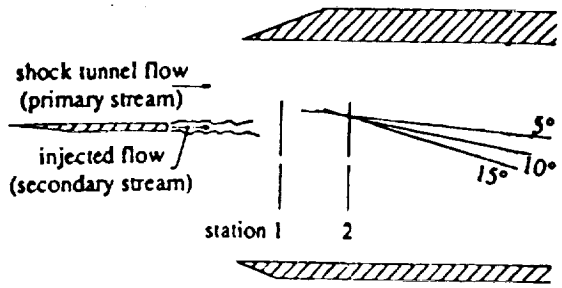

Fig. 4 Experimental model.

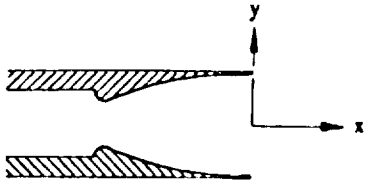

Fig. 5 Sketch of the injector nozzle.

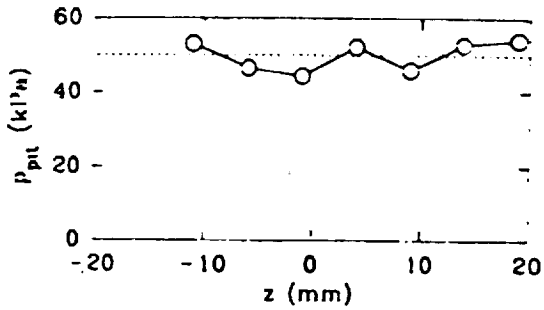

Fig. 6 Pitot pressure at exit of injector nozzle.

Three different wedges were employed to compress the mixing region through 5, 10, and 15 degrees. Eleven pressure transducers were mounted on each of the wedges, in two streamwise rows 4 mm either side of the centreline of the wedge. The transducer spacing along both rows was 8 mm. To investigate the distribution of flow properties, a 7 probe pitot rake with a 5 mm spacing between the probes, was utilized.

RESULTS

Pitot Survey

Two pitot surveys at the stations shown in Fig. 4 were made over a number of runs. (An example of the pitot pressure histories obtained from the probe are presented in Fig. 7.) To implement the model of the interaction process, a knowledge of the Mach number distribution ahead of the shock is necessary. The assumption of a constant static pressure across the width of the pitot survey permits easy calculation of a Mach number distribution from the measured pitot pressures using the Rayleigh supersonic pitot relation (Liepmann and Roshko, 1957). The Mach number distributions calculated from the pitot pressures are presented in Fig. 8. The value of static pressure assumed for the Mach number calculations was 3.18 kPa (the static pressure in the undisturbed primary stream). This is a reasonable assumption since, at the second station, the pressure was calculated to be within 3 % of 3.18 kPa across the width of the survey, for the initial mismatch of pressures given in Table I.

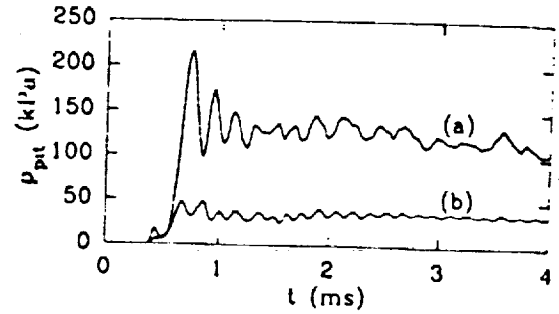

Fig. 7 Sample pitot pressure signals from a probe a) in the shock tunnel flow, and b) near the centre-line of the injected flow.

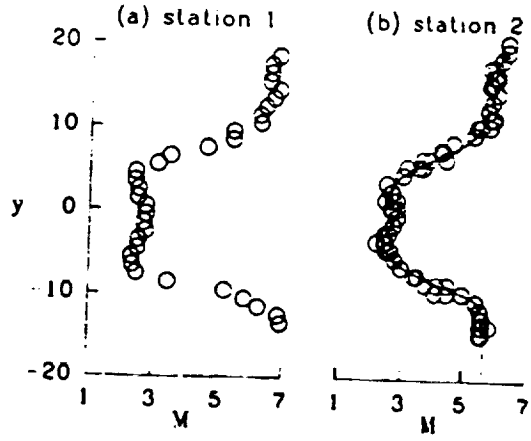

Fig. 8 Calculated Mach number distributions from pitot pressure results.

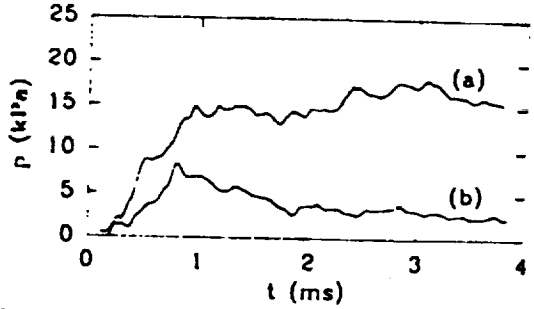

Fig. 9 Static pressure signals from the transducer midway along the matrix, 10 degree case. a) injector removed, shock tunnel flow only. b) shock tunnel plus injected flow.

Static Pressure

In order to test the shock interaction model, measurements of the pressure along the 5, 10 and 15 degree turning angle wedges were obtained. Signals from the transducer midway

along the transducer matrix in the 10 degree wedge are presented in Fig. 9. For each of the transducers, results obtained with hydrogen injection (e.g. Fig. 9b) were normalised using the signals obtained with the injector removed (e.g. Fig. 9a). Normalization in this manner, provides a degree of compensation for non-uniformities present in the nozzle flow and arising through shock wave boundary layer interactions. The mean levels for the 11 normalized signals over a time period from 2 ms to 3 ms (for the time base displayed in Fig. 9) are presented in Fig. 10. The standard deviations of each signal over the same time interval are represented by the bars given in Fig. 10.

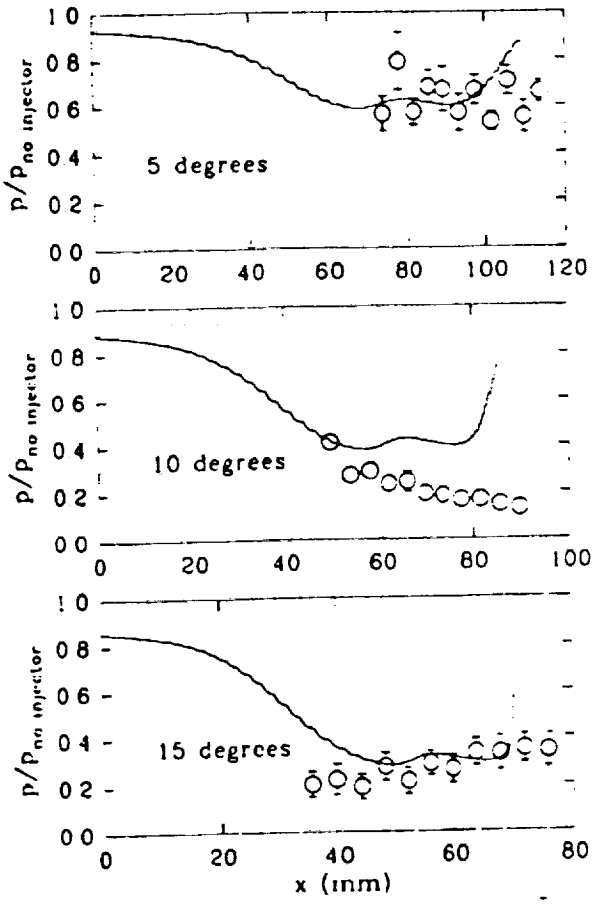

Fig. 10 Normalized static pressure results. ○ = experimental results. ~ = results from theoretical model.

By assuming the Mach number distribution (Fig. 8b) inferred from the pitot pressure at station 2, the appropriate wedge turning angle, and that $\gamma = 1.4$, it was possible to apply the shock interaction model. The solid lines given in Fig. 10 are the results from the model, calculated using the method of characteristics solution described briefly in a previous section.

CONCLUSIONS

Examination of Fig. 10 indicates that there appears to be some agreement between the theoretical model and the experimental results. Unfortunately, the experimental Mach number distribution was much broader than anticipated, resulting in a clustering of transducers near the bottom of the dip in the pressure distribution. The lowest pressure experienced on the wedge is in reasonable agreement with the theoretical model, except for the 10 degree turning angle case. The current interaction model is limited to conditions of uniform pressure and flow direction ahead of the shock wave. Furthermore, the Mach number distribution used in the theoretical model was obtained from a single streamwise location (station 2, Fig. 4), whereas the mixing region would have developed over the length required for the shock to traverse the mixing layer. More data will be required to validate the current model and assess the influence of fluctuating properties on the interaction process.

Further experiments are planned in which attempts will be made to more closely match the static pressure in each stream. The development of the mixing layer will be closely monitored using the pitot rake at a number of streamwise locations. In addition, the distribution of the transducers in the shock inducing wedge will be altered in an attempt to detect the spacial form of the changes in static pressure.

REFERENCES

GOURLAY, C M (1992) Private correspondence.

HAYES, W D (1957) The vorticity jump across a gasdynamic discontinuity. J Fluid Mech. 2, 595-600.

HYDE, C R, SMITH, B R, SCHETZ, J A and WALKER, D A (1990) Turbulence measurements for heated gas slot injection in supersonic flow. AIAA J. 28, 1605-1614.

JACOBS, J W (1992) Shock-induced mixing of a light gas cylinder. J Fluid Mech. 234, 629-649.

KUMAR, A, BUSHNELL, D M and HUSSAINI, M Y (1989) Mixing augmentation technique for hypervelocity scramjets. J Propulsion and Power. 5, 514-522.

LIEPMANN, H W and ROSHKO, A (1957) Elements of Gasdynamics. John Wiley & Sons, New York, NY.

LORDI, J A, MATES, R E and MOSELLE, J R (1966) Computer program for the numerical solution of nonequilibrium expansion of reacting gas mixtures. NASA CR-472.

McINTOSH, M K (1968) Computer program for the numerical calculation of frozen and equilibrium conditions in shock tunnels. Report, Dept Physics, Australian National University, Canberra.

MORGAN, R G and STALKER, R J (1983) Fast acting hydrogen valve. J Phys E: Sci Instrum. 16, 205-207.

PAPAMOSCHOU, D and ROSHKO, A (1988) The compressible turbulent shear layer: an experimental study. J Fluid Mech. 197, 453-477.

ROY, G D (1991) Subsonic and supersonic mixing and combustion enhancement. ISABE Paper 91-7093.

STALKER, R J and CRANE, K C A (1978) Driver gas contamination in a high-enthalpy reflected shock tunnel. AIAA J. 16, 277-279.

STALKER, R J and MORGAN, R G (1988) Free piston shock tunnel T4 - initial operation and preliminary calibration. NASA CR-181721.

SULLINS, G A, GILREATH, H E, MATTES, L A, KING, P S and SCHETZ, J A (1991) Instabilities in confined supersonic mixing layers. ISABE Paper 91-7097.

A Time-Of-Flight Mass Spectrometer for High Speed Flows

K. A. Skinner and R. J. Stalker

ABSTRACT

A time-of-flight mass spectrometer has been constructed to measure time resolved concentrations of gas molecules present in hypersonic, high enthalpy flows. Sampling is achieved in-situ by forming a molecular beam from the flow using a compact series of 3 hollow conical skimmers. Ionization of molecules in the molecular beam by a repetitively pulsed electron beam allows many mass spectra to be obtained during the test flow of an impulse facility, effectively giving a time history of species concentrations. The instrument has been used in a free piston reflected shock tunnel flow and has demonstrated detection of all species present at levels higher than 2% in the flow, allowing measurement of relative concentrations of major molecular species.

INTRODUCTION

At present, impulse facilities such as shock tunnels and expansion tubes are the only practical ground-based means of simulating aerodynamic conditions at speeds in excess of 2.5 km/s. The duration of test flow however, is only about a millisecond, requiring special instrumentation. It is especially desirable to measure species concentrations in the test flow since the chemical state of the test gas may be altered by the high transient temperatures produced. Also, the flow of test gas in a reflected shock tunnel is followed by a flow of driver gas, usually of a different composition. The breakdown of the interface between these two gas slugs causing mixing of the driver and test gases limits the available test time. Measurements of species concentrations are the most sensitive method of determining the duration of test flow and in the past have been the basis of most estimates[1]. Furthermore, studies of supersonic combustion ramjets have, to date, primarily relied on pressure and heat transfer measurements to infer the behaviour of the fuel-air mixing and reaction rates. Profiles of species concentrations downstream of a fuel jet injected into a hypersonic airstream would be a more sensitive measure of the appropriate values of mixing rates, ignition delay times and reaction rates for modeling supersonic combustion.

A quadrupole mass spectrometer was used by Crane and Stalker[2] in a reflected shock tunnel. They used a two stage hollow conical skimmer gas sampling system. The short duration of the flow meant that the ions from only a single species of molecule could be recorded during each test flow. To obtain relative concentrations, Crane and Stalker relied upon sampling multiple test flows and measured the total ion production each shot for

normalization. This method assumed repeatability of the test flow and of the behaviour of the mass spectrometer despite variations in total ion production. They estimated errors in their relative species concentration measurements of 30%.

EXPERIMENTAL DESIGN

The instrument reported here was designed for use in T4, an existing free piston reflected shock tunnel[3]. At the upstream end are three co-axial, hollow conical skimmers used to sample the flow. (Figure 1). Behind the second and third skimmers are vacuum chambers evacuated by diffusion pumps. There is no vacuum chamber behind the first skimmer as the flow through it vents back out into the free stream flow. Gas passing through the skimmers is expanded and collimated into a molecular beam entering the interior high vacuum chamber. 20 mm behind the final skimmer, an electron beam intersects the molecular beam, causing ionization of some molecules. The ions produced are accelerated along a metre long flight tube to an electron multiplier particle detector. The signal from this particle detector is recorded on a digital storage oscilloscope.

Extraction of gas samples by forming a molecular beam from a continuum flow is a technique developed in the 1950-60's[4][5][6]. Ideally, the axial streamtube experiences no disturbance other than the strong expansions inside each skimmer. In practice, as the flow expands from continuum to free molecular, there is interference from flow particles reflecting off the outside (for large half-angles) or the interior (for small half-angles) of the skimmer. These particles can penetrate the beam and scatter the undisturbed particles. Bird[7] examined the effect of Knudsen number and skimmer geometry on molecular beam interference using a Monte-Carlo method and concluded that with correct design the interference can be negligible. Correct design consists of short skimmers, a lip radius much less than the orifice diameter and a Knudsen number based on orifice diameter outside the range of 0.1 to 2. The Knudsen number at the third skimmer is approximately 50 and the length of the skimmer is less than half the length of that studied by Bird. Very little interference from the third skimmer was expected.

A further influence on the sample is that an expansion of a mixture of gases to free molecular flow can cause a relative depletion of lighter particles on the axis. Sebacher[8] and Sherman[9] suggest that diffusion in the strong pressure gradients near the start of the expansion inside the skimmer is the mechanism responsible. The work of Fenn and Anderson[10] indicates scattering from background molecules penetrating the flow after the beam has translationally frozen as the cause. Either explanation allows for a variation with mass ratio - the latter allows

for an additional variation with molecular diameter. Whatever the physical situation, the state of knowledge about the process is not sufficient to make purely theoretical corrections to species concentrations and thus calibration is required to account for its effect.

An essential aspect of the success of the instrument is that the production of the molecular beam be achieved as quickly as possible. The front skimmer served to both decrease the density and increase the Mach number of the flow entering the second skimmer. After the initial strong expansion, further increases of the inter-skimmer distance had diminishing effect on the density. The second skimmer samples this expanded flow on the axis. Off-axis flow passes around the second skimmer experiencing a normal shock recovery of pressure to a stagnation pressure higher than the free stream static pressure. This flow can then vent back out into the free stream. For an incident Mach number of 5.5, the recovery shock Mach number is at least 10.8 for a ratio of specific heats from 1.3 to 1.4. The maximum inter-skimmer distance was then found from a method of characteristics calculation. This gave the density at the second skimmer as 0.03 times the free stream density. To produce the fastest possible expansion, the orifice diameter of the second skimmer was chosen to be as small as practicably manufacturable (0.5 mm). The third skimmer colimates the flow 40 mm behind the second skimmer. Approximate calculations give the density in the molecular beam as 0.0001 times the free stream density. For a free stream test flow of air at 0.05 kg/m^3 and an enthalpy of 9 MJ/kg, (typically a low density shot) the expansion through the skimmers results in a molecular beam density of 5×10^{-6} kg/m^3, or a flux of 10^{11} particles/mm^2/μsec. The production of this beam is achieved in a distance of 75 mm with an external diameter of the skimmers of only 50 mm. This is small enough to allow the probe access to complex flow fields such as scramjet nozzles, a region inaccessible to optical methods of species measurement.

Mass Separation

Separation of different mass components of the molecular beam is achieved with an ion time-of-flight system[11]. An electron beam intersects the molecular beam 20 mm behind the third skimmer. This region is held at a potential above ground by a surrounding cylindrical electrode co-axial with the drift tube. The potential gradient within the intersection region is set by adjacent co-axial electrodes at the either end (see figure 1). The electron beam is formed by accelerating electrons emitted from a 6W tungsten filament through a gate electrode, through a 2 mm diameter hole in the side of the central cylindrical electrode. The electron gun can be pulsed on for 200 nsec,

producing a beam of 1 to 2 mAmps. The beam diameter is estimated as 3 mm from an analysis using a charged particle trajectory simulation program SIMION[12]. The ions are formed at a potential of 250 V in a field gradient of 20 V/mm, which for a 3 mm beam diameter gives an energy spread of +/-12%.

After ionization, the ions are accelerated down a potential field gradient to a field-free drift region 1m long. The flight time, t, along this region depends on the mass simply as:

$$t = L\sqrt{\frac{m}{2qE}}$$

where L is the length of the drift region, m/q is the mass to charge ratio and E is the energy given to the ion. As the ions are produced in a field gradient, the spatial variation in the electron beam causes a variation in energy of the ion beam. This causes a proportional arrival time spread. The electron gun was pulsed on for 200 nsec every 0.055 msec, producing a packet of ions which were then detected and recorded on a storage oscilloscope. The oscilloscope sampled the signal at 10 MHz for 6.4 msec, allowing 117 complete spectra to be obtained during each firing of the shock tunnel. The limiting resolution is determined by the sampling rate of the data storage and the degree to which the peaks spread at higher mass numbers because of the energy spread.

CALIBRATION

From the free stream values, the concentrations of the species present are altered by the measurement process in three ways. Firstly, the possibility of light molecule depletion on the axis of the expansion inside the skimmers. This can be expressed as a relative calibration factor, F.

$$\frac{[A]'}{[B]'} = F\frac{[A]}{[B]}$$

where primed quantities are actual concentrations in the molecular beam and unprimed concentrations are values in the free stream which are to be measured. In the molecular beam, the relative number of ions formed for each species is proportional to their ionization cross-section. Hence in the ion beam, the concentrations are given by

$$\frac{[A^+]}{[B^+]} = \frac{\sigma(A)}{\sigma(B)}\frac{[A]'}{[B]'}$$

The efficiency of collection of ions of each species may vary. Again the concentrations can be related by a constant calibration factor, provided external effects such as vacuum level and acceleration potentials are held constant. This leads to a final expression

$$\frac{\text{Measured A}}{\text{Measured B}} = F \times \frac{\sigma(A)}{\sigma(B)} \times C\frac{[A]}{[B]}$$

That is, all effects on the sample are proportional effects, and a single calibration factor is sufficient to describe them all. However it also indicates that where F and C are not unity, calibration using known gas mixtures must be performed. Calibration factors were obtained for mixtures of He-N_2, H_2-N_2, and Ar-N_2. These factors showed no variation with enthalpy or density over the range examined and so were taken to be constant for a particular geometry. For molecules of very similar mass and size, (for example N_2, NO and O_2), F and C were both taken to be unity.

For a diatomic molecule, the dissociative ionization complicates the measurement of pre-dissociated products in the test flow. For example, N_2 molecules produce N atoms under electron impact ionization. The collection efficiency of these atomic nitrogen will be different from pre-existing atomic nitrogen in the test flow because species produced by electron impact dissociation have a random kinetic energy up to the energy of the chemical bond broken. Assumptions then, must be made about the values of F and C for dissociated species.

PERFORMANCE

Figure 2 shows spectra from air test gas at an enthalpy of 9 MJ/kg. The noise in the baseline was generated within the preamplifier. The presence of a peak can often be recognized when the area of the peak is only 2% of the area of the peak of N_2 (typically the largest peak in most flows studied). Measurements of mole fractions of the components of the test and driver gases for this run are shown in Figure 3. These are calibrated using measurements of peak sizes from runs with test gas mixtures of He-N_2 and Ar-N_2 at similar conditions. The composition of the driver gas was known to be 15% Ar-85% He. The independently calibrated measurements of relative concentration arrived at the same ratio. The errors in each data point are approximately 5% absolute.

The instrument was used for 147 shots of the shock tunnel with a turn around time of one and a half hours when all went well. Some difficulty was experienced from charged particles in the free stream flow. These often caused arcing and loss of electric potentials in tests at higher enthalpies and densities. Some success at overcoming this was found with a temporary electrostatic filter ahead of the third skimmer. The tungsten filament and electronics did not suffer overly from the tunnel environment. Vibration did not have any effect and the three skimmers were not physically degraded by the flow.

CONCLUSIONS

The time-of-flight mass spectrometer has been coupled with a compact sampling system to measure species

concentrations in hypersonic flows. The ability to detect molecular species present at levels of only 2% by number has been shown. The current limitation on detection is the background noise generated in the signal preamplifier, which leaves the possibility of a more sensitive instrument. The limitations on measurement are the ability to resolve the peaks, the knowledge of the ionisation cross-section and the ability to calibrate for gas dynamic mass separation of disparate mass particles. When these problems are minimised, the error can be less than 5% for relative concentrations of major species. This is the same level of accuracy that can be achieved by most shock tunnel instrumentation and is superior to other methods of species concentration measurements.

ACKNOWLEDGMENTS

The authors wish to thank The Australian Research Council and NASA grant NAGW-674 for financial assistance.

REFERENCES

1. Crane, K.C. and Stalker, R.J. "Driver gas contamination in a high enthalpy reflected shock tunnel," *AIAA*, Vol. 16, pp. 277-278, 1978.
2. Crane, K.C.A. and Stalker, R.J., "Mass-spectrometric analysis of hypersonic flows," *J. Phys D.*, Vol.10, pp. 679-685, 1977.
3. Jacobs, P.A., "Quasi-one-dimensional modeling of free-piston shock tunnels", *31st Aerospace Sciences Meeting & Exhibit*, Jan 11-14, 1993, Reno, NV, AIAA 93-0352.
4. Kantrowitz, A. and Grey J., "A high intensity source for the molecular beam. Part 1. Theoretical," *Rev. Sci. Inst.*, Vol. 22, p 328-332, 1951.
5. Becker, E.W. and Bier, K., *Z. Naturforsch*, Vol 9a, p 975-986, 1954.
6. Skinner, G.T., "Molecular beam for the study of high-temperature-gas collision processes," *Phys. Fluids*, Vol. 4, p1172-1176, 1961.
7. Bird, G.A., "Transition regime behaviour of supersonic skimmers," *Phys. Fluids*, Vol. 19, pp. 1486-1491, 1976.
8. Sebacher, D.I., "Diffusive separation in shock waves and freejets of nitrogen-helium mixtures," *AIAA*, Vol. 6, No. 1, 1968.
9. Sherman, F.S. "Hydrodynamical theory of diffusive separation of mixtures in a free jet", *Phys Fluids*, Vol. 8, No. 5, pp 773-779, 1965
10. Fenn, J. B. and Anderson, J. B. "Background and sampling effects in free jet studies by molecular beam measurements," *Proceedings of 4th International Symposium on Rarefied Gas Dynamics*, Toronto, Academic Press, New York, pp. 311-330, 1966.
11. Wiley, W.C. and McLaren, I.H. "Time-of-flight mass spectrometer with improved resolution," *Rev. Sci. Inst.* Vol. 26, No. 12, pp.1150-1157, 1955.
12. EGG-cs-7233 Rev. 2 prepared by EG&G Idaho Inc, PO Box 1625, Idaho Falls, ID 83414, USA.

Figure 1. Skinner and Stalker

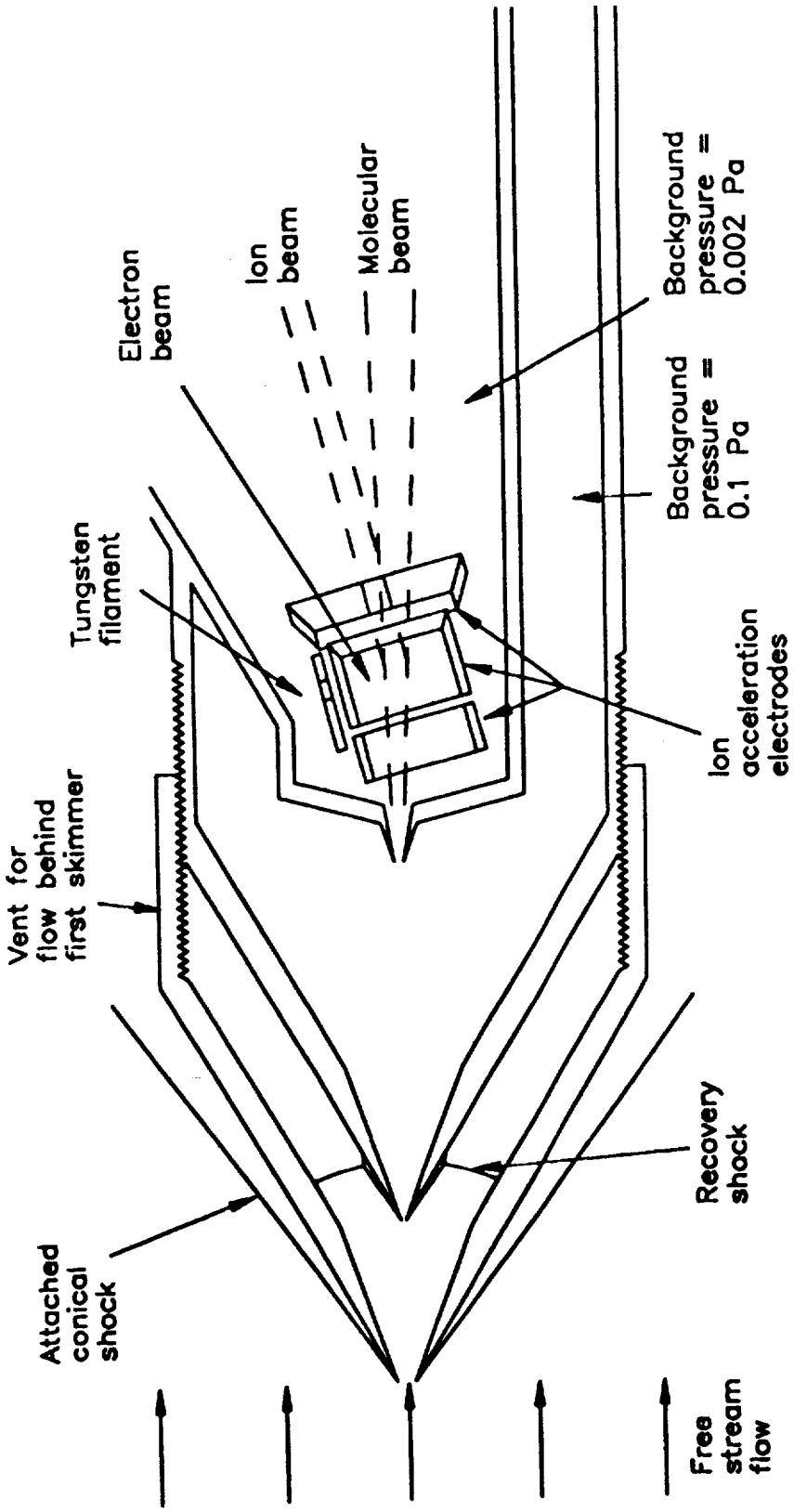

Figure 2 Skinner and Stalker

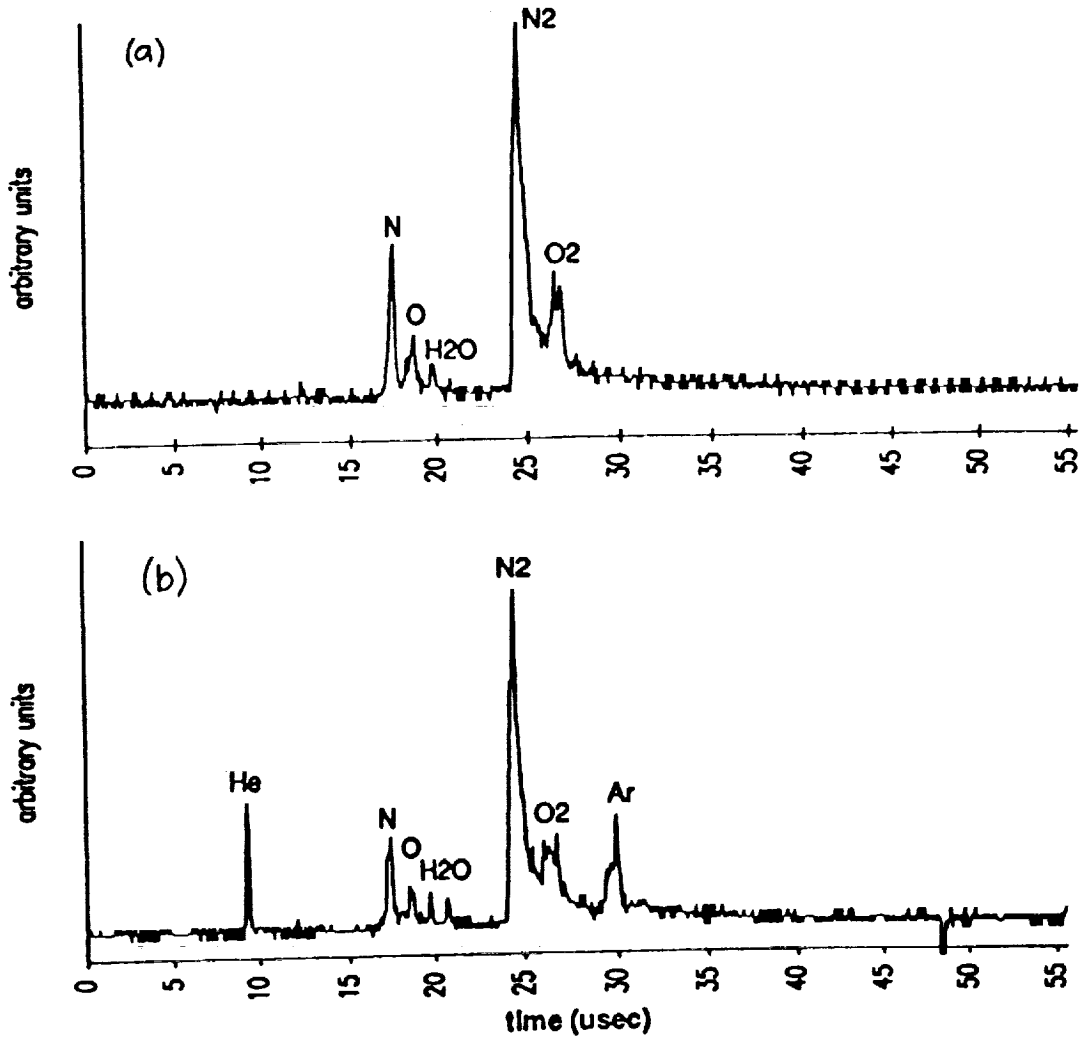

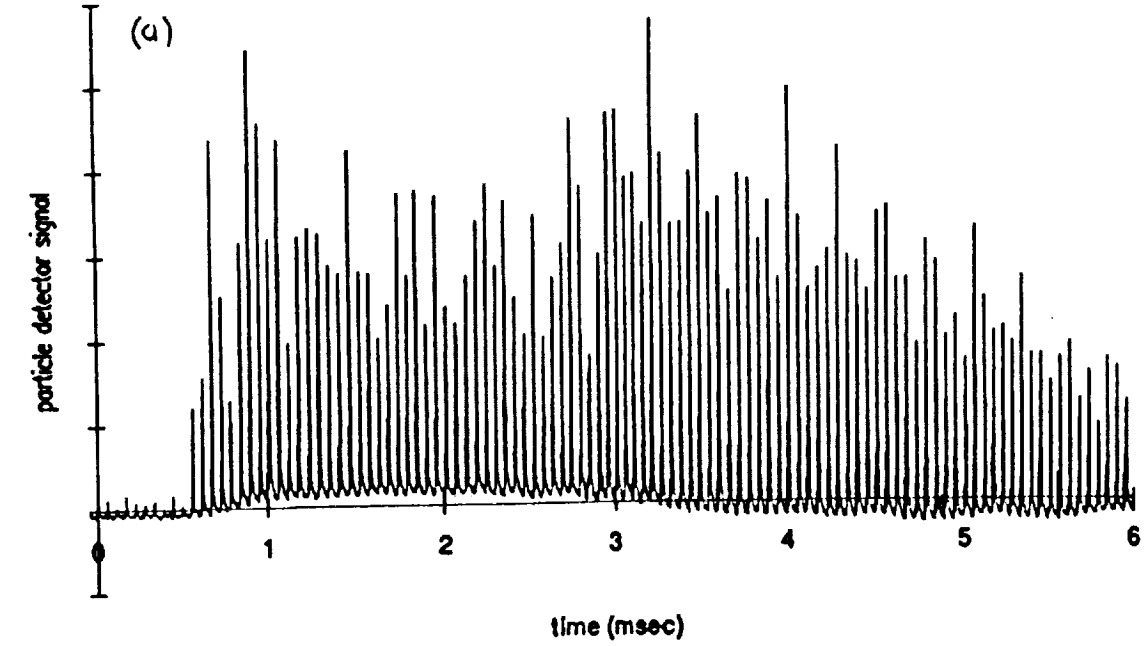
(a)
particle detector signal
0
1
2
3
4
5
6
time (msec)

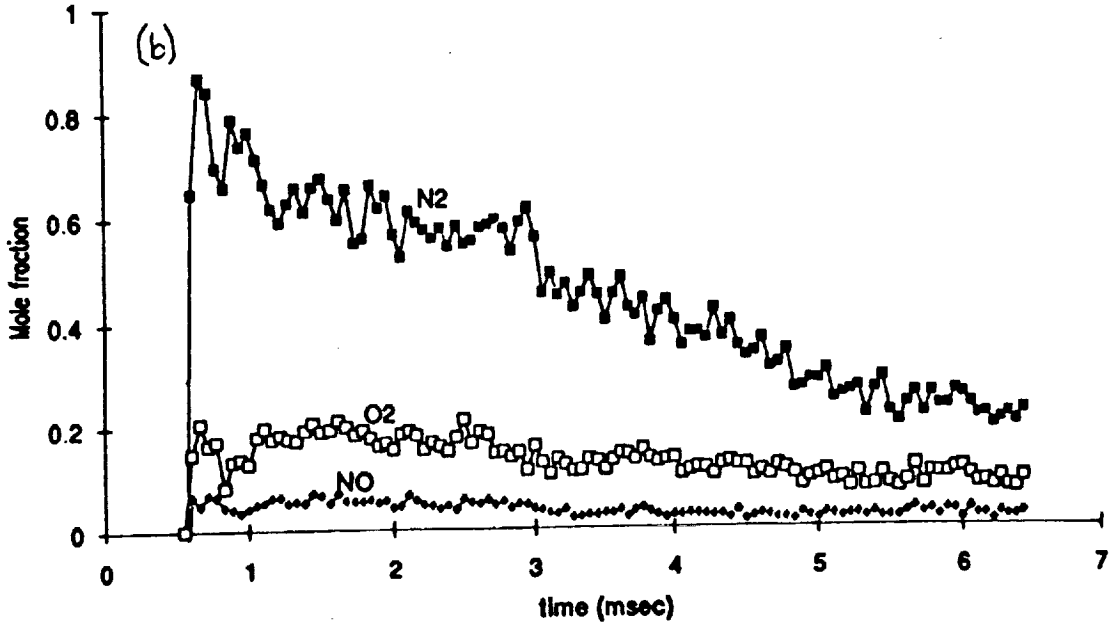
(b)
Mole fraction
0
0.2
0.4
0.6
0.8
1
N2
O2
NO
0
1
2
3
4
5
6
7
time (msec)

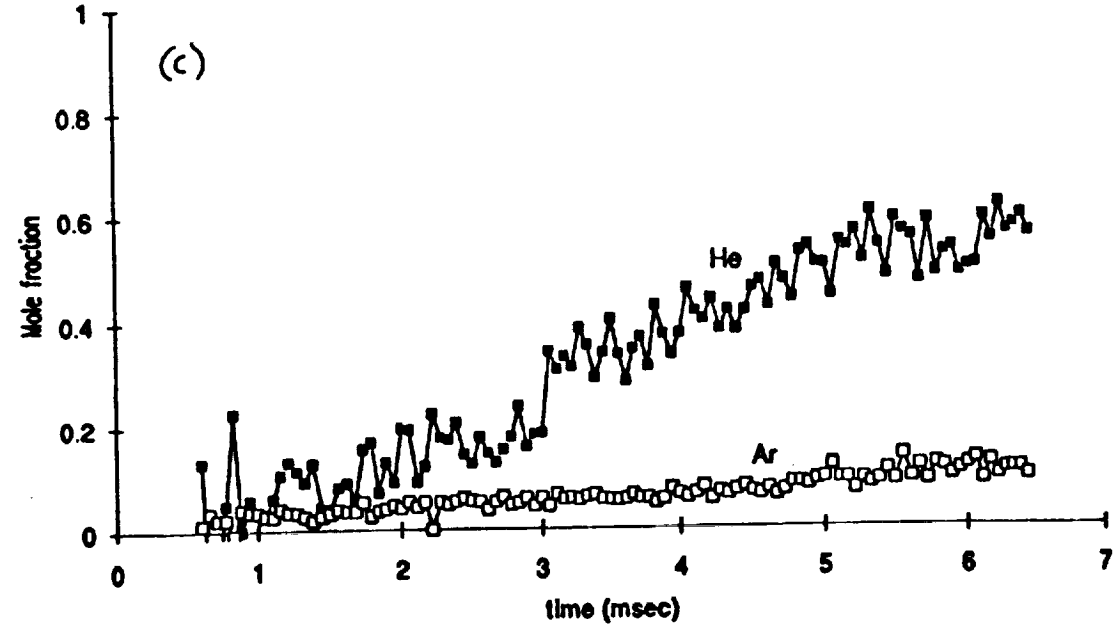
(c)
Mole fraction
0
0.2
0.4
0.6
0.8
1
He
Ar
0
1
2
3
4
5
6
7
time (msec)

11th Australasian Fluid Mechanics Conference
University of Tasmania, Hobart, Australia
14-18 December 1992

MEASURING THE EFFECT ON DRAG PRODUCED BY NOSE BLUNTNESS ON A CONE IN HYPERVELOCITY FLOW

L.M. PORTER, D.J. MEE and J.M. SIMMONS

Department of Mechanical Engineering
University of Queensland
QLD 4072, AUSTRALIA

ABSTRACT

Presented in this paper is a preliminary investigation into the effect of nose bluntness on the drag of a conical body in hypersonic flows at Mach numbers above 5 and velocities above 5 kms^{-1}. Experiments have been performed in the T4 hypersonic shock tunnel facility. Since the test time in this facility is of the order of 1 ms, conventional drag measurement techniques can not be used successfully. The new drag measurement technique designed and developed by Sanderson and Simmons (1991) especially for use in short flow duration hypervelocity shock tunnel facilities has been used.

1 INTRODUCTION

The past decade has seen a renewed interest in the development of hypersonic vehicles. A number of different concepts have emerged for the design and application of such vehicles but one issue common to them all is the problem associated with the choice of nose geometry. This is also an issue in the design of an axisymmetric scramjet being proposed as the propulsion system for a disposable launch vehicle where the forebody of the centrebody of the scramjet will be conical. Ideally, in each instance a sharp nose would be used to reduce the pressure drag. However, a pointed slender nose is difficult to cool and does not offer the capability to carry large payloads. These practical limitations have motivated research into the aerodynamic characteristics of a blunted cone. The blunted cone simulates the nose geometry of interest while at the same time may be analysed using simple models. Research into nose cones in subsonic and low supersonic flight regimes is quite extensive but at hypersonic (Mach number greater than 5) and hypervelocity (flight speed greater than 5 kms^{-1}) conditions this is not the case.

The drag force is a fundamental parameter in the design of any flight vehicle but its measurement in hypersonic impulse facilities is inhibited by the very short test times involved. If a conventional force balance or accelerometer balance were to be used to measure drag then the time for a stress wave to traverse a test model would be required to be two orders of magnitude less than the characteristic wind tunnel test time. For an aluminium or steel test model in which the speed of a one-dimensional elastic stress wave is approximately 5 kms^{-1} this requirement would give a maximum model size of 50 mm in a facility having a test time of 1 ms. This is impractical. In order to measure the drag on a larger model in the shorter test time flows the flexibility of the model becomes quite significant and the passage of stress waves within the model needs to be considered. A novel technique for drag measurement in hypersonic impulse facilities has been developed by Sanderson and Simmons (1991). This technique takes into account the distributed mass effects and depends on the interpretation of the transient stress waves propagating within the model and its supporting structure.

The aims of this investigation were twofold. This was the first time the technique had been used in an experimental program. Thus, it was intended to prove through this work that this newly developed technique could be relied upon to provide accurate and reliable measurements of drag. The second aim was to obtain a preliminary measurement of the influence of nose bluntness on the drag on a slender cone. It is envisaged that once having shown that the technique can be used to detect small changes in drag on a cone a more comprehensive investigation into nose bluntness effects can be conducted.

2 EXPERIMENTS

2.1 Facility

The experiments were performed in the T4 free piston driven shock tunnel facility (Stalker and Morgan, 1988). A contoured axisymmetric Mach 5 nozzle was used to expand the gas from the stagnation region to the appropriate test conditions. The nozzle exit plane was 265 mm in diameter and the nozzle throat diameter was 25 mm. The tunnel was operated in a tailored mode so that the static pressure and enthalpy would be constant throughout the flow test time. The results to be presented here were performed in a test gas of air with a freestream Mach number of 5.2. The test gas was at a nominal stagnation enthalpy of 14 MJ/kg and a static pressure of 16 kPa. This condition corresponds to a flight speed of approximately 5.3 kms^{-1}.

2.2 Drag Measurement Technique

The model is attached to a "sting" in the form of a slender elastic bar (see Figure 1). The sting is suspended by vertical threads to allow free movement in the axial direction. Strain gauges located on the sting record the passage of stress waves resulting from the impulsively applied drag force as they are transmitted from the model into the sting.

The dynamic behaviour of the model/sting combination may be modelled as a time-invariant, causal, linear system described by the convolution integral,

$$y(t) = \int_0^t g(t - \tau)\, u(\tau)\, d\tau \qquad (1)$$

where u(t) is the single input to the system, y(t) is the resulting output and g(t) is the unit impulse response function. The unit impulse response function is the response of a system to an impulsive force acting over a very short time (in the limit as time goes to zero), but with a time integral which is finite. Knowing the response of the system to a unit impulsive force it is possible to determine the response of the system to excitation by any arbitrary force via Equation 1. Alternatively, and what is done here, y(t) is obtained from the strain gauge output and a numerical deconvolution process is performed to obtain u(t), the time-history of drag applied to the model.

The unit impulse response function may be obtained numerically from a dynamic finite element program. It has been demonstrated (Simmons et al., 1992) that the technique is insenstive to small changes in the impulse response and that

PRECEDING PAGE BLANK NOT FILMED

PAGE 116 INTENTIONALLY BLANK

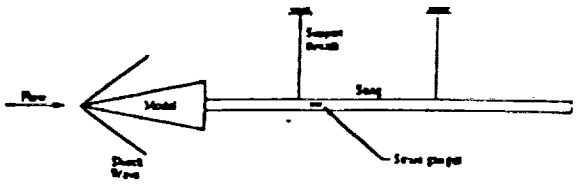

Figure 1. Drag balance configuration.

the unit impulse response function is in turn relatively insensitive to the loading distribution, which will change with varying nose bluntness. The unit impulse response determined for the sharp cone has thus been used in the numerical deconvolution to obtain the drag for all the tests. A complete description of the drag measurement technique is given by Sanderson and Simmons (1991).

2.3 Variable Nose Bluntness Slender Cone Model

Figure 2 shows a diagram of the model/sting arrangement with the finite element mesh used to calculate the unit impulse response function superimposed.

Experiments were performed on a 5° semi-vertex angle aluminium cone of length 571.5 mm. A total of 11 variable nose tips was used ranging in nose radius from 0.2 mm to 18.0 mm in steps of 1.8 mm. These correspond to bluntness ratios of 0.004 to 0.36 where the bluntness ratio is the ratio of the nose radius to the cone base radius. As the nose bluntness is increased, the length of the cone decreases as the base area is kept constant.

Theoretical analysis of a distributed mass model of the model/sting system as performed by Sanderson and Simmons (1991) shows that the mechanical time constant is proportional to the mass of the model. In order that the mechanical time constant of the drag force balance be kept small so that a measurement may be obtained in the small test times, the base area of the cone model was hollowed out to reduce the mass of the cone by almost 50%. Choice of model and sting materials was also dictated by the system time constant (Sanderson and Simmons, 1991). The resulting mechanical time constant of the system was 500 μsec.

Behind the base of the cone there was a PVC buffer to stop motion of the freely suspended model after the test flow. Removing the mass from the cone base served the additional function of ensuring that the pressure in the cavity between the cone and the PVC buffer was negligible by providing a large volume for gas to fill. The base pressure was monitored throughout the tests and the results confirmed this supposition.

The sting had a length of 2.5 m and was constructed from brass tubing of 34.92 mm outside diameter and 1.63 mm wall thickness, making its bending stiffness high. The sting length was chosen so that interference from the stress wave reflected from the end of the sting would not occur during the flow test time. As the speed of propagation of stress waves in brass is 3.600 kms^{-1} a sting length of 2.5 m allowed a test time of 1.3 ms. This estimate of test time takes into account the positioning of the strain gauges 300 mm from the model/sting interface (Figure 1).

2.4 Instrumentation

Kulite UHP-5000-060 semi-conductor strain gauges were used to measure the system output y(t). These gauges have a gauge factor of 155 but they are highly temperature sensitive. This made it necessary to use a modified Wheatstone bridge circuit to compensate the gauge output signals against undesirable temperature effects. Four strain gauges were used. Two gauges were attached to a separate piece of the sting material and placed near the sting so that they saw the same thermal environment but no mechanical strain. The two strain measuring gauges were arranged so that the circuit was sensitive only to axial loads. This was achieved by aligning the gauges in the axial direction and locating them along the neutral axis of bending of the sting so as to eliminate any possible bending effects created by the two wire support system of the sting (Figure 1).

The experiments were conducted in two stages. The first stage was to establish the flow condition and its repeatability. To do this centreline measurements of the static and Pitot pressures in the test flow were obtained. Measuring the drag on the cone model for various nose bluntnesses comprised the second stage of the experiments. Throughout these experiments Pitot pressure measurements were obtained to monitor the test flow properties from one shot to the next. Measurements of the pressure in the base area of the cone were also obtained. Additional instrumentation consisted of the measurement of the shock speeds in the shock tube and stagnation pressures. This is standard procedure as it is these quantities which are used to determine the conditions of the test gas.

3 RESULTS AND DISCUSSION

3.1 Test Flow Conditions

The conditions in the test section were numerically determined using ESTC (McIntosh, 1968) and NENZF (Lordi et al., 1966). The shock speed in the shock tube and the stagnation pressure were measured and used as inputs to ESTC to determine the temperature of the test gas in the stagnation region after shock reflection. The test gas undergoes a steady expansion from the stagnation region to the test flow properties at the exit plane of the nozzle. NENZF is a one-dimensional non-equilibrium code which predicts the properties of the test gas at the exit plane of the nozzle given the stagnation pressure and temperature. The test flow properties thus calculated are shown in Table I.

Measurements made of the test section Pitot pressure and static pressure were found to agree well with those predicted by NENZF. Typical Pitot pressure and static pressure traces are given in Figures 3 (a) and (b). The test flow properties were found to be repeatable to within 10%.

3.2 Drag Measurement Results

Figure 4 shows the raw signal output from the semi-conductor strain gauge bridge. Signals from two separate runs at a nose radius of 0.2 mm are shown here to establish the repeatability of the experimental results. It can be seen that the strain gauge measurements of the system output, y(t), were repeatable to better than 1%.

The strain gauge signal was deconvoluted numerically as described in Section 2.2 to obtain the time history of the drag

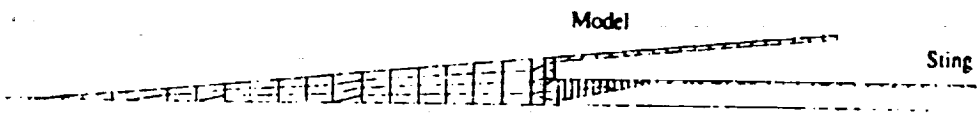

Figure 2. Finite element model of sharp cone model and sting.

Table I. Properties of test flow.

Stagnation Enthalpy MJ/kg	Mach No.	Static Pressure kPa	Pitot Pressure kPa	Static Temperature K	Flow Velocity km/s	Density kg/m3
14.4	5.2	16	555	1860	4.50	0.02784

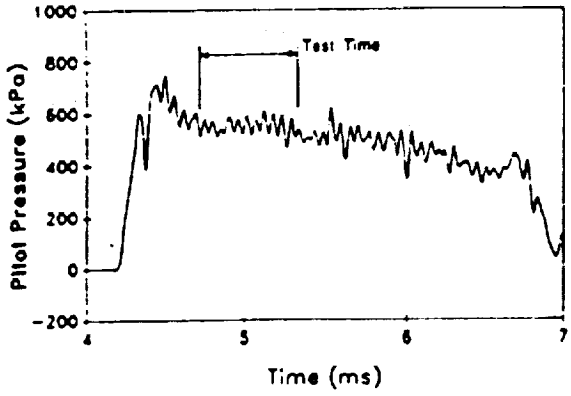

(a)

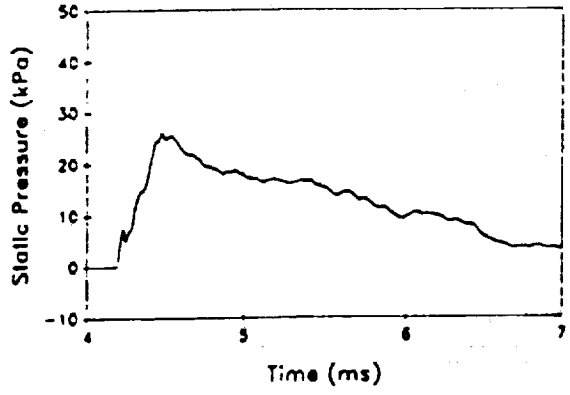

(b)

Figure 3. (a) Measured Pitot pressure and (b) measured static pressure.

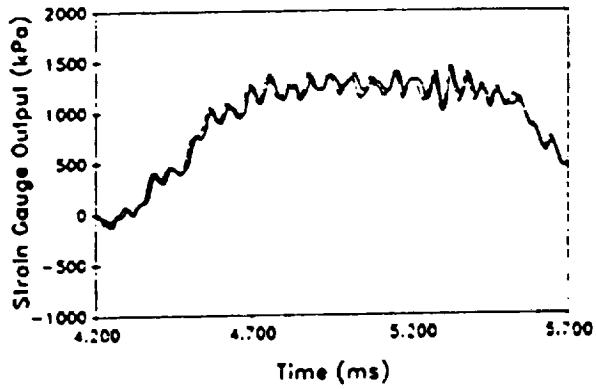

Figure 4. Signal output from strain gauge bridge (converted to stress) for two separate runs for a nose radius of 0.2 mm.

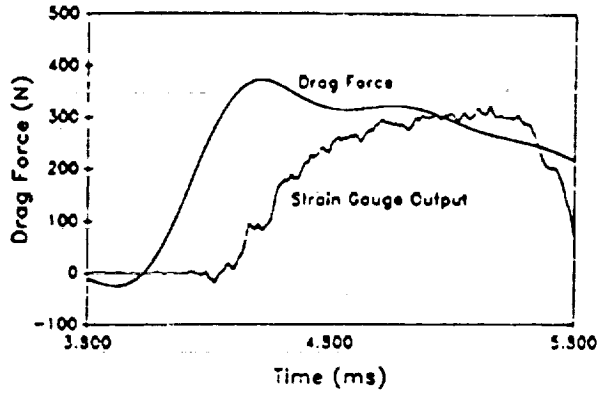

Figure 5. Comparison between signal from strain gauge bridge before (raw signal) and after (drag force) deconvolution for a nose of 10.8 mm.

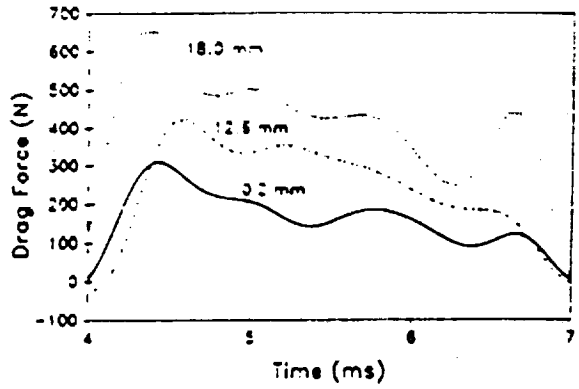

Figure 6. Comparison of the drag force time histories for cones having nose radii of 0.2 mm, 12.6 mm and 18.0 mm.

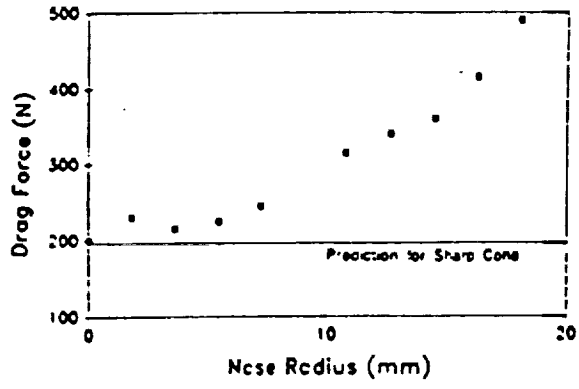

Figure 7. Drag force versus nose radius.

on the model. This drag measurement technique is inherently noisy as the deconvolution process tends to amplify any noise present in the original output signal, y(t). The strain gauge output signal itself is noisy as a result of the stress wave propagation within the model and sting. It was thus necessary to pass all the drag measurements resulting from the numerical deconvolution process through a 2 kHz, 6 pole Butterworth low-pass digital filter.

Figure 5 shows the measured drag in its time-averaged form for a nose radius of 10.8 mm in comparison with its corresponding strain gauge output signal before deconvolution. The time during which the static pressure is steady to within 10% variation (Figure 3) indicates the time of the flow in which the test flow conditions are deemed to be steady. This test time may be identified by the regions of steady drag in the plots of the time history of the drag force

acting on the model (Figures 5 and 6). Figure 6 gives a comparison between the drag measured for the three different nose radii of 0.2 mm, 12.6 mm and 18.0 mm.

Comparison between the static pressure traces (Figure 3) and the drag force traces (Figures 5 and 6) show that the drop in the drag force beyond the test flow time seems to follow the drop in the static pressure after the test time. This indicates that the drag measurement technique is giving faithful measurements of the drag even beyond the test time. The measured drag would be expected to drop with a drop in the static pressure because the drag force on the cone can be split into a pressure drag and a skin friction drag and the pressure drag component, dependent on the flow static pressure, is the larger of the two.

3.3 The Effect of Nose Bluntness on Drag on a Slender Cone

The results from this preliminary investigation into the effects nose bluntness has on cone drag are summarised in Figure 7. It would appear that at the smaller nose bluntnesses the effect on the total drag is relatively minor. The drag shows an increase from the sharp nose value of about 20 % at a nose radius of 7.2 mm (bluntness ratio of 0.144). However, beyond this radius the drag increases more rapidly so that at a nose radius of 18.0 mm (bluntness ratio of 0.36) the value of drag is about 245% greater than for the drag on the sharp cone.

It is uncertain whether the small increase in the value of drag at the 1.8 mm nose radius is due to a real physical effect. It is difficult to draw any conclusions based on this single preliminary result.

A theoretical prediction of the total drag on a sharp cone has been made and is also shown in Figure 7. The pressure drag was predicted using Taylor-Maccoll theory (Taylor and Maccoll, 1932) and found to be 159 N for the case being studied here. An estimate for the skin friction drag on the cone was made based on laminar boundary layer theory (White, 1974) and found to be 36 N. This gives a total drag of 195 N for a sharp, 5° semi-vertex angle and 571.5 mm long cone travelling in air at the condition at which the experiments presented here were conducted. The value of drag measured for the sharp cone was 200 N, thus reinforcing the accuracy of the drag measurement technique used.

4 CONCLUSION

These preliminary results show that the drag measurement technique has been developed to the stage where it can be used as an accurate and reliable research tool. It has been seen that the technique gives a faithful measurement of the time history of drag on a model and can resolve small changes in drag measurement.

The preliminary drag measurement results reveal a steadily increasing effect of nose bluntness on the drag on a cone. The effect at the smaller nose bluntnesses is relatively small, with a 20% increase in drag at a nose bluntness ratio of 0.144. This is encouraging for the design of a hypersonic space plane or a centrebody for an axisymmetric scramjet where a slightly blunted nose is required to reduce stagnation point heating. However, further experiments need to be performed at these smaller nose radii and at a finer resolution to determine the significance, if any, of the jump in drag at the 1.8 mm nose radius.

Further investigation at the larger nose bluntnesses would also be of interest. The results presented here indicate that the drag on a slender cone will continue to increase beyond a nose radius of 18.0 mm. Future experiments will be needed to reveal what effect a further increase in nose radius will have on the drag.

5 REFERENCES

LORDI, J A, MATES, R E and MOSELLE, J R (1966) Computer program for numerical solution of nonequilibrium expansion of reacting gas mixtures. NASA CR-472.

McINTOSH, M K (1968) Computer program for the numerical calculation of frozen and equilibrium conditions in shock tunnels. Dept. of Phys. ANU, Canberra.

SANDERSON, S R and SIMMONS, J M (1991) Drag balance for hypervelocity impulse facilities. AIAA J., 29, 2185-2191.

SIMMONS, J M, DANIEL, W J, MEE, D J and TUTTLE, S L (1992) Force measurement in hypervelocity impulse facilities. Proceedings of Workshop on New Trends in Instrumentation for Hypersonic Research, ONERA Le Fauga - Mauzac, France, 27 April to 1 May.

STALKER, R J and MORGAN, R G (1988) The University of Queensland Free Piston Shock Tunnel T4 - Initial Operation and Preliminary Calibration. NASA CR-181721, Sept. 1988.

TAYLOR, G I and MACCOLL, J W (1932) The air pressure on a cone moving at high speed - I Proc. Royal Soc. (London) Ser. A 139, 278-297.

WHITE, F M (1974) Viscous Fluid Flow. McGraw-Hill, Inc., New York., Inc., New York.

11th Australasian Fluid Mechanics Conference
University of Tasmania, Hobart, Australia
14-18 December 1992

A STUDY OF REYNOLDS ANALOGY IN A HYPERSONIC BOUNDARY LAYER USING A NEW SKIN FRICTION GAUGE

G.M. KELLY, A. PAULL and J.M. SIMMONS

Department of Mechanical Engineering
University of Queensland
QLD 4072, AUSTRALIA

ABSTRACT

Skin friction measurements have been made in T4, the University of Queensland's hypervelocity free piston shock tunnel. The measurements were made on a flat plate in a compressible boundary layer. They are compared with heat transfer measurements made simultaneously. It is found that in the region where the boundary layer was laminar the results compare favourably with those predicted by Reynolds analogy. The onset of transition can be clearly seen with both types of instrumentation.

INTRODUCTION

Hypervelocity impulse facilities, such as free piston shock tunnels and expansion tubes, have an important role in the development of technologies for hypersonic flight. They are capable of generating the high-enthalpy flows associated with external aerodynamics of space planes at near orbital velocities and the internal aerodynamics of scramjet propulsion systems. Important model test parameters are drag and skin friction but their measurement is complicated greatly by the very short test times of impulse facilities. Skin friction measurement is complicated further by the fact that the wall pressure can be an order of magnitude greater than the wall stress generated by skin friction. Skin friction gauges for use in conventional shock tunnels have been reported. However, their ability to perform satisfactorily in the very short duration flows associated with free piston shock tunnels and expansion tubes does not appear to have demonstrated. This paper reports the development of a transducer capable of measuring skin friction with a rise time of about 20 μs. Results prove the effectiveness of the concept when used to measure skin friction on a flat plate. Reynolds analogy is examined by comparing the output from heat transfer gauges and skin friction gauges. The onset of transition is also observed using both devices.

GAUGE DESIGN

The gauge design is shown schematically in Figure 1. It comprises a thin metal disk or thermal cover (10 mm diameter and 0.4 mm thick) mounted flush with the surface of the model and bonded to a stack of two piezoelectric transducer elements (each 7 x 7 mm and 1.5 mm thick). The material chosen for the elements was the piezoceramic PZT-7A. Its rigidity and density were such that, for the configuration in Figure 1, gauge natural frequencies were above 300 kHz. In theory, the elements appropriately orientated and with electrodes on the appropriate surfaces, respond only to shear force generated by skin friction, but in practice there was a small pressure dependency (normal to the disk). For this reason the two-element gauge was designed, with one piezoceramic element inverted with respect to the other.

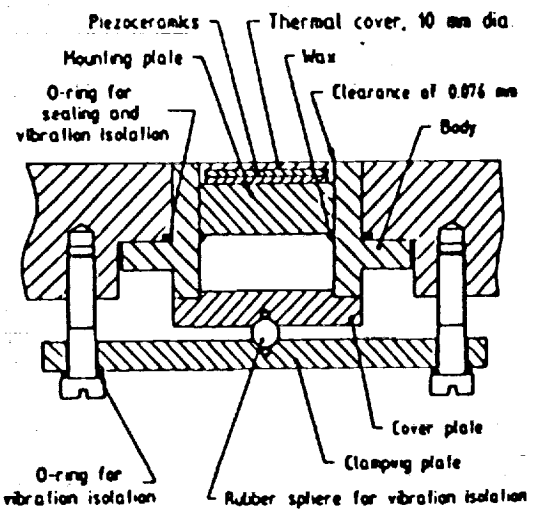

Figure 1 Schematic of skin friction gauge

One element provides an output e_1 proportional to the sum of the effects of skin friction τ and pressure p applied to the disk, and the other provides an output e_2 proportional to the differences [Equations (1) and (2) below].

A weighted summation of the two outputs therefore provides a direct measurement of shear stress.

$$e_1 = a_1\tau + b_1p \quad (1)$$

$$e_2 = a_2\tau - b_2p \quad (2)$$

A calibration procedure would involve using a known laminar boundary layer for a condition in the shock tunnel to determine constants a_1 and a_2. To determine the pressure sensitivity it is necessary to apply a transient pressure, with $\tau = 0$, to the transducer to

determine the ratio of constants b_1/b_2. Hence, an unknown shear stress τ can be determined from Equation (3) and simultaneous measurement of outputs e_1 and e_2.

$$e_1 + (b_1/b_2)e_2 = [a_1 + (b_1/b_2)a_2]\tau \qquad (3)$$

Piezoceramics exhibit a Curie temperature above which they begin to depolarise. To avoid this, the thickness of the thermal cover and its material were chosen to prevent unacceptable levels of conductive heat transfer from the hot test gas in the boundary layer. Several materials were evaluated. Invar was finally chosen because it has a very small coefficient of thermal expansion, thereby preventing the transducer elements from being strained due to thermal expansion of the disk.

The impulsive nature of the flow in free piston shock tunnels results in stress waves in the model, with the skin friction gauge exposed to a vibration-induced acceleration environment. To counteract this, rubber and felt vibration isolation was included in the design (Figure 1). The technique effectively lowered acceleration induced output from the gauge to a level that could be handled by filtering during signal processing.

The shear stress levels on the models were typically 200-1000 Pa, but for some of the flow conditions they were less than 100 Pa. Since the charge produced by the piezoceramic elements is small (of the order of 5 pC for some conditions), amplification of the signal was required. To minimise noise contamination, a charge amplifier was located as close as possible to the site of signal detection.

EXPERIMENT

To determine b_1/b_2 a small shock tube was used to apply a transient pressure and no shear stress to the skin friction gauge. The shear stress calibration yielding a_1 and a_2 was determined as mentioned previously using heat transfer measurements in a laminar boundary layer for a condition in the shock tunnel. Measurements were made of the heat transfer close to the site of the gauge and Reynolds analogy was then used to determine the skin friction.

Reynolds analogy can be stated as

$$\frac{C_H}{c_f} = \frac{1}{2} Pr^{-2/3} \qquad (4)$$

where C_H is the coefficient of heat transfer and c_f the coefficient of skin friction. Pr is the Prandtl number. Using van Driest's determination of skin friction in a compressible, flat plate, laminar boundary layer (van Driest, 1952) and the assumption that the free stream conditions remain effectively constant, Reynolds analogy can be reduced to

$$\frac{q_w}{\tau} = \frac{-Pr^{-2/3} c_p[T_\infty(1 + r\frac{\gamma-1}{2}M_\infty^2) - T_w]}{U_\infty} \qquad (5)$$

Where T_∞ = free stream temperature, K
V_∞ = free stream velocity, m/s
M_∞ = free stream Mach Number
q = heat transfer, kW/m²
τ = shear stress, kPa
c_p = specific heat
r = recovery factor

Having determined the sensitivities of the gauges to shear stress from one test condition, these values were then used for the other three test conditions.

The flat plate model used was made of aluminium with a leading edge of steel (Figure 2). It was 600 mm in length and 228 mm in width. There were six skin friction gauges in the model, the first at a distance 145 mm from the leading edge and the others at 65 mm intervals downstream of it. At the site of every skin friction gauge a piezoelectric pressure transducer was positioned to one side and a thin film heat transfer gauge to the other. Their centres were set at the same distance from the leading edge. The sensing element on the skin friction gauge was a 10 mm diameter disk. The heat transfer gauge was 1.7 mm in diameter and the pressure tappings were 2 mm diameter. The available test time depended on the condition used, since for higher enthalpy conditions the signal was contaminated by noise earlier. For higher energy flows vibration travelled through the model earlier, reducing the available test time. The range of conditions used is listed in Table I. Condition 1 is that used for calibration purposes. Figure 3 shows the heat transfer distribution along the plate for the calibration test approximately 500 μs after the start of the flow. This was the condition used to determine the shear sensitivities of the gauges. These sensitivities have then been used to determine shear stress profiles for the three other conditions.

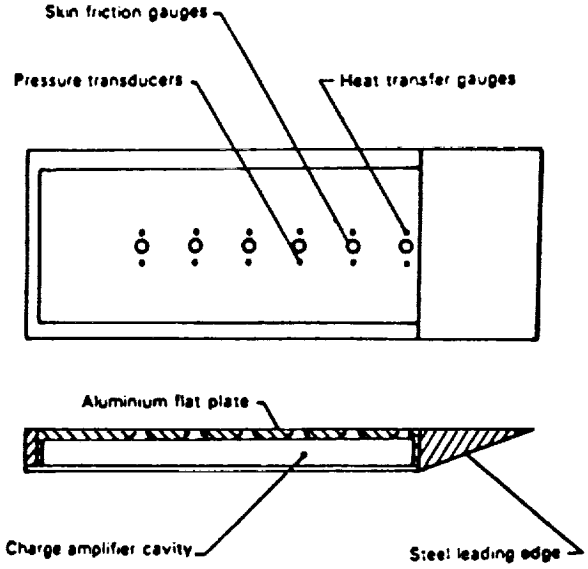

Figure 2 Schematic of flat plate model

RESULTS

Figure 4 shows the time-histories of heat transfer and the corresponding skin friction at position 1, 145 mm from the leading edge for condition 2. This condition was not used for calibration because transition occurs. The scale on the vertical axis is for both shear stress and heat transfer. The units are kPa and MW/m² respectively.

It can be seen from this trace that whilst the skin friction and heat transfer exhibit the same trends, rapid changes in the heat transfer due to transition tend to lag the skin friction. This is consistent with the development

of the thermal boundary layer. Basically the thermal profile develops more slowly than the velocity profile. Initially when the thermal boundary layer is thin the heat transfer rate is high and the responses of both the heat transfer gauge and the skin friction gauge are virtually simultaneous. Later in time, as the boundary layer grows, the heat transfer lags the skin friction. This effect becomes more marked downstream where the boundary layer is thicker. As the boundary layer thickens the heat transfer rate decreases.

Table 1 Four test conditions

	1	2	3	4
Stagnation enthalphy, MJ/kg	4.58	7.27	7.59	9.06
Stagnation temperature, K	3522	4663	4921	5685
Stagnation pressure, MPa	11.16	9.375	20.04	51.3
Temperature, K	574.5	1129	1180	1297
Pressure, kPa	3.8	4.3	9.17	22.6
Density, kg/m^3	0.023	0.013	0.027	0.06
Velocity, m/s	2829	3488	3562	3791
Mach number	5.9	5.3	5.3	5.4

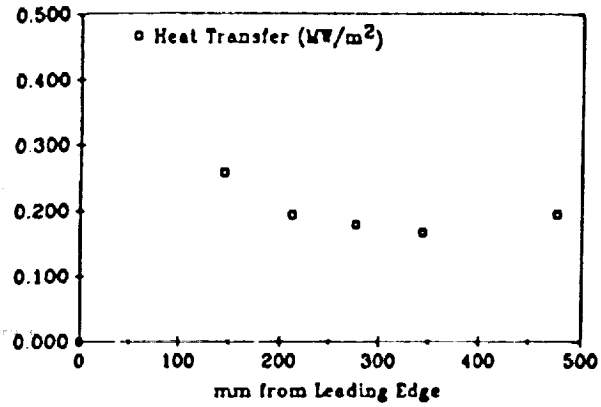

Figure 3 Heat transfer measurements (condition 1) used to calibrate skin friction gauges

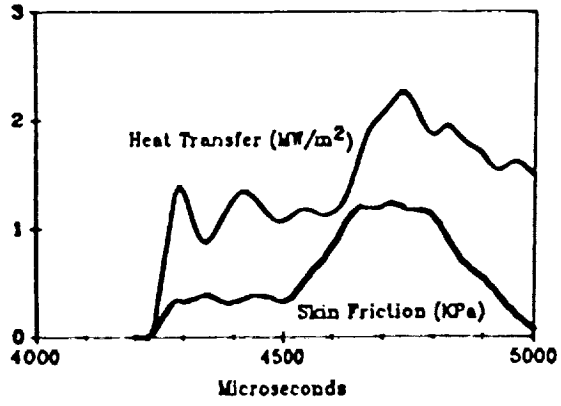

Figure 4 Skin friction and heat transfer time-histories at 145mm from leading edge for condition 2

It can be seen that the heat transfer trace and the skin friction trace follow each other. As noted however, in unsteady flow one lags the other as expected. It is therefore very important to calibrate one against the other only when conditions are steady and only in laminar flow (condition 1).

Figure 5 shows condition 2 at approximately 0.5 ms into the test time. Figure 6 shows condition 3. In both figures the rapid departure of skin friction and heat transfer distributions indicates the onset of transition. Figure 7 shows the theoretical prediction for shear stress from the heat transfer measurements and Reynolds analogy (open circles) for condition 2. The closed squares on this figure indicate the experimental shear stress measured in the flow.

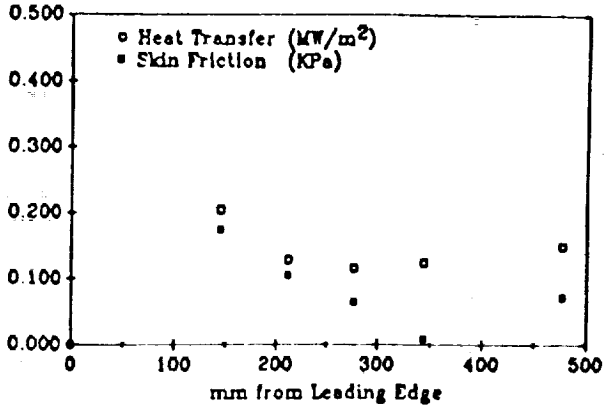

Figure 5 Heat transfer and skin friction along plate for condition 2

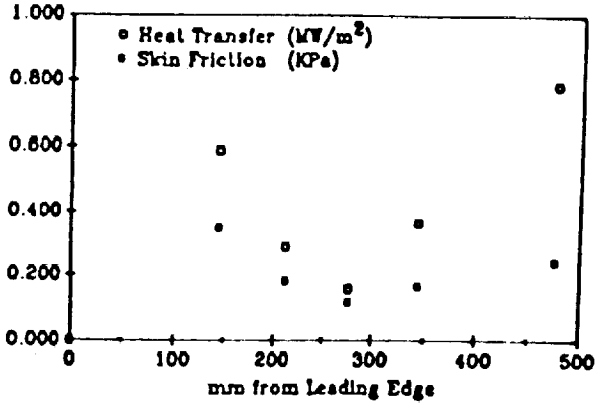

Figure 6 Heat transfer and skin friction along plate for condition 3

It can be seen from Figure 7 that when the flow is laminar (for the first three locations) agreement between theoretical predictions and experimental measurements is excellent. However, once the flow undergoes transition the measured values depart from theory. Although measurement and theory still follow the same trend, there is no longer a uniform scaling factor. For Figure 5 as well, it can be seen that when the flow is laminar, the skin friction and heat transfer results decay at similar rates and it is only once the flow undergoes transition that this pattern is disturbed. It must also be remembered that the heat transfer results tend to lag the skin friction

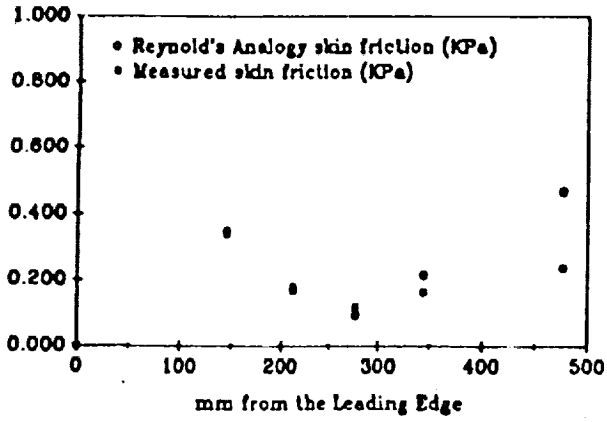

Figure 7 Measured and predicted skin friction along plate for condition 3

output. When change occurs, as in the onset of transition, this effect becomes noticeable.

Figure 8 shows results for condition 4. It appears that transition is occurring by the second gauge. The Reynolds number at gauge 2 is approximately 1.02×10^6 and the unit Reynolds number is 4.8×10^6 m^{-1}. From results previously reported by He and Morgan (1989), it can be seen that for these values one would expect transition to occur somewhere between 200 and 260 mm from the leading edge. Gauge 2 is positioned at 210 mm from the leading edge.

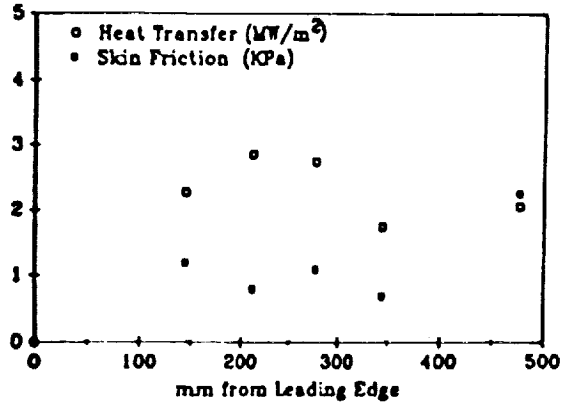

Figure 8 Heat transfer and skin friction along plate for condition 4

The discrepancy in Figure 8 between the skin friction and heat transfer trends at position two is a direct result of the lag between skin friction and heat transfer. It is evident though that the traces generally follow each other although only at the first point does Reynolds analogy hold. This once again is in agreement with the fact that Reynolds analogy is only purported to be held when conditions are laminar. It is interesting that during transition the general trend is still followed, although the factor between the two traces is no longer consistent.

CONCLUSIONS

It is concluded that where the flow is laminar, measurement of skin friction and heat transfer are consistent with Reynolds analogy. With the onset of transition Reynolds analogy, as expected, breaks down.

Also the skin friction gauge is shown to be an effective means of measuring shear stress. The gauge has a rise time of about 20 μs, sufficiently short for most shock tunnel applications and approaching the rise times needed for expansion tube applications.

ACKNOWLEDGEMENTS

This work was supported by the Australian Research Council under Grant A5852080 and by NASA under Grant NAGW-674. The authors wish to acknowledge the invaluable technical contribution of John Brennan and the scholarship support from Zonta International Foundation.

REFERENCES

DUNN, M G, (1981) Current Studies at Calspan Utilizing Short-Duration Flow Techniques. Proceedings of the 13th International Symposium on Shock Tubes and Waves, edited by C E Treanor and J G Hall, State Univ. of New York, Albany, NY, 32-40.

HE, Y and MORGAN, R G, (1989) Transition of compressible high enthalpy boundary layer flow over a flat plate. 10th Australasian Fluid Mechanics Conference, Univ Melb, 11B-2, 11-15.

KELLY, G M, SIMMONS, J M, and PAULL, A (1991) Skin-friction gauge for use in hypervelocity impulse facilities. AIAA Journal, 30, 844-845.

VAN DRIEST, E R, (1952) Investigation of Laminar Boundary Layer in Compressible Fluids Using the Crocco Method. NACA TN 2597.

11th Australasian Fluid Mechanics Conference
University of Tasmania, Hobart, Australia
14-18 December 1992

ENERGY REDISTRIBUTION OF NONEQUILIBRIUM HYPERVELOCITY FLOW IN A SCRAMJET DUCT

N.R. WARD and R.J. STALKER

Department of Mechanical Engineering
University of Queensland
QLD 4072, AUSTRALIA

ABSTRACT

Chemically and vibrationally frozen shock tunnel test flow is passed through a model scramjet duct with the aim of examining heat release and its effects on the flow in analogy to the heat release resulting from combustion. Experimental investigations are carried out using a differential interferometer optics system for a range of shock tunnel test conditions. The resulting images are then compared to a numerical simulation using chemical and vibrational nonequilibrium flow theory fitted to the duct shape imposed boundary conditions.

NOTATION

P = pressure
T = temperature
ρ = density
θ = flow direction
M = mach number
α = dissociation fraction
e_v = vibrational energy
γ = ratio of specific heats
δ = intake wedge angle
μ = shock angle
t = time
C_1, C_2, η_1, η_2 = chemical rate constants
C, K_2 = vibrational rate constants
θ_d = characteristic temperature for dissociation
θ_v = characteristic temperature for vibration
ρ_d = characteristic density for dissociation
e_v^* = equilibrium vibrational energy
τ = vibrational relaxation time
R = gas constant
h = enthalpy
h_q = partial derivative of h with respect to q
u = velocity
u_n = component of velocity normal to shock
a_f = frozen speed of sound
n = refractive index
I = interferogram intensity
ε = divergence angle of wollaston prism
λ = wavelength of laser light
w = displacement of wollaston prism from lens focus
f_2 = focal length of main lens
x = distance along centreline of model
W = width of model
P_s = stagnation pressure
T_s = stagnation temperature
h_s = stagnation enthalpy

INTRODUCTION

As a means of investigating the gas dynamic effects of the heat release produced by combustion of hydrogen in a scramjet duct it is intended to simulate such heat release by using chemically and vibrationally excited shock tunnel test flow to provide the energy release instead of combustion. Energy stored in the dissociation of molecules and in vibrational modes can be converted to heat energy. This evades the problems of imperfect mixing and flow disruption caused by an injector, and isolates the heat release process from the ignition process present in combustion.

The T4 shock tunnel is capable of producing high enthalpy test flow which contains significant levels of dissociation and vibrational excitation. These are frozen in the free stream flow and energy redistribution only recommences after the flow crosses the intake shocks of the scramjet, in much the same way as combustion would occur in a premixed scramjet. See figure 1.

In this paper it is aimed to investigate this heat release in a scramjet model over a range of T4 test conditions. For this study a nitrogen test gas is chosen.

Experimentally it is difficult to accurately measure flow conditions using electronic gauges without disturbing the flow. Also, such methods involving gauges only provide data at discrete locations, allowing fine detail in the flow to be missed. To avoid such problems the experimental investigations are carried out using optics to study the flow through the scramjet.

The optical system used is the *Differential Interferometer*, or *Schlieren Interferometer*. A variation on the basic system is used making it a double pass system, largely because of space constraints but also because this configuration doubles the sensitivity. See figure 2.

This system provides interferograms in which fringe shifts are related to *gradient of* refractive index within the flow field.

These experimental results obtained from the T4 shock tunnel are then compared to a numerical simulation. Chemical and vibrational non-equilibrium theory is used to computationally predict the flow pattern through the scramjet duct for the free stream conditions corresponding to the experiments.

EXPERIMENTAL METHOD

The differential interferometer used to experimentally investigate the chemically and vibrationally non-equilibrium flow in the scramjet model as produced by

the T4 shock tunnel is shown schematically in figure 2. A pulsed ruby laser is used as the light source and all mirrors are ground to an accuracy of one tenth of a wavelength or better. A spatial filter with a 5 μm pinhole is used to clean up the light source and a precision quartz wollaston prism is used with a 4 minute prism angle. The image retrieval system consists of CCD camera with 210 mm lens close mounted connected to a triggered framegrabber. Pressure gauges at the end of the shock tube trigger the camera to then trigger the laser before clearing the CCD registers and storing the image in memory of an IBM 286 computer. This is then viewed and printed.

The model used is 150 mm wide with open sides and is rear mounted in the T4 test section. Hardened gauge plate steel is used on all leading edges of the model. The intake wedges are 204 mm long and 10 degrees. The shock tunnel test section is fitted with 200 mm diameter precision crown glass windows, flat to within one tenth of a wavelength. A pitot probe is fitted above the model to check the timing of the laser against the test flow period.

NUMERICAL CALCULATIONS

The computer program predicts flow variables throughout the scramjet duct, from the free stream before the leading edge shocks to the parallel duct behind the shocks after crossing. The test model for the T4 experiments has a gap at the end of the angled intake wedges to allow the shocks to escape without reflection, and the parallel duct was designed to be narrow enough to deny entry to the expansion from the end of the wedge. This allows the definition of three 'zones' of flow, as shown in figure 3. The flow is symmetrical about the centre line, so only the bottom half is calculated.

The first zone is assumed to be chemically and vibrationally frozen, and the flow to be steady and parallel. Consequently pressure P, temperature T, density ρ, flow direction θ, mach number M, dissociation fraction α and vibrational energy e_v are all constant.

The shock angle μ for the shock emanating from the leading edge of the intake wedge, of angle δ, is calculated by solving the following equation derived by continuity considerations and the Rankine-Hugoniot equation for density ratio across a shock:

$$\frac{\tan(\delta+\mu)}{\tan\mu} = \frac{\gamma+1}{2}\left(\frac{M^2\sin^2(\delta+\mu)}{1+\frac{\gamma-1}{2}M^2\sin^2(\delta+\mu)}\right) \qquad (1)$$

The flow variables are then found behind the shock using the Rankine Hugoniot equations for pressure, temperature and Mach number ratios across a shock.

As the flow passes along the surface of the wedge it adjusts chemically and vibrationally, as described by Vincenti and Kruger (1965), according to the following equations:

$$\frac{d\alpha}{dt} = [C_1 T^{\eta_1}\alpha + C_2 T^{\eta_2}(\frac{1-\alpha}{2})]\rho[(1-\alpha)e^{-\theta/T} - \frac{\rho}{\rho_d}\alpha^2] \qquad (2)$$

and

$$\frac{de_v}{dt} = \frac{e_v^* - e_v}{\tau} \qquad (3)$$

where

$$e_v^* = \frac{R\theta_v}{e^{\theta/T}-1} \qquad (4)$$

$$\tau = \frac{C\,e^{(K_1 T)^{1/3}}}{P} \qquad (5)$$

As it does so the temperature changes according to:

$$dT = -\frac{1}{h_T}(h_\alpha d\alpha + h_{e_v} de_v + u du) \qquad (6)$$

where the enthalpy h is given by

$$h = (\frac{7}{2}+\frac{3}{2}\alpha)RT + \alpha R\theta_d + (1-\alpha)e_v \qquad (7)$$

and for some q h_q is the partial derivative of $h(T,\alpha,e_v)$ with respect to q

and the component of velocity normal to the shock changes according to:

$$du_n = -\frac{u_n}{\rho h_\rho(u_n^2/a_f^2-1)}(h_\alpha d\alpha + h_{e_v} de_v) \qquad (8)$$

where h_q is here the partial derivative of $h(\rho,P,\alpha,e_v)$ with respect to q

The pressure changes according to:

$$dP = -\rho u du \qquad (9)$$

from conservation of momentum.

These differential equations are integrated using a second order Runge-Kuta method to obtain the chemically and vibrationally adjusting flow along the surface of the intake wedge.

As u_n changes the flow direction changes due to the component of u tangential to the shock remaining constant. At the surface of the wedge however the flow direction must be parallel to the wall. This boundary condition requires the superposition of a weak Prandtl-Meyer expansion/compression on the chemically and vibrationally adjusting flow. For a deflection of -dφ at the wall for the adjusting flow the Prandtl-Meyer perturbation provides the equal and opposite deflection, and gives a perturbation in the other flow variables according to:

$$\frac{dP}{P} = \frac{\gamma M^2}{\sqrt{M^2-1}}d\phi \qquad (10)$$

$$\frac{dM}{M} = -\frac{(1+\frac{\gamma-1}{2}M^2)}{\sqrt{M^2-1}}d\phi \qquad (11)$$

$$\frac{dT}{T} = \frac{(\gamma-1)M^2}{\sqrt{M^2-1}}d\phi \qquad (12)$$

These perturbations are communicated along Mach lines throughout zone 2. They are added to the adjusting flow base values which are calculated for each streamline leading off from the leading shock. In this way the flow is calculated in zone 2, and the shape of the leading shock is altered in accordance with the perturbed conditions behind it caused by the Prandtl-Meyer perturbations.

The flow in zone 3 is calculated in a similar way, using the symmetry imposed boundary condition of flow along the duct centre line being parallel to the duct centre line. For each streamline final conditions ahead of the second shock are used to calculate conditions behind the shock which are then starting conditions for the integration of the chemically and vibrationally adjusting base flow in zone 3. To these base conditions the Prandtl-Meyer perturbations are added.

From the flow variables throughout the duct the refractive index of the flow n and its gradient dn/dx can be calculated using the Gladestone-Dale equation, applied to nitrogen molecules and gas with Gladestone-Dale constants as given in Alpher and White (1958), as described by Merzkirch (1974):

$$n-1 = \rho(K_{N_2}(1-\alpha)+K_N\alpha) \qquad (13)$$

From the gradient dn/dx, a knowledge of the T4 test section and model geometries and specifications of the differential interferometer optics system the fringe intensity I of the resulting interferogram can be calculated using the equation:

$$I = \frac{1}{2}(\cos[2\pi(\frac{2e}{\lambda})(\frac{w}{f_2})x+Wf_2(\frac{dn}{dx}))]+1) \qquad (14)$$

The numerically predicted differential interferogram is imported into the same electronics which holds the experimental interferogram. In this way a pictorial image can be produced, and this can then be compared to the experimental image.

RESULTS AND DISCUSSION

A set of experiments was carried out using the T4 shock tunnel, the results of which are presented here.

Chemical processes were initially assumed to dominate the non-equilibrium flow so the test conditions were chosen to maintain a high dissociation fraction α whilst varying the flow pressures and then to choose some other conditions with much lower α to compare. A mach five nozzle was used over this range of enthalpies and pressures. A differential interferometer image was recorded for each shot together with traces of shock speed within the shock tube, stagnation pressure at the entrance to the converging-diverging nozzle, pitot pressure at the model and the laser high voltage output trace.

The images recorded showed a curvature of the fringes after both the leading edge shock and the second shock, decaying away quite quickly in zones 2 and 3 respectively. See figure 4.

The displacement of these fringes was observed to vary for different enthalpy and pressure conditions, but in all cases the deflection of the fringes was upstream after both the first and second shocks. Fringe curvature upon entry to the heated outskirts of the boundary layer can also be clearly seen.

At the conclusion of the experiments the images were analysed and the deflection of the wollaston prism calibrated. Consequently it was confirmed that a deflection upstream signifies a raising of refractive index gradient from zero and thus increasing density. This is verified by examination of the fringe shift entering the boundary layer. This corresponds to energy *absorption* rather than heat release.

The implication of this is that despite the wide range of test conditions chosen there was not recombination in any of them.

In order to complete numerical simulations for the test conditions the free stream conditions at the entrance to the scramjet were needed. These were obtained by using a non-equilibrium nozzle flow (NENZF) program to integrate from the shock tube fill pressure, the stagnation pressure during the shot and the shock speed in the shock tube.

Numerical simulations obtained using free stream conditions found in this way predicted recombination in zone 2 at least, and an effect which was almost too small to detect when chemical rate constants as given by Vincenti and Kruger (1965) were used. It was at this stage that the previously described treatment of vibrational non-equilibrium was included, using more recent values of the vibrational rate constants as given in Sharma and Park (1990). The free stream vibrational energy used was as predicted by the method of Phinney (1964). Vibrational non-equilibrium effects were found to be highly significant to the flow.

Skinner (1992) found that at the high enthalpies at which these experiments were carried out helium contamination of the test gas from the driver gas was resulting in observations of zero dissociation of nitrogen test gas, in contradiction to the pure test gas case calculated by the NENZF program. When this was used in the numerical simulation, coupled with the more complete non-equilibrium calculation involving both vibration and chemistry, the computational results were found to be in quite good agreement with experiment. See figure 5 for the numerical simulation corresponding to figure 4. Although the fringe displacement at the start of zone 2 is not sufficient to be clearly observed for this calculation, when the calculation is carried out using a lower value of the vibrational relaxation time constant C and as a consequence a lower free stream vibrational energy, the fringe shift is clearly seen and matches experiment well. As there is an accepted high level of uncertainty in these rate constants comparison against this result is justifiable. See figure 6.

It appears that a more thorough non-equilibrium nozzle flow calculation, incorporating chemistry and vibration, and further knowledge of T4 conditions which produce helium contamination will be important in the selection of shock tunnel test conditions for future experiments. It is expected that conditions will be attainable in which the nonequilibrium flow through the scramjet model duct produces heat release rather than absorption, allowing combustion simulation, although this was not the case in the experiments covered here.

SUMMARY AND CONCLUSIONS

Experimental differential interferograms of shock tunnel test flow through a model scramjet duct have been obtained over a range of high enthalpy test conditions. In all of these cases heat absorption after the intake shocks has been observed. Helium contamination is postulated. Numerical simulations of the flow, when incorporating chemical and vibrational non-equilibrium, have been found to be in good agreement with experiment. Future experiments will involve a complete non-equilibrium nozzle flow calculation to select test conditions which produce heat release.

ORIGINAL PAGE IS
OF POOR QUALITY

REFERENCES

ALPHER, R A and WHITE, D R (1958) Optical Refractivity of High Temperature Gases. I. Effects Resulting from Dissociation of Diatomic Gases. The Physics of Fluids, Volume 2 Number 2, 153-161.

MERZKIRCH, W (1974) Flow Visualisation. Academic Press, New York and London.

PHINNEY, R (1964) Nondimensional Solutions of Flows with Vibrational Relaxation. AIAA Journal, Volume 2 Number 2, 240-244.

SHARMA, S P and PARK, C (1990) Survey of simulation and diagnostic techniques for hypersonic nonequilibrium flows. J. Thermophysics. Heat Transf., Volume 4 Number 2, 129-142.

SKINNER, K (1992) Private communication. Department of Mechanical Engineering, University of Queensland, Brisbane.

VINCENTI, W G and KRUGER, C H (1965) Introduction to Physical Gas Dynamics. Robert E. Krieger Publishing Company, Malabar, Florida.

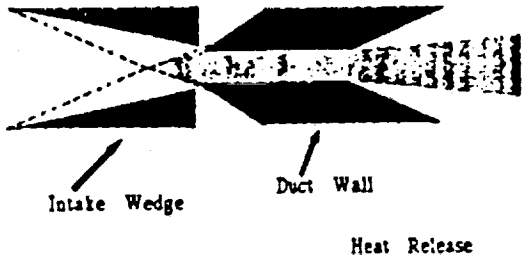

Figure 1 Heat release in a model scramjet duct.

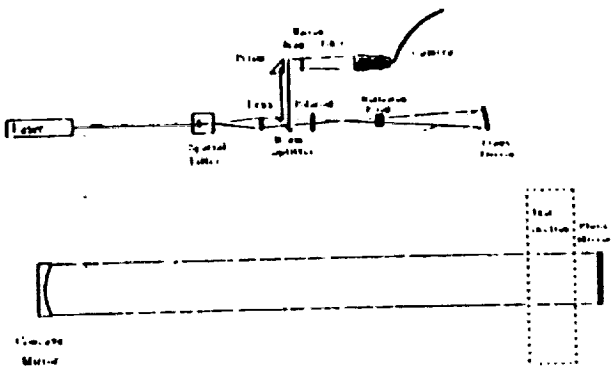

Figure 2 Differential interferometer optics system.

Figure 3 Geometry for numerical flow calculation.

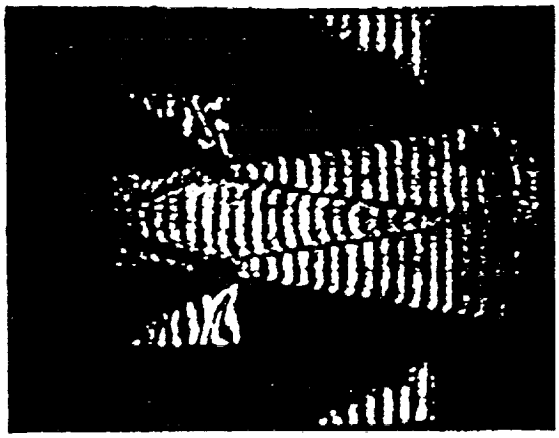

Figure 4 Experimental differential interferogram for H_t = 22 MJ/kg, P_t = 33 MPa, T_t = 9400 K.

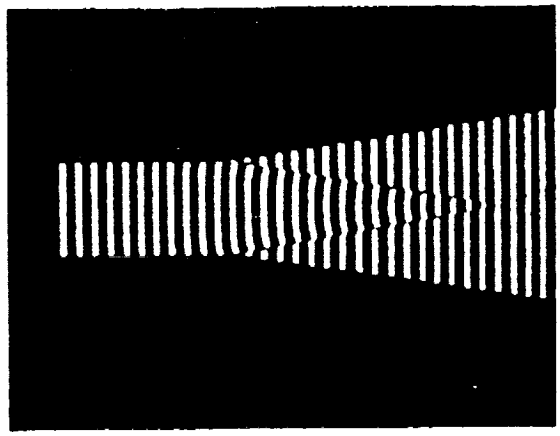

Figure 5 Numerically simulated differential interferogram for H_t = 22 MJ/kg, P_t = 33 MPa, T_t = 9400 K, frozen freestream α = 0 and e_v = 0.60 MJ/kg. Vibrational relaxation time constants used are $C = 8.31 \times 10^{-7}$ sec/Pa and $K_2 = 1.176 \times 10^{4}$ K.

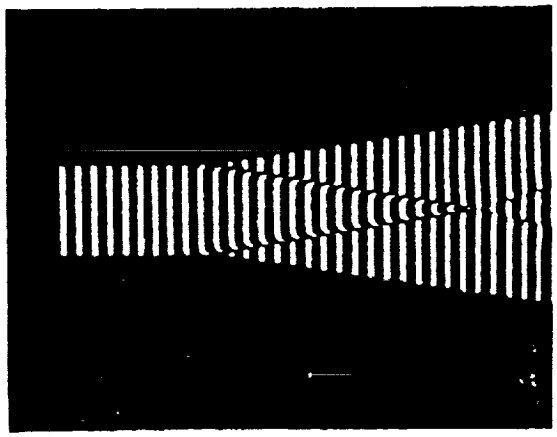

Figure 6 Numerically simulated differential interferogram for H_t = 22 MJ/kg, P_t = 33 MPa, T_t = 9400 K, frozen freestream α = 0 and e_v = 0.45 MJ/kg. Vibrational relaxation time constants used are $C = 2.07 \times 10^{-7}$ sec/Pa and $K_2 = 1.176 \times 10^{4}$ K.

11th Australasian Fluid Mechanics Conference
University of Tasmania, Hobart, Australia
14-18 December 1992

FLOW MEASUREMENTS AND CALIBRATION OF A SUPERORBITAL EXPANSION TUBE

A.J. NEELY and R.G. MORGAN

Department of Mechanical Engineering
University of Queensland
QLD 4072, AUSTRALIA

ABSTRACT

A small pilot facility has been set up at The University of Queensland to demonstrate the concept of the Superorbital Expansion Tube, a free piston driven, triple diaphragm, impulse shock facility that utilizes the enthalpy multiplication mechanism of the unsteady expansion process. The pilot facility has been operated to produce quasi-steady test flows in air with shock velocities in excess of 13 kms^{-1} and with a duration of usable test flow approaching 15 μs. Experimental conditions with total enthalpies of 78 MJ and 106 MJ and total pressures of 15 and 37 Mpa respectively are reported. A flow model that accounts for non-ideal rupture of the light tertiary diaphragm is discussed. It is shown that equilibrium calculations more accurately model the unsteady expansion process than calculations assuming frozen chemistry.

INTRODUCTION

The Superorbital Expansion Tube is a free piston driven, triple diaphragm, impulse wind tunnel. This new hypervelocity facility is designed to produce flow conditions in a variety of test gases at velocities exceeding Earth orbital velocity. Even the most capable existing ground testing facilities such as free-piston driven shock tunnels and expansion tubes are limited in the maximum flow enthalpies they can produce. With the increasing interest in the design of vehicles to be used to enter the atmosphere of other planets or return to Earth's atmosphere from beyond Earth orbit, experimental facilities such as the Superorbital Expansion Tube will be required to allow aerodynamic ground testing of flight vehicle concepts and components. This paper outlines experiments in a small pilot facility in operation at The University of Queensland which has been used to demonstrate the capabilities of a Superorbital Expansion Tube using air as the test gas. The techniques used to model the flow processes involved, particularly around the tertiary diaphragm are also discussed.

PRINCIPLE OF OPERATION OF THE FACILITY

The operation of the Superorbital Expansion Tube is described in Morgan & Stalker (1991). It uses the phenomenon of enthalpy multiplication of the test flow through an unsteady expansion as used in the standard expansion tube, described originally by Resler and Bloxsom (1952). The total enthalpy of the flow is determined by the extent of this final unsteady expansion of the test gas.

The facility with secondary driver, shock tube and acceleration tube sections all of constant area (38 mm), is shown in Figure 1. The tunnel is driven by a helium filled, free piston driver which is used to shock heat a helium filled secondary driver section (2.111 m), separated from it by a heavy diaphragm (52.5 Mpa burst pressure).

The facility can be operated in two driver modes. In the first or *reflected* mode the driver gas is stagnated at the end of the secondary driver section and exhausts into the test gas contained in the shock tube section (of adjustable length, initially 3.150 m), which is separated from the secondary driver by a thin steel secondary diaphragm (1mm, 12.4 Mpa burst pressure). In the second or *straight-through* mode the thin steel secondary diaphragm is replaced with a light cellophane diaphragm (23 μm, 90 kPa burst pressure) which ruptures with the arrival of the shock. The second mode is the preferred mode of operation. Because the primary shock speed is overtailored, the reflection of the shock in the first mode would be expected to contaminate the driver gas.

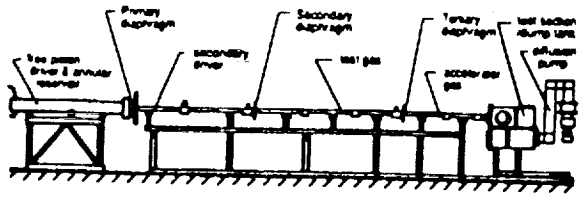

Figure 1. pilot Superorbital Expansion Tube facility

In both modes the resulting shock wave propagates into the shock tube and accelerates the quiescent test gas. The shock wave traverses the shock tube and ruptures the light tertiary diaphragm (9 μm grocery wrap, 20 kPa burst pressure) and then accelerates to a higher velocity as it passes into low pressure accelerator gas (helium or air) contained in the acceleration tube (1.289 m). The test gas following the shock is also further accelerated as it is expanded unsteadily into the acceleration tube. At the exit of the acceleration tube the test gas passes over the model mounted in the test section. Helium is the preferred accelerator gas as it has a low density and subsequently lower Mach number giving lower pressure and temperature ratios than air for the same shock speed.

It is the addition of the secondary driver section which, under the appropriate operating conditions, is able to boost the performance of the facility beyond that of a standard free piston driven expansion tube as reported by Neely and Stalker (1991). In an expansion tube the performance of the facility, that is the flow enthalpy that can be produced, is a function of the strength of the initial incident shock wave produced by the driver. Morgan and Stalker (1992) describe the performance enhancing mechanism of the secondary driver with the use of a wave diagram of the flow (Fig. 2).

The primary and secondary driver gases in regions 2 and 3 respectively, which are both helium have the same pressure and velocity. Thus if the free piston driver is operated so that the primary shock is overtailored then the helium in region 2 will have the higher speed of sound and will thus be able to drive a higher shock speed through the test gas contained in the adjacent shock tube than would be possible for a single driver arrangement where region 3 drives the test gas shock directly.

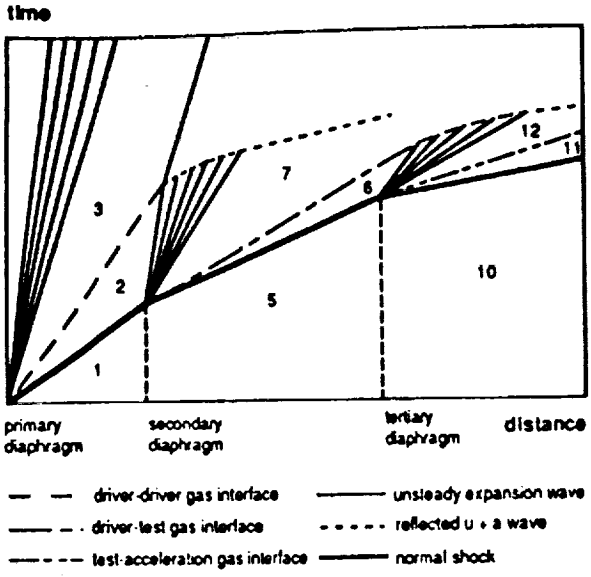

Figure 2. wave diagram of SEXT flow process

EXPERIMENTAL TESTING

To investigate the performance of the Superorbital Expansion Tube concept, a series of runs were carried out in the pilot facility using a range of filling pressures in the secondary driver (40-200 kPa), shock tube (150-10000 Pa) and acceleration tube (1-380 Pa) sections. Two distinct experimental conditions produced in the facility are set out in Table I.

Table I. experimental conditions

flow condition		78 MJ	106 MJ
run number		220	231
secondary driver fill pressure	(kPa)	60	60
shock tube fill pressure	(Pa)	500	800
acceleration tube fill pressure	(Pa)	17	10
accelerator gas		air	He
shock tube length	(m)	3.150	1.625
final primary shock speed	(ms^{-1})	6 450	-
final secondary shock speed	(ms^{-1})	6 880	7 280
final tertiary shock speed	(ms^{-1})	10 500	13 000

For the lower enthalpy condition, with a final tertiary shock velocity of 10.5 kms^{-1}, a period of quasi-steady flow in excess of 50 µs was observed. It was observed that for the high shock velocities produced in the shock tube (> 8 kms^{-1}) there was severe attenuation of the flow with the shock being slowed by up to 2 kms^{-1} when it reached the tertiary diaphragm. To avoid the resulting decrease in performance due to flow attenuation, sections of the shock tube were removed to reduce its length (to 1.625 m) so that the secondary shock reaches the tertiary diaphragm before any significant attenuation has occured. The second condition was produced with this configuration. Final tertiary shock velocities in excess of 13 kms^{-1} were achieved where a period of quasi-steady usable test flow of 15 µs duration was observed.

Static pressure levels were recorded at a number of stations down the length of the three sections. A typical record of wall static pressures measured in the acceleration tube is shown in Figure 3, illustrating the development of a region of steady flow between the tertiary shock wave and the trailing expansion wave, which terminates the test flow, as the flow is expanded.

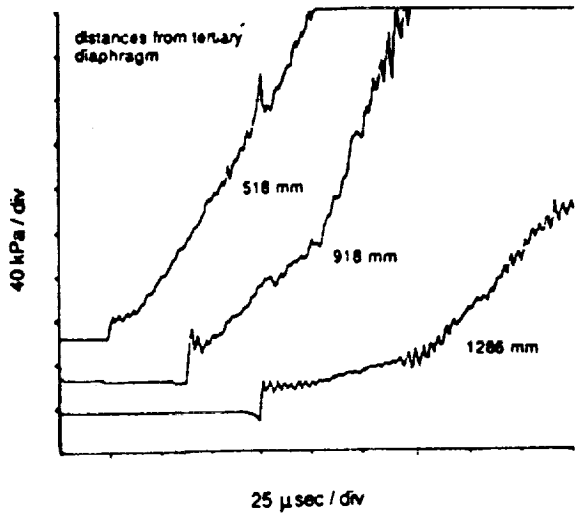

Figure 3. acceleration tube wall static pressure histories for 78 MJ condition

A standard PCB piezoelectric pressure transducer, shielded from the direct flow, and an aluminium/lead bar gauge, utilising piezoelectric film, were used alternately to measure the centreline pitot pressure levels in the test flow. Typical wall static pressure and centreline pitot pressure histories recorded at the exit of the acceleration tube are shown in Figure 4 for the two different enthalpy conditions. For the 106 MJ condition the static pressure trace shown is from an equivalent run (R226) as the exit trace was corrupted. High frequency oscillations visible on the traces are consistent with ringing of the gauges and are not a flow phenomenon.

Pitot pressure levels were observed to rise during the period of test flow as expected from the analytical model of the test flow which predicts non uniform gas states in region 8. The calculated pressure levels that bound these test flows are indicated on Figure 4 and can be seen to follow the observed behaviour. As can be seen from the pressure traces, problems were experienced with the rise time of the gauges used to measure the pitot pressure. In the case of the PCB gauge this was due to the filling of the cavity between the transducer and its shield. While the bar gauges, which were custom made, do not require protective shielding, calibration tests indicate long rise times of 4 - 6 µs. Development of the bar gauges is continuing in house, and an improved response is anticipated.

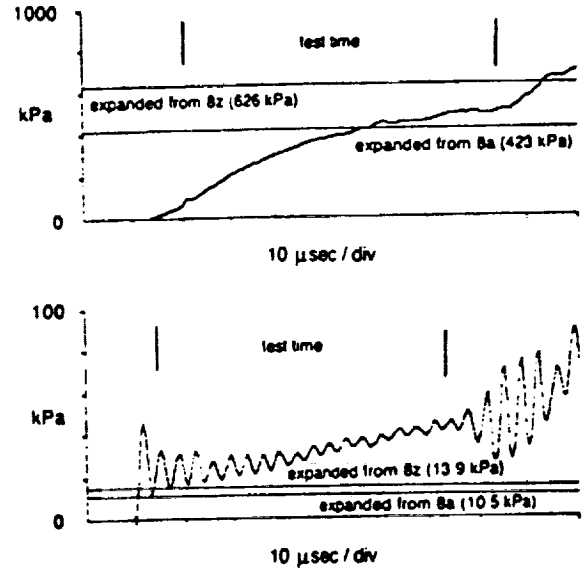

Figure 4 (a) centreline pitot pressure histories and corresponding exit wall static pressure histories for 78 MJ test condition

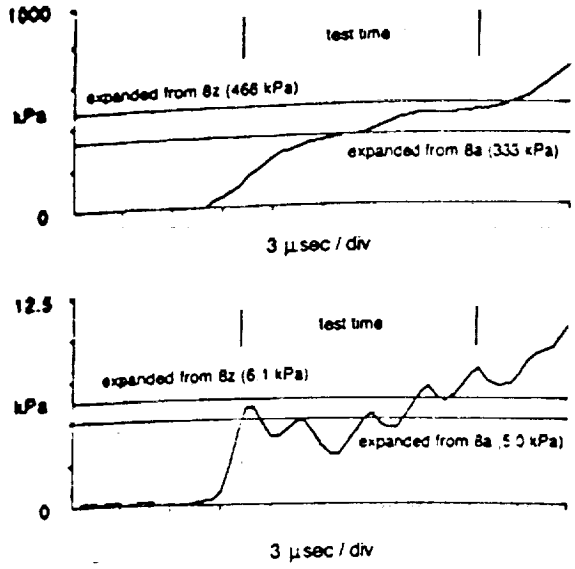

Figure 4 (b) centreline pitot pressure histories and corresponding exit wall static pressure histories for 106 MJ test condition

ANALYSIS OF THE FLOW

This paper deals with the analysis of the flow of test gas through the shock tube and acceleration tube resulting in the final test flow in the test section. No attempt is made here to model the driver flow although the perfect gas analysis from Morgan and Stalker (1992) was used to help determine the optimum driver conditions.

The observed shock speeds in the shock and acceleration tubes are used in conjunction with the known quiescent test gas pressures in these two sections to calculate the secondary and tertiary shock strengths. Real gas calculations of these conditions are made using an equilibrium analysis. The static pressure and the entropy level behind the shock are determined and these are used to determine the full gas state via an equilibrium scheme (Rizkalla 1990).

It should be noted that although the shock heated test gas in region 6 is nominally indicated as being a region of uniform flow in Figure 5, it is in fact a region in which there is a velocity gradient induced by viscous effects. The Mirels analysis (1962) was used to predict the velocity of various points in the the region and this was found to have a significant effect on the final values of pitot pressure calculated for the expanded test flow.

The lightest possible tertiary diaphragm is used to separate the air test gas and the helium accelerator gas. Ideally this diaphragm would rupture instantaneously and would have no further influence on the flow. But as has been reported in previous expansion tube work (Shinn and Miller 1977) even the lightest diaphragm does not behave ideally resulting in two principal non-ideal effects. These are reflection of the incident secondary shock wave into the oncoming test gas before the diaphragm ruptures and momentum loss from the expanded flow due to the energy required to accelerate the diaphragm mass after rupture. This nonideal behaviour can be observed on a more detailed wave diagram for the flow in the vicinity of the tertiary diaphragm (Fig. 5).

These non-ideal effects must be accounted for and have a significant influence on the calculated test gas conditions. The slug of shock heated test gas that arrives at the tertiary diaphragm (Fig.5, region 6) is processed by the reflected shock wave (region 8) and then passes through the unsteady expansion which develops behind the accelerator-test gas interface. The source of shock heated test gas for the expansion is non uniform. The first part of the test gas slug to arrive (region 8a), is stagnated by the shock that is reflected from the tertiary diaphragm and is then expanded from this state. Once the diaphragm ruptures though, this stagnation of the flow no longer occurs as the reflected shock is washed downstream by the flow and the reflected shock attenuates (region 8b..z). The test gas is thus expanded from a range of initial states.

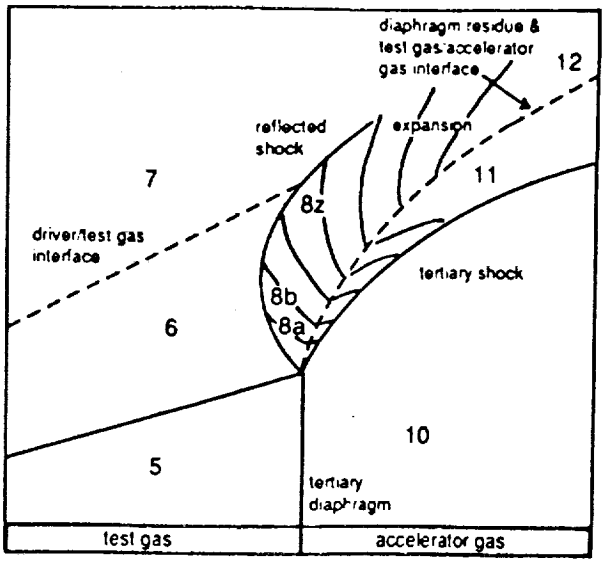

Figure 5. wave diagram for the flow near the tertiary diaphragm

Calculation of the expansion process and the resulting state of the test gas must thus be made for a range of starting conditions. It is perhaps easiest to consider the two bounding extremes of the starting flow. The first is the initial part of the test gas slug (region 8a) which is taken as initially stationary with conditions determined for a fully reflected shock bringing the gas to rest. The other extreme is the terminating case (region 8z) where the interface separating the test gas and secondary driver gas catches up with the attenuated reflected shock. The calculation of this state is less straightforward.

To determine the strength of the reflected shock at interface catchup it is necessary to model the behaviour of the tertiary diaphragm after rupture. The residual influence of the tertiary diaphragm after rupture is represented by the inertia of the diaphragm as it is washed downstream (Morgan and Stalker 1992) in a similar form to the action of a free piston. The mass of the ruptured diaphragm is accelerated downstream by the pressure behind the reflected shock. As this occurs expansion waves propagate upstream from the diaphragm, eventually attenuating the reflected shock to a Mach wave. The accelerating diaphragm also sends compression waves downstream into the accelerator gas which converge to form the tertiary shock.

As the reflected shock and the diaphragm are initially in close proximity and the sound speed behind the reflected shock is very high, it is assumed that the expansion waves emanating from the diaphragm immediately catch up with the reflected shock, thus specifying a region of uniform gas velocity between the reflected shock and the diaphragm remnants. The velocity of the diaphragm remnants is determined by the integration of its acceleration from rupture. The diaphragm velocity may then be used with the known incoming test gas velocity to determine the strength of the shock at each moment. As the reverse shock traverses the test gas it induces an entropy change in the gas which must be determined. The period it takes the shock to traverse the slug of test gas is small (< 15 μs) and it can be shown that only a small displacement of the diaphragm will occur in this time indicating that it is permissible to determine the reverse shock strength from simple theory. It should also be noted that as the initial pressure loadings on the tertiary diaphragm are small (less than 1/25th of the burst pressure) there will be no significant pre-deformation of the diaphragm suggesting one dimensional behaviour and circumferential failure of the light diaphragm material.

To determine the velocity of the gas behind the attenuated reverse shock at the point of interface catchup, it is assumed via Mirels (1963) theory that the velocity of the test flow contained between the reflected shock and the upstream interface is matched to the velocity of the interface. The gas velocity across the shock is calculated and is then expanded through the unsteady expansion.

Once these starting conditions are determined the remnants of the diaphragm on the flow are disregarded as they can have no further effect on the flow entropy. The two starting conditions are used to calculate the limits of the range of test gas flows produced at the end of the unsteady expansion. Calculation of the changing state of the flow through the unsteady expansion is implemented in a stepwise manner. The expansion process is divided up into a large number (100) of velocity increments which proceed from the calculated starting velocity of the test gas (State 8) to the final velocity after expansion (State 12). This final velocity is set equal to the observed tertiary shock speed by the assumption of full Mirels development of the slug length in the accelerator gas. Calculation across each increment is governed by the standard equation for an unsteady expansion wave which relates the change in static enthalpy to the change in velocity and the local speed of sound.

$$dh = -a\,du \qquad (1)$$

A calculation of the entropy and static enthalpy of the flow is made at the initial state 8. For equilibrium or frozen flow the expansion is isentropic. The gas condition is uniquely defined by the enthalpy and entropy and the EQSTATE code (Rizkalla 1990) is used to iterate, at the end of each computed step, a solution for pressure, temperature and gas composition. The CREK subroutines developed by Pratt and Wormeck (1976) are used to calculate the equilibrium composition at each point. The process proceeds until the final velocity is reached, thus supplying the final state of the test gas. The calculated gas states of the test flow (region 12) at the end of the acceleration tube, are set out in Table II for the two enthalpy conditions discussed in the previous section.

Table II. final test flow states calculated using equilibrium and frozen theory

flow condition	78 MJ		106 MJ	
calculation method	equilib.	frozen	equilib.	frozen
velocity (ms^{-1})	10 500	10 500	13 000	13 000
temperature (K)	5 901	236	5 526	8
pressure (Pa)	13 914	96	6 103	0.017
density ($10^{-2}\,kgm^{-3}$)	0.57	0.072	2.76	0.0004
Mach number	5.7	20.1	7.4	95
ratio of spec. heats	1.40	1.64	1.39	1.62
pitot pressure (kPa)	626	79.8	466	0.6
total pressure(MPa)	15.2	31.0	37.4	16.2

The resulting calculation of static and pitot pressure levels for each starting condition can also be seen in Figures 4a. and 4b., superimposed on those pressures measured in the experimental flow. A comparison can be made here with the effect of assuming a frozen expansion process. Calculations of the expanded state of the test gas required to match the observed final velocity for a frozen expansion were made by fixing the chemical state of the test gas after processing by the reflected shock (State 8). The resulting expanded states are set out in Table II. It can be seen that the resulting temperatures and static and pitot pressures of the expanded test gas are unrealistically low giving support to the assumption of an approximately equilibrium process occurring through the unsteady expansion. It can thus be seen that to achieve the high enthalpy flow conditions produced by the Superorbital Expansion Tube in experiments, the flow energy used to dissociate the test gas when it is shock heated in the shock tube must be at least partially restored to the flow through recombination of the test gas through the unsteady expansion. If this energy remained frozen as chemical energy the observed test conditions could not be achieved. In the Superorbital Expansion Tube, the total enthalpy is not fixed at any point in the flow as it is in shock tunnel facilities. Rather it relies on the enthalpy multiplication mechanism of the unsteady expansion and thus any increase in energy due to recombination through the unsteady expansion will be multiplied by the expansion to produce the elevated final enthalpies recorded.

CONCLUSIONS

A small pilot facility has been set up at The University of Queensland to demonstrate the concept of the Superorbital Expansion Tube, a free piston driven, triple diaphragm, impulse facility. The pilot facility has been operated to produce quasi-steady test flows with shock velocities in excess of 13 kms^{-1} and with a duration of usable test flow of 15 μs. Such high enthalpy flows are of interest in the design of any vehicle used to traverse an atmosphere at velocities exceeding Earth orbital velocity.

Consideration of the effects of boundary layer growth and non ideal diaphragm rupture on the flow have allowed a better understanding of the flow mechanism and enabled more accurate matching of calculated and observed test flow states. It has also been shown conclusively that much better agreement with experiment is achieved if the unsteady expansion process is modelled as an equilibrium process rather than as a frozen chemistry process.

These initial results have demonstrated the viability of the Superorbital Expansion Tube concept and while further testing on the pilot facility will continue, work is now proceeding on the design of a larger scale, medium size facility at The University of Queensland.

ACKNOWLEDGEMENTS

The authors gratefully acknowledge the financial support of the Australian Research Council.

REFERENCES

MIRELS, H (1963) Test Time in Low -Pressure Shock Tubes. The Physics of Fluids, 6.9

MORGAN R G and STALKER R J (1992) Double Diaphragm Driven Free Piston Expansion Tube. Proceedings of the 18th International Symposium on Shock Waves, Sendai 1991

NEELY A J, STALKER R J and PAULL A (1991) High enthalpy, hypervelocity flows of air and argon in an expansion tube. The Aeronautical Journal, June/July, 175-186

PRATT, D T and WORMECK, J J (1976) CREK: A computer program for calculation of combustion reaction equilibrium and kinetics in laminar or turbulent flows. Report WSU-ME-TEL-76-1, Washington State University

RESLER, E L and BLOXSOM, D E (1952) Very High Mach Number Flows By Unsteady Flow Principles, limited distribution monograph, Cornell University Graduate School of Aeronautical Engineering

RIZKALLA, O (1990) EQSTATE: program to calculate the equilibrium or frozen properties of a supersonic gas flow at the static and stagnation points upstream and downstream of a shock wave. General Applied Science Laboratories Inc., New York

SHINN, J L and MILLER, C G, (1978) Experimental Perfect-Gas Study of Expansion-Tube Flow Characteristics. NASA Technical Paper 1317

REPORT DOCUMENTATION PAGE

Form Approved
OMB No. 0704-0188

Public reporting burden for this collection of information is estimated to average 1 hour per response, including the time for reviewing instructions, searching existing data sources, gathering and maintaining the data needed, and completing and reviewing the collection of information. Send comments regarding this burden estimate or any other aspect of this collection of information, including suggestions for reducing this burden, to Washington Headquarters Services, Directorate for Information Operations and Reports, 1215 Jefferson Davis Highway, Suite 1204, Arlington, VA 22202-4302, and to the Office of Management and Budget, Paperwork Reduction Project (0704-0188), Washington, DC 20503.

1. AGENCY USE ONLY *(Leave blank)*	2. REPORT DATE	3. REPORT TYPE AND DATES COVERED
	December 1993	Contractor Report, CY 1992

4. TITLE AND SUBTITLE
Shock Tunnel Studies of Scramjet Phenomena, Supplement 8

5. FUNDING NUMBERS
505-70-62-16
NAGW-674

6. AUTHOR(S)
R.J. Stalker, P. Hollis, G. A. Allen, G. T. Roberts, S. Tuttle, R. J. Bakos, R. G. Morgan, M. V. Pulsonetti, C. Brescianini, D. R. Buttsworth, K. Skinner, L. Porter, D. Mee, J. Simmons, G. Kelly, N. Ward, and A. Neely

7. PERFORMING ORGANIZATION NAME(S) AND ADDRESS(ES)
University of Queensland
Department of Mechanical Engineering
St. Lucia, Queensland
AUSTRALIA

8. PERFORMING ORGANIZATION REPORT NUMBER

9. SPONSORING / MONITORING AGENCY NAME(S) AND ADDRESS(ES)
National Aeronautics and Space Administration
Langley Research Center
Hampton, VA 23681-0001

10. SPONSORING / MONITORING AGENCY REPORT NUMBER
NASA CR-191573

11. SUPPLEMENTARY NOTES
Langley Technical Monitor: R. Clayton Rogers
Interim Report 0 Supplement 8, NAGW-674

12a. DISTRIBUTION / AVAILABILITY STATEMENT
Unclassified - Unlimited

Subject Category 34

12b. DISTRIBUTION CODE

13. ABSTRACT ***(Maximum 200 words)***

Reports by the staff of the University of Queensland on various research studies related to the advancement of scramjet technology are presented. These reports document the tests conducted in the reflected shock tunnel T4 and supporting research facilities that have been used to study the injection, mixing, and combustion of hydrogen fuel in generic scramjets at flow conditions typical of hypersonic flight. In addition, topics include the development of instrumentation and measurement technology, such as combustor wall shear and stream composition in pulse facilities, and numerical studies and analyses of the scramjet combustor process and the test facility operation. This research activity is Supplement 8 under NASA Grant NAGW-674.

14. SUBJECT TERMS
Scramjets, pulse facilities, hypersonic, hypervelocity, shock waves, combustion, shock tubes

15. NUMBER OF PAGES
133

16. PRICE CODE
A07

17. SECURITY CLASSIFICATION OF REPORT	18. SECURITY CLASSIFICATION OF THIS PAGE	19. SECURITY CLASSIFICATION OF ABSTRACT	20. LIMITATION OF ABSTRACT
Unclassified	Unclassified	Unclassified	